J Solid State Electrochem (2005) 9: 138–145
DOI 10.1007/s10008-004-0564-3

ORIGINAL PAPER

Adel Attia · Markéta Zukalová · Jiří Rathouský
Arnošt Zukal · Ladislav Kavan

Mesoporous electrode material from alumina-stabilized anatase TiO_2 for lithium ion batteries

Received: 26 January 2004 / Accepted: 26 April 2004 /

Abstract A mesoporous electrode material whose structure is composed of anatase nanocrystals stabilized by alumina is reported. Powder X-ray diffraction shows the anatase phase only, but micro-Raman spectroscopy shows that the materials have a core-shell morphology with grains of bulk anatase covered by a thin rutile layer on the surface. This structure is unique when compared to analogous materials stabilized by zirconia (PNNL-1). Nitrogen adsorption isotherms demonstrate a monotonous increase in surface area and mesopore volume with increasing Al content. Thin film electrodes from these materials were characterized by lithium insertion electrochemistry. Cyclic voltammograms exhibit significant differences in Li accommodation in Al-free and Al-stabilized materials.

Keywords Titanium dioxide · Alumina · Lithium battery · Mesoporous materials

Introduction

The use of nanocrystalline oxide materials in Li-ion batteries results in higher charging rates due to smaller transport distances in the solid host [1]. By decreasing the crystal dimensions, the solid-state Li^+ diffusion is progressively replaced by surface-confined Li-storage; in other words there is a natural link between batteries and supercapacitors in the area of nanosized crystals [1]. However, ultrasmall crystals are handicapped by sluggish Li-transport [2, 3, 4] and by charge irreversibility due to parasitic surface reactions [3]. Hence, there is an optimal crystal size for the given host material for fast Li-charging/discharging [3].

Anatase TiO_2 electrodes are used in solar cells, lithium batteries and electrochromic devices [5, 6, 7, 8]. Nanocrystalline TiO_2(anatase) is a promising electrode material for Li-ion batteries, due to its good Li-storage capacity, cycling-stability and safety against overcharging [9]. Its non-toxicity, environmental compatibility, and low price are other practical advantages of TiO_2. However, the performance of nanocrystalline TiO_2 for Li-storage is significantly controlled by the particle morphology [7, 8, 10, 11]. For instance, the TiO_2 nanosheets clearly exhibit charging in the supercapacitive regime [11], and this effect is also found in mesoporous anatase made by supramolecular templating [10].

The surfactant-templated synthesis of TiO_2 mesoporous molecular sieves (analogous to siliceous mesoporous molecular sieves such as MCM-41) was announced in 1995, but this work was later questioned [12]. The synthetic procedures that appeared to be successful for mesoporous silica usually fail for TiO_2. The reason is that the original mesoporous TiO_2/template composite easily collapses during calcination (detemplating) because of the easy crystallization of titanium dioxide [12, 13]. The only exception to this rule is templating by triblock copolymers, as pioneered by Stucky et al [14, 15, 16], which gives well-organized mesoporous anatase materials upon calcination [10, 14, 15, 16, 17]. An alternative synthetic strategy is based on protecting the surfactant-templated mesoporous TiO_2framework by deliberately adding an inorganic component. This synthetic protocol was first demonstrated by Elder et al [18] on zirconia-stabilized TiO_2 (Zr/Ti = 1/3), called PNNL-1. The material contained anatase crystallites, ~3 nm in size, which were separated by a solid solution of amorphous $Zr_xTi_{1-x}O_4$. It exhibited enhanced thermal stability and interesting electrochemical properties compared to those of ordinary nanocrystalline anatase [7].

A. Attia (✉)
Department of Physical Chemistry,
National Research Centre,
El-Tahrir St., Dokki, 12622 Cairo, Egypt
E-mail: adel_attia@hotmail.com
Fax: +002-02-3370931

A. Attia · M. Zukalová · J. Rathouský · A. Zukal · L. Kavan
J. Heyrovský Institute of Physical Chemistry,
Academy of Sciences of the Czech Republic,
Dolejškova 3, 182 23 Prague 8, Czech Republic

There are various examples of advanced materials based on the titania/alumina system. Alumina coating is widely used for stabilization of TiO_2 (rutile)-based white pigments against photodecomposition [19]. Recently, Durrant et al [20] and Fujishima et al [21] reported that a similar alumina coating on TiO_2 (anatase) also prevents charge recombination in dye sensitized solar cells, and so leads to significant improvement of the efficiency of solar energy conversion. Aluminum was found to be crucial to the stabilization of the anatase lattice during chemical transport reactions in the TiO_2-$TeCl_4$ systems, and large anatase single crystals could only be synthesized with the aid of Al-stabilization [22]. A special form of mesoporous alumina has been frequently used as a template for the fabrication of anatase nanotubes and nanowires [23, 24, 25, 26, 27]. Zhang and Banfield [28] reported that the anatase-to-rutile phase transformation is retarded to higher temperatures with the addition of Al_2O_3 to anatase TiO_2. This is reminiscent of the analogous behavior of zirconia in a composite with anatase [7].

Ceder et al [29] were first to report that Al-doping is beneficial for the development of cathode materials for Li-ion batteries based on $LiCoO_2$and $LiMn_2O_4$. By theoretical arguments following from first-principle calculations, as well as by their experimental verification, it was demonstrated that Al-substitution in these oxides increases the formal potential of Li-insertion, increasing the energy density of practical batteries. Wakihara et al [30] reported that Al doping increased the cyclability of spinel $Li_xAl_yMn_{2-y}O_4$cathodes. Analogously, the cycle performance and diffusion coefficient of Li^+ in $LiNiO_2$ was improved by Al-substitution. However, the insertion potential of Li in $Li_xAl_yNi_{1-y}O_2$was actually smaller than that of $LiNiO_2$, which contrasts with the previously reported behavior of $LiCoO_2$ [29]. For all of the above-mentioned reasons, we were motivated to study the effect of alumina on the electrochemical performance of anatase TiO_2, and the results of our investigation are summarized in this paper.

Experimental

Materials

The synthesis of Al-stabilized titania [31] followed essentially the same synthetic protocol as that of Zr-stabilized titania [7, 18]. A solution of Keggin cations $Al_{13}O_4(OH_{24})^{7+}$was prepared by dissolving 13.1338 g of $AlCl_3.6H_2O$ in 420 ml of water, and the pH was adjusted to 3.95 with concentrated ammonium hydroxide. This solution was slowly added to a solution of $(NH_4)_2Ti(OH)_2(C_3H_2O_3)_2$(Tyzor LA, DuPont) and cetyltrimethylammonium chloride (CTAC, Lonza) as described below.

For sample A, 8.27 g of Tyzor and 8.82 g of CTAC solution were combined. Then 6.62 ml of the solution of Keggin cations was diluted to 80 ml with water, and was slowly added to the Tyzor/CTAC mixture with vigorous stirring. A white precipitate formed immediately, and this was aged in a Teflon bomb at room temperature overnight, one day at 70 °C, and 2 days at 100 °C, and subsequently isolated by washing and centrifuging. The prepared material was calcined at 450 °C for 3 h.

For samples B and C, the corresponding syntheses were performed in a similar fashion to that for sample A, except, in the case of sample B, 6.82 g of Tyzor and 33.9 ml of the Keggin cations solution were used, and, in the case of sample C, 4.54 g of Tyzor and 66.18 ml of the Keggin cations solution were used.

The Ti/Al atomic ratios found by elemental analysis after calcination were 25, 11, and 6 for samples A, B, and C, respectively. A reference Al-free blank material (further abbreviated BL) was prepared by an identical synthetic protocol as for samples A–C, but without the addition of the solution of Keggin cations. Another reference Al-free material was pure anatase from Bayer (PKP09040, surface area 154 m^2/g).

Characterization

Adsorption isotherms of nitrogen (Linde, purity 5.6) at 77 K were measured on a Micromeritics ASAP 2010 instrument. Before the adsorption measurement, all samples were degassed at 350 °C overnight. X-ray diffraction measurements were carried out with a Siemens D-5005 diffractometer in the Bragg-Brentano geometry using Cu $K\alpha$ radiation. The lattice constants were calculated using the Eva Diffracplus v5.0 software. Micro-Raman spectra were measured using a Jobin-Yvon T64000 spectrometer equipped with an Olympus BH2 microscope. The spectra were excited in a back scattering geometry by Ar^+ laser (Innova 305, Coherent), $\lambda = 514.5$ nm. The laser beam was focused either to the surface of one selected grain or into its bulk. The focus length was adjusted and measured by a micrometer manipulator on the Olympus microscope.

Preparation of electrodes

The electrodes were prepared as described in [7, 8], by using CH_3COOH and Triton X-100 as dispersing agent and surfactant, respectively. The powder material was first dispersed into a paste by slow mixing with 0.1 M CH_3COOH under continuous mortaring. After ~20 mins of homogenization, the slurry was mixed with Triton X-100 and further homogenized. The SnO_2(F) coated glass from Nippon sheet Glass, 10 Ω/square, served as a support for the electrode preparation. Scotch tape at the edge of the support defined the film thickness and left part of the support uncovered for electrical contact. The film was finally calcined for 3 h in air at 450 °C. Alternatively, a titanium grid (5×15 mm, Goodfellow) was used as the electrode support. These electrodes were prepared by dip-coating; the coated area was ~5×5 mm. The prepared electrodes were dried in air, and finally calcined as in the case of $SnO_2(F)$ electrodes. The Ti-supported electrodes usually showed better mechanical stability during electrochemical cycling, but their electrochemical performance was, in general, comparable.

Electrochemistry

Electrochemical measurements were carried out in a one-compartment cell using an Autolab Pgstat-30 (Ecochemie) potentiostat controlled using GPES-4 software. Both the reference and auxiliary electrodes were from Li metal, so potentials are referred to the Li/Li^+ (1 M) reference electrode. $LiN(CF_3SO_2)_2$(Fluorad HQ 115 from 3 M) was dried at 130 °C/1 mPa. Ethylene carbonate (EC) and 1,2-dimethoxyethane (DME) were dried over a 4 Å molecular sieve (Union Carbide). The electrolyte solution, 1 M $LiN(CF_3SO_2)_2$ + EC/DME (1/1, v/v) contained 15–40 ppm H_2O as determined by Karl Fischer titration (Metrohm 684 coulometer). All operations were carried out under argon in a glove box (Labstar 50, M. Braun, GmbH; the working atmosphere typically contained < 1 ppm H_2O and < 1 ppm O_2). In all cyclic voltammetry experiments, the direction of the first potential sweep was (1) equilibrium potential, (2) lower vertex potential, and (3) upper vertex potential.

Results and discussion

Structures of the samples

Figure 1 shows the X-ray diffractograms of the Al-stabilized samples A, B and C. They can be indexed as pure anatase, without any signatures from other phases (alumina, rutile, and so on). The coherent length of the anatase nanocrystals was determined from the line broadening using the Scherrer equation (Table 1). Apparently, the size of nanocrystals decreases with increasing Al content. The lattice constants were calculated from powder diffractograms (as in Fig. 1). The *a*constant increases and the *c* constant decreases with increasing Al content, even if we refer our data to the same parameters for Al-free nanocrystalline anatase (Table 1). The contraction of the *c* axis and elongation of the *a*axis causes an overall decrease in the unit cell per formula unit ($a^2c/2$). The differences are rather small, and we should also consider the experimental error in analyzing broad X-ray diffraction peaks (Fig. 1) and the natural variations of lattice constants for various preparations even in the case of pure nanocrystalline anatase. Hence, the lattice constants may not necessarily scale with the Al-content monotonously. On the other hand, the contraction of the anatase unit cell is reminiscent of the same effect in Al-doped rutile, where the cells shrinks steadily with increasing Al-content up to ~0.8 mol% Al_2O_3, which is considered to be the "solubility" of Al_2O_3 in rutile [19].

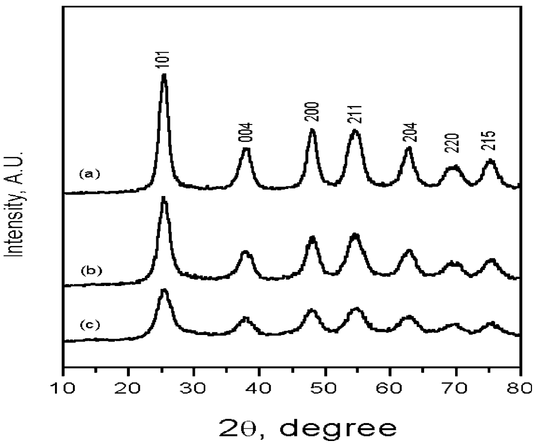

Fig. 1 XRD patterns of samples A–C indexed as the anatase phase

The solubility of Al_2O_3 in anatase is unknown [19], but we may assume, from the analogy, that Al can take the form of either isomorphic (substitutional or interstitial) doping in the anatase lattice, or it can form some X-ray amorphous separate phase of ultrasmall nanocrystals (Al_2O_3 or $Ti_xAl_yO_2$) embedded in-between the anatase nanocrystals. The isomorphic doping by Al is also supposed for other oxidic structures [30, 32], while in the Al-TiO_2 system, it plays a decisive stabilizing role for the formation of macroscopic crystals (containing ~0.2% Al) [22]. Apparently, the substitution of Ti^{4+} (ionic radius 0.605 Å) by Al^{3+} (ionic radius 0.535 Å, octahedral O-coordination) gives rise to the compression of the unit cell and/or TiO_6 octahedra. The O-vacancies, which are created by isomorphic Al^{3+}/Ti^{4+} substitution or interstitial doping, provide the driving force for the lattice distortion [19], and for the structural stabilization of the anatase single crystal [22].

The isomorphic substitution of Ni by Al in $LiNiO_2$ analogously enhances the structural stability [32]. On the

Table 1 Structural and electrochemical properties of Al-doped TiO_2 samples, compared to those for pure anatase

Property	Sample A	Sample B	Sample C	TiO_2 anatase	
				Bayer[a]	BL[b]
Ti/Al (atomic)	25	11	6	∞	∞
Al_2O_3(wt%)	2.5	5.5	9.6	0	0
Crystal size (nm)	5.6	4.1	3.0	10	21
a-constant (Å)	3.7810	3.8075	3.7875	3.7760	–
c-constant (Å)	9.3807	9.3664	9.3363	9.5139	–
$S_{BET}(cm^3/g)$	55	92	185	154	73
$V_{ME}(cm^3/g)$	0.036	0.062	0.110	–[c]	–[c]
D_{ME} (nm)	2.6	2.7	2.4	–[c]	–[c]
E_f (V vs. Li/Li^+)	1.85	1.84	1.83	1.88	1.85
$k_0 \cdot (10^{10} cm/s)$	2.3	0.9	0.9	3.0	5.0
$D \cdot (10^{17} cm^2/s)$	5.4	6.5	6.0	3.4	4.6

S_{BET} = BET surface area; V_{ME} = mesopore volume; D_{ME} = mean mesopore diameter; E_f = formal potential of Li-insertion; k_0 = rate constant of Li-insertion; D = chemical diffusion coefficient of Li^+; [a] Bayer PKP09044 (reference material of pure anatase); [b] BL = blank synthesized as A–C, but without addition of Al-precursor; [c] mesoporous ordering is not defined

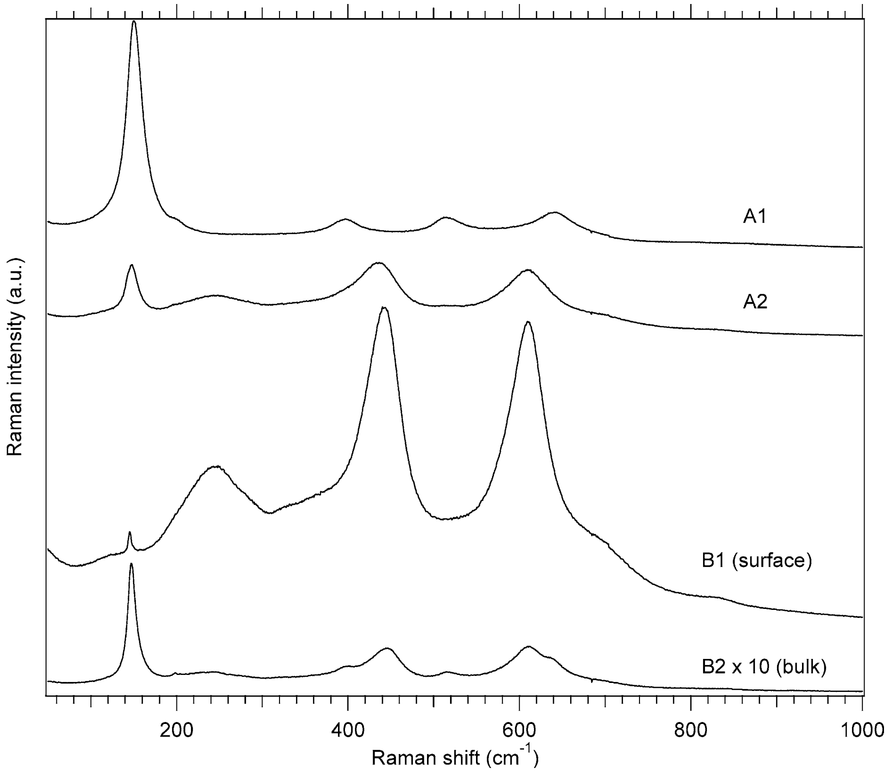

Fig. 2 The micro-Raman spectra. A1: typical spectrum of sample A; A2: selected grain of sample A showing the rutile phase on the surface; B1: sample B with laser focus at the surface; B2: the same position of laser spot as for B1, but laser focus moved by ~2 μm into the bulk. The spectra are offset for clarity, but the intensity scales are identical for spectra A1, A2, and B1. The intensity was multiplied by a factor of 10 for the spectrum B2

other hand, bimodal morphology is assumed in zirconia-stabilized anatase [18], since the formation of solid solution of Zr in anatase is limited to low concentrations of Zr only [8]. We cannot distinguish from the present X-ray data (Fig. 1) between the isomorphic doping or bimodal structures. However, oxygen vacancies in the lattice can hardly compensate for large concentrations of Al in TiO_2, as for example, in sample C, and both structures need to coexist in the Al-rich materials. Assuming the Al_2O_3 solubility to be similar in anatase and rutile (≈0.8%) [19], all of our samples A–C are already saturated with substitutional/interstitial doping, and their structures are bimodal. From the standard Gibbs energy of formation, the Al_2O_3 is more stable (−1582.4 kJ mol^{-1}) than TiO_2 (−889.5 kJ mol^{-1}). Consequently, the strong covalent interactions Al-O-Ti, either within the lattice or at the interface of the anatase/Al-rich phase, contribute to the distortion of the anatase lattice.

Further insight into the structure and phase composition of our materials is obtained from micro-Raman spectroscopy. This technique allows a local analysis to be carried out on a sample area of ~1×1 μm^2. It upgrades the data from powder X-ray diffraction. The latter technique gives bulk information only, evidencing the sole presence of anatase in samples A–C (Fig. 1). The micro-Raman spectra of sample A (with the lowest content of Al) usually confirmed the presence of pure anatase. Curve A1 in Fig. 2 is a typical Raman spectrum of the sample A. Sometimes we were able to select grains of different spectra in sample A (see curve A2 in Fig. 2), which is characteristic of rutile. However, a more detailed investigation indicated that sample A was not composed of isolated grains of anatase and rutile, but that the rutile formed a surface layer on the anatase core.

This core/shell morphology is expressed more explicitly in sample B (see Fig. 2). The laser focus was moved from the surface (B1) to ~2 μm into the bulk of the material (B2). Such Raman depth profiling indicates that the surface layer is composed of rutile, whereas the bulk of the sample is formed of anatase (the spectrum B2 is actually a convolution of the surface and bulk signal, due to laser focusing). Similar behavior was also found for sample C [31]. Our data is reminiscent of the data obtained by Zhang et al [33], who have reported on the micro-Raman detection of rutile and brookite on the surface of anatase grains made by vapor hydrolysis of Ti(IV) tetraisopropoxide. Also in this case, the core/shell morphology was selectively detected by micro-Raman spectroscopy, even though the material exhibited only the anatase diffraction pattern [33].

The mechanism of rutile formation in Al-stabilized materials is unknown. We may only note that, in contrast to the materials A–C, no rutile shell was detected in the Zr-stabilized material PNNL-1, prepared by a very similar synthetic protocol [7]. All Raman spectra of PNNL-1 showed the anatase peaks independent of the laser focusing.

Nitrogen adsorption isotherms on samples A–C are shown in Fig. 3. The shapes of these isotherms are similar to those of aluminosilicate mesoporous molecular sieves with a pore size under 3 nm [34]. They are characterized by an almost linear increase in the adsorbed amount in the region of p/p_o between 0.1–0.4, in

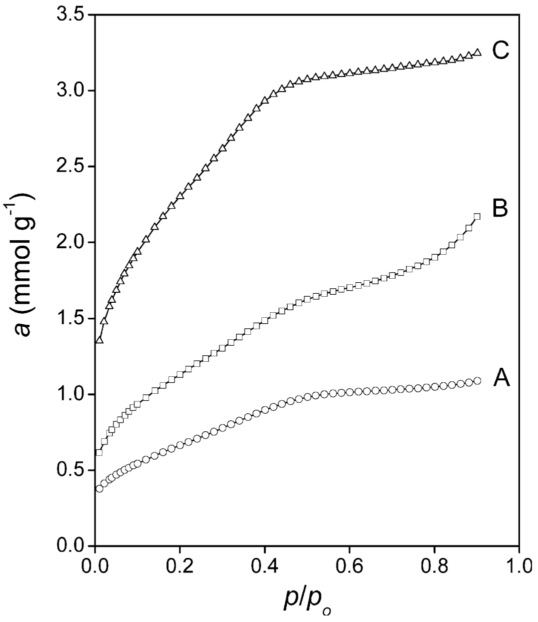

Fig. 3 Adsorption isotherms of nitrogen at 77 K on samples A–C

which the mesopore filling occurs. A small increase in the adsorbed amount at higher relative pressures corresponds to the adsorption on the outer surface of particles. The upward deviation of the isotherm of sample B at $p/p_o > 0.7$ can be explained as a consequence of capillary condensation of nitrogen in the interparticle space.

The BET surface area, S_{BET}, was calculated using data in a relative pressure range from 0.05–0.20. The mesopore volume V_{ME} was determined from the amount adsorbed at the relative pressure $p/p_o = 0.6$. The mesopore diameter D_{ME} was calculated by means of the geometric formula $4V_{ME}/S_{BET}$. These data (Table 1) reveal that (i) the dispersity of aluminum doped TiO_2 is lower than that of aluminosilicate mesoporous molecular sieves, and (ii) the content of aluminum plays a decisive role. Sample A, containing formally 2.5 wt% of Al_2O_3, represents a dispersed material of very low mesoporosity. It seems obvious that this sample consists of unconsolidated anatase particles with a small amount of aluminum oxide in-between them. The mesopore volume is directly proportional to the content of Al (Table 1). This dependence deviates from linearity for low Al contents, which is understandable, since even pure TiO_2 should have some small V_{ME} value. As the size of anatase particles does not change dramatically (Table 1), it is obvious that the increase in the mesoporosity is caused by the presence of Al only. It can be supposed that the mesoporous aluminum oxide particles are in an intimate contact with the particles of anatase.

Electrochemistry

Figure 4 shows a comparative set of voltammograms for the Al-stabilized samples A–C and the Al-free sample (BL) in 1 M $LiN(CF_3SO_2)_2 + EC/DME$ (1/1, v/v) at a scan rate of 0.5 mV/s. The accommodation of Li^+ in the anatase lattice is indicated by cathodic/anodic peaks at ~1.7 and 1.95 V vs. Li/Li^+, respectively. The peaks correspond to the insertion or extraction of lithium according to the equation:

Fig. 4 Cyclic voltammetry of Al-stabilized samples (A–C) and Al-free blank sample (BL) in 1 M $LiN(CF_3SO_2)_2 + EC/DME$ (1/1, v/v); scan rate 0.5 mV/s. The mass of active electrode material is different for each of the plots shown

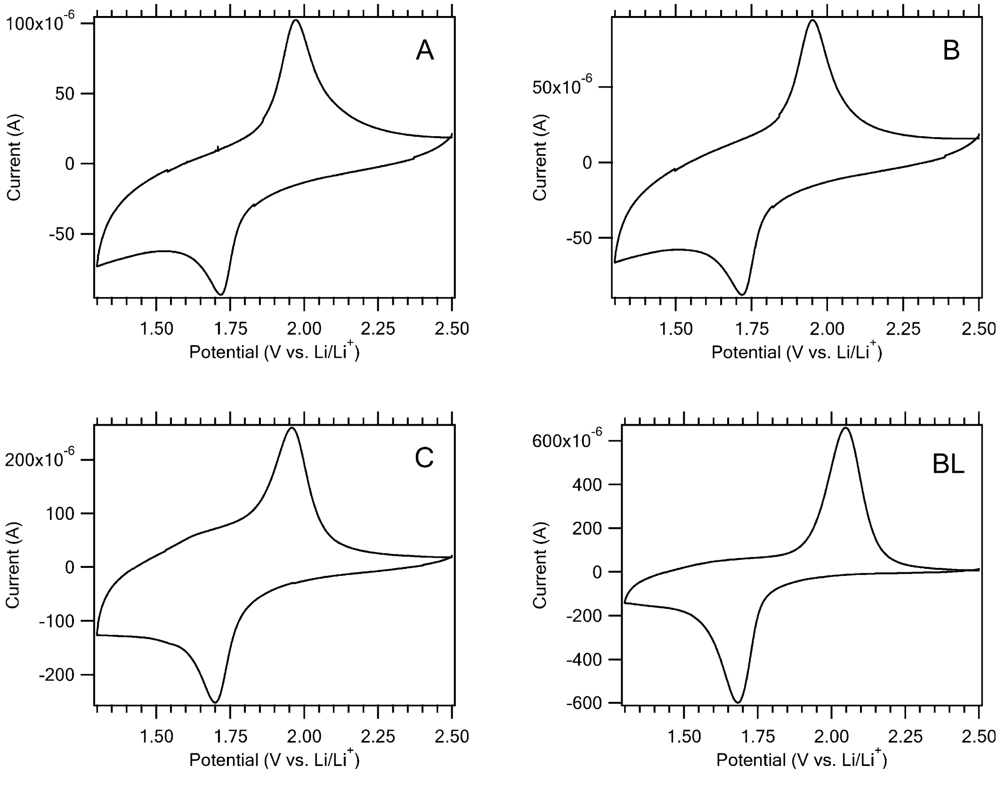

$$\mathrm{TiO_2} + x\left(\mathrm{Li^+} + \mathrm{e^-}\right) \leftrightarrow \mathrm{Li}_x\mathrm{TiO_2}, \qquad (1)$$

During the first negative voltammetric scan, electrons are injected into the Al-stabilized anatase crystal, forming Ti^{3+} states, while the Al ion has a fixed oxidation state of $+3$. Once the process starts, Li^+ penetrates into the bulk material and more Li^+ can enter the surface until the oxide is heavily doped with Ti^{3+}. The Li insertion coefficient, x, determined from the anodic branch of cyclic voltammograms A–C, varied between 0.24 and 0.48 (somewhat smaller than that of pure anatase [7, 8, 35, 36]). Sample B usually showed the largest Li-storage capacity, close to $x = 0.5$. By comparative blank experiments, we have found that pure alumina had negligible capacity for lithium insertion. At the same conditions as for Li-insertion into anatase, the voltammetric response of alumina was dominated by capacitive charging only. Therefore, the presence of alumina may decrease the overall Li-insertion capacity of our materials. A similar drop in Li-insertion capacity was also traced for Zr-stabilized anatase PNNL-1, which, however, contained a larger proportion of the ballast inorganic component [8]. In our case, the small drop in Li-storage capacity, due to the small amounts of inactive alumina in the samples, might be compensated for by the increase in the surface area (Table 1), which promotes Li-accommodation on the voltammetric time scale. This provides a rational for the optimum performance found for sample B.

Reaction (1) was extensively studied with anatase electrodes, both theoretically [37, 38, 39] and experimentally [7, 8, 9, 22, 36, 37, 40, 41, 42, 43, 44]. These studies [43, 44, 45, 46, 47, 48, 49] demonstrated that anatase converts during reaction (1) into lithium-poor tetragonal phase $Li_{0.01}TiO_2$ with the anatase structure (space group $I4_1/amd$) and orthorhombic lithium titanate, $Li_{0.5}TiO_2$ (space group Imma). The insertion of Li into the rutile lattice is indicated by a cathodic voltammetric peak at ~1.4 V [7], which is, however, not detectable in Fig. 4. Therefore, the rutile shell (seen by Raman spectroscopy, but not by X-ray diffraction, see above) is apparently too thin to give rise to distinct voltammetric features of Li-insertion into rutile.

A more detailed analysis of the cyclic voltammograms (as in Fig. 4) shows that there is a small dependence of the formal potential of Li-insertion, E_f (averaged peak potentials of the insertion and extraction processes) on the Al-content. Table 1 demonstrates that the E_f values tend to decrease with increasing Al-content (from pure TiO_2 to sample C). This potential decrease is reminiscent of the same effect in Al-doped $LiNiO_2$ [32], but it contrasts with the opposite trend found in $LiCoO_2$ [29]. It suggests some energy barrier in Al-containing anatase, as the accommodation of Li requires more driving force (more negative potential) compared to that of pure anatase. This effect may well be due to the rutile shell on the anatase grains, since rutile is less active for Li-insertion [7, 22]. Alternatively, we may assume that the above-discussed distortion of the anatase lattice impedes the Li-insertion. If the unit cell volume decreases in Al-stabilized TiO_2 (vide ultra), the given amount of Li is less easily inserted into the smaller volume of the sample's unit cell compared to the more open unit cell of pure anatase. On the other hand, the increased Al-content causes a considerable increase in the BET surface area and mesopore volume (Table 1). This improves the conditions of Li-insertion, since the relative area of the electrolyte/solid interface is larger.

Another striking difference between the cyclic voltammograms of Al-stabilized materials and those of pure anatase is a broad envelope of features at potentials negative to the Li-insertion into anatase (between ~1.3–1.6 V, see Fig. 4). Voltammetric charge in this potential region indicates surface confined pseudocapacitive processes, either in amorphous titania [10] or in anatase nanosheets [11]. The observed voltammogram is also reminiscent of identical features in Zr-stabilized mesoporous anatase [7], and it is tempting to give a similar interpretation for the Al-stabilized analogues presented here.

Hagfeldt et al [36] have suggested that the cyclic voltammogram of Li-insertion into anatase can be evaluated assuming irreversible charge transfer kinetics. The standard rate constant of charge-transfer, k_0, can be determined from the peak current density I_p and the peak potential E_p according to the equation:

$$I_p = 0.227 nFAck_0 \exp\left[-\alpha nF\left(E_p - E_f'\right)/RT\right], \qquad (2)$$

where n is the number of electrons in reaction (1), A is the electrode area (approximated by its equivalent BET surface area), F is the Faraday constant, α is the charge-transfer coefficient ($\alpha \approx 0.5$), E_f' is the formal potential determined for the slowest scan (0.1 mV/s in our case), and c is the maximum concentration of Li^+ (or Ti^{3+}) in the accumulation layer. Assuming the limiting composition of the insertion product to be $Li_{0.5}TiO_2$ (see reaction 1), the concentration c equals 0.024 mol/cm^3. As the cathodic branch of cyclic voltammograms might be perturbed by parasitic breakdown reactions (like trace humidity) more accurate values can be determined for the anodic peak. The rate constant k_0 was calculated from several cyclic voltammograms recorded for the given electrode material at varying scan rates (between 0.1–10 mV/s). The values found (see Table 1) are greater by one order of magnitude than that of Zr-stabilized anatase of PNNL-1, $k_0 = 4.10^{-11}$ cm/s [7]. The rate constants of Al-stabilized anatase are comparable to the values of non-stabilized anatase (Table 1) as well as to those of other pure anatase nanocrystals [7, 36].

The peak current (I_p) also scales with the square root of the scan rate, v, as is expected for diffusion-controlled irreversible kinetics [36, 42]:

$$I_p = 0.4958 nFAc(D\alpha nFv/RT)^{1/2} \qquad (3)$$

where D is the chemical diffusion coefficient of Li^+. Equation 3 can be used for the determination of D. The values found (again from the anodic branch of the cyclic voltammograms) are collected in Table 1. They compare well to the corresponding values of nanocrystalline anatase [36] and organized mesoporous anatase [10]. Generally however, the diffusion coefficients of Li^+ in anatase are known to vary over a broad range (from 10^{-17} to 10^{-13} cm^2/s) depending on the material morphology [10, 36, 42, 50]. The largest values were found for an anatase single crystal electrode $D \approx 10^{-13}$ cm^2/s [22] and for compact anatase films, which were prepared by CVD or similar methods (from 10^{-15} to 10^{-14} cm^2/s) [41, 42, 50]. These films may mimic the single crystal electrode (for direct comparison of CVD versus nanocrystalline anatase, see [41]). In general, the diffusion coefficients tend to decrease with decreasing particle size for oxidic Li-insertion hosts [2, 3, 4]. This trend is not seen in our materials, which again illustrates the special behavior of Al-stabilized materials. Their electrochemical properties are not characterized by particle size alone; other less-common effects, such as lattice distortion and core-shell morphology, are at play. Obviously, such a complex picture should be taken into account for other Li-insertion hosts stabilized by Al and other inorganic components.

Conclusions

Mesoporous Al-stabilized TiO_2 (anatase) was prepared via supramolecular templating. The material exhibited a unique core (anatase)/shell (rutile) structure, which can be seen only using micro-Raman spectroscopy, not by X-ray diffraction or Li-insertion electrochemistry.

The prepared materials exhibits a considerable increase in surface area with Al content. The mesopore volume increases in the same series, but the mesopore diameter is roughly uniform (from 2.4 to 2.6 nm).

The Li-insertion electrochemistry of our Al-stabilized materials exhibits similar features to the Zr-stabilized material, PNNL-1. In both cases, there are specific voltammetric features at potentials from ~1.3–1.6 V, which are missing in pure anatase. The Al-stabilization improves Li-insertion by enhancing the active surface area, but it also decreases the Li-storage capacity. Therefore, optimum materials are found to contain medium Al-contents.

Acknowledgements This work was supported by the Grant Agency of the Czech Republic through Grant No. 203/03/0824. A. Attia would like to thank the Czech Ministry of Education and Sports for partial financial support.

References

1. Jamnik J, Maier J (2003) Phys Chem Chem Phys 5:5215
2. Levi MD, Aurbach D (1999) Electrochim Acta 45:167
3. Kavan L, Prochazka J, Spitler TM, Kalbac M, Zukalova M, Drezen T, Grätzel M (2003) J Electrochem Soc 150:A1000–A1007
4. Choi YM, Pyun SI (1997) Solid State Ionics 99:173
5. Grätzel M (2001) Nature 414:338
6. Hagfeldt A, Grätzel M (1995) Chem Rev 95:49
7. Kavan L, Attia A, Lenzmann F, Elder SH, Grätzel M (2000) J Electrochem Soc 147:2897
8. Kavan L, Grätzel M, Rathousky J, Zukal A (1996) J Electrochem Soc 143:394
9. Huang SY, Kavan L, Grätzel M, Exnar I (1995) J Electrochem Soc 142:142
10. Kavan L, Rathousky J, Grätzel M, Shklover V, Zukal A (2000) J Phys Chem B 104:12012
11. Kavan L, Kalbac M, Zukalova M, Exnar I, Lorenzen V, Nesper R, Grätzel M (2004) Chem Mater 16:477
12. Putnam RL, Nakagawa N, McGrath KM, Yao N, Aksay IA, Gruner SM, Navrotsky A (1997) Chem Mater 9:2690
13. Takahashi R, Takenaka S, Sato S, Sodesawa T, Ogura K, Nakanishi K (1998) J Chem Soc Farad T 94:3161
14. Yang P, Zhao D, Margolese DI, Chmelka BF, Stucky GD (1998) Nature 396:152
15. Yang P, Zhao D, Margolese DI, Chmelka BF, Stucky GD (1999) Chem Mater 11:2813
16. Alberius PCA, Frindell KL, Hayward RC, Kramer EJ, Stucky GD, Chmelka BF (2002) Chem Mater 14:3284
17. Crepaldi EL, Soler-Illia GJAA, Grosso D, Cagnol F, Ribot F, Sanchez C (2003) J Am Chem Soc 125:9770
18. Elder SH, Gao X, Li J, Liu D, McCready DE, Windisch CF (1998) Chem Mater 10:3140
19. Gesenhues U, Rentschler T (1999) J Solid State Chem 143:210
20. Palomares E, Clifford JN, Haque SA, Lutz T, Durrant JR (2003) J Am Chem Soc 125:475
21. Zhang XT, Liu HW, Taguchi T, Meng QB, Sato O, Fujishima A (2004) Sol Energ Mat Sol C 81:197
22. Kavan L, Grätzel M, Gilbert SE, Klemenz C, Scheel HJ (1996) J Am Chem Soc 118:6716
23. Li F, Zhang L, Metzger RM (1998) Chem Mater 10:2470
24. Lin Y, Wu GS, Yuan XY, Xie T, Zhang LD (2003) J Phys–Condens Mat 15:2917
25. Matsumuoto Y, Ishikawa Y, Nishida M, Seiichiro I (2000) J Phys Chem B 104:4204
26. Michailowski A, AlMawlawi D, Cheng G, Moskovits M (2001) Chem Phys Lett 349:1
27. Zhang X, Yao B, Zhao L, LIang C, Zhang L, Mao Y (2001) J Electrochem Soc 148:G398–G400
28. Zhang H, Banfield JF (2000) J Mater Res 15:437
29. Ceder G, Chiang YM, Sadoway DR, Aydinol MK, Jang YI, Huang B (1998) Nature 392:694
30. Song D, Ikuta H, Uchida T, Wakihara M (1999) Solid State Ionics 117:151
31. Attia A, Elder SH, Jirasek R, Kavan L, Krtil P, Rathousky J, Zukal A (2001) Stud Surf Sci Catal 135:361
32. Wang GX, Zhong S, Bradhurst DH, Dou SX, Liu HK (1999) Solid State Ionics 116:271
33. Zhang YH, Chan CK, Porter JF, Guo W (1998) J Mater Res 13:2610
34. Prokesova P, Mintova S, Cejka J, Bein T (2003) Mat Sci Eng C 23:1001
35. Kavan L, Kratochvilová K, Grätzel M (1995) J Electroanal Chem 394:93
36. Lindström H, Södergen S, Solbrand A, Rensmo H, Hjelm J, Hagfeldt A, Lindquist SE (1997) J Phys Chem B 101:7717
37. Lunell S, Stashans A, Lindström H, Hagfeldt A (1997) J Am Chem Soc 119:7374
38. Mackrodt WC (1999) J Solid State Chem 142:428
39. Nuspl G, Yoshizawa K, Yamabe T (1997) J Mater Chem 7:2529
40. Hengerer R, Kavan L, Krtil P, Grätzel M (2000) J Electrochem Soc 147:1467
41. Lindström H, Södergen S, Solbrand A, Rensmo H, Hjelm J, Hagfeldt A, Lindquist SE (1997) J Phys Chem B 101:7710

42. Van de Krol R, Goossens A, Schoonman J (1999) J Phys Chem B 103:7151
43. Van de Krol R, Goossens A, Meulenkamp EA (1999) J Electrochem Soc 146:3150
44. Van de Krol R, Goossens A, Meulenkamp EA (2001) J Appl Phys 90:2235
45. Wagemaker M, Van de Krol R, Kentgens APM, Van Well AA, Mulder FM (2001) J Am Chem Soc 123:11454
46. Henningsson A, Andersson MP, Uvdal P, Siegbahn H, Sandell A (2002) Chem Phys Lett 360:85
47. Wagemaker M, Kentgens APM, Mulder FM (2002) Nature 418:397
48. Luca V, Hanley TL, Roberts NK, Howe RF (1999) Chem Mater 11:2089
49. Wagemaker M, Kearley GJ, Van Well AA, Mutka H, Mulder FM (2003) J Am Chem Soc 125:840
50. Cantao MP, Cisneros JI, Torresi RM (1994) J Phys Chem 98:4865

Mat. Res. Soc. Symp. Proc. Vol. 820 © 2004 Materials Research Society R5.3.1

Anatase Inverse Opal: Preparation and Electrochemical Properties

Marketa Zukalova, Martin Kalbac and Ladislav Kavan
J. Heyrovsky Institute of Physical Chemistry, Academy of Sciences of the Czech Republic,
Dolejskova 3, CZ-182 23, Prague 8, Czech Republic

ABSTRACT

Anatase inverse opal was synthesized both in the powder form and in the thin layer by means of templating with latex spheres. The voids between close-packed latex particles were filled via deposition from the titanium (IV) isopropoxide solution, electrochemical deposition from the solution of $TiCl_3$, and liquid phase deposition from the $(NH_4)_2TiF_6$ solution. The resulting material exhibited a regular fcc ordering of macropores surrounded with the framework consisting of the anatase nanocrystallites of 20 nm in size. Electrochemical performance for lithium insertion of anatase inverse opal was sluggish compared to that of non-templated anatase with more dense packing of nanocrystals.

INTRODUCTION

Anatase inverse opal is a macroporous solid with highly ordered porous structure over a large area, which has attracted considerable interest recently [1-5]. High refractive index of the wall material together with a pore size of hundreds nanometers (comparable to the wavelengths of visible light) are responsible for its photonic crystal properties. Owing to its ability to inhibit the range of wavelengths from propagation through the material over all directions, this unique structure offers many applications in sensors, optoelectronics, chromatography, and photocatalysis. Recently, Mallouk et al.[6] reported on the enhancement of the light harvesting efficiency of the dye-sensitized solar cell (Grätzel cell) by coupling a TiO_2 photonic crystal layer to a conventional film of TiO_2 nanoparticles. By tailoring of the stop band position, this assembly could improve the photocurrent efficiency by 26% due to localizing of the red part of solar spectrum in the composite structure [6].

The efficiency of the photoanode of the dye-sensitized solar cell could be strongly influenced either by structural parameters or by electrochemical properties of the composite materials of this electrode. Hence, deeper insight into the structure of anatase inverse opal together with the study of its electrochemical properties provide necessary feedback for tuning the synthetic protocol of anatase inverse opal with respect to the best performance of this structure in the dye-sensitized solar cell. Structure and texture of anatase inverse opal were studied by SEM, TEM, XRD, Raman spectroscopy, and nitrogen adsorption measurements. Properties of our material were also investigated by lithium insertion electrochemistry. Because of the similarity in heterogeneous charge-transfer processes taking place either during lithium insertion into anatase lattice or during transport of electrons from the photoexited dye to the back contact of the photoanode of Grätzel cell, this method represents a possibility to evaluate the applicability of anatase inverse opal in the dye-sensitized solar cell.

EXPERIMENTAL DETAILS

The inverse opal powder was prepared according to a modified protocol pioneered in Ref.[2,5]. The solution of latex particles in water (4.5vol.%, 500 nm in diameter, kindly provided by MPICI Golm) was centrifuged at 4000 rpm for 26 hours. After drying at ambient temperature, 1 g of the template was soaked with 2-propanol. Subsequently 20 ml of titanium(IV) isopropoxide was added drop vise and the mixture filtered on a Buechner funnel. The composite was dried in air and annealed at 575°C for 2.5 hours. Electrodes were prepared as follows: 0.3 g of the powder was mixed under slow addition of 4 x 0.15 ml of 10 % aqueous solution of acetylacetone, 0.3 ml of 4 % aqueous solution of hydroxypropylcellulose (MW 100,000) and 0.3 ml of 10 % aqueous solution of Triton-X100. The obtained slurry was deposited on a sheet of conducting glass using a doctor-blading technique. The film was finally calcined for 30 min in air at 450°C. Thin-film electrodes were fabricated with the aid of a latex template film on conducting glass electrode (F-doped SnO_2, TEC 8 from Libbey-Owens-Ford, 8 Ω/square). The layer of latex template was grown by vertical deposition from the suspension of polystyrene latex spheres (Seradyn Co., 243 nm in diameter) according to Ref.[6]. The voids in the opal template layer on conducting glass were filled by electrochemical deposition from 50 mM aqueous solution of $TiCl_3$, pH 2.4 by galvanostatic oxidation at 10 $\mu A/cm^2$ for 10 hours [7] or liquid phase deposition from a mixture of 0.2 M $(NH_4)_2TiF_6$ + 0.3 M H_3BO_3, pH 3, adjusted by HCl [8]. UV-Vis spectra were measured on Hewlett Packard 8450 diode array spectrometer. Scanning electron microscopy (SEM) images were obtained by Jeol JSM-03. Transmission electron microscopy (TEM) images were obtained on Tecnai F30 microscope with 300 keV field emission electron gun. Powder X-ray diffractometry (XRD) was studied on a Siemens D-5000 diffractometer using CuKα radiation. Raman spectra were excited by Ar^+ laser at 2.54 eV (Innova 305, Coherent).

Electrochemical measurements were carried out in the one-compartment cell using an Autolab Pgstat-30 (Ecochemie) controlled by GPES-4 software. The reference and auxiliary electrodes were from Li metal, hence potentials are referred to the Li/Li^+ (1M) reference electrode. $LiN(CF_3SO_2)_2$ (Fluorad HQ 115 from 3M) was dried at 130°C/1 mPa. Ethylene carbonate (EC) and 1,2-dimethoxyethane (DME) were dried over the 4A molecular sieve (Union Carbide). The electrolyte solution, 1 M $LiN(CF_3SO_2)_2$ + EC/DME (1/1 by volume) contained 10-15 ppm H_2O as determined by Karl Fischer titration (Metrohm 684 coulometer). All operations were carried in a glove box under argon (containing typically 1-5 ppm of O_2 and H_2O).

RESULTS

Figures 1 A, B confirm the regular arrangement of macropores in the powder form of inverse opal made by filling of the voids in the latex template from a propanolic solution of Ti(IV) isopropoxide. The diameter of pores is ca. 350 nm, which is smaller by ca. 30 % compared to diameters of pristine latex spheres (500 nm). The surface area S_{BET} of 40 m^2/g, determined from adsorption measurements, represents the value typical for macroporous solids.

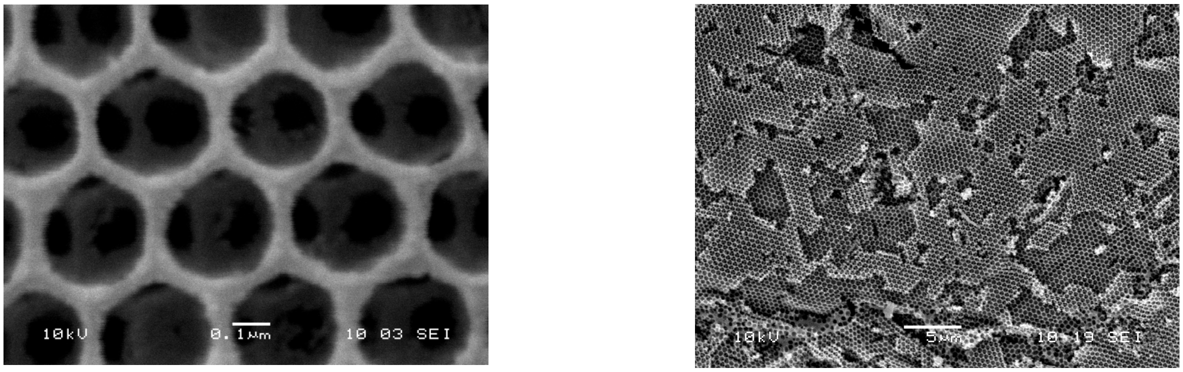

Figure 1 A, B. SEM pictures of the inverse opal powder made from a propanolic solution of titanium(IV) tetraisopropoxide, scale bars correspond to 0.1 and 5 µm, respectively.

The TEM image of inverse opal in figure 2 reveals its framework consisting of anatase nanocrystals of ca. 10-20 nm in size. X-ray diffractogram of the powder inverse opal in figure 3 can be indexed as a pure anatase phase. The crystallite size (coherent length of the crystal lattice) was approximated from the X-ray line width to be about 20 nm, which is in remarkable accord with the TEM image. The phase analysis of thin layers of inverse opal was carried out by Raman spectroscopy (data not shown). Electrochemical tests also proved the presence of only anatase phase in the walls of our material. In contrast to thin films prepared by liquid phase deposition, whose SEM image does not show any ordering (data not shown), figure 4 evidences the regular arrangement of macropores in the thin layer made by electrodeposition. In the case of liquid phase deposited layers, the inverse opal structure is covered with the compact layer of TiO_2 growing outside the voids due to the excess of the liquid precursor.

The position of the stop band in absorption spectra of the inverse opal structure is controlled by the diameter of latex spheres used as a template. A spectral position of the stop band for an inverse opal photonic crystal can be calculated by a modified version of Bragg's law combined with Snell's law [1]:

$$\lambda = 2d_{hkl}(n_{avg}{}^2 - \sin^2\theta)^{1/2}/m \qquad (1)$$

where λ is the free-space wavelength of light of the stop band maximum, m is the order of Bragg diffraction, n_{avg} is the average refractive index of the macroporous material:

$$n_{avg} = [(1\text{-}f)n^2_{TiO2} + fn^2_{air}]^{1/2} \qquad (2)$$

which gives $n_{avg} \cong 1.5$ for anatase inverse opal, f is the fraction of volume filling, i.e. 0.74 assuming close packing of spheres, n_{TiO2} and n_{air} are refractive indices of TiO_2 and air, respectively, θ is the angle measured from the normal to the planes, and d_{hkl} is the interplanar spacing. For normal incidence of light ($\theta = 0^o$) eq. 1 simplifies as follows [1]:

$$\lambda = 2d_{hkl}\, n_{avg}/m \qquad (3)$$

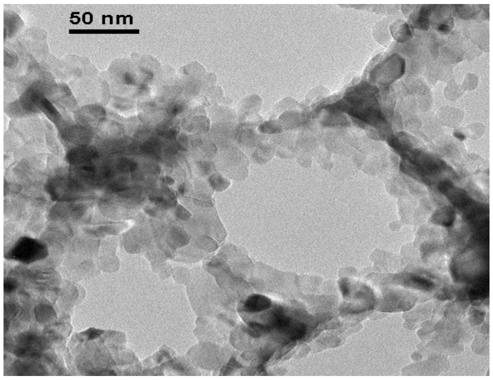

Figure 2. TEM image of the powder form of the anatase inverse opal.

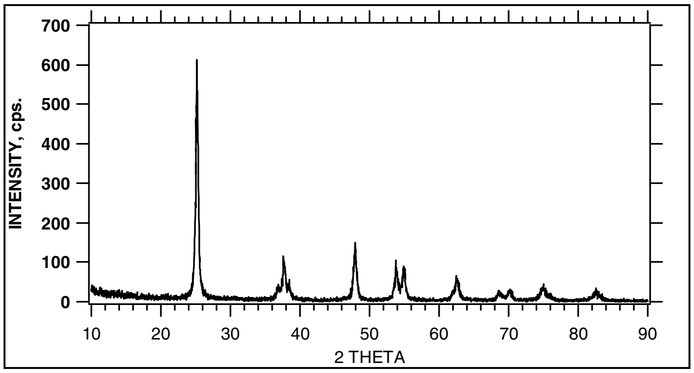

Figure 3. X-ray diffractogram of the powder form of anatase inverse opal.

By the comparison of the theoretical wavelength of the stop band maximum, calculated according to eq. 3 for the thin film of anatase inverse opal made by electrodeposition with the position of the stop band in the absorption spectrum of our material (figure 5) we can either decide between the fcc or hcp ordering of air voids or evaluate the regularity of ordering over a large area.

Equation 3 gives theoretical wavelength of the stop band maximum of 440 nm for the sphere diameter of 180 nm (figure 4) and fcc ordering, which is in good agreement with the position of the stop band in the spectrum at 420-480 nm, in contrast to the value of 350 nm, calculated for hcp arrangement of the macropores.

Figures 6 A, B show cyclic voltammograms of anatase inverse opal thin film made by electrodeposition and the non-templated blank layer made by identical procedure. The integral anodic voltammetric charge for Li-extraction of the electrode in fig. 6 B was 103 mC/cm^2

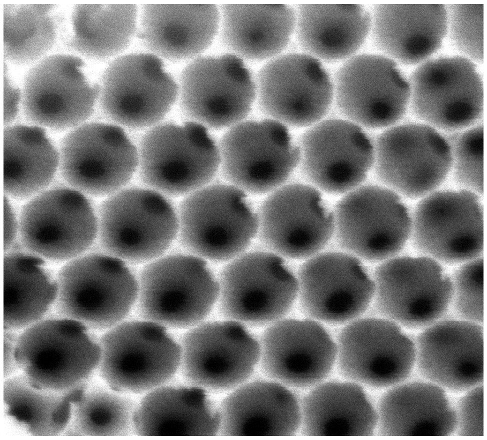

Figure 4. SEM picture of the inverse opal layer made by electrodeposition from $TiCl_3$ solution, picture size 1073 x 1073 nm.

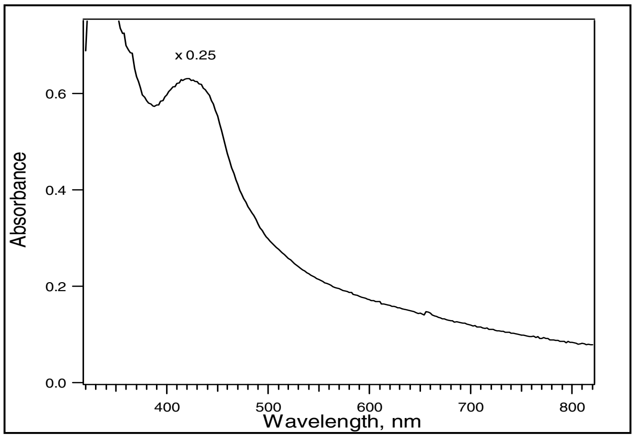

Figure 5. UV-Vis spectrum of the anatase inverse opal thin film made from ordered latex particles of 243 nm in diameter, deposited on conducting glass.

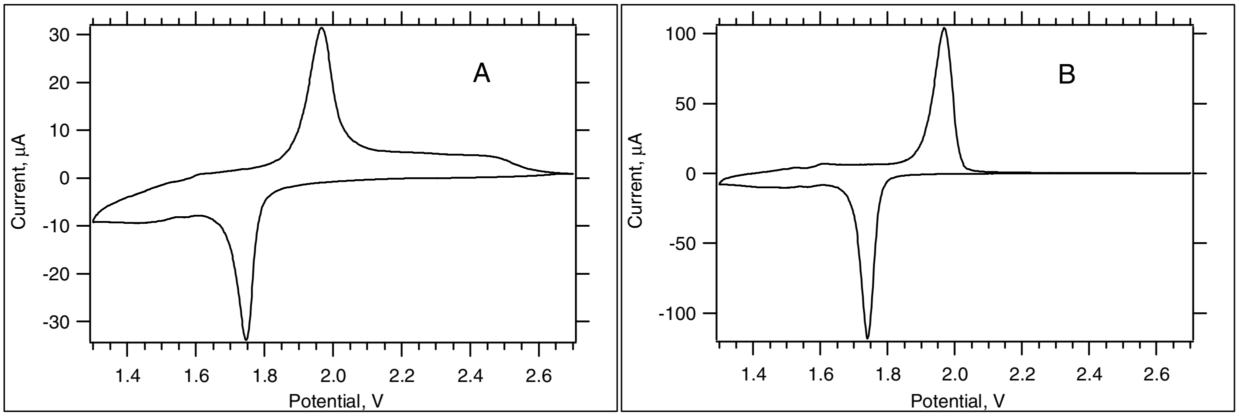

Figure 6 A, B. Cyclic voltammograms of Li-insertion into the prepared materials. Electrolyte solution: 1 M $LiN(CF_3SO_2)_2$ + EC/DME (1:1 by volume); scan rate 0.1 mV/s. [A] Thin layer of anatase inverse opal made by electrodeposition from $TiCl_3$ (10 µA/cm^2, 10 hours, pH 2.4), [B] the same as[A] but non-templated.

at 0.1 mV/s, which is considerably more than corresponding value of 70 mC/cm^2 calculated for the templated electrode (fig. 6 A). The analogous trend was also observed for the integral anodic voltammetric charge determined from cyclic voltammograms of either templated or non-templated thin layers prepared by liquid phase deposition, either the powder form of anatase inverse opal or non-templated nanocrystalline anatase (data not shown).

CONCLUSIONS

Anatase inverse opal synthesized both in the powder form and in the thin layer was characterized as a regular macroporous structure with fcc ordering of air voids and anatase nanocrystallites of 20 nm in size within the framework. This material exhibits sluggish electrochemical performance for Li-insertion compared to non-templated anatase with more dense packing of nanocrystals. This is probably due to limited number of necking points resulting into poor electrical contacts between the particles in the extremely open nanocrystalline network.

ACKNOWLEDGEMENT

This work was supported by Grant Agency of the Czech Republic, contract No. 203/03/0824.

REFERENCES

1. Schroden, R. C.; Al-Daous, M.; Blanford, C. F.; Stein, A. *Chem.Mater.* **2002,** *14* 3305-3315.

2. Stein, A.; Schroden, R. C. *Current Opinion in Solid State and Material Science* **2001,** *5* 553-564.

3. Johnson, N. P.; McComb, D. W.; Richel, A.; Treble, B. M.; De La Rue, R. M. *Synthetic Metals* **2001,** *116* 469-473.

4. Gu, Z. Z.; Kubo, S.; Fujishima, A.; Sato, O. *Appl.Phys.A* **2002,** *74* 127-129.

5. Holland, B. T.; Blanford, C. F.; Stein, A. *Science* **1998,** *281* 538-540.

6. Nishimura, S.; Abrams, N.; Lewis, B. A.; Halaoui, L. I.; Mallouk, T. E.; Benkstein, K. D.; Van de Langemaat, J.; Frank, A. J. *Journal of the American Chemical Society* **2003,** *125* 6306-6310.

7. Kavan, L.; O`Regan, B.; Kay, A.; Grätzel, M. *Journal of Electroanalytical Chemistry* **1993,** *346* 291-307.

8. Nishimura, S.; Shishido, A.; Abrams, N.; Mallouk, T. E. *Appl.Phys.Lett.* **2002,** *81* 4532-4534.

NANO
LETTERS

2005
Vol. 5, No. 9
1789−1792

Organized Mesoporous TiO_2 Films Exhibiting Greatly Enhanced Performance in Dye-Sensitized Solar Cells

Markéta Zukalová,[†] Arnošt Zukal,[†] Ladislav Kavan,*,[†,‡]
Mohammad K. Nazeeruddin,[‡] Paul Liska,[‡] and Michael Grätzel*,[‡]

J. Heyrovský Institute of Physical Chemistry, Academy of Sciences of the Czech Republic, Dolejškova 3, CZ-18223 Prague 8, Czech Republic, and Laboratory of Photonics and Interfaces, EPFL, Ecublens, CH-1015 Lausanne, Switzerland

Received July 20, 2005; Revised Manuscript Received August 1, 2005

ABSTRACT

The Pluronic P123 templated mesoporous TiO_2 film was grown via layer-by-layer deposition and characterized by a novel methodology based on the adsorption of *n*-pentane. Multiple-layer depositions did not perturb the mesoporous structure significantly. Our TiO_2 film was sensitized by a newly developed Ru-bipyridine dye (N945) and was applied as a photoanode in dye-sensitized solar cell. The 1-μm-thick mesoporous film, made by the superposition of three layers, showed enhanced solar conversion efficiency by about 50% compared to that of traditional films of the same thickness made from randomly oriented anatase nanocrystals.

The dye-sensitized solar cell (DSC) presents an attractive alternative to solid-state photovoltaics. This cell demonstrated solar conversion efficiency over 10% at a very competitive cost.[1,2] Its operation is driven by electron injection from photoexcited dye into the conduction band of TiO_2 (anatase). Until now, the photoanode was fabricated from randomly oriented anatase nanocrystals.[1−3] Recently, a photoanode for DSC was also made from ZnO nanowires, but its efficiency was limited by the small surface area of the nanowires.[4] Here we report on highly efficient DSC, whose photoanode was prepared from organized mesoporous TiO_2 film. The film was grown via a modified surfactant templating route, pioneered by Stucky et al.[5] The previously reported mesoporous films were of submicrometer thicknesses only.[6−11] Such thin films provide insufficient physical surface area per unit of projected area (roughness factor; *RF*) rendering low light harvesting by the monolayer of adsorbed dye on the TiO_2 surface.[1] To fabricate thicker films with larger *RF* values, we have implemented a simple technique of repeated layer-by-layer deposition by dip coating.

First, syntheses of organized TiO_2 were based on solvolysis of $TiCl_4$ in ethanol containing amphiphilic triblock copolymer of ethylene oxide and propylene oxide (Pluronic) as the structure directing agent.[5,12] They gave mesoporous TiO_2 in the form of powders or xerogels.[5,12] Later on, thin films were grown on glass or silicon[10,11] by dip or spin coating. This seemingly trivial technique involves a complex mechanism, called evaporation-induced self-assembly.[10,13,14] Hence, the quality of produced films is crucially dependent on experimental details, such as ambient humidity and withdrawal rate.[7] The synthetic protocol was further varied by replacing $TiCl_4$ with Ti(IV) tetraethoxide[7−9,15] and by replacing ethanol with 1-butanol.[8] A composite of Pluronic templated TiO_2 with regioregular poly(3-hexyl thiophene) is applicable for solid-state photovoltaics,[7,16] but the performance of actual cells is limited by poor hole transport[16] and incomplete filling of mesopores.[7] The Pluronic templated TiO_2 was also modified by CdS or CdSe nanoparticles for a liquid-junction photoelectrochemical cell.[17,18] The sensitization of TiO_2 to visible light was demonstrated successfully, but a solar conversion efficiency was not reported.[17,18] Recently, a photoanode for DSC was fabricated from wormlike TiO_2 made by Pluronic templating, but the mesoporous film was not ordered.[3]

Our films were grown from a solution made by the slow addition of 9.7 g of HCl (37% Aldrich) to 12.7 g of titanium ethoxide (Aldrich) under vigorous stirring. Separately, 4.0 g of block copolymer Pluronic P123 [$OH(CH_2CH_2O)_{20}$-$(CH_2CH(CH_3)O)_{70}(CH_2CH_2O)_{20}H$ from BASF] was dissolved in 36.3 g of 1-butanol (Aldrich) and added to the HCl/$Ti(EtO)_4$ solution. This solution was aged by stirring at ambient temperature for at least 3 h. The films were deposited

---

* Corresponding authors. E-mail: kavan@jh-inst.cas.cz; michael.graetzel@epfl.ch.
[†] J. Heyrovský Institute of Physical Chemistry.
[‡] Laboratory of Photonics and Interfaces.

10.1021/nl051401l CCC: $30.25

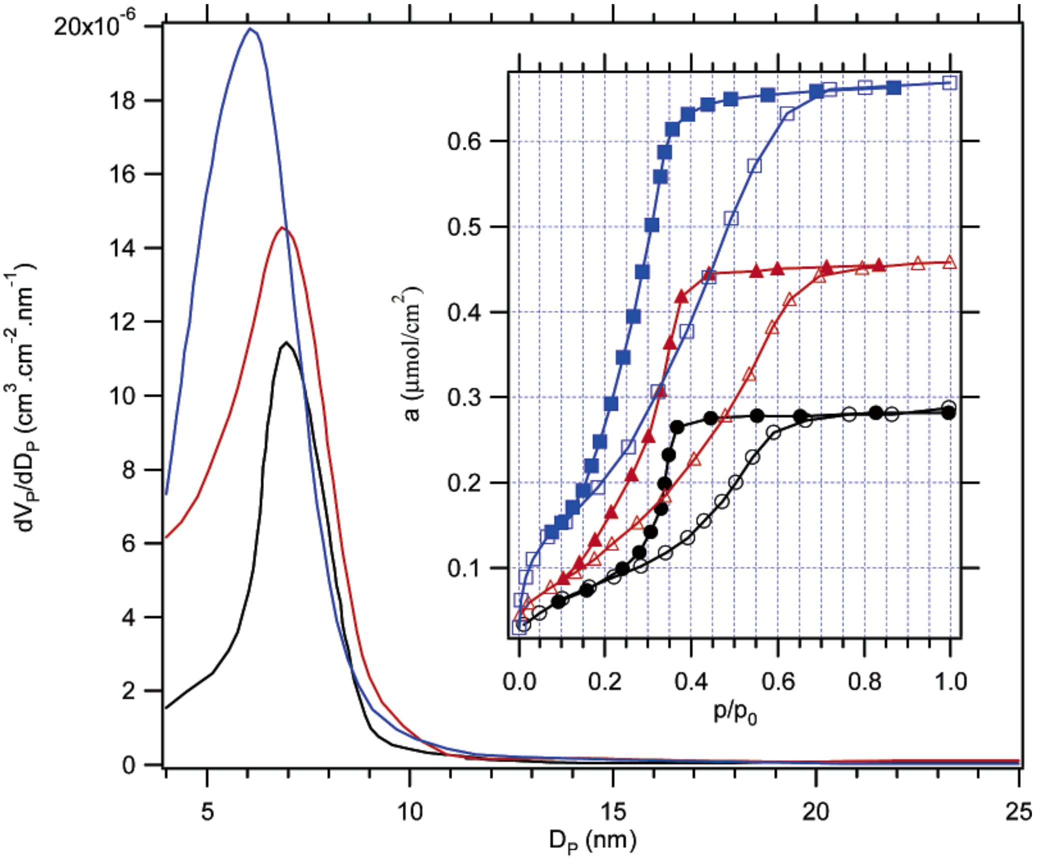

Figure 1. Pore size distributions of Pluronic-templated TiO_2 films made from one layer (black curve), two layers (red curve), or three layers (blue curve). The distribution was calculated from the desorption branches of the *n*-pentane isotherms. Inset: the adsorption isotherms of *n*-pentane on Pluronic-templated TiO_2 films. The isotherms for films made from one, two, or three layers are displayed with the same color coding. Solid symbols denote desorption.

by dip coating (withdrawal rate of 0.8 mm/s) onto 7.5 × 2.5 cm^2 sized slides of glass or F-doped SnO_2 (TEC 8 from Libbey-Owens-Ford, 8 Ω/square). The layer was aged at 75% relative humidity at a temperature of 24−25 °C for 30 h. Subsequently, the layer was calcined in air at 350 °C for 2 h (heating rate: 1 °C/min). For the preparation of thicker films consisting of two or three layers, the described procedure was repeated once or twice. Finally, the film was calcined at 450 °C for 30 min. The three-layer film had a thickness of 1.0 μm (alpha-step profilometer, Tencor Instruments). For comparison, a standard nonorganized nanocrystalline TiO_2 film was grown via a sol−gel route and subsequently impregnated with $TiCl_4$[2]. This synthetic protocol was optimized previously for DSC application with 10.4% conversion efficiency, albeit this top performance is only achievable on films 18 μm in thickness.[2] The solar tests and employed experimental procedures are described in detail elsewhere.[2] In the present study, the TiO_2 films were sensitized by two dyes: N719 = bis(tetrabutylammonium) *cis*-dithiocyanatobis-(2,2′bipyridine-4-COOH,4′-COO$^-$) ruthenium(II))[4] or N945 = *cis*-dithiocyanato(4,4′-dicarboxy-2,2′-bipyridine)(4,4′-di-(2-(3,6-dimethoxyphenyl)ethenyl)-2,2′-bipyridine) ruthenium-(II). The N945 sensitizer is reported here for the first time. It shows the lowest-energy metal-to-ligand charge-transfer transition at λ_{max} = 545 nm with a molar extinction coefficient of $\epsilon = 18\,600$ M^{-1} cm^{-1}. The corresponding values for N719 are λ_{max} = 530 nm; $\epsilon = 13\,500$ M^{-1} cm^{-1}. The electrolyte solution was 0.6 M *N*-methyl-N-butyl imidazolium iodide, 30 mM I_2, 0.5 M *tert*-butylpyridine, 0.1 M guanidine thiocyanate in acetonitrile/valeronitrile (85/15, v/v). Photocurrent−voltage curves were measured under simulated 1 Sun illumination (air mass, AM 1.5); the electrode active area, determined by the aperture of a black mask, was 0.158 cm^2.

Surface areas of small amounts of porous materials are often measured by krypton adsorption at 77 K (boiling point of nitrogen). Krypton has the equilibrium vapor pressure of 212 Pa at 77 K and a melting point of 115.8 K; hence, the adsorption of Kr is not suitable for mesopore structure analysis.[19] Here we employed the adsorption of *n*-pentane, which has a melting point of 143.5 K and saturation vapor pressure of 118 Pa at 195 K (cooling by dry ice). The adsorption isotherm of *n*-pentane at 195 K is particularly suitable for the analysis of porous structure because the capillary condensation in mesopores occurs at the conditions when the bulk liquid phase is stable. Figure 1 (inset) shows the actual isotherms of mesoporous TiO_2 films on glass. To the best of our knowledge, this is the first application of *n*-pentane for the analysis of mesoporosity of solid thin films. Our isotherms were measured directly on the actual glass-supported films and not (as it is the usual practice[3,6,8]) on powder-like materials scraped from the support.

The adsorption of krypton and *n*-pentane was calibrated using anatase powder (Aldrich), whose BET-nitrogen surface

Table 1. Porosity Characterization of Pluronic-Templated Titania Films on Glass[a]

no. of layers	$(RF)_{\mathrm{Kr}}$	$(RF)_{\mathrm{P}}$	$(V_{\mathrm{ME}})_{\mathrm{P}}$ (cm^3/cm^2)	$(D_{\mathrm{ME}})_{\mathrm{P}}$ (nm)
1	169	180	2.82×10^{-5}	7.3
2	321	310	4.79×10^{-5}	7.3
3	466	459	6.69×10^{-5}	6.7

[a] $(RF)_{\mathrm{Kr}}$, roughness factor from krypton adsorption isotherm; $(RF)_{\mathrm{P}}$, roughness factor from *n*-pentane adsorption isotherm; $(V_{\mathrm{ME}})_{\mathrm{P}}$, mesopore volume, $(D_{\mathrm{ME}})_{\mathrm{P}}$, mesopore diameter corresponding to the maximum of the pore size distribution.

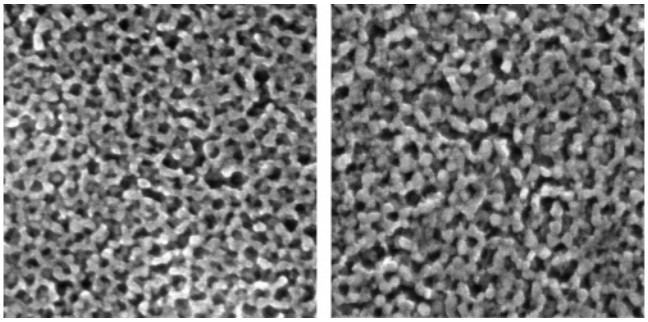

Figure 2. Scanning electron microscopy images of Pluronic-templated TiO_2 films. Left chart: one-layer film, right chart: three-layer film. The actual size of each image is 300 × 300 nm^2.

area was 10.9 m^2/g. The actual surface area of films was expressed in terms of the roughness factor, *RF*. The mesopore volume $(V_{\mathrm{ME}})_{\mathrm{P}}$ was expressed analogously in cm^3 per cm^2 of the geometric area of the film. The mesopore volume and pore size distribution were calculated from the desorption branch of the *n*-pentane isotherm.[20]

The roughness factors, $(RF)_{\mathrm{Kr}}$ and $(RF)_{\mathrm{P}}$, obtained from the krypton and *n*-pentane isotherms, respectively, are identical within experimental errors (Table 1). The pore size distributions are displayed in Figure 1, and the diameters of the mesopores $(D_{\mathrm{ME}})_{\mathrm{P}}$ corresponding to the maximum of these curves are also listed in Table 1. Obviously, the porous structure is not changed much during the repeated dip-coating procedure. This is due to some shrinking of the inorganic framework during calcination, which makes the mesopores smaller than the micelles of the Ti−Pluronic precursor. Hence, the underneath films are almost intact by subsequent layer deposition. The electron microscopy images (Figure 2) confirm that the morphologies of the one-layer film (left chart) and three-layer film (right chart) are similar, showing the expected mesopore size around 7 nm (cf. Table 1). We note only small broadening of the distribution curve, and shift to smaller mesopores, because of repeated calcination of "old" layers.

Figure 3 displays the results of solar cell tests. The spectra of incident monochromatic photon-to-current conversion efficiency (IPCE) exhibit a maximum of 49% for the N945 sensitizer on mesoporous TiO_2. From the overlap integral of this curve, one predicts a short circuit photocurrent density of 6.9 mA/cm^2. Under standard global AM 1.5 solar conditions, the cell gave a photocurrent density of $I_{\mathrm{p}} = 7 \pm 0.5$ mA/cm^2, an open circuit potential of $U_{\mathrm{OCP}} = 0.799$ V, and a fill factor of ff = 0.72, yielding 4.04% conversion efficiency. Under similar conditions, the N719 sensitized solar cell showed IPCE = 37%, $I_{\mathrm{p}} = 4.93$ mA/cm^2, $U_{\mathrm{OCP}} = 0.815$ V, and ff = 0.73, yielding a conversion efficiency of 2.95%. The higher efficiency of the N945 dye-sensitized solar cell is caused by stronger light absorbance of N945 across the visible spectrum with superior response in the red region.

For comparison, a TiO_2 film composed of randomly oriented nanoparticles was also tested under identical conditions. When sensitized by N945, the 0.95-μm-thick film gave a conversion efficiency of only 2.21%, which increased to 2.74% by surface treatment with $TiCl_4$ prior to dye deposition. Obviously, the solar-conversion efficiency of DSC with

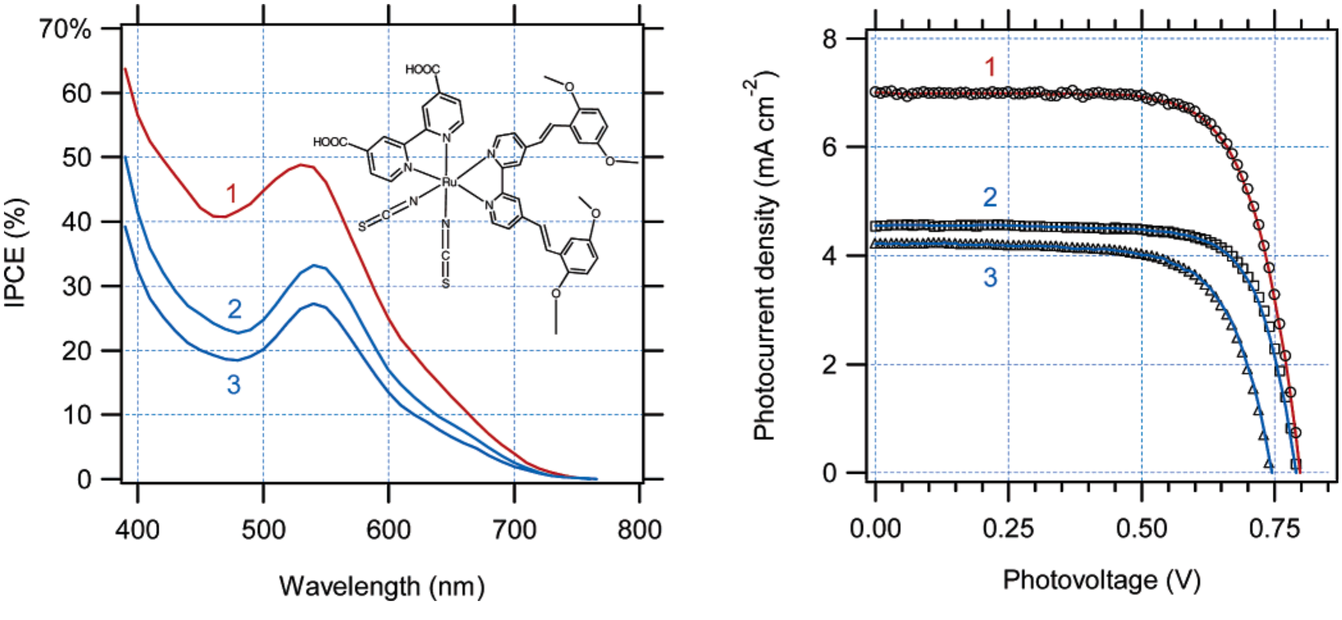

Figure 3. IPCE (left chart) and photocurrent−voltage characteristics (right chart) of a solar cell, based on TiO_2 films sensitized by N945. Pluronic-templated three-layer film; 1.0-μm-thick (1), nonorganized anatase treated by $TiCl_4$; 0.95-μm-thick (2), nonorganized anatase nontreated by $TiCl_4$; 0.95-μm-thick (3). Inset shows the chemical formula of N945 dye.

organized mesoporous film (4.04%) is larger by about 50% compared to the efficiency of 1-μm-thick film composed of randomly associated nanoparticles, which was optimized previously for DSC application.[1,2] This improvement results from a remarkable enhancement of the short circuit photocurrent. The roughness factor of ca. 460 is strikingly high for a 1-μm-thick film.[4] It is larger by a factor of 5 or 50 compared to the *RF* value of a film of randomly oriented 12-nm-sized TiO_2 particles or ZnO nanowires, respectively.[4] This huge surface area appears to be very accessible to both the dye and the electrolyte, as is apparent from the remarkable photocurrent densities and IPCE values obtained. They are unprecedented for such thin films in dye-sensitized photovoltaic devices, opening up new avenues for advancing the performance of this new generation of photovoltaic cells. Further improvement can be expected if the crystallinity of the mesoporous TiO_2 skeleton is enhanced, for example, by calcination under simultaneous blocking of mesopores.[21]

Acknowledgment. This work was supported by EC project Molycell (SES6-CT-2003-502783), EC-COST D35.0002, and by the Grant Agency of the Czech Republic (contract no. 203/03/0824). Financial support by the Swiss Office of Energy and the European Research and Development Office of the U.S. Air Force is also acknowledged.

References

(1) Grätzel, M. *Nature* **2001**, *414*, 338.
(2) Nazeeruddin, M. K.; Pechy, P.; Renouard, T.; Zakeeruddin, S. M.; Humphry-Baker, R.; Comte, P.; Liska, P.; Cevey, L.; Costa, E.; Shklover, V.; Spiccia, L.; Deacon, G. B.; Bignozzi, C. A.; Grätzel, M. *J. Am. Chem. Soc.* **2001**, *123*, 1613.
(3) Hou, K.; Tian, B.; Li, F.; Bian, Z.; Zhao, D.; Huang, C. *J. Mater. Chem.* **2005**, *15*, 2414.
(4) Law, M.; Greene, L. E.; Johnson, J. C.; Saykaly, R.; Yang, P. *Nat. Mater.* **2005**, *4*, 455.
(5) Yang, P.; Zhao, D.; Margolese, D. I.; Chmelka, B. F.; Stucky, G. D. *Nature* **1998**, *396*, 152.
(6) Crepaldi, E. L.; Soler-Illia, G. J. A. A.; Grosso, D.; Cagnol, F.; Ribot, F.; Sanchez, C. *J. Am. Chem. Soc.* **2003**, *125*, 9770.
(7) Coakley, K. M.; Liu, Y.; McGehee, M. D.; Frindell, K. L.; Stucky, G. D. *Adv. Funct. Mater.* **2003**, *13*, 301.
(8) Choi, S. Y.; Mamak, M.; Coombs, N.; Chopra, N.; Ozin, A. *Adv. Funct. Mater.* **2004**, *14*, 335.
(9) Alberius, P. C. A.; Frindell, K. L.; Hayward, R. C.; Kramer, E. J.; Stucky, G. D.; Chmelka, B. F. *Chem. Mater.* **2002**, *14*, 3284.
(10) Grosso, D.; Soller-Illia, G. J. A. A.; Babonneau, F.; Sanchez, C.; Albouy, P. A.; Brunneau, A. B.; Balkenende, A. R. *Adv. Mater.* **2001**, *13*, 1085.
(11) Yun, H.; Miyazawa, K.; Zhou, H.; Honma, I.; Kuwubara, M. *Adv. Mater.* **2001**, *13*, 1377.
(12) Yang, P.; Zhao, D.; Margolese, D. I.; Chmelka, B. F.; Stucky, G. D. *Chem. Mater.* **1999**, *11*, 2813.
(13) Boettcher, S. W.; Bartl, M. H.; Hu, J. G.; Stucky, G. D. *J. Am. Chem. Soc.* **2005**, *127*, 9721.
(14) Grosso, D.; Cagnol, F.; Soller-Illia, G. J. A. A.; Crepaldi, E. L.; Amenitsch, H.; Brunet-Bruneau, A.; Bourgeois, A.; Sanchez, C. *Adv. Funct. Mater.* **2004**, *14*, 309.
(15) Bartl, M. H.; Boettcher, S. W.; Hu, E. L.; Stucky, G. D. *J. Am. Chem. Soc.* **2004**, *126*, 10826.
(16) Coakley, K. M.; McGehee, M. D. *Appl. Phys. Lett.* **2003**, *83*, 3380.
(17) Bartl, M. H.; Puls, S. P.; Tang, J.; Lichtenegger, H. C.; Stucky, G. D. *Angew. Chem.* **2004**, *116*, 3099.
(18) Bartl, M. H.; Boettcher, S. W.; Frindell, K. L.; Stucky, G. D. *Acc. Chem. Res.* **2005**, *38*, 263.
(19) Sing, K. S. W. *Colloids Surf., A* **2004**, *241*, 3.
(20) Dollimore, D.; Heal, G. R. *J. Appl. Chem.* **1964**, *14*, 109.
(21) Tang, J.; Wu, Y.; McFarland, W.; Stucky, G. D. *Chem. Commun.* **2004**, *2004*, 1670.

NL051401L

Available online at www.sciencedirect.com

ScienceDirect

Inorganica Chimica Acta 361 (2008) 656–662

Inorganica Chimica Acta

www.elsevier.com/locate/ica

Structural parameters controlling the performance of organized mesoporous TiO_2 films in dye sensitized solar cells

Markéta Zukalová [a], Jan Procházka [a], Arnošt Zukal [a], Jun Ho Yum [b], Ladislav Kavan [a,*]

[a] *J. Heyrovský Institute of Physical Chemistry, v.v.i., Academy of Sciences of the Czech Republic, Dolejškova 3, CZ-18223 Prague 8, Czech Republic*
[b] *Laboratory of Photonics and Interfaces, Institute of Chemical Sciences and Engineering, Swiss Federal Institute of Technology, CH-1015 Lausanne, Switzerland*

Received 1 February 2007; received in revised form 25 April 2007; accepted 6 May 2007
Available online 16 May 2007

Dedicated to Michael Grätzel.

Abstract

Titanium dioxide films with organized mesoporous structure were investigated as photoanodes in dye sensitized solar cells. High-quality films were grown on FTO supports by implementing the protocol of supramolecular templating with an amphiphilic triblock copolymer, Pluronic P123. Thicker films were obtained by repeated dip-coating and calcination cycles of up to 10 layers. The TiO_2 films were crack-free, optically transparent, and had thicknesses exceeding 2 μm, while still preserving the organized mesoporous morphology. Their roughness factors, determined from Kr-adsorption isotherms, exceeded 500. The sorption of N-3 and N-719 dyes was fitted to a surface coverage of 0.31 molecules/nm^2, which is about one third of the ideal dye loading assumed for the (1 0 1) anatase face. The solar performance of multilayer films sensitized with N-945 dye scaled linearly for 1–3 layer films, but approached a plateau for thicker films.

Keywords: Dye sensitized solar cells; Titanium dioxide

---

1. Introduction

In 1985, Grätzel et al. [1] pioneered the spectral sensitization of titanium dioxide (anatase) to visible light by adsorbed Ru(II)-bipyridine complexes. Subsequent research milestones have been highlighted by the application of thin films of nanocrystalline (mesoscopic) anatase [2], optimization of ruthenium dyes [3–5] and replacement of liquid electrolyte solutions by an organic hole-conductor [6]. This strategy has demonstrated photoelectrochemical solar cells, the so-called "Grätzel cells", representing nowadays a credible alternative to conventional Si-based solid-state photovoltaics [7,8].

One of the key issues in optimization of the Grätzel cells consists in the morphological engineering of the TiO_2 photoanode, while the maximization of the electrode surface area (roughness factor, r_f) represents one of the obvious research targets. The roughness factor is defined as:

$$r_{\mathrm{f}} = \frac{A}{A_0} \tag{1}$$

where A is the total physical area of the electrode material (determined, e.g. from a krypton adsorption isotherm at 77 K) and A_0 is the projected electrode area. To evaluate the quality of particular electrodes, the incident photon to current conversion efficiency (IPCE) can be used as a testing parameter

$$\mathrm{IPCE} = \frac{Jhc}{\lambda P_{\mathrm{L}} e} \tag{2}$$

where J is the photocurrent density, h is the Planck constant, c is the velocity of light, λ is the wavelength, and P_{L} is the monochromatic light intensity (in W/m^2). It is

---

* Corresponding author.
E-mail address: kavan@jh-inst.cas.cz (L. Kavan).

0020-1693/$ - see front matter © 2007 Elsevier B.V. All rights reserved.
doi:10.1016/j.ica.2007.05.012

determined in front of the window, and is not corrected for absorption and reflection losses in the window, electrolyte solution and electrode. For a sensitized TiO_2 surface, the IPCE can also be expressed using the dye and substrate parameters [9]

$$\mathrm{IPCE} = \eta_{\mathrm{inj}}(1 - 10^{-\varepsilon\Gamma}) = \eta_{\mathrm{inj}}(1 - 10^{-\varepsilon r_f \Gamma_0}) \tag{3}$$

where η_{inj} is the quantum yield of charge injection from the photoexcited dye ($\eta_{\mathrm{inj}} \approx 100\%$ in many practical cases), ε is the extinction coefficient, and Γ is the overall surface concentration of the dye (in moles per projected electrode area, A_0). Obviously, $\Gamma = r_f \cdot \Gamma_0$, where Γ_0 is the specific surface coverage (in moles per physical electrode area, A). For a typical dye, $Ru(SCN)_2L_2$ (L = 2,2′-bipyridyl-4,4′-dicarboxylic acid) coded as N-3, the surface coverage was determined experimentally for a flat rutile surface to be $\Gamma_0 \approx 0.56$ molecules/nm^2 by Kavan et al. [9], and the same value was reported for anatase by Parkinson et al. [10,11]. Alternative sources quote 0.77–1.16 molecules/nm^2 depending on the particular anchoring structure [12], but significant structural adjustment of N-3 on the TiO_2 nanocrystal has to be taken into account, too [13]. Eq. (3) gives the maximum theoretical IPCE to be 0.27% for a monolayer of N-3 on a flat surface [9]. Experimental value for an anatase single crystal was 0.11% [9].

Although, IPCE is a useful parameter in evaluation of solar cells, a more practical criterion is the overall energy conversion efficiency for white solar light, ϕ_{sol} defined as

$$\phi_{\mathrm{sol}} = \frac{J_{\mathrm{sc}} U_{\mathrm{oc}} f}{P_{\mathrm{sol}}} \tag{4}$$

where J_{sc} is the short circuit photocurrent density, U_{oc} is the cell open-circuit voltage, f is the fill factor and P_{sol} is the incident intensity of white solar light (in W/m^2; for AM 1.5 solar light $P_{\mathrm{sol}} = 1$ kW/m^2).

The classical liquid-junction Grätzel cells nowadays achieve ϕ_{sol} exceeding 10% [7,8]. Such high values were obtained for mesoscopic TiO_2 films composed of statistically sintered anatase crystals, exhibiting the naturally most abundant face (101) but no apparent long-range ordering. The optimum TiO_2 electrodes were composed of two layers, *viz.* 20 nm-sized anatase crystals (10 μm thick layer) deposited on top of F–SnO_2 (FTO) conducting glass, and overlaid subsequently with a layer of 400 nm-sized anatase crystals (4 μm thick) [5]. The coarse overlayer improved the light harvesting of the composite electrode by light scattering on the larger crystals.

There is an obvious challenge to explore the solar efficiency of nanocrystalline TiO_2 (anatase) films, exhibiting a more organized morphology, such as inverse opal [14], nanotubes [15,16] or nanorods [17]. In the first case, the enhancement of red absorbance by photonic effects was predicted [14], but a sluggish charge transport in the inverse opal has to be taken into account too [18]. Nanotubes and nanorods are expected to show superior electron transport properties. Indeed, an ultrathin film (360 nm) of TiO_2 nanotubes exhibited $\phi_{\mathrm{sol}} = 2.9\%$ after sensitization with bis(tetrabutylammonium) *cis*-dithiocyanatobis(2,2′bipyridine-4-COOH,4′-COO$^-$) ruthenium(II) coded as N-719. This efficiency was promoted by $TiCl_4$ treatment, but films thicker than ca. 500 nm were not accessible by the reported synthetic protocol, which was based on anodic oxidation of Ti metal [15]. Recently, however, thicker nanotube array films (up to 5.7 μm) were demonstrated by Frank et al. [16]. Upon sensitization with N-719, they exhibited $\phi_{\mathrm{sol}} = 3\%$, and superior electron transport properties compared to traditional sol–gel nanocrystalline anatase [16].

In 2005, we developed an alternative fabrication procedure for TiO_2 photoanodes with highly oriented mesoporous films made by supramolecular templating with amphiphilic triblock copolymers (Pluronic) [19]. Our synthesis employed a protocol pioneered by Stucky et al. [20], but the key upgrade consisted of a reproducible upscaling of the film thickness [19]. Electrodes of ca. 1 μm film thickness were made *via* triple layer-by-layer deposition. The electrodes were sensitized by 4,4′-dicarboxy-2,2′-bipyridine(4,4′-di-(2-(3,6-dimethoxyphenyl)ethenyl)-2,2′-bipyridine) coded as N-945. They exhibited excellent solar performance ($\phi_{\mathrm{sol}} = 4.04\%$ for film thickness 1 μm) comparing favorably to that of conventional films from non-organized anatase [19]. Similar promising results were obtained for N-3 sensitized films in liquid-junction cells ($\phi_{\mathrm{sol}} = 3.64\%$ and 5.31% for film thicknesses 1 μm and 2.5 μm, respectively) [21] and for solid state dye sensitized solar cells based on poly(3-octylthiophene) ($\phi_{\mathrm{sol}} = 0.52\%$) [22]. This paper reports further investigation of this procedure. Our central motivation was to explore possibilities of further increase of the roughness factor by increasing the number of successively deposited layers.

2. Experimental

2.1. Materials

TiO_2 films were grown from a solution made by slow addition of 9.7 g of HCl (37% Aldrich) to 12.7 g of titanium ethoxide (Aldrich) under vigorous stirring. Separately, 4.0 g of block copolymer Pluronic P123 [$OH(CH_2CH_2O)_{20}(CH_2CH(CH_3)O)_{70}(CH_2CH_2O)_{20}H$ from Aldrich] was dissolved in 36.3 g of 1-butanol (Aldrich) and added to the HCl/Ti(EtO)$_4$ solution. This solution was aged by stirring at ambient temperature for at least 3 h. The films were deposited by dip coating (withdrawal rate of 0.8–1.25 mm/s) onto 7.5 cm × 2.5 cm^2 sized slides of glass or F-doped SnO_2 glass slides (TEC 8 from Libbey-Owens-Ford, 8 Ω/□). To this purpose, we have used a home-made set-up for vibration-free dip-coating. It consisted of a hydraulic piston, which was operated by a precision pump (KD Scientific, USA). The layer was aged at 75% relative humidity and temperature 24–25 °C for 24 h. Subsequently, the layer was calcined in air at 350 °C for 2 h (heating rate: 1 °C/min). For the preparation of thicker films consisting of more layers, the described procedure was repeated.

In some cases, the prepared films were further processed for improvement of their crystallinity as described in Ref. [23]. Briefly, the film was treated for 6 h at 200 °C in a stream of nitrogen saturated with furfuryl alcohol (Aldrich). During this treatment the film color turned to deep brown. Subsequently, the film was exposed to pure nitrogen at 500 °C (temperature ramp 3°/min) and was kept at 500 °C for 5 h. Finally, the film was heated at 400 °C in O_2 for 30 min, while the film turned back to colorless.

The N-3 and N-719 dyes were purchased from Solaronix SA (Switzerland) and were used as received. The N-945 dye was laboratory-synthesized in EPF-Lausanne, and was available from our previous work [19]. Immediately after calcination, the still warm electrode (ca. 50 °C) was dipped in $3–5 \times 10^{-4}$ M solution of the N-3, N-719 or N-945 dye in acetonitrile + *t*-butanol solution (1/1, v/v). The first two dyes served for determination of surface coverage; the N-945 served for solar tests. The electrolyte solution was 0.6 M *N*-methyl-*N*-butyl imidazolium iodide, 40 mM I_2, 0.075 M lithium iodide, 0.26 M *tert*-butylpyridine, 0.05 M guanidine thiocyanate in acetonitrile/valeronitrile (85/15, v/v). The electrodes were soaked in the solution for 19 h to secure complete attachment of the sensitizer dye on the electrode surface.

2.2. Methods

Adsorption isotherms of krypton at 77 K were measured with a Micromeritics ASAP 2020 instrument. Before the adsorption measurement, all samples were degassed at 523 K overnight. The BET surface areas were calculated using the data in the range of relative pressure p/p_0 from 0.05 to 0.25. Following the usual practice, the saturation vapor pressure p_0 of the supercooled liquid krypton and the atomic cross-sectional area of 0.21 nm^2 were used. The layer thicknesses were measured by alpha-step profilometer, Tencor Instruments. Scanning electron microscopy images were obtained at Hitachi FE SEM S-4800 microscope.

The amount of adsorbed N-3 or N-719 dye was determined spectrophotometrically. The N-3 sensitized electrode was dipped into 5.00 mL of 10^{-4} M NH_4OH. The electrode sensitized with N-719 was dipped into 3.00 mL of phosphate buffer (pH 7). The mixture was stirred, until complete desorption of the dye into the liquid took place. The resulting dye solution was analyzed spectrophotometrically in a 1.00 cm quartz optical cell (Hellma). The concentration was calculated using the following extinction coefficients (in $M^{-1} cm^{-1}$ at $\lambda = 500$ nm): 13 100 for N-3 and 13 600 for N-719. They were determined by using fresh standard solutions, which were prepared by dissolving a known amount of crystalline dye in the respective solvent. (We should note that the standard solutions were slightly unstable. For instance, the 10^{-5} M solution of N-719 exhibited attenuation of the optical density by 28% after 27 days of storage at ambient conditions. Also note that the spectrophotometric data in the used media differ from those reported in the literature for ethanolic solution of N-3 [3] and N-719 [24]).

For photoelectrochemical tests, the dye-coated TiO_2 film was illuminated through the conducting glass support. The light source was a 450 W xenon lamp that was focused to give light power of 1000 W/m^2, the equivalent of one Sun at AM 1.5, at the surface of test cell. The spectral output of the lamp was matched in the wavelength region of 340–800 nm with the aid of a Schott KG-5 sunlight filter. This reduced the mismatch between the simulated and the true solar spectrum to less than 2%. The differing intensities were regulated with neutral wire mesh attenuator. The applied potential and cell current were measured using a Keithley model 2400 digital source meter.

3. Results and discussion

The synthesis of mesoporous films is based on the method called evaporation-induced self-assembly (EISA) [25]. This is a complicated sol–gel process taking place in a film, which was initially deposited *via* dip-coating of a liquid precursor on a solid substrate. The quality of the films produced is crucially dependent on experimental details, such as withdrawal rate in the dip-coating, ambient humidity and type of precursor [26–29]. The film thickness (L) scales with the withdrawal rate (U) according to the Landau–Levich equation [30]

$$L = 0.94 \frac{(\eta U)^{2/3}}{\gamma^{1/6}(\rho g)^{1/2}} \tag{5}$$

where η is the viscosity, γ is the surface tension, ρ is the density of the liquid, and g is the acceleration of gravity. This relationship was derived for the formation of fluid films. In addition to this, the preparation of a mesoporous solid film includes not only the deposition of the fluid layer, but also the aging (accompanied by the evaporation of volatile components) and calcination. It is obvious that the shrinkage of the film takes place during the last two steps of preparation. This effect could influence the value of the proportionality constant in Eq. (5), but the dependence of $\log L$ versus $\log U$ remains linear with the slope of 2/3 regardless of the film shrinkage.

The dependence of the film thickness L on the withdrawal rate U is shown in Fig. 1. The experimental points for $L > 300$ nm were fitted to a straight line with a slope of 0.696, which is close to the theoretical value of 0.667 from Eq. (5). Thinner films deviate from this dependence, presumably due to the surface roughness of the substrate. Obviously, the deposition of mesoporous TiO_2 film by dip-coating is limited to sub-micron thicknesses only. Such films do not provide a sufficient roughness factor for applications in Grätzel cells (cf. Eq. (3)). To address this issue, we grew films with $L \approx 1$ µm by successive deposition of three layers [19].

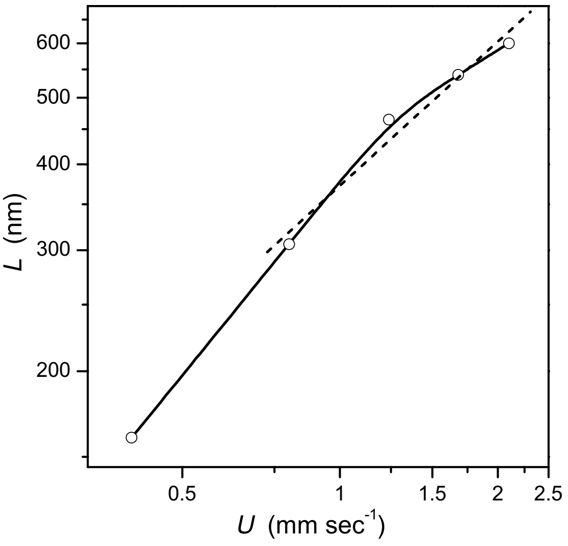

Fig. 1. TiO_2 layer thickness (L) as a function of withdrawal rate (U) for dip coating of F–SnO_2 support from the Pluronic P123-Ti$(EtO)_4$ precursor.

A further upgrade of the dip-coating protocol is presented here. By careful control of the deposition conditions (see Section 2) we have succeeded in deposition of mechanically stable and crack-free films composed of up to 10 layers; $L \approx 2.3$ μm. Fig. 2 shows the top-view SEM image of this film. The surface of the 10th layer still exhibits the organized mesoporous morphology, which is well reminiscent of that of the 1st or 3rd layer shown in our earlier work [19]. The film had excellent adhesion to the FTO support and no mechanical defects or cracks. Also the films exhibited good optical transparency to visible light. The surface coverage of the dye was tested using N-3 and N-719. The reason for this selection of dyes was the availability of the literature data for the area occupied by one molecule at the anatase surface, which resulted both from experiments and theoretical modeling [9–13,24]. The actual values of Γ_0 were reported between 0.56 and 1.16 molecules/nm^2 for N-3 [9–13,24] and 0.96 molecules/nm^2 for N-719 [24].

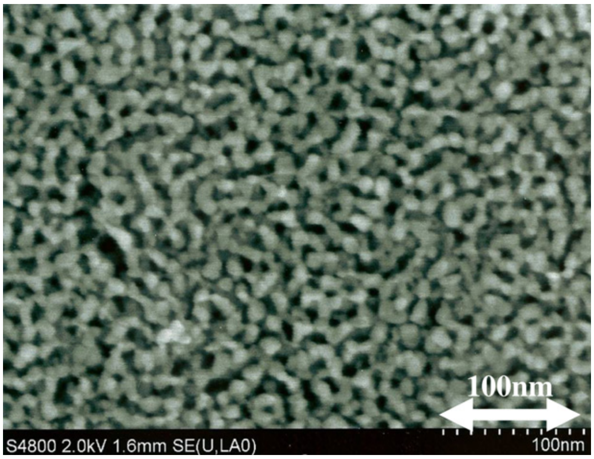

Fig. 2. SEM image of the surface of mesoporous film made from 10 successively deposited layers.

The experimental surface concentrations, Γ were determined spectrophotometrically to be between 9 and 48 nmol/cm^2 for all our films (1–10 layers) sensitized with N-3 or N-719. Using the actual extinction coefficients for the given dyes, and assuming $\eta_{\mathrm{inj}} = 100\%$, the expected IPCEs can be determined from Eq. (3). This procedure supposes that our rough films behave as ideally transparent media, i.e. the Rayleigh scattering of light inside the film can be neglected. The latter is, however, significant in conventional films from colloidal precursors. For instance, Fillinger and Parkinson estimated that the optical density of these films can be doubled by scattering [10], while this effect can be deliberately maximized in bilayer films containing large particles [5]. On the other hand, our mesoporous films are composed of ultrasmall and non-agglomerated nanocrystals embeded in a glass-like matrix of "amorphous" TiO_2 [19]. This, presumably, allows neglect of the scattering effects, and use of the homogeneous-medium concept (Eq. (3)) for our data processing.

Fig. 3 shows the calculated IPCEs within these approximations. To increase the number of experimental data points for the given number of layers, we have varied the withdrawal rate in dip coating. This provided a tool for fine tuning of the film thickness (cf. Eq. (5)). The calculated IPCEs are plotted against the roughness factor determined from measured BET surface areas by Kr adsorption. If we assume that the specific surface area, "seen" by the adsorbate molecule (Kr in BET measurement) is identical to the

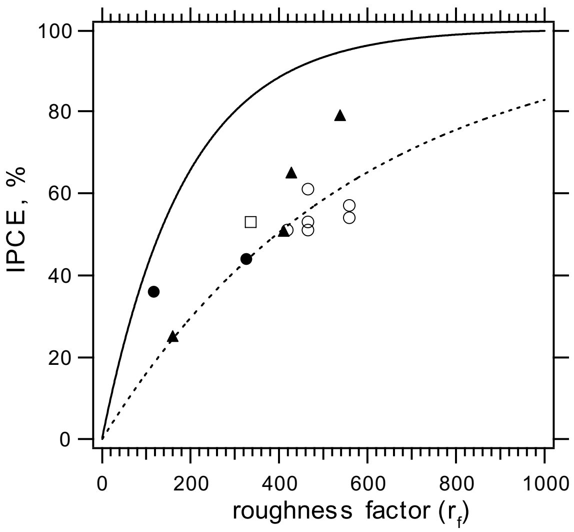

Fig. 3. Calculated IPCEs from Eq. (3). The surface concentrations of the N-3 or N-719 on a TiO_2 electrode were determined spectrophotometrically, and IPCEs are plotted as a function of roughness factor (from Kr adsorption isotherm). Full triangles denote electrodes composed from 1, 3, 5, and 10 layers sensitized with N-3. The other points refer to electrodes sensitized with N-719. Full points = 1 layer; square = 2 layers; open points = 3 layers. The full line is a theoretical curve for N-719, assuming $\Gamma_0 = 0.96$ molecules/nm^2; the dashed line is a fit of experimental data for $\Gamma_0 = 0.31$ molecules/nm^2.

surface area "seen" by the N-3 or N-719 molecules, we can fit the experimental data, both for N-3 and N-719 to a surface coverage of $\Gamma_0 = 0.31$ molecules/nm^2 (dashed line in Fig. 3). Also shown in Fig. 3 is the fit for $\Gamma_0 = 0.96$ molecules/nm^2, which has been modeled for ideal anchoring of N-719 to the anatase (101) face (full line in Fig. 3). An identical theoretical curve can also be assumed for N-3, whose extinction coefficient and Γ_0 are very similar to these for N-719 [9–13,24].

Obviously, the surface coverage found is only about one third of the ideal coverage for a perfect monolayer. We may speculate that the reason for this incomplete dye loading is the presence of "amorphous" TiO_2 in the mesoporous framework [20]. This argument is supported by the fact that the 5- and 10-layer films deviate significantly from the fit towards larger Γ_0 (cf. Fig. 3) because these films passed through numerous calcination cycles during which the crystallization of anatase progressed.

The results of solar cell tests are summarized in Table 1 for electrodes, which were sensitized with N-945 dye. The motivation for using this dye resulted from beneficial optical parameters of N-945 compared to those of N-3 or N-719: the red-shifted absorption maximum, larger extinction coefficient, and better solar efficiency ϕ_{sol} [19]. The solar performance of a sensitized TiO_2 photoanode is influenced by its surface area, expressed by the roughness factor, crystallinity, porosity, quality of crystal interconnects, etc. The increase in surface area raises the amount of adsorbed dye on the film surface, and the presence of defect-free and well interconnected anatase crystals is essential for the electron transport from the dye to the substrate current collector.

Fig. 4 confirms that repeated dip-coating increases the roughness factor (r_f) and the solar efficiency ϕ_{sol}. However, this expected conclusion is valid only for the films composed of ca. 1–5 layers, but for a larger number of layers both these parameters reach a saturation plateau. The solar conversion efficiency of 4.63% was determined for a 1.9 μm thick mesoporous TiO_2 film consisting of 8 layers. The film consisting of 10 layers exhibited similar solar efficiency, despite ca. 20% increase in the layer thickness (Table 1).

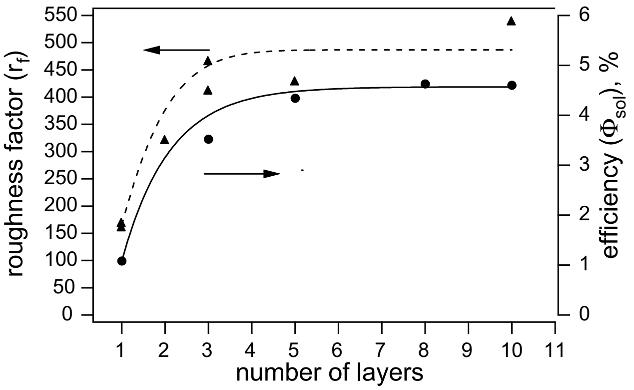

Fig. 4. Roughness factor and solar conversion efficiency (at 1 Sun) as a function of the number of layers. Triangles and dots denote the roughness factor and the efficiency, respectively. Both the full and dashed lines represent curve fitting of the corresponding experimental data.

At first sight, this seems to be simply a result of the almost identical roughness factor for thicker films, but there is, actually, no exact proportionality between r_f and ϕ_{sol}. For instance, the ϕ_{sol} of a 5L film remains unaffected, if a post-deposition heat treatment at 425–500 °C is applied during the film fabrication (Table 1). However, such heat treatment causes a considerable drop of r_f already under the mildest conditions used (2 h at 425 °C; Table 1). Also for the 1L film, there is no dramatic decrease in ϕ_{sol}, even if the film is treated at extreme temperatures (the maximum applicable temperature is limited by the heat stability of FTO glass).

The post-deposition heat treatment is beneficial, because it causes crystallization of "amorphous" TiO_2 to anatase, but, at the same time, the crystal growth and the pore infilling lead to a drop of the light harvesting efficiency of the film. The same phenomena occur, actually, during repeated annealing of multilayer films: the "older underlayers" had to pass through many calcination cycles, during which the

Table 1
The results of solar cell tests on mesoporous TiO_2 thin films prepared by repeated dip-coating

Number of layers, thermal treatment	L (μm)	El. area (cm^2)	ϕ_{sol} @1Sun(%)	U_{OC} (mV)	J_{SC} (mA/cm^2)	f	r_f
1L		0.156	1.08	727	2.00	0.74	161
1L 500 °C 2 h		0.156	1.30	767	2.25	0.75	
1L 425 °C 2 h, 525 °C 2.5 h		0.158	1.32	798	2.22	0.74	
1L 525 °C 2.5 h		0.158	1.59	788	2.72	0.75	
1L 550 °C 2 h		0.156	0.92	767	1.60	0.75	
3L	0.8	0.084	3.52	765	6.13	0.75	412
3L[a]	1.0[a]	0.158	4.04[a]	799[a]	7.0[a]	0.72[a]	466[a]
5L	1.3	0.084	4.52	746	8.08	0.75	429
5L	1.3	0.158	4.34	765	7.68	0.74	429
5L 425 °C 2 h	1.3	0.158	4.42	783	7.56	0.75	290
5L 425 °C 2 h, 500 °C 2 h	1.3	0.158	4.39	758	7.91	0.73	
8L	1.9	0.158	4.63	749	8.61	0.72	
10L	2.3	0.158	4.57	748	8.14	0.75	539
10L reproduced			4.60	731	8.57	0.73	

[a] Data from Ref. [19].

crystallinity of old layers improved, but the overall roughness factor did not increase markedly. Obviously, the solar performance of our mesoporous TiO_2 films arises from interplay between the roughness factor and crystallinity, while both parameters can be optimized by the number of layers and/or by heat treatment. High quality films can be fabricated from 3 to 5 layers, which translate into a film thickness of ca. 1 μm (Table 1 and Fig. 4). Further increase of the film thickness (number of layers) is meaningless within the limits of this synthetic protocol.

Stucky et al. [31] have developed an interesting method for improvement of the crystallinity of Pluronic-templated TiO_2 films by intermediate stabilization of the mesostructure with pore-confined carbon, resulting from the pyrolysis of furfuryl alcohol. The carbon filling preserves the framework structure during extensive calcination, and it is finally burned off in oxygen. Consequently, crystalline films with accessible mesopores and superior photoanodic performance for UV light (band-gap excitation) can be fabricated [31].

We have repeated this procedure for our standard 1L and 3L films (see Section 2). The re-crystallized 1L film, indeed, exhibited the ϕ_{sol} increased by 2.9% in average, which matches the conclusion of Ref. [31] about the improved photoanodic performance of the re-crystallized 1L film. However, our 3L film did not show any significant improvement of ϕ_{sol}, and sometimes even smaller values of ϕ_{sol} were measured for yet unclear reasons in parallel experiments. Although the crystallization of carbon-protected mesoporous film does improve the photoelectrochemical properties of the film under band-gap excitation [31], the dye sensitization might be less efficient due to trace carbon impurities at the TiO_2 surface. Hence, we have to develop alternative synthetic routes towards crystalline mesoporous films. In our future experiments we intend to influence the process of anatase crystallization and pore collapse by the modification of the precursor composition.

4. Conclusions

Photoanode materials for dye sensitized solar cells were fabricated via repeated layer-by-layer deposition of mesoporous TiO_2 films on FTO supports. The synthetic protocol implemented the strategy of supramolecular templating with an amphiphilic triblock copolymer, Pluronic P-123. The TiO_2 films obtained consisted of up to 10 layers made by successive dip coating and calcination. They were crack-free, optically transparent, and had thicknesses exceeding 2 μm, while still preserving the organized mesoporous morphology. Their roughness factors, determined from Kr-adsorption isotherms, exceeded 500.

To assess the light harvesting efficiency, the amount of adsorbed ruthenium bipyridine dye, N-3 or N-719, was determined spectrophotometrically. The average surface coverage of either dye on the TiO_2 surface was ca. 0.3 molecules/nm^2, which is about one third of the ideal dye loading assumed for the (1 0 1) anatase face. This dye coverage increased as a result of prolonged thermal treatment.

The solar performance of multilayer TiO_2 films sensitized with N-945 dye scales linearly for 1–3 layer films, but approached a plateau for thicker films. The solar conversion efficiency of 4.63% was found for a 1.9 μm thick mesoporous TiO_2 film consisting of 8 layers. This value compares favorably to that of traditional films of the same thickness made by sintering of non-organized anatase nanoparticles. Obviously, the optimization of such mesoporous films for dye sensitized solar cells presents an interplay between the quality of anatase crystals and their surface area.

The amount of "amorphous" TiO_2 in the mesoporous film can be minimized by thermal treatment. However, prolonged calcination also causes collapse of the organized mesopore morphology and the loss of active electrode area (roughness factor). There can be an interim stabilisation of the structure and the roughness factor of the film by a carbon deposit made by pyrolysis of furfuryl alcohol inside the mesopores, but this treatment does not lead to a significant increase of solar conversion efficiency. Consequently, new synthetic procedures are focused at modification of the precursor, and experiments are under way in our lab to improve the thermal stability of mesoporous TiO_2 films.

Acknowledgements

This work was supported by EC-COST D35.0002 and by the Academy of Sciences of the Czech Republic (Contract No. N100500652). We thank M.K. Nazeeruddin, P. Péchy, P. Liska, and P. Comte for kind assistance.

References

[1] J. Desilvestro, M. Grätzel, L. Kavan, J. Moser, J. Augustynski, J. Am. Chem. Soc. 107 (1985) 2988.
[2] B. O'Regan, M. Grätzel, Nature 353 (1991) 737.
[3] M.K. Nazeeruddin, A. Kay, I. Rodicio, R. Humphry-Baker, E. Mueller, P. Liska, N. Vlachopolous, M. Grätzel, J. Am. Chem. Soc. 115 (1993) 6382.
[4] M.K. Nazeeruddin, P. Pechy, T. Renouard, S.M. Zakeeruddin, R. Humphry-Baker, P. Comte, P. Liska, L. Cevey, E. Costa, V. Shklover, L. Spiccia, G.B. Deacon, C.A. Bignozzi, M. Grätzel, J. Am. Chem. Soc. 123 (2001) 1613.
[5] P. Wang, S.M. Zakeeruddin, P. Comte, R. Charvet, R. Humphry-Baker, M. Grätzel, J. Phys. Chem. B 107 (2003) 14336.
[6] U. Bach, D. Lupo, P. Comte, J. Moser, F. Weissortel, J. Salbeck, H. Spreitzer, M. Grätzel, Nature 395 (1998) 583.
[7] M. Grätzel, Prog. Photovolt. Res. Appl. 14 (2006) 429.
[8] M. Grätzel, Nature 414 (2001) 338.
[9] L. Kavan, M. Grätzel, S.E. Gilbert, C. Klemenz, H.J. Scheel, J. Am. Chem. Soc. 118 (1996) 6716.
[10] A. Fillinger, B.A. Parkinson, J. Electrochem. Soc. 146 (1999) 4559.
[11] Y. Lu, D. Choi, J. Nelson, O.B. Yang, B.A. Parkinson, J. Electrochem. Soc. 153 (2006) E131.
[12] V. Shklover, M.K. Nazeeruddin, S.M. Zakeeruddin, C. Barbe, A. Kay, T. Haibach, W. Steurer, R. Herman, H.U. Nissen, M. Grätzel, Chem. Mater. 9 (1997) 430.
[13] P. Persson, M.J. Lundqvist, J. Phys. Chem. B 109 (2005) 11918.
[14] S. Nishimura, N. Abrams, B.A. Lewis, L.I. Halaoui, T.E. Mallouk, K.D. Benkstein, J. Van de Langemaat, A.J. Frank, J. Am. Chem. Soc. 125 (2003) 6306.

[15] G.K. Mor, K. Shankar, M. Paulose, O.K. Varghese, C.A. Grimes, Nano Lett. 6 (2006) 215.

[16] K. Zhu, N.R. Neale, A. Miedaner, A.J. Frank, Nano Lett. 7 (2007) 69.

[17] J. Jiu, S. Isoda, F. Wang, M. Adachi, J. Phys. Chem. B 110 (2006) 2087.

[18] L. Kavan, M. Zukalova, M. Kalbac, M. Grätzel, J. Electrochem. Soc. 151 (2004) A1301.

[19] M. Zukalova, A. Zukal, L. Kavan, M.K. Nazeeruddin, P. Liska, M. Grätzel, Nano Lett. 5 (2005) 1789.

[20] P. Yang, D. Zhao, D.I. Margolese, B.F. Chmelka, G.D. Stucky, Nature 396 (1998) 152.

[21] K. Hou, B. Tian, F. Li, Z. Bian, D. Zhao, C. Huang, J. Mater. Chem. 15 (2005) 2414.

[22] E. Lancelle-Beltran, P. Prene, C. Boscher, P. Belleville, P. Buvat, S. Lambert, F. Guillet, C. Boissiere, D. Grosso, C. Sanchez, Chem. Mater. 18 (2006) 6152.

[23] U.H.F. Bunz, Angew. Chem. 106 (1994) 1127.

[24] M.K. Nazeeruddin, S.M. Zakeeruddin, R. Humphry-Baker, M. Jirousek, P. Liska, N. Vlachopolous, V. Shklover, C.H. Fischer, M. Grätzel, Inorg. Chem. 38 (1999) 6298.

[25] C.J. Brinker, H. Sellinger, J. Fan, Adv. Mater. 11 (1999) 579.

[26] K.M. Coakley, Y. Liu, M.D. McGehee, K.L. Frindell, G.D. Stucky, Adv. Funct. Mater. 13 (2003) 301.

[27] P.C.A. Alberius, K.L. Frindell, R.C. Hayward, E.J. Kramer, G.D. Stucky, B.F. Chmelka, Chem. Mater. 14 (2002) 284.

[28] S.Y. Choi, M. Mamak, N. Coombs, N. Chopra, G.A. Ozin, Adv. Funct. Mater. 14 (2004) 335.

[29] M.H. Bartl, S.W. Boettcher, E.L. Hu, G.D. Stucky, J. Am. Chem. Soc. 126 (2004) 10826.

[30] C.J. Brinker, G.W. Scherer, Sol–Gel Science: the Physics and Chemistry of Sol–Gel Processing, Academic Press, London, 1990.

[31] J. Tang, Y. Wu, W. McFarland, G.D. Stucky, Chem. Commun. 2004 (2004) 1670.

Multilayer Films from Templated TiO_2 and Structural Changes during their Thermal Treatment

Jan Procházka*, Ladislav Kavan*, Valery Shklover**, Markéta Zukalová*, Otakar Frank*, Martin Kalbáč*, Arnošt Zukal*, Hana Pelouchová*, Pavel Janda*, Karel Mocek*, Mariana Klementová***, Dina Carbone****

*J. Heyrovský Institute of Physical Chemistry, v.v.i, Academy of Sciences of the Czech Republic, Dolejškova 3, CZ-18223-Prague 8, Czech Republic

**Laboratory of Crystallography, Department of Materials, ETH Hönggerberg, Wolfgang-Pauli-Str. 10, CH-8093 Zürich, Switzerland

***Institute of Inorganic Chemistry, v.v.i., Academy of Sciences of the Czech Republic, CZ-250 68 Řež near Prague, Czech Republic

****ESRF Grenoble, 38043 Grenoble Cedex, France

Abstract

Organized mesoporous thin films consisting of TiO_2 nanoparticles were deposited on the conductive glass substrates. The films were grown by implementing the protocol of supramolecular templating with the amphiphilic triblock copolymer, Pluronic P123. The templated multilayer films were manufactured by repeated dip coating followed by a thermal treatment at 350°C/2h after deposition of each layer. The post thermal treatment of the multilayer films was applied to improve the anatase crystallinity while keeping the open morphology and small particle size. The morphological changes and final collapse of the mesoporous structure during the post thermal treatment at 425-540°C were investigated. The upper temperature limit is given by the thermal stability of glass substrates. The limitations of the multilayer preparation technique at the manufacturing temperature of 350°C were evaluated. The structure does not further increase its specific surface area (roughness factor) after deposition of more than 3-5 layers. The new surface area added by deposition of the top layer is compensated by the decrease of the surface area due to sintering of the bottom layers. Morphology of the P123 templated TiO_2 structure was determined as likely the tightest arrangement of randomly positioned particles of certain size on a given pore

diameter. The bulk material consists of three dimensional (3D) pores with two and half dimensional (2.5D) crust on the surface.

1. Introduction

The mesoporous network of TiO_2 nanoparticles is used in many applications such as solar cells, photocatalytic, electrochromic and light-emitting devices. Considerable effort has been spent on the development of TiO_2 mesoporous thin films consisting of ultra small particles. The high-quality transparent mesoporous TiO_2 films on the F-doped tin oxide conducting glass (FTO) are particularly useful for solar cells based on the spectral sensitization of titanium dioxide (anatase) to visible light (Grätzel cell).[1-3]

Past few years have been in a sign of systematic research effort to prepare sophisticated organized TiO_2 structures. Stucky et al.[4-6] have discovered a promising strategy using amphiphilic triblock co-polymers (Pluronic) as the structure-directing agents. This synthetic protocol was further developed by Ozin et al.,[7] Sanchez et al.[8] and Smarsly et al.[9] We have further upgraded this strategy by a reproducible scaling up of the film thickness. Highly efficient TiO_2 electrodes of ca. 1 μm film thickness were fabricated for the Grätzel cell via triple layer-by-layer deposition.[10] The promising applications of Pluronic-templated TiO_2 for the liquid-junction [11] and the solid-state Grätzel cell [12] were also confirmed by others. Thin films of mesoporous TiO_2 were grown by dip coating via a procedure called evaporation-induced self assembly (EISA).[13-15] The film quality was significantly influenced by experimental conditions, such as ambient humidity, withdrawal rate, type of titania precursor and solvent.[6,7,16,17]

Nearly all applications, including the Grätzel cell, require high overall porosity, large surface area and well developed crystallinity of the anatase nanoparticles. However, TiO_2 fabricated via supramolecular templating with Pluronic contains significant amount of amorphous titania [4-6,8] in which anatase nanocrystals are embedded. Other phases beyond anatase were not reported very frequently, but Sanchez et al.[8] found brookite, which grew somewhat unexpectedly by thermal transformation of anatase in small-size inorganic domains. Zukalová et al.[18] further found that these materials contain small amount of monoclinic TiO_2(B), the presence of which had been mostly overlooked by then. Recently, Smarsly et al.[9] also confirmed the presence of TiO_2(B) in the Pluronic-templated materials. They also reported that the content of amorphous titania was between 40 to 60 mol% depending on the calcination temperature, while a phase-pure anatase was obtained after calcination at 600°C.[9] Both the quantitative determination of amorphous TiO_2 and the detection of TiO_2(B) was carried out via electrochemical methods.[9,18]

The crystallinity of TiO_2 film can be improved by a high temperature thermal treatment. However, it is accompanied by fusing, particle growth and eventually, collapse of the structure. In this paper, we have carried out a search for the optimal thermal treatment in relation to the surface area and crystallinity of the nanoanatase mesoporous films. We have developed the manufacturing techniques for multilayer films up to 2.3 μm thickness. By extending the protocol of layer-by-layer deposition [10] up to ten layers, we have probably found the natural limit of increasing the surface area (roughness factor) in these films.

The mesopores in the common single-layer Pluronic templated TiO_2 films were frequently characterized by electron microscopy (SEM and TEM) and by small angle X-ray scattering using classical X-ray sources such as CuK_α [6-8,14,16]. In this paper, we have employed various microscopic and diffraction techniques to follow the structural changes in our multilayer mesoporous films. Besides electron and scanning probe microscopy methods, the structure of our films was analyzed using the synchrotron radiation and the grazing-incidence small angle X-ray scattering (GISAXS). To the best of our knowledge, this methodology, applied on multilayer films, is here presented for the first time.

2. Experimental Section

2.1. Materials

The TiO_2 films were grown from a solution made by a slow addition of 9.7 g of HCl (37 % Aldrich) to 12.7 g of titanium ethoxide (Aldrich) under vigorous stirring. Separately, 4.0 g of block copolymer Pluronic P123 [$OH(CH_2CH_2O)_{20}(CH_2CH(CH_3)O)_{70}(CH_2CH_2O)_{20}H$] from Aldrich was dissolved in 36.3 g of 1-butanol (Aldrich) and added to the $HCl/Ti(EtO)_4$ solution. This solution was aged by stirring at ambient temperature for at least 3 hours. The films were deposited by dip coating (withdrawal rate of 0.8 mm/s to 1.25 mm/s) onto 5.0 cm x 1.3 cm^2 sized slides of F-doped SnO_2 glass slides (TEC 8 from Libbey-Owens-Ford, 8 Ω/square; further abbreviated FTO). For this purpose, we have used a home made set-up for vibration-free dip-coating. It consisted of a hydraulic piston, which was operated by a precision pump (KD Scientific, USA). The layer was aged at 75% relative humidity and temperature 24 – 25 °C for 24 hours. Subsequently, the layer was calcined in air at 350 °C for 2 hours (heating rate: 1 °C/min). For the preparation of thicker films consisting of more layers, the described procedure was repeated up to ten times. In addition to pure TiO_2 films, also doped materials were prepared exhibiting inhibited particle growth. These materials were grown by following the above P-123 templating synthetic protocol, but with a proprietary doping treatment.

These multilayer films were then thermally post-treated at temperatures 425 – 540°C for 1-8 hours to promote the anatase crystal phase development. A series of about one hundred samples was prepared for characterization and selected analyses. All the prepared TiO_2 films were crack-free and optically transparent. The film thickness was linearly proportional to the number of layers even after the post thermal treatment (PTT). In contrast to the literature [9] no collapse of the TiO_2 structure in one direction occurred upon heating.

2.2. Characterization Methods

Adsorption isotherms of krypton at 77 K were measured with a Micromeritics ASAP 2020 instrument. Before the adsorption measurement, all samples were degassed at 523 K overnight. The BET surface areas were calculated using the data in the range of relative pressure p/p_0 from 0.05 to 0.25. Following the usual practice, the saturation vapor pressure p_0 of the supercooled liquid krypton and the atomic cross-sectional area of 0.21 nm^2 were used. The specific surface area is expressed by the roughness factor, which is the physical surface area of the TiO_2 electrode divided by the projected electrode area. The film thicknesses were measured by alpha-step profilometer, Tencor Instruments. Scanning electron microscopy (SEM) images were acquired at Hitachi FE SEM S-4800 microscope. Transmission electron microscopy (TEM) studies was carried out on a JEOL JEM 3010 microscope operating at 300 kV (LaB_6 cathode, point resolution 1.7 Å) with an EDX (Energy Dispersive X-ray) detector attached. Images were recorded by a CCD camera with resolution of 1024 x 1024 pixels using the Digital Micrograph software package. Powder samples were dispersed in ethanol and the suspension was sonicated for 10 minutes. A drop of very dilute suspension was placed on a carbon-coated grid and allowed to evaporate at ambient temperature. Atomic force microscopic (AFM) characterization and imaging was carried out at Nanoscope IIIa Multimode Atomic Force Microscope (Veeco, USA) operating in the tapping mode using silicone cantilevers (OTESPA, Veeco, USA).

Grazing incidence small angle X-ray scattering (GISAXS) measurements were carried out at the ID1 unit of the Grenoble ESRF facility using 10 keV beam. We used a position sensitive detector placed along the direction perpendicular to the sample surface, so that during GISAXS acquisition we could acquire a Q_x-Q_z map in one scan, or integrate the intensity on the whole detector (about 2 degrees). Generally the GISAXS scans are shown in Q space. This can be done using the simple relations:

$$Q_x = 2\cdot\pi\cdot\sin(\Theta)/\lambda, \text{ and } Q_z = 2\cdot\pi\cdot\sin(\Theta_{PSD})/\lambda$$

λ is the radiation wavelength (1.2397 Å), Θ is the diffraction angle and Θ_{PSD} is the angle along the PSD detector. In this way it is straightforward to calculate the average particle distance:

$$D = 2.\pi/Q_{max}$$

where Q_{max} is the position of the first ordering peak in Q_x. Relative density of the film was determined from the critical angle values of the reflectivity scans. The beam penetrated more than one layer at 0.4 degrees indicating a very porous structure. Particle size and different types of pore sizes were associated with the maximum intensity of the peaks from grazing incidence small angle x-ray scattering (GISAXS) scans. The coherent domain size of TiO_2 particles was also calculated from the diffraction patterns of wide-angle X-ray scattering (WAXS) using the Scherrer equation.

Electrochemical lithium insertion was studied by cyclic voltammetry using the Autolab PGSTAT 30 (Ecochemie) potentiostat controlled by a GPES-4 software. The reference and auxiliary electrodes were from Li metal, hence, potentials are referred to the Li/Li^+ (1M) reference electrode. $LiN(CF_3SO_2)_2$ (Fluorad HQ 115 from 3M) was dried at 130°C/1 mPa. Ethylene carbonate (EC) and 1,2-dimethoxyethane (DME) were dried over the 4A molecular sieve (Union Carbide). The electrolyte solution was 1 M $LiN(CF_3SO_2)_2$ + EC/DME (1/1 by volume). All operations were done under argon in a glove box.

3. Results and Discussion

3.1. Film morphology of the bulk, top crust and individual layers

The multilayer films prepared by the modified Stucky's protocol [10] and characterized by the above methods had sometimes different parameters than the previously reported [4-6,8]. While there was a reasonably good agreement on the TiO_2 primary particle size (7-10 nm), the pore size values in the literature vary from about 7 nm to about 15 nm. Our analysis evidences the presence of even larger pores, from about 20 nm to about 30 nm in the FTO substrate direction (Figure 1). This most likely happens due to the multiple calcination steps at 350°C and sintering of the bottom layers after deposition of each additional layer.

Figure 1 shows changes of the pore size based on the information from GISAXS. The individual scans are in the left chart of Fig.1, and the results are summarized in the plot on the right. The detector does accumulate intensity values collected through the entire profile. These values depend on the penetration depth of the beam. At small incident angles up to about 0.2 degrees, the penetration depth is less than 20 nm. At approximately 0.4 degrees the beam penetrates through the first layer (250 nm). This top layer has been calcined only once, therefore, we could not see many changes in the 0.1 - 0.4 degrees range. There is only a slight difference in parameters of the top crust and the pore size under it. From 0.4 degrees the penetration depth rapidly increases to about one micron at 1 degree. GISAXS has detected only a minor increase of the TiO_2 particle size in the 0.4-1.0 degrees region, but there was a major change of the pore size parameter in the bottom layers.

We have determined the structure of the mesoporous film as an assembly of two different morphologies. The three dimensional (3D) structure under the surface is in fact only two and half dimensional (2.5D) on the top. In the bulk, the particles can grow in any direction (left and right, forward and backward, up and down), while directly on the surface they meet with the air and the fusion cannot progress in the "up" direction. The competitive particle growth and limited sintering in one direction caused a preferential fusion of particles to the sides creating a crust on the surface, parallel to the substrate. The 2.5 D crust is denser than the 3D structure underneath.

Typical explanations including that presented in our recent work [10] described the oriented-like assemblies as a result of self organization of TiO_2 nanoparticles. This self organization takes place as a result of both P123-templating and ageing. Although it is possible that some co-polymers are able to create an oriented structure we believe that in the P123 case the limited growth in one direction on the surface has created a geometry looking similar to hexagonal or even to decagonal formations. Based on our current analysis it seems that the previously reported self-organized ordered structure of TiO_2 with the particular parameters (listed below) determined by XRD and other methods might in fact be the tightest packing of 7-10 nm particles on a pore of 15-25 nm in diameter.

The P123-directed pore size and shape is obvious from TEM image in Figure 2A. The P123 micelles do not have a regular spherical shape as the Figure 2A indicates. TEM also revealed an organized structure consisting of parallel oriented ropes of TiO_2 particles. However, this formation may be just a part of the top crust (Figure 2B). In general, the presence of this ordering in the bulk of the sample processed at 350°C was exceptional. The TiO_2 particle size of 8-10 nm determined from TEM (Figure 2C and 2D) agrees well with the value of 8.9 nm obtained by GISAXS.

Figure 3 shows SEM images of two identically prepared P123 templated structures. The sample in Fig. 3A consists of pure TiO_2, while the structure in Fig. 3B was made from doped TiO_2 with inhibited particle size growth (see Experimental Section). Plain TiO_2 particles fused to size of about 8 nm and are situated on approximately 20 nm pores. These pores are imprints of the P123 micelles that were burned off during the thermal processing. The thermally stabilized TiO_2 particles made by doping grew only to the size of about 3 nm and appear to be randomly distributed around the micelles. Obviously, the small particles do not seem to be organized (Figure 3B). The particle organization emerges only after the particles fused together to a certain size (Figure 3A). The ex-micelle pores in the SEM images are roughly spherical, and they look similarly in the TEM picture (Figure 2A).

Some of the former interpretations of the small angle X-ray scattering (SAXS) of Pluronic-templated TiO_2 bulk materials, reported on a cubic mesophase space group (*Im3m*) that was indexed with d-spacings of 7.6, 5.3 and 4.3 nm for the (110), (200) and (211) peaks, respectively, in bulk powder materials after calcination.[4] The SAXS on thin TiO_2 films provides less detailed data, as there is limited number of peaks (often only one), evidencing just short-range ordering.[16] However, the cubic, hexagonal and lamellar phases are distinguishable in some cases. Better ordering is traceable by SAXS for films prior to calcination or after mild calcinations. Most of these studies evidenced that mesopores are perpendicular to the surface.

Based on our GISAXS results supported by other analytical data, the indexes might actually be a perfect fit for the TiO_2 particle size (7.6 nm) and the intermediate distance between particles with two medians at 5.3 nm and 4.3 nm. This statement matches a general rule valid in sintering that the pore size corresponds to approximately a half of the particle size.

Figures 4A and 4B describe our model of the morphology of the P123 templated structure. We assume that the organization of particles is random. However, the close packing of the fused particles on the P123-originating pores makes the structure looking regular. The pores in the bulk are completely surrounded by the framework of titania, while directly on the surface the ex-micelles form holes. We proportionally overlaid the model of 8 nm particles on 20 nm pore with a SEM picture of the real structure in Figure 4C. The projection of this model to the actual structure is quite satisfactory.

The particle size of 8-10 nm and the pore size were determined by number of methods. TEM pictures (Figures 2C and 2D) and SEM images (Figure 3A) confirm the average primary particle size received from the GISAXS analysis (8.9 nm and 18 nm pore size on the surface). The particle size agrees well with the references [7,8,19,20] but others have also reported on considerably smaller anatase particles from 2.4 to 6 nm.[4,5,21] Sanchez et al. reported that the anatase crystal size grew from 5 to 12 nm with the calcination temperature increasing from 400 to 600°C (4 hours calcination, ramp 1°C/min).[8]

3.2. Multilayer film thickness and TiO_2 surface area development

As we have already shown, the large ex-micelle pore size increases stepwise from the top to the bottom layers of the TiO_2 film (Figure 1). This is due to the structure opening at the multiple calcination steps. We have observed a slight increase of the TiO_2 coherent domain size in the same direction. The surface area (roughness factor) of a multilayer TiO_2 film increases linearly up to ca. three layers.[10] Beyond this point the surface area expressed by the roughness factor practically freezes at values in the range of 400-500 (Figure 5). Above three layers, the surface area increase due to the deposition of a new layer is compensated by a loss of surface during the thermal processing step at 350°C (sintering of the underneath layers). Thickness of the film increases linearly with the deposition of each additional layer, while the surface area remains almost unchanged after deposition of more than three layers.

In contrary to the stagnation of the surface area, a progressive improvement of the nanoanatase crystallinity has been observed above three layers. This is caused by the multiple thermal treatments upon deposition of each layer. Five layer films (5L) of 1.3 μm standard thickness and roughness factor of 410-430 have been selected for the post thermal treatment experiments reported below.

3.3. Film morphology changes during the post thermal treatments (PTT)

The motivation for PTT was to improve the crystallinity of nanoanatase, while preserving the highly porous morphology of the P123 templated TiO_2 mesoporous films. For the investigation of nanoanatase in presence of trace amounts of other phases (including amorphous titania and TiO_2(B)), the electrochemistry of Li-insertion turned to be a particularly suitable method.[9,18] The cyclic voltammograms of Li-insertion/extraction in Figure 6 evidences a fast conversion of TiO_2(B) into the anatase above 500°C. Moreover, complete conversion of TiO_2(B) into anatase can be also achieved by a calcination at 450°C for about 40 hours.[22]

Selected thermal treatments at 425°C for 8 hours and 540°C for 1 hour (which was below and above the full conversion point of TiO_2(B) into anatase) were applied to the five-layer TiO_2 films. The morphology changes, particle size growth, porosity, structure collapse and other parameters were monitored and the results are summarized in Table 1.

Morphology changes during the post thermal treatments are shown in Figure 7, which summarizes the results of AFM and SEM analyses. Both methods display the development of the particle size, fusion and collapse of the P123-originating porosity. The thermally post treated film at 425°C/8h consists of parallel patterns of particles (Figure 7B). The structure had not existed before the PTT, so it is not directly associated with the organization of particles caused by the P123-templating. Apparently the model of particles competing during the fusion process seems to be more appropriate.

At 540°C/1h the sintering has created an open structure with a broad particle size and pore size distribution (Figure 7C). The P123-originating porosity has practically disappeared. Figure 8 evidences that large pores created by the collapse of the P123 porosity are ranging from 30 to 70 nm with maximum at 45 nm as determined by GISAXS. The pore size distribution related to the intermediate distance between particles is very broad with three GISAXS maxima at 17, 10 and 6 nm. The GISAXS reflective scans in Figure 8 indicate disappearance of the original structure at elevated temperature. The "critical angle" determined from these scans is often used as a film density parameter. In our case it has remained constant at 1.3 degrees. The critical angle value of 1.64 deg was received for a dense TiO_2 layer with no porosity. If the film had densified, the critical angle would have increased. This is in agreement with the film thickness that also remained constant at 1.3 μm.

Data in Table 1 confirm that there is a significant drop of the film's area (roughness factor) as a result of PTT. The drop of roughness factor from 429 to less than 100 indicates an extensive fusion, the two above parameters indicate neither overall density change of the film (Table 1) nor its collapse in one direction as previously reported.[9] It means that the morphology changes inside the film occur in a constant volume. Figure 7 illustrates that the sintering causes the particle size growth. The small interparticle pores disappear, while framework of the shell structure opens. The large *ex*-P123 pores are less influenced, and the film thickens is almost intact. This can be considered as redistributing of the TiO_2 material and porosity during the PTT within the same volume.

The surface area of TiO_2 decreased to a one fourth at 540°C compared to that before the PTT and the average particle size increased approximately three times. The sintering proceeded slower at 425°C. The particle size received from GISAXS measurements was 11.8 nm. Figure 9 displays diffraction patterns at different penetration depths. The origin of two sharp extra peaks in the surface scans is not clear. The coherent domain size from these patterns was calculated using the Scherrer equation. The obtained values of 11-12 nm are in accordance with the SEM and AFM observations. The P123 originating porosity seems to be partially preserved at this temperature although the pore size has shrunk from approximately 20 nm to about 15 nm (Table 1) and morphology changes are apparent. The roughly hexagonal morphology has turned into a structure consisting of curved parallel ropes of particles (Figure 7B). The pattern also looks as an organized configuration despite a different morphology (see above).

Besides the P123-originating pores we have received tri-modal porosity of 6.8, 5.7 and 4.8 nm at 425°C. These values roughly correspond to a half of the particle size. The collapse of the P123-porosity further proceeds and it is nearly complete at 540°C. After one hour at this temperature, the average particle size grew to 20-25 nm, fusing into even larger aggregates. The originally complicated structure with many parameters fused into a framework with a broad particle size distribution. The primary particles of 20 nm in size are often aggregated in 30 nm and larger clusters. Figures 10 and 11 compare the GISAXS measurements of the five-layer films before and after the PTT. Shifting of the parameters is in Table 1.

The critical incident angle for all these samples is approximately 0.13 degrees (see Table 1). The penetration depth of the beam was only few nanometers at this angle and at 0.1 degree we actually scan only few nanometers underneath the surface. When moving the angle to 0.3 degrees, we significantly increase the penetration depth and collect the signal from the surface and from the bulk. Figures 10 and 11 describe both the changes on the surface and throughout the bulk of the top layer (up to penetration depth of 200 nm). It is obvious that structural changes on the surface are more dramatic than in the bulk. While there is hardly any detectable pore size maximum on the PTT 540°C/1h sample, the bulk in not completely averaged out and still shows some regularities. For the sample 425°C/8h, the P123-originating pores shrink and reorganize. Subsequent temperature increase towards 540°C causes that the structure sinters all together and the pores open, approximately doubling their size. The line crossing the Figure 10 and 11 helps to emphasize these changes.

4. Conclusions

We have determined limitations of the repeated dip coating and calcination procedure for manufacturing of multilayer films made of mesoporous TiO_2. We have described in detail the sintering process reducing the surface area of TiO_2 and increasing the pore and particle size in the bottom layers. The three-layer films prepared via repeated dip coating procedure exhibit maximum surface area achievable by this method. We could not increase surface area by deposition of additional layers, however, we improved the nanoanatase crystallinity by addition of new layers and thermal processing at 350°C. The five layer film represents an optimum, connecting the sufficient surface area and good anatase crystallinity.

We have introduced our model of the formation of the ordered structure based on particles competing for the TiO_2 matrix during the sintering process. The P123 copolymer seems to add the structure required porosity but it does not seem organize the particles in a certain oriented way. Since P123 is a non-ionic surfactant, the driving force for the micelle forming is just the difference in hydrophilicity between polyethylene oxide (PEO) and polypropylene oxide (PPO) chains of the molecule. The mesoporous structure is formed as a result of the competition between association of the titanium dioxide hydrate and P123, and crystallization. Since the binding affinites between the non-ionic surfactant and framework material are much weaker compared to those in ionic templates, the resulting porous structure is less ordered.

The shells consist of randomly distributed TiO_2 nanoparticles. However, number of morphologies can be achieved in the fusing process by adjustments of thermal treatment conditions. The growth of particles during their crystallization process seems to form variety of ornamental structures depending on the calcination temperature and the TiO_2 particle size. This is especially noticeable on the film surface, where the sintering is constrained in one direction creating a denser crust layer parallel to the substrate.

The target of this study was to investigate the possibility of improving the crystallinity of nanoanatase by post thermal treatments at temperatures higher than 350°C used in the manufacturing process. The experiments were performed in the range of 425-540°C and we have monitored the particle size growth and morphology development during the post thermal treatments.

The collapse of the surface area significantly limits the use of temperatures above 500°C. Even if the loss of surface area was partially compensated by an improvement of the anatase crystallinity, it is unlikely that temperatures above 450°C would be feasible for preparation of the TiO_2 structure, unless doping is used.

Post thermal treatment at 425°C does not produce phase pure anatase, however it seems to be a reasonable compromise combining sufficient film surface area (roughness factor) and almost perfectly developed nanoanatase crystallinity.

Aknowledgements. This work was supported by the Czech Ministry of Education, Youth and Sports (contract No. LC-510 and COST D35 1P05OC069) and by the EC project Heteromolmat STRP 516982. The support from the European Synchrotron Facilities in Grenoble is greatly appreciated.

Figure captions

Figure 1. GISAXS measurements: Pore size increase throughout the TiO_2 film - from the top to the bottom. The measurements were taken at different incident angles with different penetration depth of the beam (A); summarized results plotted into a graph showing an increase of the pore size in deep layers (B). The logarithmic scale bar in (A) represents one order of a magnitude of counts per second.

Figure 2. TEM pictures of the basic P123 templated structure before post thermal treatment: A) light spots about 20 nm in size show the P123 pore with rather irregular shape left after P123 micelles; B) top crust image; C) particle size distribution D) average particle size (8-10 nm).

Figure 3. SEM images of templated film - top view: (A) TiO_2 particles 8 nm in diameter surrounding 20 nm P123 pores; (B) doped thermally-stabilized TiO_2 particles 2-3 nm in diameter surrounding 20 nm P123 pores.

Figure 4. Model of the close packing of 8 nm particles on the 20 nm diameter A) single units; B) top view – 2.5D crust; C) proportional projection of our model onto a real TiO_2 structure. Main parameters of the P123 templated structure are the P123 pore size, the TiO_2 primary particle size and the intermediate distance between particles.

Figure 5. Surface area (roughness factor) and film thickness development during the multiple deposition of individual TiO_2 layers.

Figure 6. Cyclic voltammograms of Li^+ insertion into TiO_2 at 0.1mV/sec. The crystal phase development after a post thermal treatment at 500°C/30min is demonstrated. TiO_2(B) and amorphous TiO_2 convert into the anatase phase (labeled A) at this thermal treatment.

Figure 7. The AFM and SEM characterization: Morphology changes of P123 templated five-layer films after the post thermal treatment A) No treatment; B) 425°C/8h; C) 540°C/1h. Scale: AFM – 500 x 500 nm^2; SEM – all pictures magnification 250,000x.

Figure 8. TiO_2 film overall density and morphology changes determined by GISAXS reflective scans. Critical angles (film density parameters) indicate the overall density of TiO_2 films to be around $1.3 g/cm^3$. The logarithmic scale bar represents one order of a magnitude of counts per second.

Figure 9. Diffraction patterns of five-layer film post thermally treated at 425°C/8h. Scherrer calculations of the particle size from scans with different penetration depth provided consistent results between 11-12 nm. The values are in a good agreement with AFM and other characterizations. The deeper scan (0.4°) with a higher penetration depth indicates a slight increase of the particle size in the bottom layers. The scale bar represents 20000 counts per second.

Figure 10. Comparison of GISAXS scans at incident angles A) 0.1° (surface: penetration depth <20nm) and B) 0.3° (penetrates from the top to 20-200 nm under the surface) of five-layer films with no post thermal treatment and post thermally treated at 425°C/8h and 540°C/1h. The dashed vertical line indicates the position of the peak maximum of the sample before the PTT. The logarithmic scale bars represent one order of a magnitude of counts per second.

Figure 11. GISAXS detector maps at 0.1 degree (surface: penetration depth <20nm) and 0.3 degrees (penetrates from the top to 20-200 nm under the surface). The maps describe the morphology changes occurring during the PTT. The vertical line on the right indicates the starting point of the pore diameter. We see a shift to a smaller porosity at 425°C and finally opening of the structure and an increase of the pore size.

Table 1. Structural parameters of the five-layer P123 templated TiO_2 film before and after PTT.

Sample	Physical characteristics			GISAXS					
	Roughness Factor (cm^2 TiO_2/cm^2)	TiO_2 Film Thickness (μm)	Anatase Crystal Phase (%)	Critical Angle (deg)	Ex-P123 Pore Size (nm)	Multimode Porosity Max1 (nm)	Max2 (nm)	Max3 (nm)	TiO_2 Primary Particle Size (nm)
5L	429	1.3	50	0.13	20	6.4	5.6	4.7	8 to10
5L 425°C/8h	328	1.3	80-90	0.132	15	6.8	5.7	4.8	11 to 12
5L 540°C/1h	96	1.3	100	0.13	27-45	17	10	6.1	20 to 40

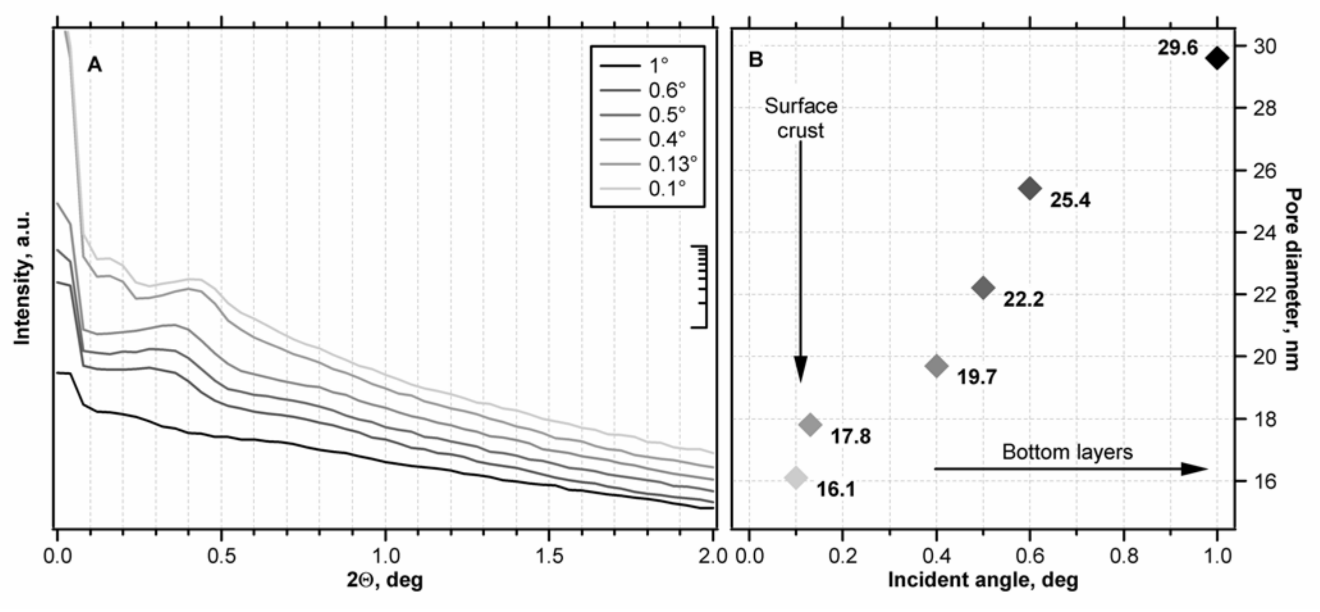

Figure 1. GISAXS measurements: Pore size increase throughout the TiO_2 film - from the top to the bottom. The measurements were taken at different incident angles with different penetration depth of the beam (A); summarized results plotted into a graph showing an increase of the pore size in deep layers (B). The logarithmic scale bar in (A) represents one order of a magnitude of counts per second.

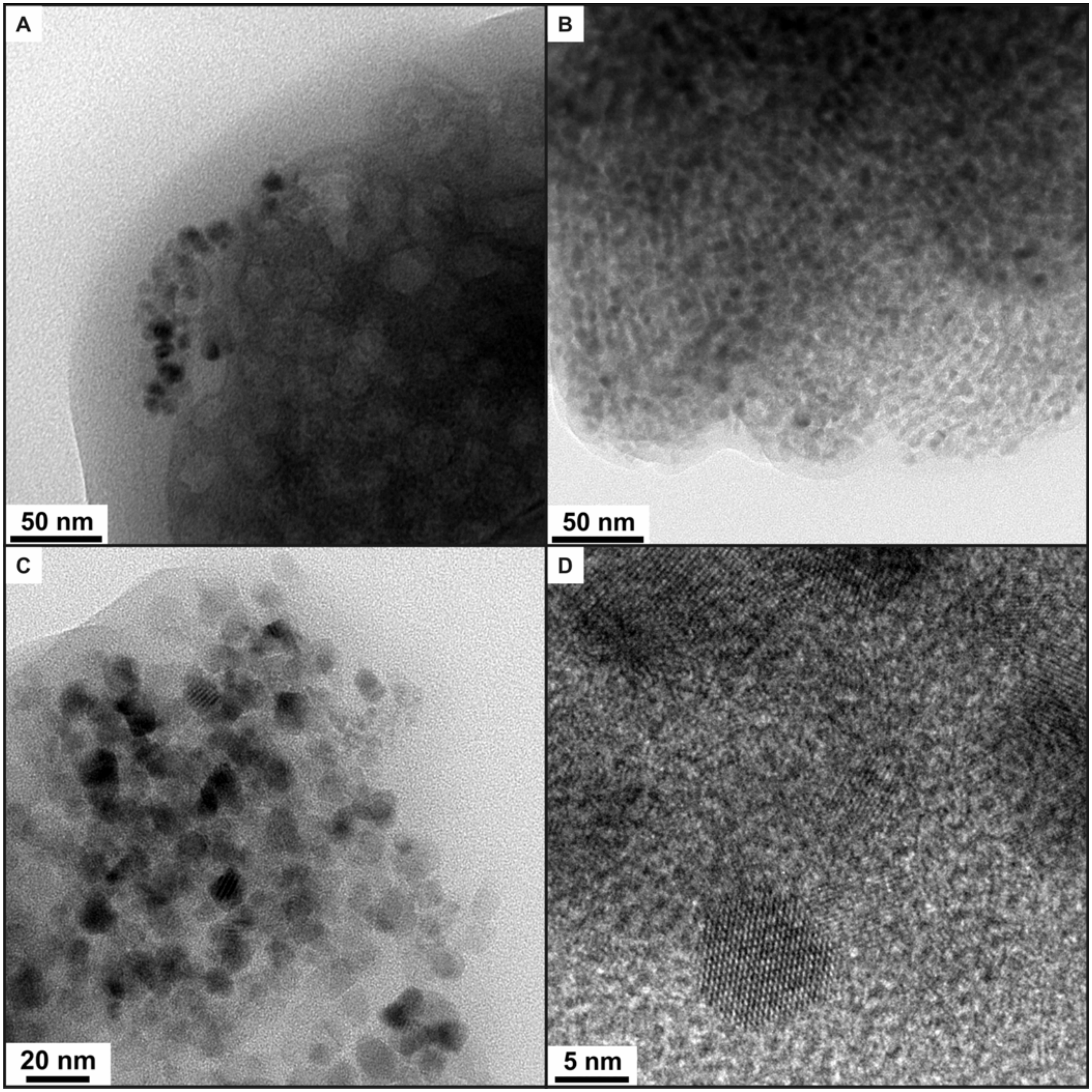

Figure 2. TEM pictures of the basic P123 templated structure before post thermal treatment: A) light spots about 20 nm in size show the P123 pore with rather irregular shape left after P123 micelles; B) top crust image; C) particle size distribution D) average particle size (8-10 nm).

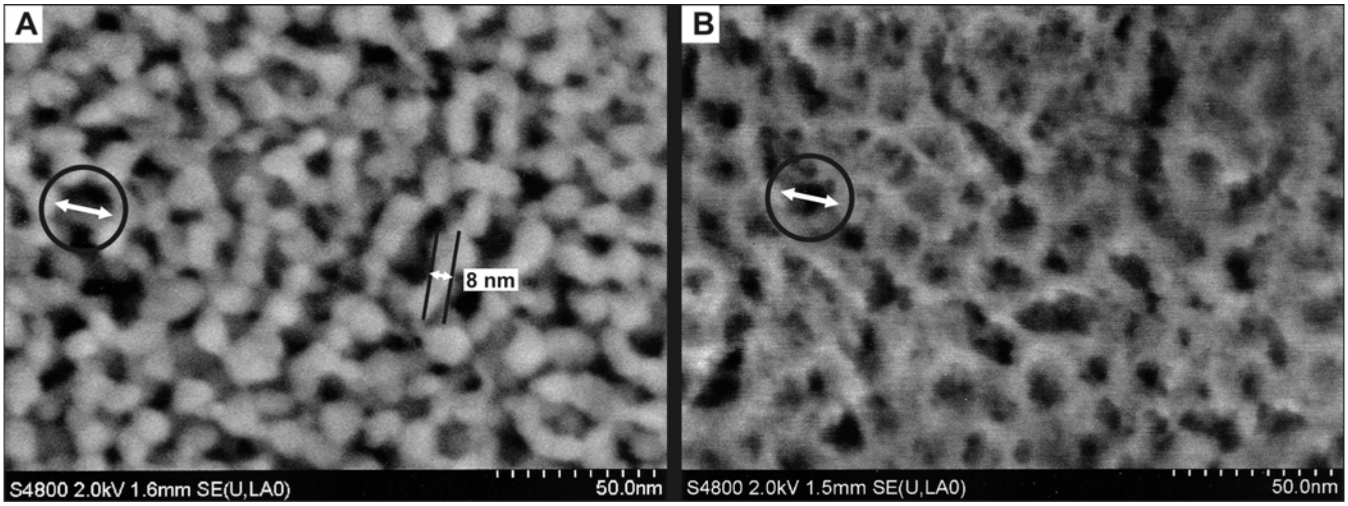

Figure 3. SEM images of templated film - top view: (A) TiO_2 particles 8 nm in diameter surrounding 20 nm P123 pores; (B) doped thermally-stabilized TiO_2 particles 2-3 nm in diameter surrounding 20 nm P123 pores.

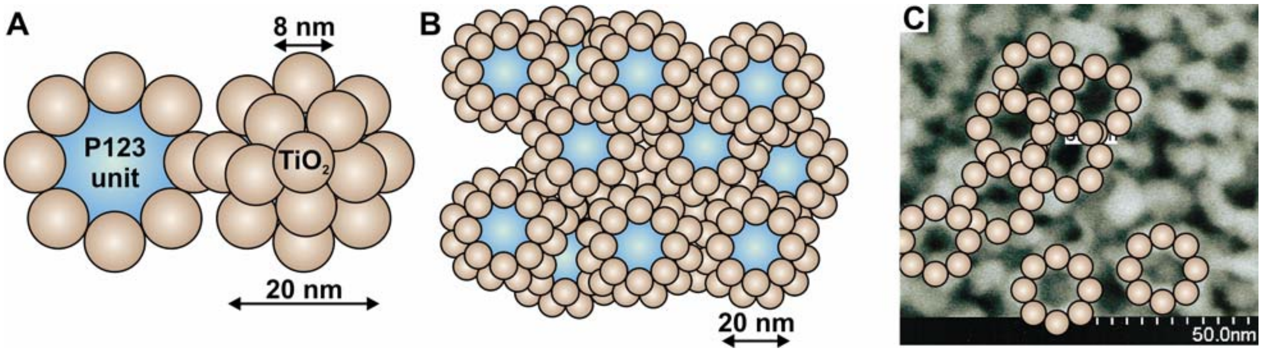

Figure 4. Model of the close packing of 8 nm particles on the 20 nm diameter A) single units; B) top view – 2.5D crust; C) proportional projection of our model onto a real TiO_2 structure. Main parameters of the P123 templated structure are the P123 pore size, the TiO_2 primary particle size and the intermediate distance between particles.

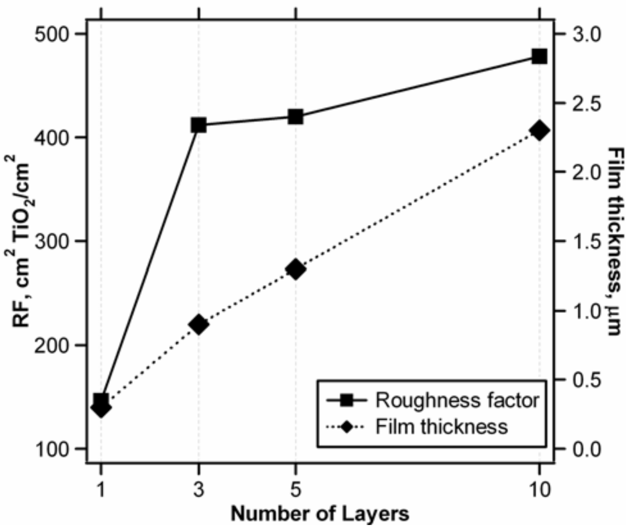

Figure 5. Surface area (roughness factor) and film thickness development during the multiple deposition of individual TiO_2 layers.

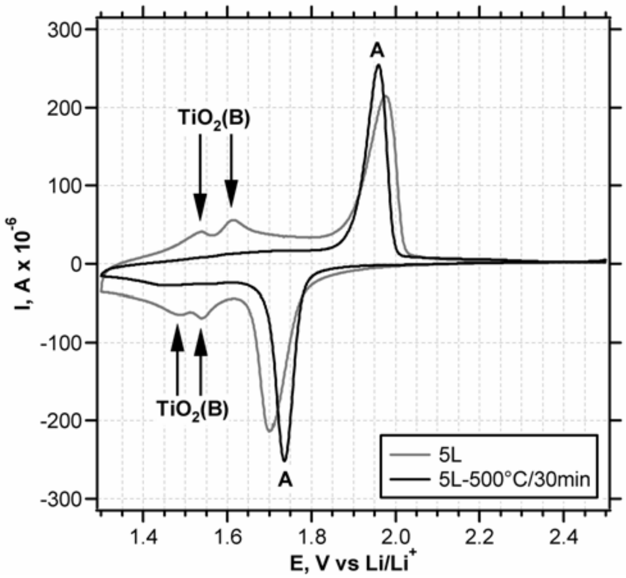

Figure 6. Cyclic voltammograms of Li$^+$ insertion into TiO$_2$ at 0.1mV/sec. The crystal phase development after a post thermal treatment at 500°C/30min is demonstrated. TiO$_2$(B) and amorphous TiO$_2$ convert into the anatase phase (labeled A) at this thermal treatment.

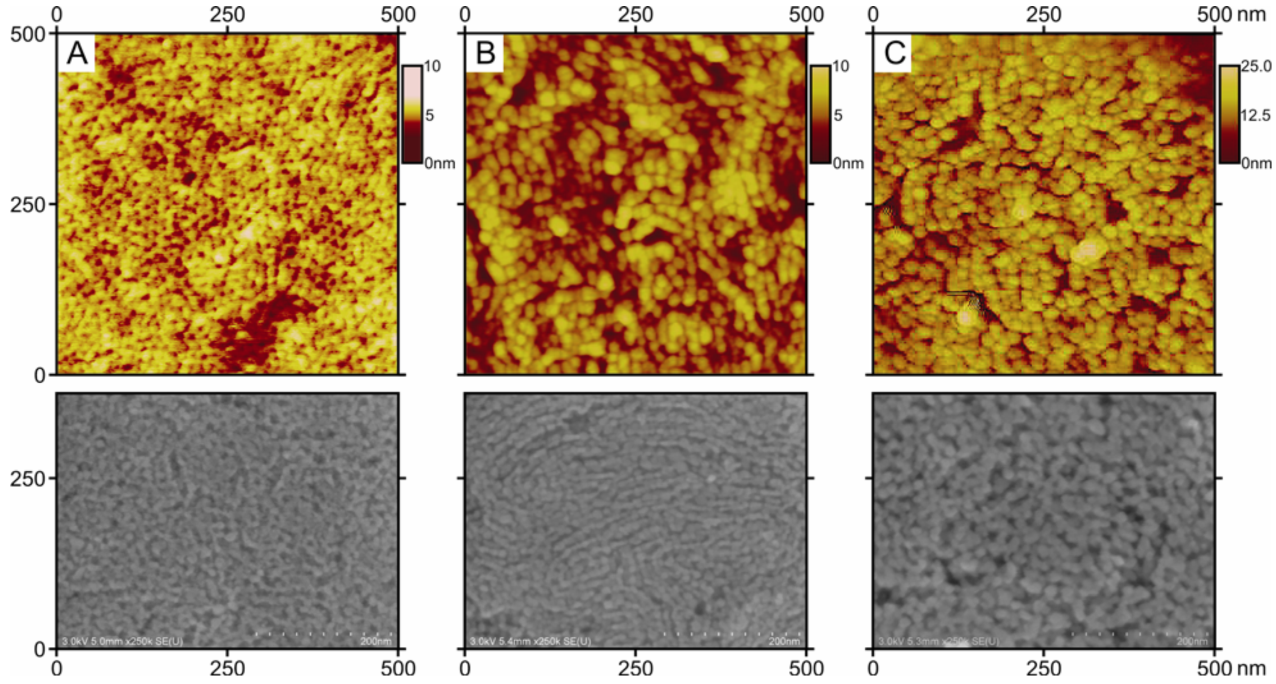

Figure 7. The AFM and SEM characterization: Morphology changes of P123 templated five-layer films after the post thermal treatment A) No treatment; B) 425°C/8h; C) 540°C/1h. Scale: AFM – 500 x 500 nm^2; SEM – all pictures magnification 250,000x.

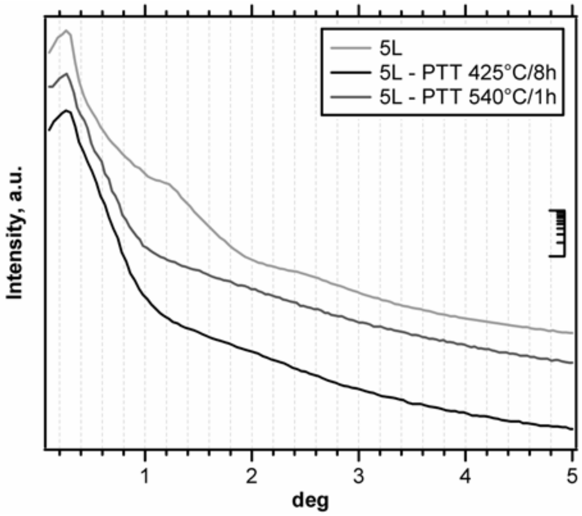

Figure 8. TiO_2 film overall density and morphology changes determined by GISAXS reflective scans. Critical angles (film density parameters) indicate the overall density of TiO_2 films to be around 1.3g/cm^3. The logarithmic scale bar represents one order of a magnitude of counts per second.

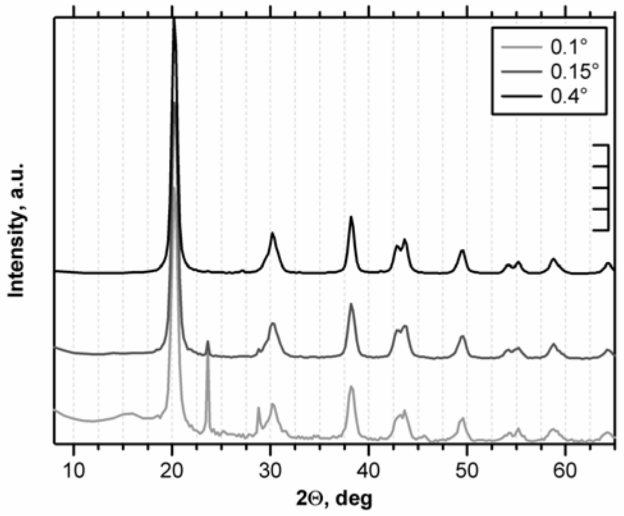

Figure 9. Diffraction patterns of five-layer film post thermally treated at 425°C/8h. Scherrer calculations of the particle size from scans with different penetration depth provided consistent results between 11-12 nm. The values are in a good agreement with AFM and other characterizations. The deeper scan (0.4°) with a higher penetration depth indicates a slight increase of the particle size in the bottom layers. The scale bar represents 20000 counts per second.

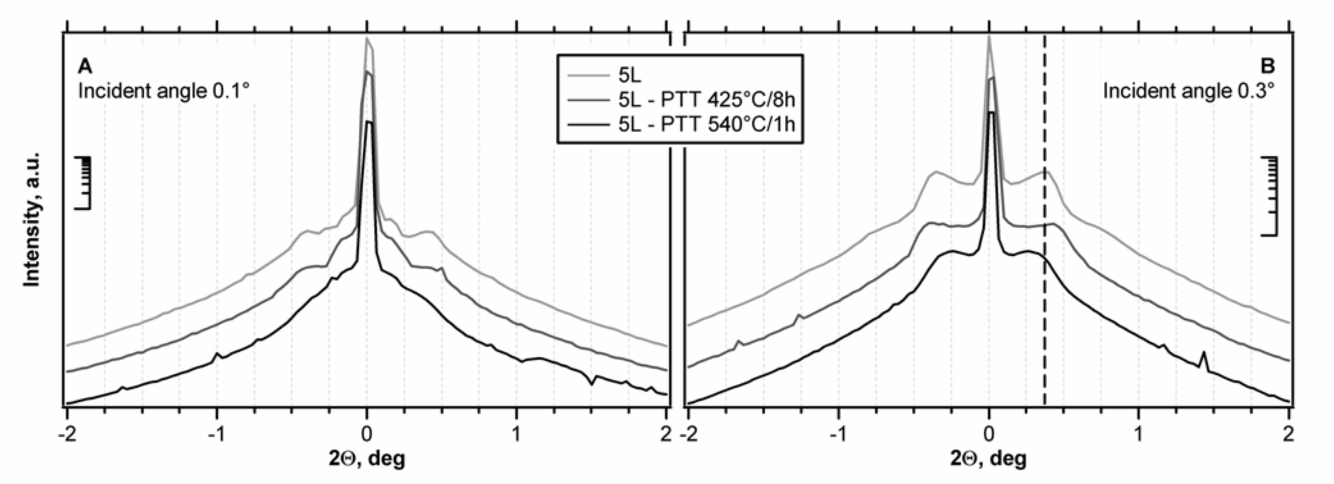

Figure 10. Comparison of GISAXS scans at incident angles A) 0.1° (surface: penetration depth <20nm) and B) 0.3° (penetrates from the top to 20-200 nm under the surface) of five-layer films with no post thermal treatment and post thermally treated at 425°C/8h and 540°C/1h. The dashed vertical line indicates the position of the peak maximum of the sample before the PTT. The logarithmic scale bars represent one order of a magnitude of counts per second.

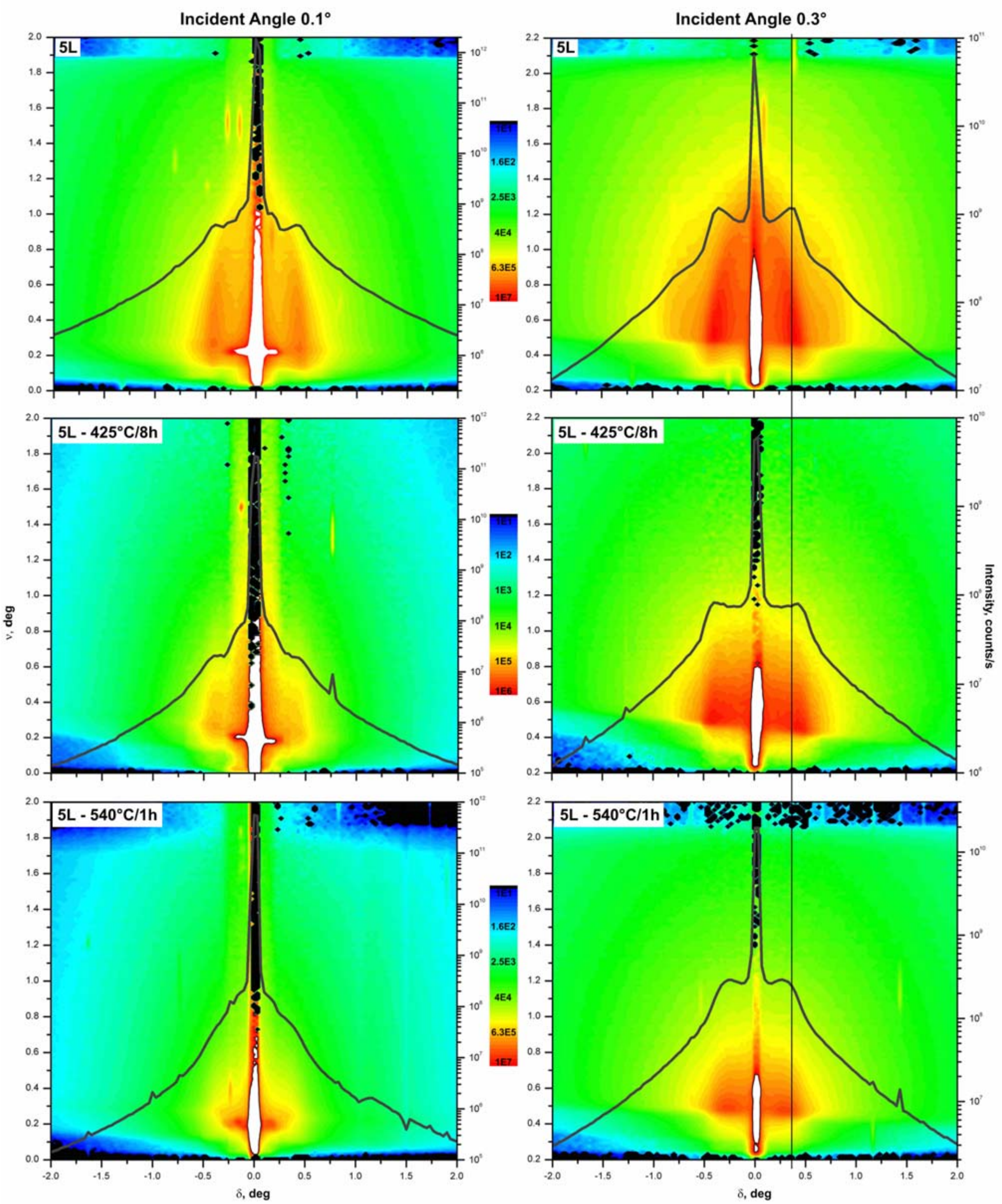

Figure 11. GISAXS detector maps at 0.1 degree (surface: penetration depth <20nm) and 0.3 degrees (penetrates from the top to 20-200 nm under the surface). The maps describe the morphology changes occurring during the PTT. The vertical line on the right indicates the starting point of the pore diameter. We see a shift to a smaller porosity at 425°C and finally opening of the structure and an increase of the pore size.

References

(1) Wu, N.L.; Wang, S.Y.; Rusakova, I.A. *Science* **1999**, *285*, 1375.

(2) Grätzel, M. *Nature* **2001**, *414*, 338.

(3) Grätzel, M. *Chem. Lett.* **2005**, *34*, 8.

(4) Yang, P.; Zhao, D.; Margolese, D.I.; Chmelka, B.F.; Stucky, G.D. *Nature* **1998**, *396*, 152.

(5) Yang, P.; Zhao, D.; Margolese, D.I.; Chmelka, B.F.; Stucky, G.D. *Chem. Mater.* **1999**, *11*, 2813.

(6) Alberius, P.C.A.; Frindell, K.L.; Hayward, R.C.; Kramer, E.J.; Stucky, G.D.; Chmelka, B.F. *Chem. Mater.* **2002**, *14*, 3284.

(7) Choi, S.Y.; Mamak, M.; Coombs, N.; Chopra, N.; Ozin, G.A. *Adv. Funct. Mater.* **2004**, *14*, 335.

(8) Crepaldi, E.L.; Soler-Illia, G.J.A.A.; Grosso, D.; Cagnol, F.; Ribot, F.; Sanchez, C. *J. Am. Chem. Soc.* **2003**, *125*, 9770.

(9) Fattakhova-Rohlfing, D.; Wark, M.; Brezesinski, T.; Smarsly, B.M.; Rathousky, J. *Adv. Funct. Mater.* **2007**, *17*, 123.

(10) Zukalova, M.; Zukal, A.; Kavan, L.; Nazeeruddin, M.K.; Liska, P.; Grätzel, M. *Nano Lett.* **2005**, *5*, 1789.

(11) Hou, K.; Tian, B.; Li, F.; Bian, Z.; Zhao, D.; Huang, C. *J. Mater. Chem.* **2005**, *15*, 2414.

(12) Lancelle-Beltran, E.; Prene, P.; Boscher, C.; Belleville, P.; Buvat, P.; Lambert, S.; Guillet, F.; Boissiere, C.; Grosso, D.; Sanchez, C. *Chem. Mater.* **2006**, *18*, 6152.

(13) Brinker, C.J.; Sellinger, H.; Fan, J. *Adv. Mater.* **1999**, *11*, 579.

(14) Boettcher, S.W.; Bartl, M.H.; Hu, J.G.; Stucky, G.D. *J. Am. Chem. Soc.* **2005**, *127*, 9721.

(15) Grosso, D.; Cagnol, F.; Soller-Illia, G.J.A.A.; Crepaldi, E.L.; Amenitsch, H.; Brunet-Bruneau, A.; Bourgeois, A.; Sanchez, C. *Adv. Funct. Mater.* **2004**, *14*, 309.

(16) Coakley, K.M.; Liu, Y.; McGehee, M.D.; Frindell, K.L.; Stucky, G.D. *Adv. Funct. Mater.* **2003**, *13*, 301.

(17) Bartl, M.H.; Boettcher, S.W.; Hu, E.L.; Stucky, G.D. *J. Am. Chem. Soc.* **2004**, *126*, 10826.

(18) Zukalova, M.; Kalbac, M.; Kavan, L.; Exnar, I.; Grätzel, M. *Chem. Mater.* **2005**, *17*, 1248.

(19) Liu, K.; Zhang, M.; Shi, K.; Fu, H. *Mater. Lett.* **2005**, *59*, 3308.

(20) Liu, K.; Fu, H.; Shi, K.; Xiao, F.; Jing, L.; Xin, B. *J. Phys. Chem. B* **2005**, *109*, 18719.

(21) Bartl, M.H.; Puls, S.P.; Tang, J.; Lichtenegger, H.C.; Stucky, G.D. *Angew. Chem.* **2005**, *119*, 3099.

(22) Kavan, L.; Rathousky, J.; Grätzel, M.; Shklover, V.; Zukal, A. *J. Phys. Chem. B* **2000**, *104*, 12012.

Table of Contents Synopsis

Multilayer mesoporous TiO_2 films were grown using the supramolecular templating with by Pluronic P123. Post thermal treatments were used to align the morphology, particle size and anatase crystal phase parameters. The synopsis graph depicts our model of closest packing of TiO_2 particles on P123 pores.

Synopsis Artwork

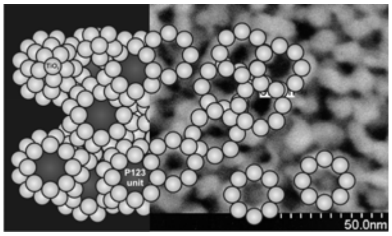

J Solid State Electrochem
DOI 10.1007/s10008-006-0256-2

ORIGINAL PAPER

Electrochemical impedance spectroscopy of mesoporous Al-stabilized TiO_2 (anatase) in aprotic medium

Adel Attia · Marketa Zukalova · Lubomir Pospisil ·
Ladislav Kavan

Received: 22 June 2006 / Revised: 23 November 2006 / Accepted: 8 December 2006

Abstract High-frequency electrochemical impedance spectroscopy was used to investigate the mesoporous film of Al-stabilized TiO_2 on F-doped SnO_2 support in 1 M $Li(CF_3SO_2)_2N$ in ethylene carbonate/dimethoxyethane (1:1 *v*/*v*). Kinetic parameters, viz. charge transfer resistance and chemical diffusion coefficient, were determined. Charge transfer resistance increased with time of contact of electrode in the above aprotic electrolyte solution. The increase followed exponential dependence, whereas the double layer capacitance, simultaneously, decreased exponentially with time. These effects were discussed in terms of the solid–electrolyte interface, which undergoes chemical changes upon contact with the electrolyte solution.

Keywords Impedance spectroscopy · Solid–electrolyte interface · Titanium dioxide · Anatase · Lithium insertion

Introduction

Anatase TiO_2 electrodes find application in solar cells, lithium ion batteries, and electrochromic devices [1–3]. Due to its good Li-storage capacity, cycling stability, and safety against overcharging [4], nanocrystalline TiO_2 (anatase) represents a promising electrode material for Li-ion batteries. Aluminum is known to stabilize the titania matrix, but it does not contribute to the electrochemical accommodation of lithium due to the fixed valence of Al^{3+}. Hence, the specific faradaic capacity of the Al_2O_3/TiO_2 system for Li-insertion is smaller than that of pure TiO_2 [5–7]. Nevertheless, Al and other doping metals in Li–host structures may influence their electronic properties and, thus, improve the voltage and other electrochemical characteristics of the electrode materials [8].

There has been accordingly considerable interest in Al doping of ternary oxides, $LiMO_2$ (M is a metal), which are active for lithium storage. Theoretical and experimental studies confirm that Al substitution of the transitional metal cation increases the cell voltage [9]. Ohzuku et al. [10] demonstrated this effect for Al doping in layered $LiNiO_2$. Jang et al. [11] observed that the open circuit potential (OCP) of $LiAl_yCo_{1-y}O_2$ increased systematically with increasing content of Al, and there was also an improvement in lithium diffusivity, cycle life, and charge capacity. Chen and Dahn [12] studied $LiCoO_2$ covered by ZrO_2, Al_2O_3, and SiO_2 and have found that Al_2O_3-coated $LiCoO_2$ exhibited the best cycle life.

Aluminum was found to be crucial for stabilization of the anatase lattice during chemical transport reactions in the TiO_2–$TeCl_4$ systems, and a large anatase single crystal could only be grown with the aid of Al stabilization [13]. A special form of mesoporous alumina has been frequently used as a template for the fabrication of anatase nanotubes

---

Adel Attia is currently on leave from the Department of Physical Chemistry, National Research Center, El-Tahrir St., Dokki 12622, Cairo, Egypt.

A. Attia (✉) · M. Zukalova · L. Pospisil · L. Kavan
J. Heyrovský Institute of Physical Chemistry,
Academy of Sciences of the Czech Republic,
Dolejškova 3,
182 23 Prague 8, Czech Republic
e-mail: adel_attia@hotmail.com

Present address:
A. Attia
State Key Lab for Physical Chemistry of Solid Surfaces,
Department of Chemistry, Xiamen University,
Xiamen 361005, China

and nanowires [14–18]. Zhang and Banfield [19] reported that the anatase to rutile phase transformation retarded to higher temperatures by the addition of Al_2O_3 to anatase TiO_2. A similar effect was also traced for zirconia in anatase [2]. In our previous works [20, 21], the Al-stabilized anatase was shown to exhibit smaller particle size and larger Li-diffusion coefficient than the reference Al-free anatase. Hence, our Al–TiO_2 material turns to be particularly suitable for investigation of effects occurring at the electrode surface, such as the formation of solid–electrolyte interface (SEI).

The SEI is essential for the action of graphite anodes, but it is also formed at oxidic Li–host structures, operating at larger potentials than graphite [22, 23]. In the case of Al–TiO_2, the lattice distortion and core-shell morphology played an important role affecting the electrochemical properties. In the present work, our earlier investigation of these electrode materials has been upgraded by employing electrochemical impedance spectroscopy (EIS). We have selected for this study the most promising Al–TiO_2 material, having the largest Brunauer–Emmett–Teller (BET) surface area, and superior Li-insertion kinetics from cyclic voltammetry (CV; for details see Refs. [20, 21]).

Experimental

Materials

The synthesis of Al-stabilized titania followed the same protocol as described previously [20, 21]. The solution of Keggin cations $Al_{13}O_4(OH_{24})^{7+}$ was prepared by dissolving 13.13 g of $AlCl_3 \cdot 6H_2O$ in 420 ml of water, and the pH was adjusted to 3.95 with concentrated ammonium hydroxide. The solution of Ti precursor was prepared by mixing 4.54 g of $(NH_4)_2Ti(OH)_2(C_3H_2O_3)_2$ (Tyzor LA, DuPont) and 8.82 g cetyltrimethylammonium chloride (CTAC, Lonza). Then, 66.18 ml of the solution of Keggin cations was diluted to 80 ml with water and added slowly at vigorous stirring to the Tyzor/CTAC mixture. A white precipitate, which formed immediately, was aged in a Teflon bomb at room temperature overnight, at 70 °C for 1 day, and at 100 °C for 2 days, and subsequently isolated by washing and centrifuging. Finally, the material was calcined at 450 °C for 3 h. A reference Al-free blank material was prepared in the same way, but the addition of the solution of Keggin cations was omitted. The final Al-modified TiO_2 contained 9.6 wt.% of Al_2O_3 and exhibited the BET surface area of 185 $m^2\ g^{-1}$. This value compares favorably to the BET surface area of a blank Al-free TiO_2 (73 $m^2\ g^{-1}$) prepared by the same synthetic protocol without Al addition.

Preparation of electrodes

The electrodes were prepared similarly to that in Refs. [2, 3] by using CH_3COOH and Triton X-100 as dispersing agent and surfactant, respectively. The powder material was dispersed into a paste by slow mixing with 0.1 M CH_3COOH under continuous grinding in agate mortar. After about 20 min of homogenization, the slurry was mixed with Triton X-100 and further homogenized. The SnO_2(F)-coated glass from Nippon sheet glass, 10 Ω/square, served as a support for the electrode preparation. The Al–TiO_2 electrode was prepared by a doctor blade method. Scotch tape placed at the edge of the support defined the film thickness and left part of the support uncovered for electrical contact. The geometrical area was defined by masking with Scotch tape at the glass edges and was 0.385 cm^2 in all experiments. The electrode was finally calcined for 3 h in air at 450 °C. Stylus profilometry and scanning electron microscopy evidenced that the thickness of the electrode film was around 1 μm.

Characterization

X-ray diffraction was studied on a powder material using a Siemens D-5005 diffractometer in the Bragg–Brentano geometry with CuKα radiation. EIS measurements were carried out in a one-compartment cell using Hewlett-Packard 4192A gain phase impedance analyzer. The freshly immersed electrode was first subjected to one CV scan starting from the OCP and progressing as follows: OCP → 3 V → 1.1 V → 3 V (all potentials vs Li/Li^+). At this stage, the working electrode was disconnected, relaxed at OCP for a defined time, and the EIS

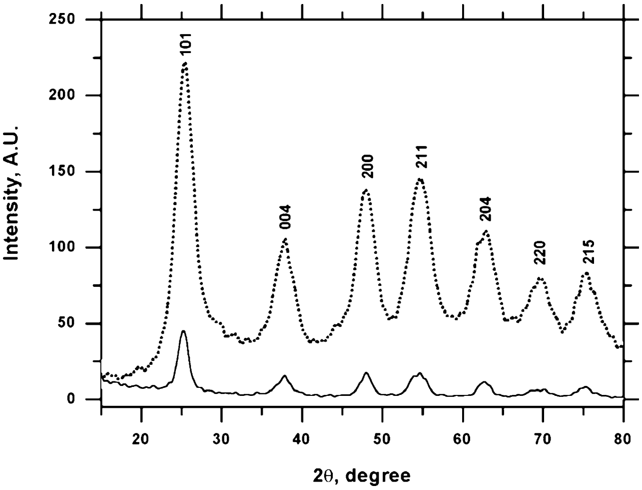

Fig. 1 Powder X-ray diffraction patterns of Al–TiO_2 (*dashed line*) compared to blank sample (*solid line*) prepared by the same synthetic method and with no addition of Al precursor. The Miller indices of the Bragg peaks are indicated near each peak

measurements followed. The impedance measurements (from 12 MHz to 5 Hz) were carried out at open circuit voltage. The time of contact was measured from the completion of the cyclovoltammetric experiment until the start of the EIS measurement. Non-linear fitting and physical modeling of the data were performed by using Equivcrt software version 4.55 (Equivcrt, "Equivalent Circuit") developed by Boukamp [24]. The time interval between each EIS measurement was 10 min. This makes the electrode time exposure to the electrolyte minimum at the beginning. Both the reference and auxiliary electrodes were from Li metals. $LiN(CF_3SO_2)_2$ (Fluorad HQ 115 from 3 M) was dried at 130 °C/1 mPa. Ethylene carbonate (EC) and 1,2-dimethoxyethane (DME) were dried over the 4-Å molecular sieve (Union Carbide). The electrolyte solution, 1 M $LiN(CF_3SO_2)_2$+EC/DME (1:1 *v*/*v*), contained 15–40 ppm H_2O as determined by Karl Fischer titration (Metrohm 684 coulometer). All operations were carried out under argon atmosphere in a glove box.

Results and discussion

Characterization of electrodes

Figure 1 shows the powder X-ray diffractogram of the electrode material compared to that of the reference material obtained by the same synthetic route but without addition of Al (see "Experimental" section). All peaks can be indexed as anatase phase only. Although a solid solution between alumina and titania was reported to form above 1,000 °C [25], the formation of such a species is improbable at our experimental conditions. The coherent domain size was about 3 nm, as calculated from the X-ray line broadening (Scherrer formula) [26]. The presence of a thin layer of rutile on TiO_2 (anatase) core was detected by micro-Raman spectroscopy on the Al-containing sample (data not shown). The layer is obviously too thin to be detectable by X-ray diffraction [20, 21]. These results confirm our previously reported data [20, 21] on almost identical samples.

Electrochemical impedance spectral analysis

Steady-state ac-impedance measurements are more reliable than pulse techniques where cathodic pulses can increase the surface lithium concentration to or even beyond the limiting composition of the electrode. In such a case, any measurable diffusion could arise from different processes. A surface layer formed on the electrode due to decomposition of the electrolyte may influence the insertion of Li^+ into the host material. The formation of solid electrolyte interface on TiO_2 has not been systematically investigated yet. However, there is typically about 4–9% of irreversible charge during the first cycle(s) of Li-insertion into TiO_2 (anatase) [3, 26] that is reminiscent of the SEI formation on other oxidic materials, such as $LiMn_2O_4$ [23]. In addition to this, the slight charge irreversibility of Li-insertion at the time scale of CV may also indicate small retention of Li^+ inside the anatase lattice after completing the CV scan [3, 26]. The Li-ion transport through the SEI, as well as the residual Li, should consequently be considered for understanding of the electrochemical data in general and the EIS in particular.

Figure 2 (curves a–g) shows typical Nyquist plots obtained for the Al-doped mesoporous anatase electrode, which were immersed for different times in the electrolyte at OCP. Impedance spectrum during the first 10 min of immersion time was instable in time; hence, the values were not considered for data fit using the Equivcrt software [24]. The impedance spectra consisted of two separated arcs, one at the ultrahigh and the other at high-frequency ranges. The

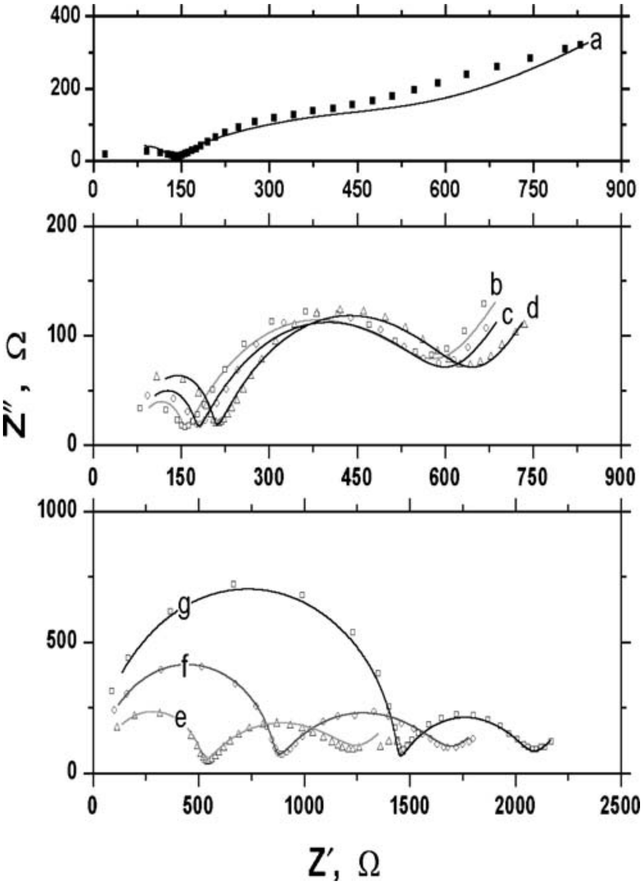

Fig. 2 Impedance measurements represented in Nyquist form of Al–TiO_2 electrode in 1 M $Li(CF_3SO_2)_2N$ in EC/DME (1:1 by mass). The lowest frequency was 5 Hz. The electrode immersion time in the electrolyte solution was 20, 30, 40, 50, 60, 70, and 80 min for *curves a–g*, respectively. *Solid line* represents fitting, whereas *markers* represent the experimental data

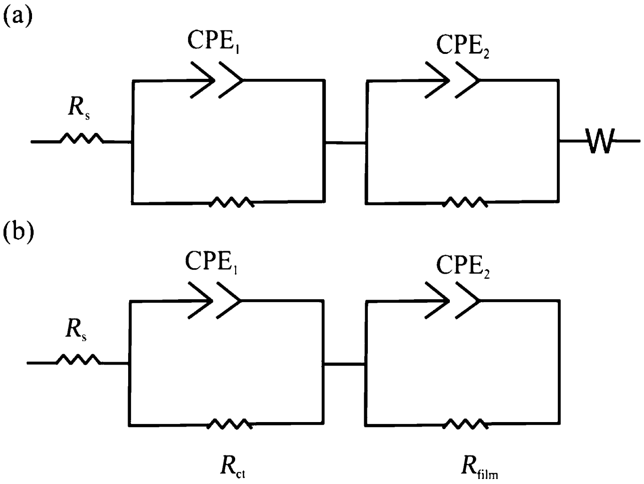

Fig. 3 Equivalent circuit used for analysis of high-frequency electrochemical impedance spectroscopy of Al–TiO_2 electrode (**a** with linear part, **b** without linear part)

low frequency data inclined to a straight line with a slope of approximately 45 °. The impedance spectra of Al–TiO_2 electrode at different times of contact with the electrolyte solution exhibited a typical behavior of a blocking electrode at the minimum time of immersion. In general, the presence of the second semicircle indicates a response of grain interior–grain boundary phase system [27]. The spectrum showing a response at the whole frequency range may be regarded as an imperfect semicircle (Fig. 2, curve a). This indicates that the electrode behaves as having a high polarization resistance, which may be caused by a larger interface impedance and charge accumulation on the surface.

It is likely that the Li^+ desolvation before its interaction with the electrode material is involved in the observed high polarization resistance. The early work of De Levie [28] showed that, for porous electrodes, the phase angle of the impedance is half of that of the equivalent flat electrode and that the absolute magnitude of the impedance of a porous electrode is proportional to the square root of the value equivalent to a flat electrode. De Levie's conclusion, indeed, applies to our spectrum (Fig. 2, curve a). Other models leading to depressed complex impedance plot were also considered [29, 30], but they do not seem to be suitable for our case (*vide infra*).

The electrochemical impedance spectra at Fig. 2, curves b–d, contains two semicircles and a short linear part at the lowest frequency. The only difference between both spectra is the time of immersion. The diameter of the first semicircle increased with the time of immersion. Figure 2, curves e–g, demonstrates that the diameter increase is manifested well in the semicircle at ultrahigh frequency, whereas the diameter of the second semicircle at high-frequency region decreases. The linear part started to decline by increasing the time of electrode immersion (Fig. 2, curves a–e). In this case, the impedance is dominated by the electron transfer resistance.

Figure 3a shows the equivalent circuit, which was used to fit experimental impedance spectra of Al–TiO_2 at different time interval of immersion. It is a serial combination of the solution resistance R_s, two parallel circuits, and a Warburg mass transfer impedance. Each of the parallel circuits contains a constant phase element and a parallel resistor. Element CPE_1 reflects the behavior of the double layer capacitance to which is connected a parallel charge transfer resistance R_{ct}. The other circuit containing CPE_2 and R_{film} represents the capacity of the surface film and the rate of electron transfer across it (expressed as R_{film}). This circuit describes well the impedance spectra with two semicircles and a linear part (as shown in spectra b, c, and d of Fig. 2). Table 1 shows the fitting parameters used. It describes the impedance spectra with two semicircles and a linear part (corresponding to spectra b, c, and d in Fig. 2). Both parallel circuits are connected to W in series that is related to the Warburg diffusion impedance.

Table 1 Fitting parameters for the proposed equivalent circuits

Time (min)	R_s (Ω)	CPE_1-t (F)	CPE_1-p	R_2 (Ω)	CPE_2-t (F)	CPE_2-p	R_3 (Ω)	W-R (Ω)	W-t (s)	W-p	χ^2	Sum of square
20	65.37	1.875E-8	1.306	40.37	0.0014276	0.86764	100.3	1,378	307.2	0.26502	0.02494	3.0934
30	79.62	2.3663E-7	1.031	70.54	6.5121E-4	0.58657	428.3	907.4	862.7	0.5	0.00325	0.39996
40	81.24	1.64E-7	1.042	89.1	6.53E-4	0.58024	428.9	1,383	3,024	0.5	0.00251	0.30911
50	81.58	1.54E-7	1.018	121	6.081E-4	0.5994	439.2	1,620	4,127	0.5	0.00142	0.17197
60	49.87	7.08E-8	1.013	457.7	3.74E-4	0.59343	750.6	N/A	N/A	N/A	0.00173	0.17677
70	48.61	4.44E-8	1.049	781	3.47E-4	0.57765	916.3	N/A	N/A	N/A	0.00126	0.13569
80	37.63	4.65E-8	1.035	1,384	4.36E-4	0.67509	706.1	N/A	N/A	N/A	9.64E-5	0.09543

χ^2 and sum of square are the fitting parameters.

R_s Electrolyte resistance, *CPE_1-t/CPE_1-p* elements of constant phase element (magnitude and exponent parts, respectively) at high frequency range, R_2 charge transfer resistance, *CPE_2-t* and *CPE_2-p* elements of constant phase element (magnitude and exponent parts, respectively) at lower frequency range, R_3 resistance of electron transfer across the electrode film, *W-R/W-t/W-p* elements of Warburg impedance associated to chemical diffusion into the electrode material

The second equivalent circuit, Fig. 3b, is almost the same as that aforementioned in Fig. 3a. It is solely characterized by the absence of linear part. This equivalent circuit describes well the spectra e, f, and g in Fig. 2, which have two semicircles with a small linear part. In this study, CPE_1 represents again the double layer capacitance, whereas CPE_2 stands for a charge accumulation process caused by a slow interfacial process in which guest ions incorporate from the electrolyte into the surface film and, eventually, into the host lattice. The constant phase element is connected with the surface distribution of the interfacial capacitance, which showed that the frequency dispersion can be a property of the double layer itself. In this study, the dominant process is the interaction of Li^+ with the surface structure. Therefore, we consider our model to be similar to that in Ref. [29] for an irreversible reaction. In the present case, the "ladder network" consists of only two parallel circuits connected in series. This phenomenon is more common in the case of intercalation electrodes, which can be described by an adsorption capacitance, C_{ad}, in parallel with R_{lattice} incorporated ions to lattice [31]. The two arcs in the higher-frequency range are due to reactions at the electrolyte/electrode interface, and the inclined line in the lower-frequency range is attributed to a Warburg diffusion impedance through the electrode. However, as it was mentioned before, the second semicircle may be considered as a charge accumulation caused by a slow interface process in which guest ions incorporate from electrolyte into the electrode material [31]. We suggest that the reverse process can occur analogously. It can be represented by the same equivalent circuit, i.e., desorption capacitance, C_{des}, in parallel to resistance, R_{lattice}, due to extraction of incorporated ions from the electrode material. Conway [32] gave an evidence for the close resemblance between the adsorption and intercalation processes derived from fundamental thermodynamics.

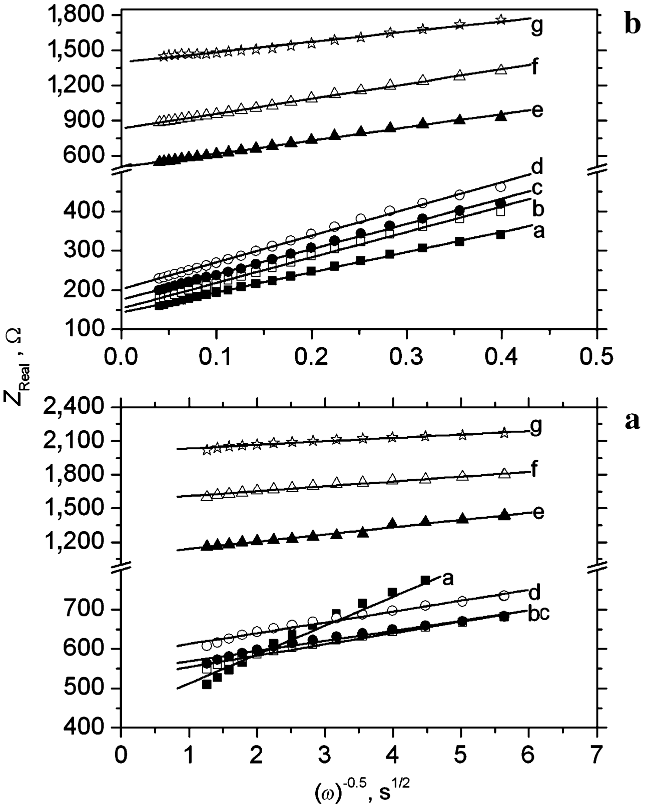

Fig. 4 Real part of impedance as a function of $\omega^{-0.5}$ for **a** low angular frequencies and **b** high angular frequencies. At each graph, the *curves* *a*, *b*, *c*, *d*, *e*, *f*, and *g* represent the time of contact of 20, 30, 40, 50, 60, 70, and 80 min, respectively

It is reported elsewhere [33] that low-frequency CPE can influence the diffusion modeling due to change of the value of the diffusion coefficient by two orders of magnitude. Due to this influence, we determined the diffusion coefficient by an alternative method. Nonetheless, the capacitive behavior of CPE at low frequencies can be attributed to back contact. However, this could not be considered true, as Warburg and CPE exponents should be proportional [34].

Figure 4a, b presents the dependence of the real part of impedance on $\omega^{-0.5}$. The plot shows, separately, high- and low-frequency dependencies (the minimum was 5 Hz). Charge transfer resistance was determined from the intercept of the straight lines at different contact time, whereas the slope of the lines was used for determination of the diffusion coefficient according to the following equations:

$$R = R_s + R_{ct} + \frac{\sigma}{\omega^{1/2}} \tag{1}$$

$$\sigma = \frac{R_g T}{A(2D)^{1/2}(nF)^2\left(\frac{1}{C_O^\infty} + \frac{1}{C_R^\infty}\right)} \tag{2}$$

where R is the real part of impedance, R_s is the solution resistance, R_{ct} is the charge transfer resistance, σ is the Warburg coefficient, ω is angular frequency, R_g is the universal gas constant, T is absolute temperature, A is the geometrical area of the electrode (0.385 cm^2, see "Experimental" section), D is the chemical diffusion coefficient of Li^+ into the $Al–TiO_2$ film, and from it, n is the number of electrons, F is Faraday constant, and C_O^∞ and C_R^∞ are the concentrations of oxidized and reduced species, respectively.

The plot of Z_{Real} vs $\omega^{-0.5}$ yields σ as the slope and $R_{ct}+R_s$ as the intercept. Substituting σ in Eq. 2, we get the chemical diffusion coefficient, D. The obtained value was $(2.1 \pm 0.5) \times 10^{-16}$ $cm^2\ s^{-1}$ at high frequencies, whereas at low frequencies it corresponded to a value of $(3.6 \pm 0.9) \times 10^{-19}$ $cm^2\ s^{-1}$. The D value determined from the plot in Fig. 4 is comparable to the value obtained by using the linear part of impedance (Warburg impedance); however, the values are closer in the case of lower-frequency range, whereas the values at higher frequency are more realistic ones. There is a good correlation between the values obtained at low- and high-frequency range.

The found values of *D* at low frequencies obviously can hardly be assigned to the Li diffusion inside the ordinary anatase lattice, whereas the *D* values at high-frequency ranges match that of nanocrystalline anatase (10^{-14}–10^{-17} cm^2 s^{-1}) of different origins [35–38]. Our actual Al-modified TiO_2 material provided the *D* value of 6×10^{-17} cm^2 s^{-1} from CV (cf. also Refs. [20, 21]). Due to different time scales, the CV technique is suitable for investigation of the Li transport in the bulk anatase [35–38], whereas the EIS highlights the effects occurring at the electrode surface only. We consequently ascribe the smaller diffusion coefficients at low-frequency EIS to other processes than the Li diffusion in anatase, presumably, to Li-ion transport through the surface films (SEI). We may, alternatively, consider the influence of a rutile shell, which was found on the electrode surface (cf. also Refs. [20, 21]). Although the Li-insertion into rutile was not that systematically studied as that for anatase, the diffusion coefficient of Li^+ in rutile lattice might be comparable or even higher than that in anatase [13]. The ultrasmall *D* values observed here at low-frequency range would consequently hardly account for the presence of rutile shell. The passivation surface film (SEI) turns to be the only plausible explanation for our EIS data.

Charge transfer resistance

Figure 5 shows the change of charge-transfer resistance and capacitance with time of the electrode/electrolyte solution contact. The squares denote values from the intercept of slopes to Z_{Real}-axis of Fig. 4b (at high frequency). The stars denote values obtained directly from the Nyquist plot (Fig. 2). Both sets of data are obviously well comparable. Open circles are the experimental data obtained at lower frequency from Fig. 4a. The charge transfer resistance increases exponentially with time, albeit the actual values obtained for high and low frequencies exhibit a constant shift. The true capacitance was calculated from the following equation:

$$C = Q^0(\omega_{\max})^{n-1} \tag{3}$$

The true capacitance is equal to CPE (its magnitude represented by Q^{o} in Eq. (3) if $n=1$, and CPE capacitance properties decreases when *n* approaches zero, $\omega_{\max}$ is the frequency at which maximum imaginary impedance attains. The true capacitance is plotted in Fig. 5 against the increase in the time of immersion and is found to be inversely related to it.

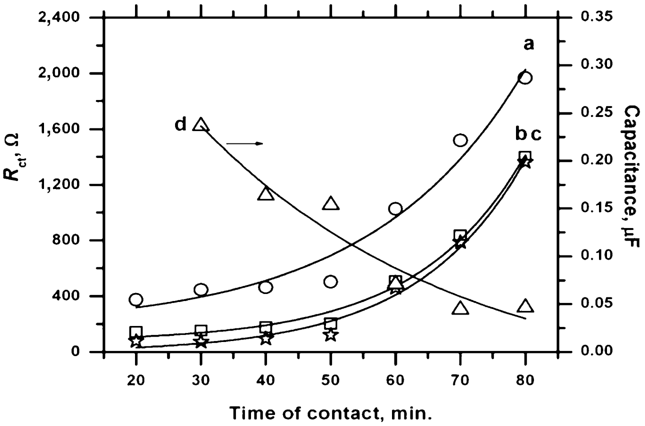

Fig. 5 Charge transfer resistance (R_{ct}) and double layer capacitance changes as a function of the immersion time of Al–TiO_2 electrode in 1 M $Li(CF_3SO_2)_2N$ in EC/DME (1:1 v/v). R_{ct} calculated from **a** lower frequency (extracted from Fig. 4), **b** semicircle intercept with *x*-axis, **c** high frequency (extracted from Fig. 4), and **d** true double layer capacitance during elapse of time of the electrode immersion in the electrolyte

The increase in the charge transfer resistance reflects changes in the electrical properties at the interface, which develops with the time of the electrode/electrolyte solution contact. It is tempting to suggest that these effects are due to the presence of small residual Li^+ inside the anatase lattice after the CV scan (see above). The final potential after the CV scan (3 V) is, obviously, well above the Li-extraction potential. Hence, relaxing of this electrode at OCP may remove traces of Li^+ from the TiO_2 host structure. Attainment of the fully de-lithiated state converts the Al–TiO_2 electrode into an insulating state. As R_{ct} scales inversely with the electrochemical reaction rate, Fig. 5 demonstrates that the reaction rate decreases with time of immersion. This decrease in the rate is attributed to the growth of SEI layer. The formation of SEI is supported by the decrease in double layer capacitance with time of immersion. Our data clearly indicate that the SEI film exhibits changes upon storage in the electrolyte solution at OCP. In this respect, we may recall the SEI chemistry on other oxidic materials, such as $LiNiO_2$ and $LiMn_2O_4$ at similar conditions: In this study, the pristine surface film is initially composed of Li_2CO_3 as the main component but converts gradually to a variety of compounds including ROLi, $ROCO_2Li$, (R = alkyl) polycarbonates, etc. [22]. Understanding the nature of SEI chemistry on Al–TiO_2 is beyond the scope of this paper, but it is clear that the EIS is a particularly suitable technique for in situ monitoring of the changes in SEI, which can hardly be detected by CV and chronoamperometry. These methods do not provide explicit data on the SEI, as they mainly reflect the bulk Li^+ transport in anatase [35–38].

Conclusions

Mesoporous Al-stabilized TiO_2 (anatase) electrode was studied by the EIS. The chemical diffusion coefficient was determined by analyzing the real impedance part vs the square root of reciprocal of angular frequency. In the high-frequency range of the impedance, the chemical diffusion coefficient values determined were close to previously obtained values. However, at the low-frequency range, the values were quite small, which can be assigned to the Li-ion transport through SEI, and are by orders of magnitude smaller than the diffusion coefficients of Li^+ in the bulk anatase lattice. Charge transfer resistance increased with time of immersion of electrode, which we attribute to the formation and gradual reconstruction of the SEI.

Acknowledgment This work supported by the Academy of Sciences of the Czech Republic (contract No. N100500652) and the EC-COST D35.0002 grant.

References

1. Hagfeldt A, Graetzel M (1995) Chem Rev 95:49
2. Kavan L, Attia A, Lenzmann F, Elder SH, Graetzel M (2000) J Electrochem Soc 147:2897
3. Kavan L, Graetzel M, Rathousky J, Zukal A (1996) J Electrochem Soc 143:394
4. Huang SY, Kavan L, Exnar I, Graetzel M (1995) J Electrochem Soc 142:L142
5. Zhong Q, von Sacken U (1995) J Power Sources 54:221
6. Ohzuku T, Ueda A, Kouguchi M (1995) J Electrochem Soc 142:4033
7. Ohzuku T, Yanagawa T, Kouguchi M, Ueda A (1997) J Power Sources 68:131
8. Aydinol MK, Kohan AF, Ceder G, Cho K, Joannopoulos J (1997) Phys Rev B 56:1354
9. Ceder G, Chiang YM, Sadoway DR, Aydinol MK, Jang YI, Huang B (1998) Nature 392:694
10. Ohzuku T, Takehara Z, Yoshizawa S (1979) Electrochim Acta 24:219
11. Jang YI, Huang B, Wang H, Sadoway DR, Ceder G, Chiang YM, Liu H, Tamura H (1999) J Electrochem Soc 146:862
12. Chen Z, Dahn JR (2003) Electrochem Solid-State Lett 6:A221
13. Kavan L, Graetzel M, Gilbert SE, Klemenz C, Scheel HJ (1996) J Am Chem Soc 118:6716
14. Li F, Zhang L, Metzger RM (1998) Chem Mater 10:2470
15. Lin Y, Wu GS, Yuan XY, Xie T, Zhang LD (2003) J Phys Condens Matter 15:2917
16. Matsumuoto Y, Ishikakwa Y, Nishida M, Seiichiro I (2000) J Phys Chem B 104:4204
17. Michailowski A, AlMawlawi D, Cheng G, Moskovits M (2001) Chem Phys Lett 349:1
18. Zhang X, Yao B, Zhao L, Liang C, Zhang L, Mao Y (2001) J Electrochem Soc 148:G398
19. Zhang HZ, Banfield JF (2000) J Mater Res 15:437
20. Attia A, Zukalova M, Rathousky J, Zukal A, Kavan L (2005) J Solid State Electrochem 9:138
21. Attia A, Elder SH, Jirasek R, Kavan L, Krtil P, Rathousky J, Zukal A (2001) Stud Surf Sci Catal 135:361
22. Aurbach D, Gamolsky K, Markovsky B, Salitra G, Gofer Y, Heider U, Oesten R, Schmidt M (2000) J Electrochem Soc 147:1322
23. Zhang SS, Xu K, Jow TR (2002) J Electrochem Soc 149:A1521
24. Boukamp BA (1986) Solid State Ionics 20:31
25. Goldberg D (1968) Rev Int Hautes Temp Refract 5:181
26. Kavan L, Kratochvilova K, Graetzel M (1995) J Electroanal Chem 394:93
27. Li H, Huang X, Chen L (1998) Electrochem Solid-State Lett 1:241
28. De Levie R (1964) Electrochim Acta 9:1231
29. Brug GJ, van den Eden ALG, Sluyters-Rehbach M, Sluyters JH (1984) J Electroanal Chem 176:275
30. Retter U, Widmann A, Siegler K, Kahlert H (2003) J Electroanal Chem 546:87
31. Li H, Huang X, Chen L (1999) J Power Sources 81–82:340
32. Conway BE (1993) Electrochim Acta 38:1249
33. Liu P, Wu H (1995) J Power Sources 56:81
34. Bisquert J, Garcia-Belmonte G, Bueno P, Longo E, Bulhoes LOS (1998) J Electroanal Chem 452:229
35. Lindstroem, Soedergen S, Solbrand A, Rensmo H, Hjelm J, Hagfeldt A, Lindquist SE (1997) J Phys Chem B 101:7710
36. van de Krol R, Goossens A, Schoonman J (1999) J Phys Chem B 103:7151
37. Cantao MP, Cisnero JI, Torresi RM (1994) J Phys Chem 98:4865
38. Kavan L, Rathousky J, Graetzel M, Shklover V, Zukal A (2000) J Phys Chem B 104:12012

Springer

Dear Author:

Please find attached the final pdf file of your contribution, which can be viewed using the Acrobat Reader, version 3.0 or higher. We would kindly like to draw your attention to the fact that copyright law is also valid for electronic products. This means especially that:

- You may print the file and distribute it amongst your colleagues in the scientific community for scientific and/or personal use.
- You may make your article published by Springer-Verlag available on your personal home page provided the source of the published article is cited and Springer-Verlag and/or other owner is mentioned as copyright holder. You are requested to create a link to the published article in Springer's internet service. The link must be accompanied by the following text: "The original publication is available at springerlink.com". Please use the appropriate DOI for the article. Articles disseminated via SpringerLink are indexed, abstracted and referenced by many abstracting and information services, bibliographic networks, subscription agencies, library networks and consortia.
- Without having asked Springer-Verlag for a separate permission your institute/your company is not allowed to place this file on its homepage.
- You may not alter the pdf file, as changes to the published contribution are prohibited by copyright law.
- Please address any queries to the production editor of the journal in question, giving your name, the journal title, volume and first page number.

Yours sincerely,

Springer-Verlag

J Solid State Eletrochem (2003) 8: 2–6
DOI 10.1007/s10008-003-0415-7

ORIGINAL PAPER

Martin Kalbáč · Markéta Zukalová · Ladislav Kavan

Phase-pure nanocrystalline $Li_4Ti_5O_{12}$ for a lithium-ion battery

Received: 15 November 2002 / Accepted: 11 June 2003 / Published online: 13 September 2003

Abstract Phase-pure nanocrystalline $Li_4Ti_5O_{12}$ with BET surface areas between 183 and 196 m^2/g was prepared via an improved synthetic protocol from lithium ethoxide and titanium(IV) butoxide. The phase purity was proved by X-ray powder diffraction, Raman spectroscopy and cyclic voltammetry. Thin-film electrodes were prepared from two nanocrystalline samples of $Li_4Ti_5O_{12}$ and one microcrystalline commercial sample. Li-insertion behavior of these electrodes was related to the particle size.

Keywords $Li_4Ti_5O_{12}$ · Lithium insertion · Nanocrystalline materials · Phase purity · Spinel

Introduction

$Li_4Ti_5O_{12}$ (spinel) was introduced in the early 1990s as a promising "zero-strain" Li-insertion host [1, 2, 3]. It accommodates three Li^+ per formula unit with a theoretical capacity of 175 mAh/g:

$$Li_4Ti_5O_{12} + 3e^- + 3Li^+ \rightarrow Li_7Ti_5O_{12} \qquad (1)$$

The spinel $Li_4Ti_5O_{12}$ is conveniently prepared by a solid-state reaction of TiO_2 and Li_2CO_3 or LiOH at 800–1000 °C [1, 2, 4, 5, 6, 7, 8, 9, 10, 11]. This synthetic route primarily yields micron-sized crystals [11]. There has been one report on "nanocrystalline" $Li_4Ti_5O_{12}$ resulting from the high-temperature reaction of TiO_2 and Li_2CO_3 [12], but neither the particle size nor preparative details were specified. The "nanosized" $Li_4Ti_5O_{12}$ offered at least a 30% improvement in rate capability at 1–10 C in a hybrid cell with a supercapacitor-like counter-electrode [12, 13]. This conclusion agrees with previous reports on TiO_2 (anatase), in which the charge capability also improved if the host material had nanocrystalline morphology [14, 15, 16].

Nanocrystalline $Li_4Ti_5O_{12}$ (spinel) with a crystal size of 30 nm was prepared by hydrothermal reaction of TiO_2 and LiOH at 130–200 °C [17]. There have been several attempts to grow nanocrystalline $Li_4Ti_5O_{12}$ (spinel) by the sol-gel method from lithium acetate and titanium(IV) isopropoxide [18, 19] or butoxide [20]. In both cases, calcination at 800 °C was necessary to obtain a reasonably pure spinel phase [19] and to improve the electrochemical performance [20]. The sol-gel product from the butoxide route exhibited a grain size of ca. 100 nm, but contained also some rutile impurities [20]. Its Li-insertion capacity was reported to be 272 mAh/g, but the charging reversibility was not tested [20]. This casts doubt on this unrealistic charge capacity. The sol-gel spinel showed considerable capacity fading during the initial 20 cycles [19], which contrasted with the high cycle-life of materials made by solid-state reactions [3, 12]. Nanocrystalline $Li_4Ti_5O_{12}$ spinels with the smallest particle sizes (9–19 nm) were prepared via hydrolytic conversion of a mixture of Li alkoxide and Ti(IV) alkoxide [21]. The product contained 0.3–0.6% anatase and exhibited excellent charge capability in thin-film electrodes [21]. This paper is aimed at further investigation and optimization of this material.

Experimental

Preparation of electrodes

The sol-gel synthesis of nanocrystalline $Li_4Ti_5O_{12}$ from Li/Ti alkoxides was described previously [21]. Here, this synthetic protocol was optimized with the aim to achieve the best phase purity, while still keeping the small particle sizes. The final synthetic protocol

---

Presented at the 3rd International Meeting on Advanced Batteries and Accumulators, 16–20 June 2002, Brno, Czech Republic

M. Kalbáč · M. Zukalová · L. Kavan (✉)
J. Heyrovský Institute of Physical Chemistry,
Academy of Sciences of the Czech Republic,
Dolejškova 3, 182 23 Prague 8, Czech Republic
E-mail: kavan@jh-inst.cas.cz
Tel.: +420-2-66053975
Fax: +420-2-86582307

towards phase-pure nanocrystalline $Li_4Ti_5O_{12}$ was as follows. Under an argon atmosphere, a 0.9 M solution of LiOEt (Aldrich) in absolute ethanol was mixed with titanium(IV) butoxide (Aldrich) in a stoichiometric molar ratio of $Li/Ti=4:5$. The clear yellowish solution was hydrolyzed with a 4 wt% aqueous solution of poly(ethylene glycol) (PEG, $M=20{,}000$; Aldrich). The amount of PEG corresponded to 150 wt% of the weight of the stoichiometrically expected for $Li_4Ti_5O_{12}$. The mixture was stirred overnight and then evaporated on a rotary evaporator at 40 °C to the consistence of a viscous slurry. This was finally fired at 500 °C under a proprietary calcination program, which was crucial for minimizing the trace anatase impurities.

The hydrothermally processed samples were prepared as follows. The ethanolic solution of Li/Ti alkoxides was hydrolyzed with water, the mixture was stirred overnight, and then evaporated in vacuum at 40 °C. The resulting viscous slurry was autoclaved at 150 °C for 16 h and then mixed with 150 wt% of PEG ($M=20{,}000$) and annealed at 500 °C as in the previous case. A commercial $Li_4Ti_5O_{12}$ (LT-2 from Titan Kogyo, Japan, 3.1 m^2/g) was also tested for comparison.

Thin-film electrodes from $Li_4Ti_5O_{12}$ were prepared as follows [14, 21]: 0.185 g of the powder precursor was mortared under slow addition of 4×0.06 mL of a 10% aqueous solution of acetylacetone. The mixture was diluted by 0.15 mL H_2O and mixed with 0.13 mL of a 4% aqueous solution of hydroxypropylcellulose (Aldrich, MW 100,000) and 0.03 mL of a 10% aqueous solution of Triton-X100 (Fluka). The obtained slurry was deposited on a sheet of conducting glass (F-doped SnO_2, TEC 8 from Libbey-Owens-Ford, 8 Ω/square) using a doctor-blading technique [14, 21]. The film thickness was adjusted by Scotch tape at the edges of the support, which also allowed making electrical contacts to the electrode. The film was finally calcined for 30 min in air at 450 °C.

Alternatively, the nanocrystalline thin-film electrodes were also prepared directly via doctor-blading and calcination of the primary slurry resulting from the sol-gel synthesis (see above). The geometric area of the $Li_4Ti_5O_{12}$ film was 0.2 cm^2. In some cases the film's area was cut down by mechanical scraping of the film's edges by a piece of glass. This served to finely adjust the charge capacity to a comparable uniform value of ca. 300 mC per electrode.

Methods

The BET surface areas were determined from nitrogen adsorption isotherms at 77 K (ASAP 2010, Micromeritics). Scanning electron microscopy (SEM) images were obtained by a Hitachi S-4700 apparatus. Transmission electron microscopy (TEM) images were obtained by a Philips EM430T microscope operating with a LaB_6 cathode at 300 kV. Powder X-ray diffractometry (XRD) was studied on a Siemens D-5000 diffractometer using Cu Kα radiation. Raman spectra were excited at 2.41 eV (2 mW) by an Ar^+ laser (Innova 305, Coherent) and recorded on a T-64000 spectrometer (Instruments, SA).

Electrochemical measurements were carried out in a one-compartment cell using an Autolab Pgstat-30 (Ecochemie) controlled by GPES-4 software. The reference and auxiliary electrodes were from Li metal; hence potentials are referred to the Li/Li^+ (1 M) reference electrode. $LiN(CF_3SO_2)_2$ (Fluorad HQ 115 from 3M) was dried at 130 °C/1 mPa. Ethylene carbonate (EC) and 1,2-dimethoxyethane (DME) were dried over 4A molecular sieve (Union Carbide). The electrolyte solution, 1 M $LiN(CF_3SO_2)_2$ + EC/DME (1:1 by mass) contained 10–15 ppm H_2O, as determined by Karl Fischer titration (Metrohm 684 coulometer). All operations were carried in a glove box under argon (containing typically 1–5 ppm of O_2 and H_2O).

Results and discussion

Figure 1 shows that our nanocrystalline $Li_4Ti_5O_{12}$ is reasonably monodisperse in mesoscopic dimensions. The TEM pattern (Fig. 1B) evidences that the particles are single crystals with a typical size of ca. 10 nm. The single-crystalline nature of the particles is confirmed by uniform fringes of the cubic lattice. One illustrative example of a relatively large single-crystal particle is highlighted in Fig. 1B. However, by inspecting at high resolution, these fringes are omnipresent in the TEM patterns, showing that the crystals are statistically oriented in the sintered film.

The BET surface areas, S_{BET}, of the as-prepared nanocrystalline materials were 183–196 m^2/g for samples of different batches. If we approximate the morphology by spherical particles of a density of $\rho=3.5$ g/cm^3, the corresponding particles size, d, can be estimated as [21]:

$$d = 6/\rho S_{BET} \tag{2}$$

Equation 2 gives $d \approx 9$ nm for the found surface areas (183–196 m^2/g), which agrees with the morphology seen by SEM/TEM (Fig. 1). The surface area of the hydrothermally grown material was $S_{BET}=140$ m^2/g. This translates into $d \approx 12$ nm. Apparently, the increase in particle size is due to Ostwald ripening at hydrothermal recrystallization [21]. The particle growth could be also visualized by comparison of SEM/TEM images of

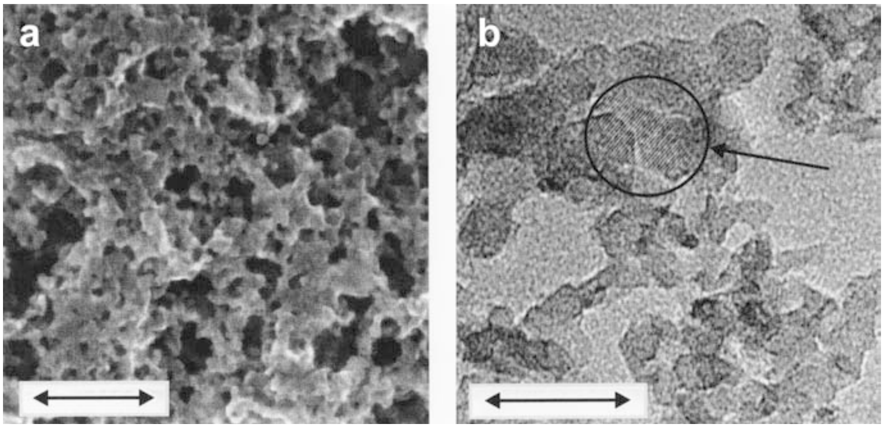

Fig. 1 (**a**) SEM image of as-received (non-autoclaved) nanocrystalline $Li_4Ti_5O_{12}$; scale bar 100 nm. (**b**) TEM image of the same material; scale bar 20 nm. *Highlighted* is one large particle exhibiting well-distinguished fringes of a cubic lattice

autoclaved and non-autoclaved (Fig. 1) materials, but the changes in actual morphologies were not that expressive to demonstrate the expected particle growth (9 → 12 nm) because of the spread of particle sizes of the real materials. The calculated (Eq. 2) particle size for the commercial LT-2 sample ($S_{\mathrm{BET}} = 3.1\ \mathrm{m}^2/\mathrm{g}$) equals 0.6 μm. In this case, the SEM pattern presents clearly distinct particles of ca. 1 μm in size (cf. fig. 1B in [21]).

Powder X-ray diffraction confirms the phase purity of our nanocrystalline spinel (Fig. 2). A careful phase analysis is important, since TiO_2 impurities (anatase, rutile) have been frequently observed in various $Li_4Ti_5O_{12}$ (spinel) materials made by sol-gel methods [19, 20, 21]. Our previous study [21] also pointed at TiO_2 anatase impurity (0.3–0.6 wt%) found in most products from the sol-gel synthesis employing Li/Ti alkoxides. Figure 2 compares the powder diffraction patterns of two typical examples of our materials (nanocrystalline as-received and hydrothermally grown spinel) with the commercial micron-sized product, LT-2. All patterns can be indexed for a cubic lattice of $Li_4Ti_5O_{12}$, while no signs of additional phases are apparent (anatase at $2\Theta \approx 25°$ and rutile at $2\Theta \approx 27°$). The commercial sample LT-2 showed, besides the main line of (400) diffraction at $2\Theta = 43.22°$, also a satellite line at 43.34°, whose assignment is not clear.

The shift of diffraction peaks in Fig. 2 shows that the lattice constant depends on the synthetic protocol. The calculated lattice constants were as follows: 0.8275 nm (nanocrystalline spinel), 0.8366 nm (hydrothermally grown nanocrystalline spinel) and 0.8369 nm (LT-2). The latter value matches well the lattice constant of $Li_4Ti_5O_{12}$ made by high-temperature syntheses: 0.8367 [1], 0.8365 [3], 0.8358 [7] and 0.8357 [6]. The value is also similar to the lattice constant of 0.8359 nm calculated from the JCP2 CAT pattern (PDF number 26-1198). Apparently, the hydrothermally grown material shows the "normal" value of the lattice constant, whereas the as-received (non-autoclaved) nanocrystalline spinel exhibits a significantly smaller constant. This conclusion matches our previous report on the sol-gel synthesis of nanocrystalline $Li_4Ti_5O_{12}$ containing small anatase contamination [21].

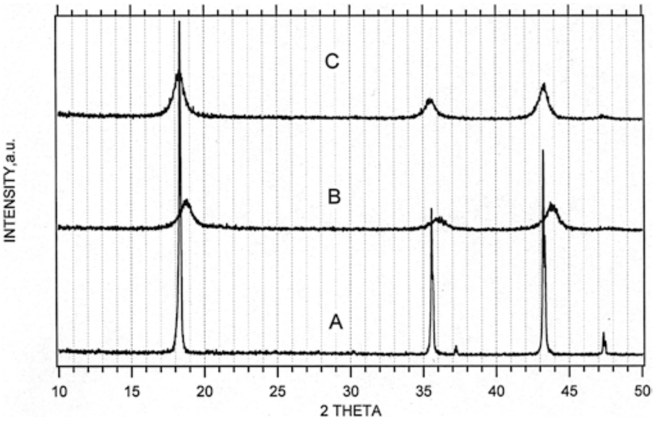

Fig. 2 Powder X-ray diffractogram of (*A*) a commercial $Li_4Ti_5O_{12}$ spinel (LT-2), (*B*) nanocrystalline $Li_4Ti_5O_{12}$ made by the synthetic procedure without hydrothermal treatment, and (*C*) hydrothermally grown nanocrystalline $Li_4Ti_5O_{12}$

The crystallite size d_c (coherent length of the crystal lattice) was approximated from the X-ray line width (w) according to the Scherrer formula:

$$d_c = 0.9\lambda / w \cos\Theta \tag{3}$$

where λ is the X-ray wavelength (0.1540562 nm) and Θ is the diffraction angle. Equation 3 gives $d_c \approx 9$ nm for the as-received (non-autoclaved) material and $d_c \approx 12$ nm for the corresponding hydrothermally grown material. These particles sizes agree surprisingly well with the particle size calculated from the BET area (Eq. 2).

The phase purity of our nanocrystalline $Li_4Ti_5O_{12}$ is also confirmed by Raman spectroscopy. This method is, reportedly, more sensitive to detect anatase impurities, even in samples which appear to be "X-ray amorphous" [22]. Figure 3 shows that our nanocrystalline spinels passed successfully this test also. It does not show any Raman band at 144 cm^{-1}, where the strongest line of anatase is expected to take place (cf. spectra C and B in Fig. 3). Also, rutile would have a peak here (143 cm^{-1}). The spectrum of our nanocrystalline spinel also matches well that of the commercial LT-2 material.

A third proof of the phase purity of our nanocrystalline spinel follows from the cyclic voltammogram of Li insertion (Fig. 4). The positions of the voltammetric peaks (1.51 V for Li insertion and 1.60 V for Li extraction) correspond to the formal potential of $Li_4Ti_5O_{12}$ spinel (cf. Eq. 1), which is reported to be 1.56 V vs. Li/Li^+ [1, 8]. The voltammogram confirms that our material is free from anatase, which would manifest itself by distinguished Li-insertion peaks at 1.75 V and 2.0 V vs. Li/Li^+ [21]. We have previously shown that the electrochemical detection of anatase is very sensitive and superior to X-ray diffraction for the spinel/anatase mixtures [21].

Hence, in this work, we present an optimized synthetic procedure which allowed us to prepare TiO_2-free spinel reproducibly. Our materials are unique, not only from the point of view of the smallest ever reported particle size (the largest S_{BET}), but also from the point of view of the phase purity, which was confirmed by three independent methods (X-ray diffraction, Raman spectroscopy and electrochemistry).

Figure 5 shows a series of galvanostatic charge/discharge cycles of electrodes prepared from nanocrystalline and commercial micron-sized material (LT-2) at charging rates of 2, 20, 50, 100 and 150 C. The maximum reversible Li-insertion capacity determined from the 2 C cycle (and/or from slow cyclic voltammetry, cf. Fig. 4) was around 300 mC for all three samples. Fast charging is always reversible, but the nanocrystalline electrodes show considerable irreversibility at 2 C. This is apparently due to breakdown processes in the

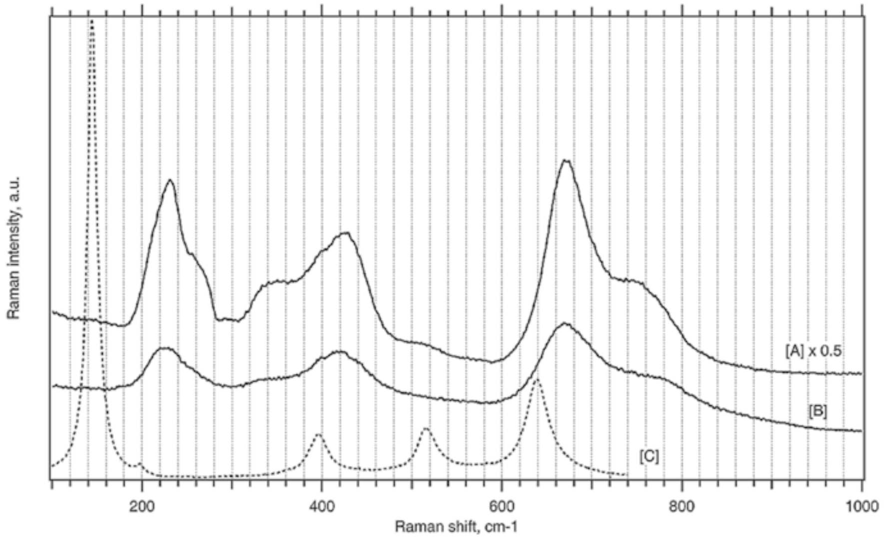

Fig. 3 Raman spectra of (*A*) the commercial micron-sized spinel LT-2, (*B*) a non-autoclaved nanocrystalline spinel, and (*C*) nanocrystalline anatase C200. The latter sample was available from the previous work [14]. The spectra are offset for clarity; the intensity scale is comparable for samples *B* and *C* but is reduced by one half for sample *A*

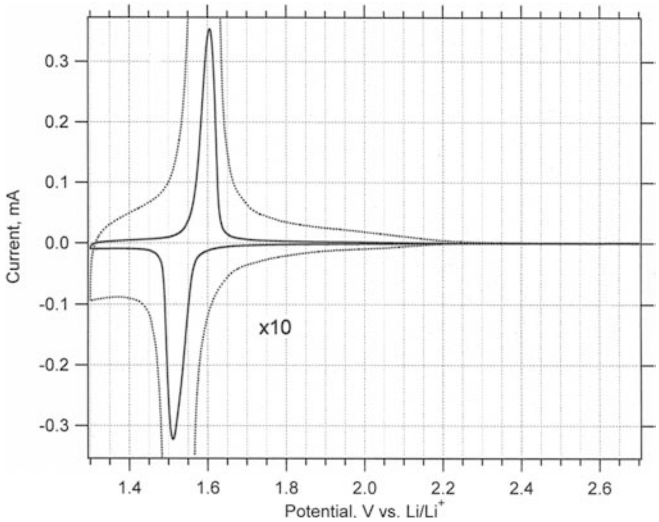

Fig. 4 Typical cyclic voltammogram of phase-pure nanocrystalline $Li_4Ti_5O_{12}$. Electrolyte solution: 1 M $LiN(CF_3SO_2)_2$ + EC/DME (1:1 by mass); scan rate 0.2 mV/s. The *dashed curve* displays the same plot, but with the current scale expanded by a factor of 10

electrolyte solution, such as reduction of trace water, which is more pronounced for high-surface-area electrodes and for fresh electrodes during the initial cycles (to minimize the second effect, we have pretreated the virgin electrodes by several charging/discharging cycles). Although we did not test the cycle life systematically in long-term experiments, there were no signs of capacity fading during the initial ca. 10 cycles.

The plots in Fig. 5 can be referred to those presented previously for non-optimized sol-gel spinels [21]. The actual charge capacity of our electrodes (Figs. 4, 5) is about twice as large, which cuts down the charge capability at very fast rates (cf. [21]). The improvement of the charging rate for the nanocrystalline material is clearly expressed if we compare the plot for the microcrystalline LT-2

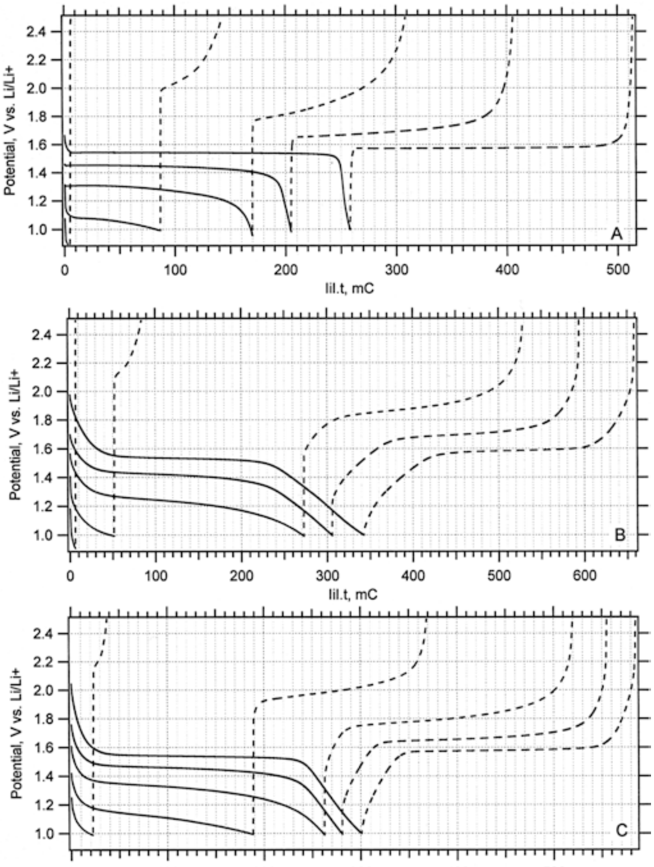

Fig. 5 Chronopotentiometric plot of (A) a commercial $Li_4Ti_5O_{12}$ spinel (LT-2), (B) nanocrystalline $Li_4Ti_5O_{12}$ without hydrothermal treatment and (C) hydrothermally grown nanocrystalline $Li_4Ti_5O_{12}$. Electrolyte solution: 1 M $LiN(CF_3SO_2)_2$ + EC/DME (1:1 by mass). The current *i* was adjusted to a charging rate of 2, 20, 50, 100 and 150 C for the *solid curves* from *top to bottom*. The *dashed curves* display the corresponding galvanostatic discharging at the same rates. For the sake of clarity, the time (*t*) is multiplied by the absolute value of the charging/discharging current, *i*

(Fig. 5A) and the autoclaved nanocrystalline materials (Fig. 5C). The latter sample could be charged to almost 70% of its nominal (2 C) capacity at the 100 C rate.

The as-received (non-autoclaved) nanocrystalline spinel (Fig. 5B) is relatively less efficient at fast charging rates, as compared to the charging performance of the autoclaved sample (Fig. 5C). Since the autoclaved sample has larger particles, this would indicate that the charge capability need not monotonously increase with decreasing particle size. In other words, there seems to be a certain optimum particle size, from which the charge capability drops down in both directions, i.e. for either larger or smaller particles.

However, there are also other factors, besides the particle size, which may play a role. The X-ray diffraction patterns show that the non-autoclaved material exhibits a smaller cubic lattice constant (see above). Autoclaving apparently restores the “normal” (larger) value of the lattice constant, which matches, obviously, the improvement in the rate of Li insertion. The hydrothermal recrystallization causes not only the particle growth, but it can also remove defects of the as-received crystals. The quenching of defects may also be beneficial for Li insertion, although the relations between defects and the Li-insertion rate need not be that straightforward. Still another effect to be considered for ultrasmall particles is the energy of Li^+–Li^+ repulsion, which is known to scale with d^{-3} and which slows down the Li^+ transport in the host lattice [23]. The relative influence of the mentioned effect is difficult to assess, although, qualitatively, they all point at the same conclusion that the hydrothermally recrystallized, medium-sized (in mesoscopic dimensions) particles present the optimum morphology for fast Li insertion in thin-film electrodes.

Acknowledgements This work was supported by NTera Ltd. and by the EC-COST Action D14/0002/99. We thank Estelle De Chambrier (NTera) for the TEM measurements.

References

1. Colbow KM, Dahn JR, Haering RR (1989) J Power Sources 26:397
2. Ferg E, Gummov RJ, de Kock A, Thackeray MM (1994) J Electrochem Soc 141:L147
3. Ohzuku T, Ueda A, Yamamoto N (1995) J Electrochem Soc 142:1431
4. Takai S, Kamata M, Fujine S, Yoneda K, Kanda K, Esaka T (1999) Solid State Ionics 123:165
5. Zaghib K, Simoneau M, Armand M, Gauthier M (1999) J Power Sources 81–82:300
6. Deschanvers A, Raveau B, Sekkal Z (1971) Mater Res Bull 6:699
7. Harrison MR, Edwards PP, Goodenough JB (1985) Philos Mag B 52:679
8. Pyun SI, Kim SW, Shin HC (1999) J Power Sources 81–82:248
9. Scharner S, Weppner W, Schmid-Beurmann P (1999) J Electrochem Soc 146:857
10. Zaghib K, Armand M, Gauthier M (1998) J Electrochem Soc 145:3135
11. Peramunage D, Abraham KM (1998) J Electrochem Soc 145:2609
12. Amatucci GG, Badway F, Du Pasquier A, Zheng T (2001) J Electrochem Soc 148:A930
13. Du Pasquier A, Laforgue A, Simon P, Amatucci GG, Fauvarque JF (2002) J Electrochem Soc 149:A302
14. Kavan L, Grätzel M, Rathousky J, Zukal A (1996) J Electrochem Soc 143:394
15. Kavan L, Attia A, Lenzmann F, Elder SH, Grätzel M (2000) J Electrochem Soc 147:2897
16. Kavan L, Rathousky J, Grätzel M, Shklover V, Zukal A (2000) J Phys Chem B 104:12012
17. Fattachova D, Krtil P (2002) J Electrochem Soc 149:A1224
18. Bach S, Pereira-Ramos JP, Baffier N (1999) J Power Sources 81–82:273
19. Bach S, Pereira-Ramos JP, Baffier N (1998) J Mater Chem 8:251
20. Shen C, Zhang X, Zhou Y, Li H (2002) Mater Chem Phys 78:437
21. Kavan L, Grätzel M (2002) Electrochem Solid-State Lett 5:A39
22. Lei Y, Zhang LD, Fan JC (2001) Chem Phys Lett 338:231
23. Choi YM, Pyun SI (1997) Solid State Ionics 99:173

Journal of The Electrochemical Society, **150** (7) A1000-A1007 (2003)
0013-4651/2003/150(7)/A1000/8/$7.00 © The Electrochemical Society, Inc.

Li Insertion into $Li_4Ti_5O_{12}$ (Spinel)

Charge Capability *vs.* Particle Size in Thin-Film Electrodes

Ladislav Kavan,[a,c,z] Jan Procházka,[b] Timothy M. Spitler,[b] Martin Kalbáč,[a] Markéta Zukalová,[a] Thierry Drezen,[d] and Michael Grätzel[c]

[a]*J. Heyrovský Institute of Physical Chemistry, Academy of Sciences of the Czech Republic, CZ-182 23 Prague 8, Czech Republic*
[b]*Altair Technologies, Incorporated, Reno, Nevada 89502, USA*
[c]*Laboratory of Photonics and Interfaces, Swiss Federal Institute of Technology, EPFL, Ecublens, CH-1015 Lausanne, Switzerland*
[d]*NTera, Limited, PSE-B, Ecublens, CH-1015 Lausanne, Switzerland*

$Li_4Ti_5O_{12}$ (spinel) materials were prepared with Brunauer-Emmett-Teller surface areas ranging from 1.3 to 196 m^2/g. The corresponding average particle sizes varied from *ca.* 1 μm to *ca.* 9 nm. Twenty-five different materials were tested as Li insertion hosts in thin-film electrodes (2-4 μm) made from a pure spinel. Trace amounts of anatase in $Li_4Ti_5O_{12}$ were conveniently determined by cyclic voltammetry of Li insertion. Electrodes from nanocrystalline $Li_4Ti_5O_{12}$ exhibited excellent activity towards Li insertion, even at charging rates as high as 250C. The charge capability at 50-250C was proportional to the logarithm of surface area for coarse particles (surface areas smaller than *ca.* 20 m^2/g). With increasing charge/discharge rates, a narrowing plateau in performance was observed for materials with surface areas between *ca.* 20 to 100 m^2/g. These materials can be charged/discharged nearly to the nominal capacity of $Li_4Ti_5O_{12}$ (175 mAh/g) within a wide range of the rates. Very small particles (surface areas $> 100\ m^2/g$) exhibit a growing decrease of charge capability at 50-250C. The Li-diffusion coefficients, calculated from chronoamperometry, decrease by orders of magnitude if the average particle size drops from *ca.* 1 μm to *ca.* 9 nm. However, the sluggish Li^+ transport in small particles is compensated by the increase in active electrode area. Materials having surface areas larger than *ca.* 100 m^2/g also tend to show increased charge irreversibility. This could be caused by parasitic cathodic reactions, due to enhanced adsorption of reducible impurities (humidity) or the quality of the spinel crystalline lattice itself. The optimum performance of thin-film $Li_4Ti_5O_{12}$ electrodes is achieved, if the parent materials have surface areas between *ca.* 20 to 110 m^2/g, with the maximum peak at 100 m^2/g.

Manuscript submitted September 12, 2002; revised manuscript received January 22, 2003. Available electronically June 3, 2003.

Spinel oxides $Li_{1+x}Ti_{2-x}O_4$; $0 \leqslant x \leqslant 1/3$ were introduced in the early 1990s as promising zero-strain Li-insertion hosts.[1-3] The cubic lattice constant, *a* (space group $Fd3m$) scales with composition (*x*) according to Eq. 1 (for *a* in nm)[4]

$$a = 0.8405 - 0.0143x \qquad [1]$$

The relations between composition (*x*) and Li-insertion thermodynamics were not studied very systematically, but the end members of the series, *i.e.*, $LiTi_2O_4$ and $Li_{4/3}Ti_{5/3}O_4$ ($Li_4Ti_5O_{12}$) exhibited the formal potential of Li insertion 1.36-1.338 V and 1.55-1.562 V, respectively.[1,5]

The $Li_{1+x}Ti_{2-x}O_4$ (spinels) are usually prepared by solid-state reactions of suitable Li- and Ti-containing precursors during 12-24 h at 800-1000°C.[1,2,4-11] The particle size was not systematically addressed in most cited works, but Abraham *et al.*[11] have reported that the solid-state reaction of TiO_2 with Li_2CO_3 or LiOH gave at 800°C micrometer-sized product. Amatucci *et al.*[12,13] have recently reported on nanocrystalline $Li_4Ti_5O_{12}$ resulting from a high-temperature solid-state reaction of TiO_2 and Li_2CO_3,[12] but neither the particle size nor preparative details were specified in their works.[12,13] Alternatively, the lithium titanate spinels can also be prepared by a reaction of butyllithium with TiO_2[5,14] or titanium (IV) isopropoxide[15] followed by calcination above 800°C. Sol-gel synthesis of $Li_4Ti_5O_{12}$ from titanium (IV) isopropoxide and lithium acetate was described by Bach *et al.*[16,17] Also in this case, the calcination at 800°C was necessary to obtain a pure spinel phase.[17]

The high-temperature solid-state reaction[1,2,4-10] is usually selected for the synthesis of $Li_4Ti_5O_{12}$, whereas the butyllithium route[5,14,15] is, reportedly, preferable for the synthesis of $LiTi_2O_4$. (Note, however, that the *ex*-butyllithium material, which is presented in Ref. 15 as $LiTi_2O_4$, exhibits the lattice constant and Li-insertion potential typical for $Li_4Ti_5O_{12}$.) A selective sol-gel synthesis of nanocrystalline $Li_4Ti_5O_{12}$ with surface areas up to 183 m^2/g has been reported by us recently.[18] The synthetic procedure employed a hydrolytic conversion of a mixture of Li and Ti(IV) alkoxides, followed by calcination at 500°C for 30 min.

$Li_4Ti_5O_{12}$ accommodates Li with a theoretical capacity of 175 mAh/g (based on the mass of the starting host material) according to the equation

$$Li_4Ti_5O_{12} + 3e^- + 3Li^+ \rightleftarrows Li_7Ti_5O_{12} \qquad [2]$$

A more detailed analysis points at two-phase equilibrium, which explains the invariance of the electrode potential on the inserted charge.[9] The spinel host structure accommodates Li^+ without significant changes of the lattice constant, *a*. Consequently, these materials show excellent cycle-life of hundreds to thousands cycles.[3,12] However, certain $Li_4Ti_5O_{12}$ materials, synthesized by the sol-gel route, also showed considerable capacity loss during 20 cycles.[17]

To the best of our knowledge, there is no report addressing the relationship between the Li insertion electrochemistry and particle size of $Li_{1+x}Ti_{2-x}O_4$ (spinels). There were several reports on TiO_2 (anatase) demonstrating that the particle size and morphology may influence the Li insertion activity of anatase significantly.[19-21] These effects are especially expressed with nanocrystalline materials[19] and organized mesoscopic structures.[20,21] Armand *et al.*[7] have prepared $Li_4Ti_5O_{12}$ particles *ca.* 0.6 μm in diameter by high-energy ballmilling. However, their electrochemical performance was not much different from that of the nonmilled starting material.[7] On the other hand Amatucci *et al.*[12,13] have reported that nanosized $Li_4Ti_5O_{12}$ (of nonspecified particle size) offered at least a 30% improvement in rate capability at 1-10 C in a hybrid cell with a supercapacitor-like counter electrode. The present paper is aimed at upgrading these reports, determining charging and discharging rates as a function of the particle size. Our preliminary communication[18] may be viewed a subset of the data contained in this report. Data produced in con-

[z] E-mail: kavan@jh-inst.cas.cz

Table I. Survey of $Li_4Ti_5O_{12}$ samples. S_{BET} is surface area determined from nitrogen adsorption isotherm; d is the particle size calculated from Eq. 3 for calcined materials. The concentration of anatase was determined from cyclic voltammetry as described in Ref. 18.

Sample	Preparative notes	S_{BET} (m^2/g) as received[a]	S_{BET} (m^2/g) calcined[b]	d (nm)	Anatase (wt %)
A1	P25, Altair NanoMaterials, USA	1.3	1.3	1300	0.99
A2	P26, Altair NanoMaterials, USA	4.6	4.0	430	0.15
A3	P42, Altair NanoMaterials, USA	12.9	12.9	130	0[c]
A4	P41, Altair NanoMaterials, USA	18.3	18.3	94	0.29
A5	P40, Altair NanoMaterials, USA	24.3	24.0	71	0.27
A6	P50, Altair NanoMaterials, USA	27.1	27.0	63	0.47
A7	P49, Altair NanoMaterials, USA	32.3	32.2	53	0.21
A8	P39, Altair NanoMaterials, USA	40.5	37.3	46	1.51
A9	P38, Altair NanoMaterials, USA	51.4	39.4	44	1.15
A10	P43, Altair NanoMaterials, USA	53.9	37.0	46	0.13
A11	P48, Altair NanoMaterials, USA	70.3	69.7	25	0.33
A12	SL14, Altair NanoMaterials, USA	75.2	61.1	28	0[c]
A13	SL15, Altair NanoMaterials, USA	85.9	68.7	25	0.037
A14	P47, Altair NanoMaterials, USA	99.4	79.5	22	0.12
A15	SL22, Altair NanoMaterials, USA	107	85.7	20	0.19
A16	SL23, Altair NanoMaterials, USA	135	91.5	19	0.16
J1	LT-1, Hohsen, Japan	3.2	3.2	540	0[c]
J2	LT-2, Hohsen, Japan	3.1	3.1	550	0[c]
J3	LT-FP, Hohsen, Japan	7.2	6.4	270	0[c]
X1	LiOEt + $Ti(OPr)_4$, Ref. 18	-	105	16	0.35
X2	X1 autoclaved	-	53	32	0.19
X3	LiOEt + $Ti(OBu)_4$, Ref. 18	-	183	9	0.13
X4	X3 autoclaved	-	119	14	0.05
X5	LiOEt + $Ti(OBu)_4$, another batch	-	153	11	0[c]
X6	LiOEt + $Ti(OBu)_4$, another batch	-	196	9	0[c]

[a] BET surface area of the starting powder (if available).
[b] Calcined at 500°C, 30 min.
[c] Anatase not detectable by cyclic voltammetry.

junction with that earlier reporting has become available for release. We now present a more systematic investigation of a broad array of polycrystalline $Li_4Ti_5O_{12}$ materials.

Experimental

Materials.—The studied materials are surveyed in Table I. Three commercial $Li_4Ti_5O_{12}$ products were obtained from Titan Kogyo Kabushiki Kaisha, Hohsen, Corp., Japan, LT-1, LT-2, and LT-FP; they are further referred to as J1, J2, and J3, respectively. The materials A1-A16 were made by Altair NanoMaterials using a proprietary commercial high-temperature process producing well-developed crystalline materials over a large size range. The materials X1-X6 were synthesized from Li/Ti alkoxides according to Ref. 18 and provide a contrast to the high-temperature formed materials (the symbol X stands for Xoliox, SA, the principal sponsor of Ref. 18). The materials X5 and X6 were prepared from lithium ethoxide and titanium tetrabutoxide in the same way as X3, but under a proprietary calcination program, which allowed the anatase impurities to be minimized. The slurry was deposited on F-doped SnO_2 support as described below.

Preparation of electrodes.—Powder $Li_4Ti_5O_{12}$ was dispersed in an aqueous medium into viscous paste according to the previously developed methods.[19,22,23] Briefly, the powder (1.0 g) was ground for at least 20 min in an agate or porcelain mortar under slow addition of 4 × 0.2 mL of 10% aqueous solution of acetylacetone. The mixture was diluted by 5 mL H_2O and mixed with 2 mL of 4% aqueous solution of hydroxypropylcelulose (Aldrich, MW 100,000) and 2 mL of 10% aqueous solution of Triton-X100 (Fluka). The resulting viscous liquid was stirred overnight before use. Sometimes the mixture was further homogenized using a titanium ultrasonic horn (Bioblock Scientific; 80 W, 30 × 2 s pulses). The obtained paste was deposited on a sheet of conducting glass (F-doped SnO_2, TEC 8 from Libbey-Owens-Ford, 8 $\Omega/\square$) using a doctor-blading technique.[19,24] The film was finally calcined for 30 min in air at 500°C. After cooling down to room temperature, the sheet was cut into ten electrodes 1.5 × 1 cm^2 in size; the geometric area of the $Li_4Ti_5O_{12}$ film was 1 × 1 cm^2. The layer thickness was about 2-4 μm (alpha-step profilometer; Tencor Instruments). The mass of active electrode material was estimated to be about 0.1-0.3 mg/cm^2. In some cases, the film's area was cut down by mechanical scraping of the film's edges by a piece of glass. This served to finely adjust the charge capacity to a comparable uniform value of *ca.* 90-140 mC per electrode.

Methods.—Electrochemical measurements were carried out in a one-compartment cell using an Autolab Pgstat-30 (Ecochemie) controlled by GPES-4 software. The reference and auxiliary electrodes were from Li metal, hence, potentials are referred to the Li/Li^+ (1 M) reference electrode. $LiN(CF_3SO_2)_2$ (Fluorad HQ 115 from 3 M) was dried at 130°C/l mPa. Ethylene carbonate (EC) and 1,2-dimethoxyethane (DME) were dried over the 4 Å molecular sieve (Union Carbide). The electrolyte solution, 1 M $LiN(CF_3SO_2)_2$ + EC/DME (1/1 by volume) contained 10-15 ppm H_2O as determined by Karl Fischer titration (Metrohm 684 coulometer). All operations were carried out in a glove box. The Brunauer-Emmett-Teller (BET) surface areas of the prepared materials were determined from nitrogen adsorption isotherms at 77 K (ASAP 2010, Micromeritics). Scanning electron microscopy (SEM) images were obtained by Hitachi S-4700 apparatus. Transmission electron microscopy (TEM) images were obtained by Philips EM430T microscope operating with LaB_6 cathode at 300 kV. Powder X-ray diffractometry (XRD) was studied on a Siemens D-5000 diffractometer using Cu Kα radiation.

Results and Discussion

Figure 1A and B show the SEM pictures of two materials, A3 (12.9 m^2/g) and A13 (68.7 m^2/g). These materials were selected to demonstrate one example of coarse particles and one example of fine particles from the same origin. (For additional SEM pictures of

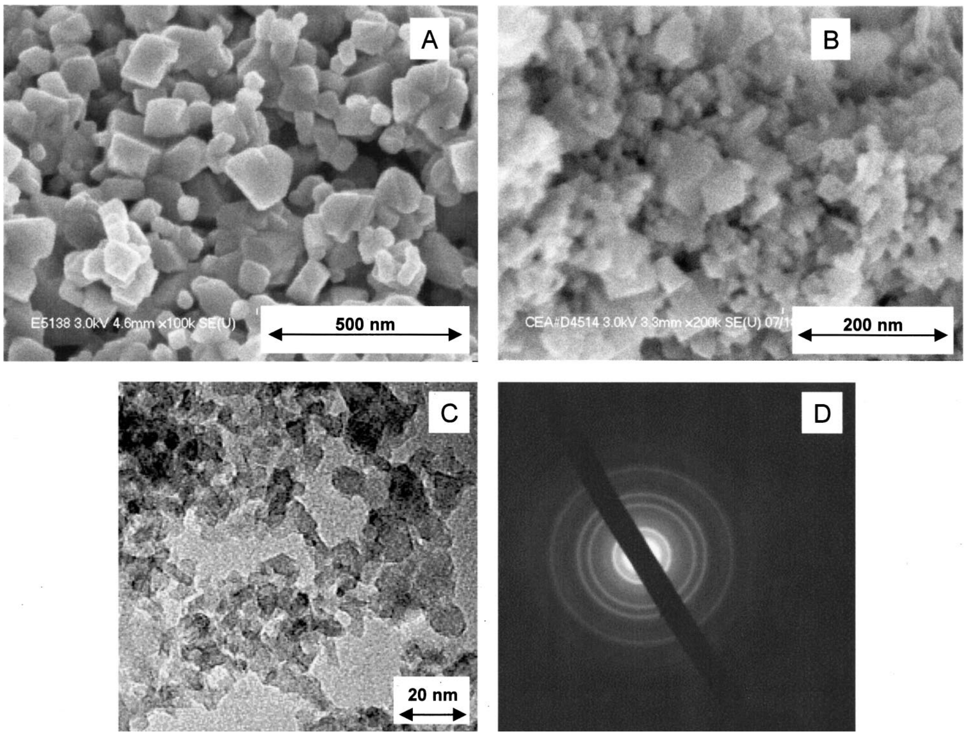

Figure 1. (A) SEM image of sample A3 (12.9 m^2/g); (B) SEM image of sample A13 (68.7 m^2/g); (C) TEM image of sample X6 (196 m^2/g); (D) selected-area electron diffractogram of sample X6 (as in chart C).

materials J2 and X3 see Ref. 18). The SEM patterns confirm roughly the expected average particle sizes (Table I), although all the tested materials are rather polydisperse. Figure 3C shows the TEM image of material X6 (196 m^2/g). The selected area electron diffraction pattern of X6 (Fig. 1D) evidences that these particles are formed from pure $Li_4Ti_5O_{12}$ spinel. A careful inspection of Fig. 1C even reveals the corresponding lattice fringes of $Li_4Ti_5O_{12}$ spinel in the individual particles. Also the XRD patterns show that all materials presented in Table I can be indexed as $Li_4Ti_5O_{12}$. The A samples (except A12 and A3) contained, according to XRD, trace amounts of rutile and anatase. Anatase was detected also in some X samples. Quantitative determination of anatase was carried out as suggested in Ref. 8 from cyclic voltammograms of Li insertion (*vide infra*).

The lattice constant, *a*, was found to fluctuate between 0.8297 to 0.8340 nm for various nanocrystalline X samples. The lattice constant of hydrothermally grown X samples (X2, X4) was 0.8366 nm, which is in good agreement with the lattice constant of $Li_4Ti_5O_{12}$ made by the conventional high-temperature synthesis, 0.8367 (Ref. 1), 0.8365 (Ref. 3), 0.8358 (Ref. 4) and 0.8357 (Ref. 8). The cubic lattice constant, *a* of $Li_{1+x}Ti_{2-x}O_4$ (spinel) is known to decrease with *x* (Ref. 4; Eq. 1), but this cannot account for the observed decrease of *a* for nanocrystalline X materials. The latter conclusion is supported by two arguments, (*i*) the lattice constant attains its normal value after hydrothermal growth and (*ii*) our X nanomaterials showed the formal potential of Li insertion of 1.55 V (*vide infra*) which indicates the Li-rich spinel ($x = 1/3$).

The average particles size, *d*, was estimated by assuming nonporous spherical grains of a density of $\rho = 3.5\ g/cm^3$ and the given surface area, S_{BET}

$$d = 6/\rho S_{BET} \qquad [3]$$

Alternatively, the crystallite size d_c (coherent length of the crystal lattice) was determined from the X-ray line width (*w*) according to the Scherrer formula

$$d_c = 0.9\lambda/w \cos\Theta \qquad [4]$$

λ is the X-ray wavelength (0.1540562 nm and Θ is the diffraction angle). The particle size can also be estimated from SEM (cf. Fig. 1). The particle sizes seen by SEM were reasonably comparable to the values calculated from Eq. 3. Most materials even showed comparable particle and crystallite sizes ($d \cong d_c$), even though Eq. 3 and 4 contain very crude assumptions (spherical and defect-free, single-crystal particles). This matches our previous experience[18-20] that statistically agglomerated nanoparticles (in contrast to some organized mesoscopic textures[20,21]) can be well approximated by Eq. 3 and 4. Table I summarizes the *d* values calculated from Eq. 3.

Figure 2 shows two examples of cyclic voltammograms. The examples were chosen to demonstrate one material with a relatively high content of anatase impurity (sample A8) and one material, which is virtually free from anatase (sample A12). (For one additional example, presenting the sample X3, see Fig. 3 in Ref. 18). The peaks of Li insertion into $Li_4Ti_5O_{12}$ (spinel) dominated cyclic voltammograms of all the tested materials. The formal potential of insertion was 1.55-1.57 V *vs.* Li/Li^+, which matched the previously reported values.[1,5,18] Hence both XRD (see above) and cyclic voltammetry confirm that all our materials (Table I) contain solely $Li_4Ti_5O_{12}$ (spinel) and not $LiTi_2O_4$ or other Li-poor spinel phases. Anatase manifest itself by small peaks at 1.75 and 2.0 V.[18-21] Assuming the insertion ratio Li/TiO_2 (anatase) = 0.5 at slow scan rates,[19-21] the integral area of the voltammetric peaks at 1.75/2 V scales with the content of anatase in the material. Hence, cyclic voltammetry of Li insertion can serve as an easy and sensitive method to analyze the $Li_4Ti_5O_{12}$-TiO_2 mixtures for trace anatase (Table I). The cathodic/anodic peaks of rutile should occur at *ca.* (1.3-1.4)/(1.6-1.7) V, respectively,[25] *i.e.*, the anodic peak of rutile overlaps that of $Li_4Ti_5O_{12}$. Rutile should be detectable in the cathodic scan, since the cathodic peak of rutile is shifted negatively to the cathodic peak of $Li_4Ti_5O_{12}$. However, the electrochemical detection of trace amounts of rutile in $Li_4Ti_5O_{12}$ is not that straightforward as the electrochemical detection of trace amounts of anatase (Fig. 2), because the Li^+ insertion into rutile is sluggish, and the charge capacity is only *ca.* 400 C/g.[25]

The effect of particle size on charging rate of $Li_4Ti_5O_{12}$ was evaluated by galvanostatic chronopotentiometry, while the charge/discharge current was adjusted to 2C, 50C, 100C, 150C, 200C, and 250C. Our thin films, made from pure $Li_4Ti_5O_{12}$, offer good model electrodes. The absence of any supporting additives, usual in con-

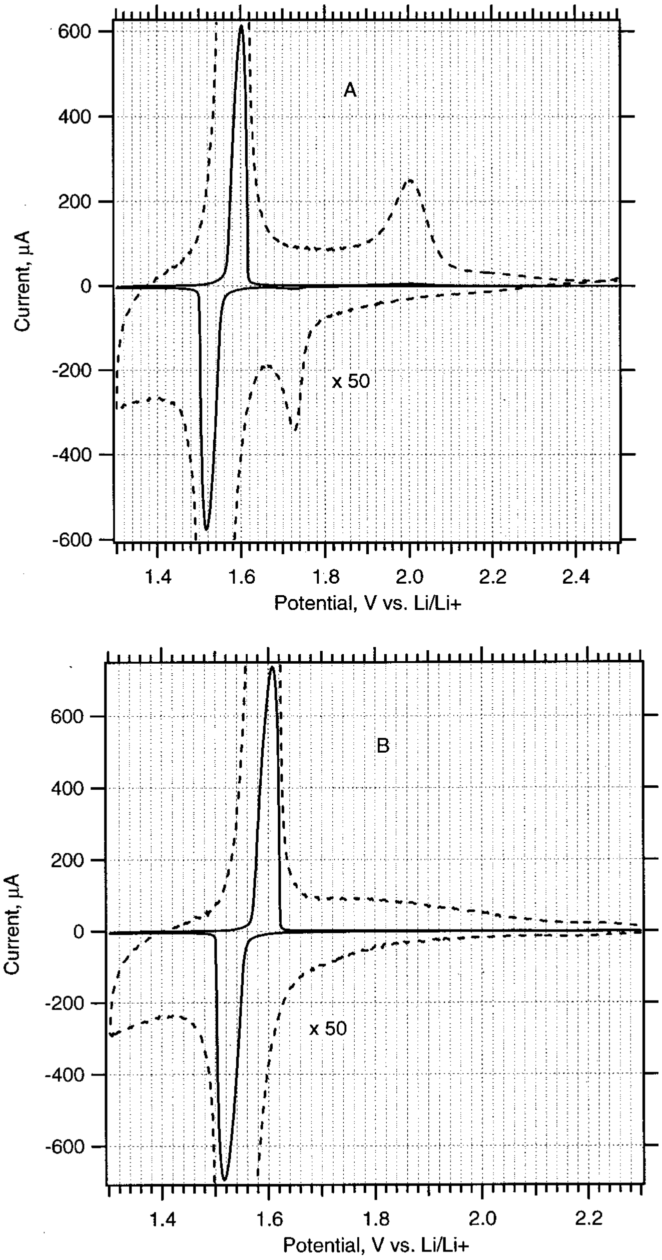

Figure 2. Examples of cyclic voltammograms of $Li_4Ti_5O_{12}$: (A) sample A8; (B) sample A12. Electrolyte solution: 1 M $LiN(CF_3SO_2)_2$ + EC/DME (1:1, v:v); scan rate 0.2 mV/s. Dashed curve displays the same plot, but with the current-scale expanded by a factor of 50.

ventional battery materials (conductive and polymeric binders), reduces the number of experimental variables. Hence, the individual electroactive materials are tested at authentic and reproducible conditions. In order to minimize the other disturbing sample-specific variables, the thickness, volume, and mass of the electroactive film were kept as constant as possible. Since the precise adjustment of the film's mass (0.1-0.3 mg) was difficult, we were monitoring the maximum electrochemical charge capacity of a given electrode instead of its mass. The maximum charge is, essentially, proportional to the film's mass, which is also roughly represented by the thickness of the layer, at the constant geometric area of the electrode. Total electrode capacity determination was easy and precise, either from slow cyclic voltammetry (scan rates $\leqslant 1$ mV/s) or chronopotentiometry at low currents ($\leqslant 2$C). According to Eq. 2, the maximum charge capacity of $Li_4Ti_5O_{12}$ equals 175 mAh/g based on the mass of the starting host material.[1,9,10,26] However, real electrodes tend to deliver about 150-160 mAh/g.[11,16,17,26] Within the experimental error of weighing of the film, the maximum reversible capacities (found at $\leqslant 2$ C or scan rates $\leqslant 1$ mV/s) were in the expected range (*ca.* 140-170 mAh/g) for all the materials listed in Table I.

To evaluate the error introduced by varying faradaic capacity (mass) of an actual electrode at different charging/discharging rates due to only partial charging/discharging of the electrode layer, Fig. 3 (charts A and B) display the fluctuation of galvanostatic charges caused by different nominal capacities of an electrode. Twelve different electrodes were fabricated from one selected low-surface-area material (A3) and one selected high-surface-area material (A16). The spread of experimental data, which is caused by uncertainty in the actual film's charge capacity (mass), is about 10-20%, assuming that the total film's charge capacity occurs within *ca.* 90-150 mC in 2-250 C range. As expected, smaller particles (Fig. 3, plot B) are less sensitive than larger particles (Fig. 3, plot A) to the fluctuations of an actual film's capacity. We further present only the data for electrodes within this safe region.

Figure 3C compares the relative charging rates of two materials with similar surface areas, but with different synthetic history, A16 (91.5 m^2/g) and X1 (105 m^2/g). Although the actual test electrode A16 had somewhat larger capacity (138 mC) than the actual test electrode X1 (114 mC), it exhibited better performance at rates >50 C (Fig. 3C).

Figure 4 shows two examples of chronopotentiometric plots. The examples were chosen to demonstrate the behavior of electrodes made of one material with relatively large particles (sample A2) and one material with relatively small particles (sample A16). (For additional examples, presenting samples X3 and J2, see Fig. 4 in Ref. 18). The charging/discharging currents were adjusted to the following values: 2, 50, 100, 150, 200, and 250C. Figure 4 demonstrates that small particles have a better charge capability than larger particles. Despite the A16 electrode being handicapped by a larger actual capacity (143 mC, function of electrode thickness) than the A2 electrode (85 mC) (cf. Fig. 3), the charge capability of A16 is considerably better, especially at high currents (Fig. 4).

A systematic screening of this effect is presented on Fig. 5. It summarizes the charge capacities from chronopotentiometric plots (as those in Fig. 4) for all the tested materials at 50-250C. The charge capabilities are roughly proportional to the logarithm of specific surface areas, if the surface areas are smaller than *ca.* 20 m^2/g. Materials, having surface areas between *ca.* 20 to 110 m^2/g exhibit a narrowing plateau charge capability as the charging/discharging rate is increasing from 50 to 250C. These materials, depending on their surface area can be charged and discharged close to the material nominal capacity, referred to the value at 2C, in a wide interval of charging rates. In other words, a certain particle size is required for a specific charging rate. Although nanoparticles in this 20-80 nm range are rather tolerant to fast charging and discharging, after an increase of the charging rate to a certain point, fading of the nominal capacity was observed. The range is quite broad and most of the materials still perform well at 150C. The high-rate charge capability is not kept for very small particles, below 20 nm (surface areas >100 m^2/g). Figure 5 demonstrates that particles corresponding to surface area between *ca.* 100-200 m^2/g seem to show decreased charge capability with increasing specific surface area. The peak performance was determined for particles characterized by surface areas around 100 m^2/g. Capacity fading from this optimum was observed for bigger and smaller particles at high charge rates.

We can apparently exclude that the slow response of larger particles is due to poor electrical contacts. In thin-film electrodes, made from micrometer-sized particles (A1, A2, J1, J2, J3), virtually every microcrystal is in a direct contact with the current collector, hence the diffusion-controlled electrochemical kinetics may set in (*vide infra*). On the other hand, in nanocrystalline film, the charge transport occurs via percolation among many necking nanoparticles of $Li_4Ti_5O_{12}$, which have almost infinite electrical resistivity in the starting (nonlithiated) state. Nevertheless, the excellent charging rate

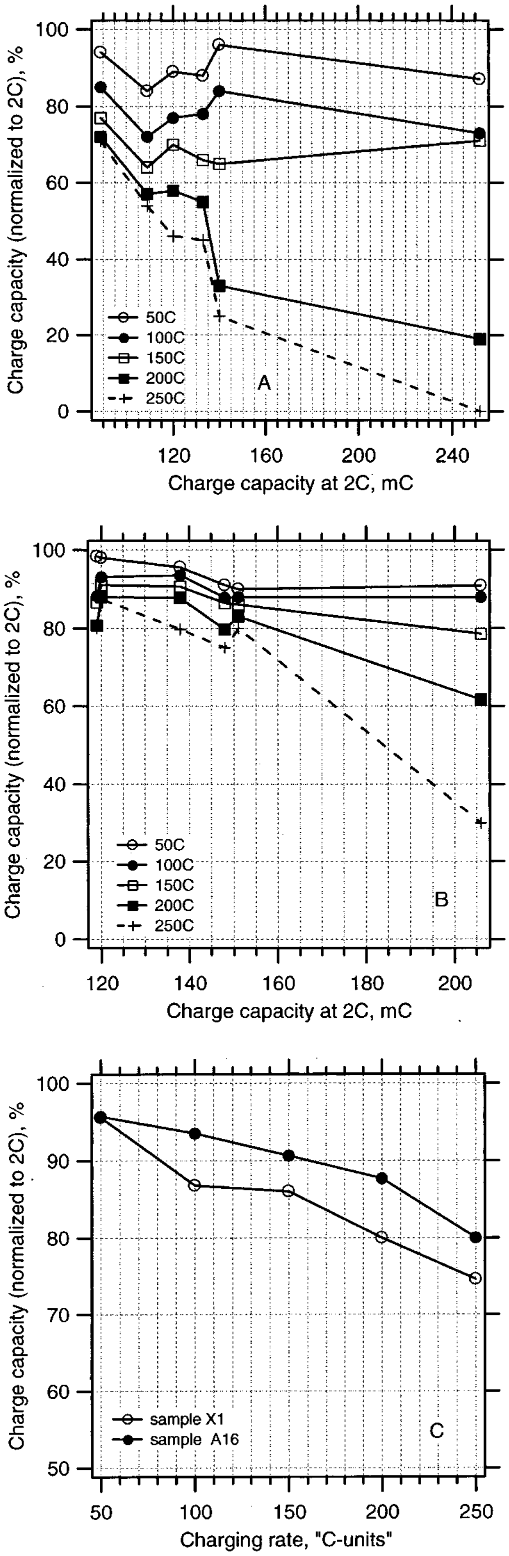

Figure 3. Examples of relative charge capacity of $Li_4Ti_5O_{12}$ from galvanostatic chronopotentiometry. Electrolyte solution: 1 M $LiN(CF_3SO_2)_2$ + EC/DME (1:1, v:v). (A) sample A3; (B) sample A16. Six different electrodes from each material (A3, A16) were characterized by their reversible capacity at 2C, and relative attenuation of this capacity is plotted at higher rates, *i.e.*, 50, 100, 150, 200, and 250C. The charge capacity was determined between the cutoff voltages of 3 and 1 V. (C) Relative charge capacity (defined as in the charts A, B) is plotted *vs.* the charging rate for sample A16 (electrode reversible charge capacity 138 mC at 2C) and X1 (electrode reversible charge capacity 114 mC at 2C).

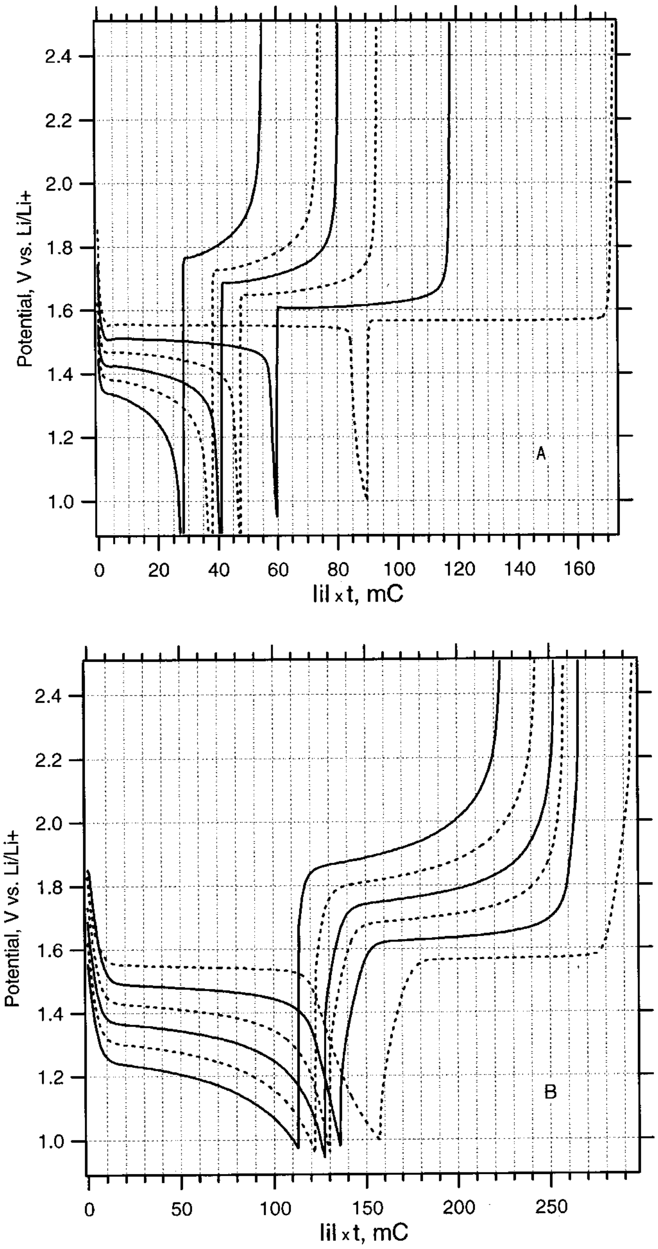

Figure 4. Examples of galvanostatic chronopotentiometry of $Li_4Ti_5O_{12}$. [A] Sample A2; [B] sample A16. Electrolyte solution: 1 M $LiN(CF_3SO_2)_2$ + EC/DME (1:1, v:v). The current, *i*, was adjusted to the charging rate of 2C (dashed curve), 50C, 100C (dashed curve), 150C, 200C (dashed curve), and 250C. For the sake of clarity, the time (*t*) is multiplied by the absolute value of charging/discharging current, *i*.

of nanocrystalline $Li_4Ti_5O_{12}$ is still clearly demonstrated, especially in the optimized range of particles sizes, *i.e.*, 20-150 nm.

The slow response of ultrasmall particles can be discussed in terms of their morphology, which influences the Li transport. The interaction energy (*W*) of Li^+-Li^+ in a host material is known to scale inversely with the particle volume[27]

$$W = \frac{\varepsilon_0^2 Y(1 + v)}{V(1 - v)(1 - 2v)} \qquad [5]$$

where ε_0^2 is the average strain per mole of inserted Li^+, *Y* is the Young's modulus, *v* is the Poisson's ratio, and *V* is the particle volume. The latter is proportional to the third power of particle size

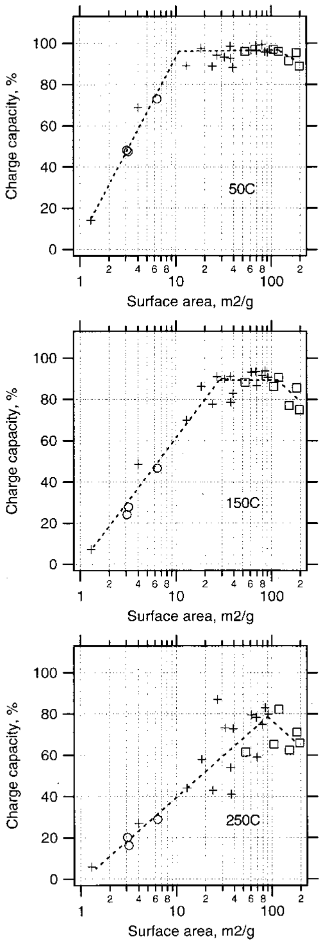

Figure 5. Charge capacity (referred to a nominal charge capacity) of $Li_4Ti_5O_{12}$ materials with varying surface areas; A samples (+), J samples (○), X samples (□)). The charging rate was 50, 100, 150, 200, and 250C, respectively for the given plots. The charge capacity was determined from galvanostatic chronopotentiometry with the cutoff voltages of 3 and 1 V. The nominal charge capacity was determined from slow cyclic voltammetry at scan rates <1 mV/s and/or from charging at 2C. Electrolyte solution: 1 M $LiN(CF_3SO_2)_2$ + EC/DME (1:1, v:v). Dashed lines are guides for eyes.

($V = \pi d^3/6$ for spherical particles, cf. Eq. 3). Hence, when particles get smaller, the stress induced by the Li^+-Li^+ repulsion (for the same Li-insertion ratio) is larger. Consequently, the solid-state Li^+-diffusion coefficients may drop by orders of magnitude, if the particles decrease.[27] We may note that the spinel crystals of 5-10 nm size have 220-1750 unit cells only. The fact that such a crystal is less active to accommodate lithium can also be rationalized in terms of the previously reported lattice shrinking;[18] the cubic lattice constant of materials X3 and X6 was found to be 0.8340 nm, which contrasts to the normal value of 0.8366 nm observed for identical materials, but after their hydrothermal growth (cf. the X4 sample).

Ultrasmall particles also tend to show larger charge irreversibility at low currents and deep cathodic cutoff potentials. The charge reversibility at 2C (cutoff potential 1 V) equals 87 and 91% for samples A16 and A2, respectively (Fig. 4). The corresponding values for X3 and J2 equal 72 and 89%, respectively (Fig. 4 in Ref. 18). This may be due to an enhanced possibility of adsorption of reducible impurities (such as humidity) on the large-area materials or impurities in the lattice or poorly formed lattice due to low temperature processing of some of the samples (X1-X6). Big particles are less sensitive to parasitic reactions, such as irreversible reduction of adsorbed protons. Our analysis points at spinel particles between 20-80 nm as the optimum robust size, taking into consideration manufacturing, handling, and providing high charging rates with good reversibility.

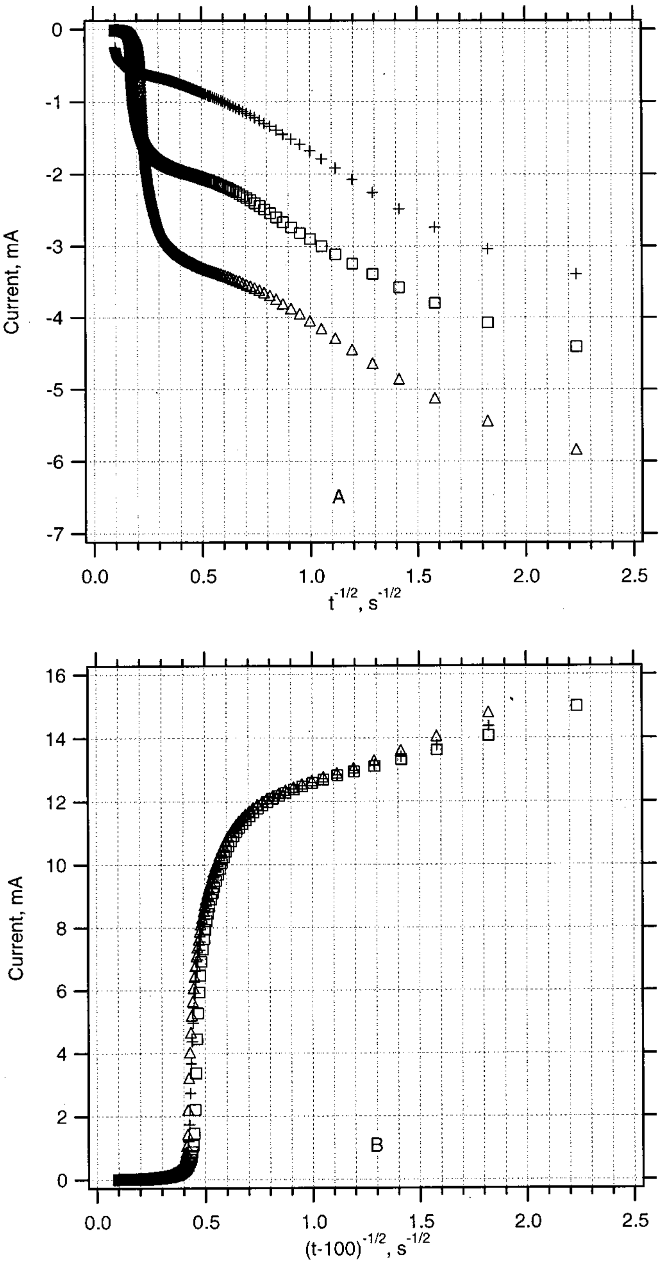

Figure 6. Example of chronoamperometric plot of a $Li_4Ti_5O_{12}$ electrode (sample A14) in 1 M $LiN(CF_3SO_2)_2$ + EC/DME (1:1, v:v). The electrode potential was stepped from 2.5 V to 1.5 (1.4 or 1.3) V and back to 2.5 V, while the time (*t*) of each potential step was of 100 s. Chart A shows the cathodic potential steps: 2.5 → 1.5 V (+); 2.5 V → 1.4 V (□); 2.5 V → 1.3 V (△). Chart B shows the corresponding anodic steps employing the same marker notation.

To get more insight into the kinetics of Li^+ insertion into the $Li_4Ti_5O_{12}$ host, a series of chronoamperometric measurements was carried out with an electrode polarized by square-wave potential steps. The potential was stepped from 2.5 to 1.5 V (1.3, 1.4 V) and back to 2.5 V, while the duration of each potential step was 100 s. Figure 6 demonstrates the example of data for one selected material (A14).

If we assume that the current after a potential step, *I* is controlled by diffusion, the chronoamperometric plot should formally obey the Cottrell equation

$$I = S_{\mathrm{el}} F D^{1/2} c \pi^{-1/2} t^{-1/2} \quad [6]$$

S_{el} is the true (physical) electrode area, c is concentration of Li^+ in the solid, and D is chemical diffusion coefficient. This formalism is valid for Li^+ insertion into anatase, both single-crystal[28,29] and nanocrystalline[21,30,31] electrodes. In the first case, the Cottrell plot (Eq. 6) is perfectly linear over long-time regions.[28,29] The matching of experimental curves and Eq. 6 are less good for polycrystalline anatase, while we observe typical S-shaped $I\text{-}t^{-1/2}$ curves[21,32] qualitatively identical to those for our spinels (cf. Fig. 6). Apparently, the classical gradient-like diffusion concept (Eq. 6) cannot be transferred to nanocrystalline solids without principal reservations. The Li accumulation in nanocrystalline particle can be extrapolated, for a limiting case $d \rightarrow 0$, to be a purely capacitive effect, *i.e.*, the charge resides only on the surface and not in the bulk, since the bulk does not exist any more. In this case, the gradient concept of Li insertion must change into the jump concept of capacitive double-layer charging.

On the other hand, the Cottrell's formalism (Eq. 6) is phenomenologically valid, at least for early stages of insertion (times around 1-10 s; cf. Fig. 6) in all our materials. For a more detailed discussion, the complex nature of the insertion into porous electrode has to be considered.[33] This involves not only the bulk solid-state diffusion (Eq. 6), but also the electrolyte phase, solid-liquid interface, and tortuosity. A proper addressing of all these issues is beyond the scope of this paper. Nevertheless, Eq. 6 can plausibly describe the system in a narrow time region (pseudo-Cottrell behavior), which also depends on the particle size.[34] When particles get smaller the interfacial region begins to dominate over the bulk, and the applicability of Eq. 6 is limited.

For the pseudo-Cottrell domains, the diffusion coefficients were calculated, assuming that the physical electrode area, S_{el}, can be approximated by its BET area. The film's mass was recalculated from the maximum reversible charge supposing the nominal specific charge capacity of 175 mAh/g of a fresh electrode (cf. Eq. 2). This evaluation routine supposes two main simplifications: (*i*) the surface area, seen by the adsorbed N_2 molecule (in BET measurement) is identical to the surface area seen by the solvated Li^+ ion, although the latter is larger, and cannot penetrate into very narrow pores. (*ii*) Each tested electrode is supposed to have a theoretical specific charge capacity (175 mAh/g, Eq. 2), although the actual specific capacity might be lower as a result of electrode aging,[3,11,17,26] imperfect particle contacts, and impurity content. Obviously, both the mentioned approximations may partly compensate each other.

In analogy to anatase,[21,28-30] the concentration, c, refers to the maximum concentration of extra (mobile) Li^+ in the $Li_4Ti_5O_{12}$. With respect to Eq. 2, this concentration is equivalent to three extra Li^+ ions in the $Li_4Ti_5O_{12}$ molecule, which translates into $c = 21.9$ mmol/cm^3. This concentration of Li^+ occurs in a thin layer underneath the surface, shortly after the cathodic potential step. Immediately after the application of the subsequent anodic step, the same Li^+ concentration occurs in the bulk, but a thin layer underneath the surface has $c \rightarrow 0$. This is the driving force for Li^+ transport, if we neglect the migration of Li^+ in the electrical field.[30]

The experimental chronoamperometric plots of all the studied electrodes have a similar shape (cf. Fig. 6), resembling that of nanocrystalline anatase.[21,30,32] During the early stages after the insertion/extraction step, we observe reasonably linear $I\text{-}t^{-1/2}$ curves for all the tested spinels. The linear parts in each plot show an identical slope, but for times longer that *ca.* 1 s, the individual $I\text{-}t^{-1/2}$ curves tend to deviate from linearity (Eq. 6). However, there still exist linear regions, even for $t > 10$ s, but with larger slopes. We may calculate the diffusion coefficients, equivalent to the linear regions in short-time dependencies ($t < \approx 10$ s) and long-time dependencies ($t > \approx 10$ s), both for the cathodic (insertion) and anodic (extraction) steps.

These four values of diffusion coefficients are summarized in Fig. 7 for all the tested materials. Three general conclusions can be drawn: (*i*) the cathodic diffusion is slower than the anodic diffusion by *ca.* one order of magnitude, both for the short-time and long-time processes. (*ii*). The long-time process is faster than the short-time process by *ca.* four orders of magnitude. (*iii*). The diffusion coefficients decrease by *ca.* three orders of magnitude, if the surface area increases from 1 to 196 m^2/g.

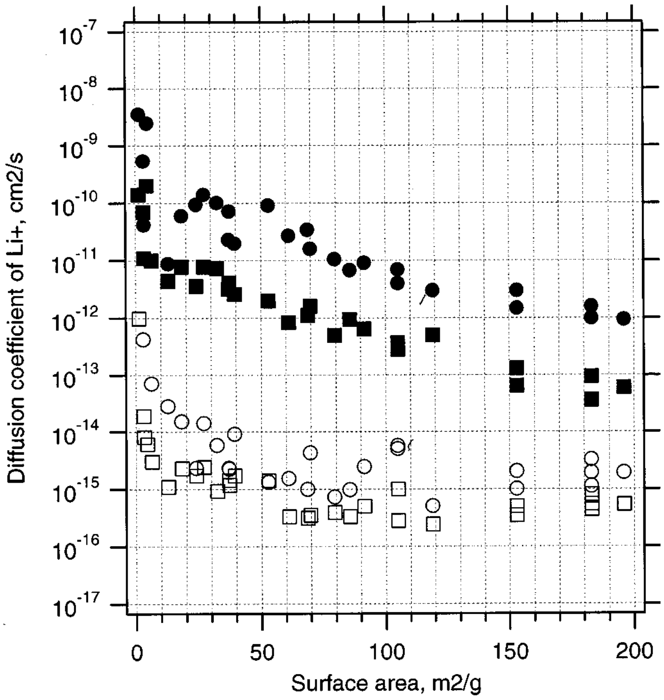

Figure 7. Solid-state diffusion coefficients of Li^+ in the $Li_4Ti_5O_{12}$ electrodes determined from chronoamperometric measurements; (●) long-time anodic step; (○) short-time anodic step, (■) long-time cathodic step, (□) short-time cathodic step.

The first conclusion is easy to understand. The insertion starts from a virtually insulating electrode material. It becomes conducting only after the charge (e^-/Li^+) injection, both from the back contact and from the electrolyte, which slows down the cathodic process. On the other hand, the anodic step starts from a good conducting material, *i.e.* the extraction currents are larger, and the total accumulated charge is almost fully drained away in times shorter than *ca.* 10 s (cf. Fig. 6).

The D values, shown in Fig. 7, are smaller than those, found for $Li_4Ti_5O_{12}$ by using neutron radiography (10^{-6} cm^2/s, Ref. 6) or cyclic voltammetry ($2 \cdot 10^{-8}$ cm^2/s, Ref. 7). The latter technique was not clearly described in Ref. 7. This paper[7] does not seem to refer to cyclic voltammetry, but to a rather special chronoamperometric measurement, made on one single microbead electrode.[35] The D values of the order of 10^{-8} cm^2/s were also measured by electrochemical impedance on Fe-modified $Li_4Ti_5O_{12}$.[36] Such large diffusion coefficients ($\approx 10^{-8}$ cm^2/s) are close to our anodic long-time values for coarse materials (Fig. 7), but a precise comparison is not possible, because the surface area (particle size) of the relevant materials reported in Ref. 7 and 36 were not specified. Bach *et al.*[16] have found D equal to $3 \cdot 10^{-12}$ cm^2/s for their sol-gel grown $Li_4Ti_5O_{12}$ but the particle size (surface area) was again not specified. Recently, D values in the range of 10^{-15} to 10^{-14} cm^2/s were reported for nanocrystalline $LiTi_2O_4$ having particle sizes 12-26 nm.[15] These diffusion coefficients are also close to ours, and we may even speculate that the authors of Ref. 15 had, actually, mismatched their $LiTi_2O_4$ with $Li_4Ti_5O_{12}$. This argument is based on the reported formal potential, 1.56 V,[15] and lattice constant, 0.829 to 0.8361 nm,[15] which both seem to point at $Li_4Ti_5O_{12}$.[1,4,5]

The D values, plotted in Fig. 7, illustrate that the micrometer-sized spinel crystals can hardly be charged with Li^+ efficiently at rates around 200C. The effective diffusion distance, δ equals

$$\delta = (\pi D t)^{1/2} \qquad [7]$$

where the time $t = 18$ s, if we assume the charging rate 200C. Figure 6A shows that the insertion process is almost fully controlled by the short-time diffusion kinetics during the first 18 s of Li^+ insertion. Assuming $D \approx 10^{-12}$ cm^2/s (for Li insertion into coarse particles), the diffusion distance is only $\delta \approx 75$ nm from Eq. 7. Hence, the micrometer-sized crystal cannot be filled with Li^+ completely at the 200C charging. This seems to point clearly at nanocrystalline materials as better host structures for fast Li^+ charging. However, the situation is more complex, since the diffusion coefficients are also smaller in nanocrystalline materials. Hence, the optimum material has to be sought as a compromise between the rate of Li^+ transport and the crystal size.

The drop in the diffusion coefficient with surface area was also found for anatase. The insertion into an anatase single-crystal electrode was characterized by a chronoamperometric diffusion coefficient $D \approx 10^{-13}$ cm^2/s,[28,29] but the nanocrystalline anatase exhibited the corresponding D values in the region of 10^{-17} to 10^{-14} cm^2/s.[21,30,31,37] Although we intuitively expect the same monotonous decrease of D with surface area (as in Fig. 7) also for TiO_2 (anatase), there is not enough systematic data in the literature. We may only note that the highest values (10^{-14} cm^2/s) were reported for compact anatase films, which were prepared by chemical vapor deposition (CVD) or similar methods.[30,31,37] These films may mimic the single-crystal electrode (for direct comparison of CVD *vs.* nanocrystalline anatase see Ref. 31). The drop of diffusion coefficients with decreasing particle size was also reported for various other insertion hosts (cf. Ref. 27, 34).

From the data shown in Fig. 5 and 7, we can draw a general conclusion, that the drop of diffusion coefficients with decreasing particle size need not be detrimental for the overall charging rate. This conclusion is mirrored also in the anatase electrochemistry; the slower Li diffusion and smaller rate constants of Li insertion, observed in small anatase particles, are more than compensated by the increase of the active electrode area.[20,21] In other words, the slow Li^+ transport in small particles is not rate-limiting, because the insertion occurs only in short distances underneath the surface. However, the mechanism of slowing down the Li^+ transport in small crystals is not yet clearly understood. Another challenge for further studies is, that there might be (at least a theoretical) chance to find a material, which would exhibit both the nanocrystalline morphology and fast Li insertion kinetics, as in a coarse material. A third challenge is to translate the ultrafast response of our optimized nanocrystalline spinels into real batteries. This requires proper addressing of two additional tasks, (*i*) to optimize a high-capacity composite of nanospinel with conductive binders and (*ii*) to find an adequately fast counterelectrode. Efforts in all these directions are under way in our labs.

Acknowledgments

This work was supported by Altair, Inc., and NTera, Ltd. Additional financial support from the EC-COST Action D14/0002/99 and Academy of Sciences of the Czech Republic (contract no. A4040804) are also acknowledged. We thank Estelle De Chambrier (NTera) for TEM measurements.

Ecole Polytechnique Fédérale de Lausanne assisted in meeting the publication costs of this article.

References

1. K. M. Colbow, J. R. Dahn, and R. R. Haering, *J. Power Sources*, **26**, 397 (1989).
2. E. Ferg, R. J. Gummov, A. de Kock, and M. M. Thackeray, *J. Electrochem. Soc.*, **141**, L147 (1994).
3. T. Ohzuku, A. Ueda, and N. Yamamoto, *J. Electrochem. Soc.*, **142**, 1431 (1995).
4. M. R. Harrison, P. P. Edwards, and J. B. Goodenough, *Philos. Mag. B*, **52**, 679 (1985).
5. S. I. Pyun, S. W. Kim, and H. C. Shin, *J. Power Sources*, **81-82**, 248 (1999).
6. S. Takai, M. Kamata, S. Fujine, K. Yoneda, K. Kanda, and T. Esaka, *Solid State Ionics*, **123**, 165 (1999).
7. K. Zaghib, M. Simoneau, M. Armand, and M. Gauthier, *J. Power Sources*, **81-82**, 300 (1999).
8. A. Deschanvers, B. Raveau, and Z. Sekkal, *Mater. Res. Bull.*, **6**, 699 (1971).
9. S. Scharner, W. Weppner, and P. Schmid-Beurmann, *J. Electrochem. Soc.*, **146**, 857 (1999).
10. K. Zaghib, M. Armand, and M. Gauthier, *J. Electrochem. Soc.*, **145**, 3135 (1998).
11. D. Peramunage and K. M. Abraham, *J. Electrochem. Soc.*, **145**, 2609 (1998).
12. G. G. Amatucci, F. Badway, A. Du Pasquier, and T. Zheng, *J. Electrochem. Soc.*, **148**, A930 (2001).
13. A. Du Pasquier, A. Laforgue, P. Simon, G. G. Amatucci, and J. F. Fauvarque, *J. Electrochem. Soc.*, **149**, A302 (2002).
14. D. W. Murphy, M. Greenblatt, S. M. Zahurak, R. J. Cava, J. V. Waszczak, G. W. Hull, and R. S. Hutton, *Rev. Chim. Min.*, **19**, 441 (1982).
15. P. Krtil and D. Fattachova, *J. Electrochem. Soc.*, **148**, A1045 (2001).
16. S. Bach, J. P. Pereira-Ramos, and N. Baffier, *J. Power Sources*, **81-82**, 273 (1999).
17. S. Bach, J. P. Pereira-Ramos, and N. Baffier, *J. Mater. Chem.*, **8**, 251 (1998).
18. L. Kavan and M. Grätzel, *Electrochem. Solid-State Lett.*, **5**, A39 (2002).
19. L. Kavan, M. Grätzel, J. Rathousky, and A. Zukal, *J. Electrochem. Soc.*, **143**, 394 (1996).
20. L. Kavan, A. Attia, F. Lenzmann, S. H. Elder, and M. Grätzel, *J. Power Sources*, **147**, 2897 (2000).
21. L. Kavan, J. Rathousky, M. Grätzel, V. Shklover, and A. Zukal, *J. Phys. Chem. B*, **104**, 12012 (2000).
22. L. Kavan, B. O'Regan, A. Kay, and M. Grätzel, *J. Electroanal. Chem.*, **346**, 291 (1993).
23. M. K. Nazeeruddin, A. Kay, I. Rodicio, R. Humphry-Baker, E. Mueller, P. Liska, N. Vlachopolous, and M. Grätzel, *J. Am. Chem. Soc.*, **115**, 6382 (1993).
24. S. D. Burnside, J. Moser, K. Brooks, M. Grätzel, and D. Cahen, *J. Phys. Chem. B*, **103**, 9328 (1999).
25. L. Kavan, D. Fattachova, and P. Krtil, *J. Electrochem. Soc.*, **146**, 1375 (1999).
26. C. H. Chen, J. T. Vaughey, A. N. Jansen, D. W. Dees, A. J. Kahaian, T. Goacher, and M. M. Thackeray, *J. Electrochem. Soc.*, **148**, A102 (2001).
27. Y. M. Choi and S. I. Pyun, *Solid State Ionics*, **99**, 173 (1997).
28. L. Kavan, M. Grätzel, S. E. Gilbert, C. Klemenz, and H. J. Scheel, *J. Am. Chem. Soc.*, **118**, 6716 (1996).
29. R. Hengerer, L. Kavan, P. Krtil, and M. Grätzel, *J. Electrochem. Soc.*, **147**, 1467 (2000).
30. R. Van de Krol, A. Goossens, and J. Schoonman, *J. Phys. Chem. B*, **103**, 7151 (1999).
31. H. Lindström, S. Södergen, A. Solbrand, H. Rensmo, J. Hjelm, A. Hagfeldt, and S. E. Lindquist, *J. Phys. Chem. B*, **101**, 7710 (1997).
32. L. Kavan, K. Kratochvilová, and M. Grätzel, *J. Electroanal. Chem.*, **394**, 93 (1995).
33. J. P. Meyers, M. Doyled, R. M. Darling, and J. Newman, *J. Electrochem. Soc.*, **147**, 2930 (2000).
34. M. D. Levi and D. Aurbach, *Electrochim. Acta*, **45**, 167 (1999).
35. M. Nishizawa, R. Hashitani, T. Itoh, T. Matsue, and I. Uchida, *Electrochem. Solid-State Lett.*, **1**, 10 (1998).
36. S. Ma and H. Noguchi, *J. Electrochem. Soc.*, **148**, A589 (2001).
37. M. P. Cantao, J. I. Cisneros, and R. M. Torresi, *J. Phys. Chem.*, **98**, 4865 (1994).

Chem. Mater. **2004,** *16,* 477−485

Lithium Storage in Nanostructured TiO_2 Made by Hydrothermal Growth

Ladislav Kavan,*[,†,⊥] Martin Kalbáč,[†] Markéta Zukalová,[†] Ivan Exnar,[‡]
Volker Lorenzen,[§] Reinhard Nesper,[||] and Michael Graetzel[⊥]

J. Heyrovský Institute of Physical Chemistry, Academy of Sciences of the Czech Republic, Dolejškova 3, CZ-18223 Prague 8, Czech Republic, High Power Lithium, Park Scientifique, PSE-B, EPFL, Ecublens, CH-1015 Lausanne, Switzerland, SusTech GmbH & Co. KG, Petersenstr. 20, D-64287 Darmstadt, Germany, Laboratory of Inorganic Chemistry, ETHZ, Wolfgang-Pauli-Str. 10, CH-8093 Zürich, Switzerland, and Laboratory of Photonics and Interfaces, EPFL, Ecublens, CH-1015 Lausanne, Switzerland

Received October 21, 2003. Revised Manuscript Received November 24, 2003

Nanostructured titania materials were prepared from $TiCl_4$ via autoclaving in 10 M NaOH at 250 °C and subsequent treatment in aqueous and/or acidic media. XRD and Raman spectroscopy evidenced the presence of anatase as the main phase, but most materials contained also some XRD-silent component. Cyclic voltammograms of lithium insertion demonstrate two pairs of reversible pseudocapacitive peaks (S-peaks) in addition to the ordinary peaks of diffusion-controlled Li insertion into the anatase lattice. The occurrence of S-peaks is associated with the nanosheet- and/or nanotubular morphology of the materials. This structure developed at hydrothermal conditions via exfoliation of the layered Na^+/H^+ titanate precursors. The S-peaks were suggested to be the signatures of quantum-size confinement in titania nanosheets. The nanosheet-containing materials are reducible by *n*-butyllithium to cubic $LiTiO_2$ (at conditions when the ordinary nanocrystalline anatase gives only the orthorhombic $Li_{0.5}TiO_2$). Consequently, the electrochemical Li-storage capacity is larger compared to that of crystalline anatase. The prepared materials also show better insertion kinetics; hence, they are promising for applications in Li-ion batteries. Depending on the applied voltage, they can be charged/discharged either as ordinary Li-insertion hosts or as supercapacitors.

Introduction

The insertion/extraction of Li to/from the TiO_2 lattice is described by the equation

$$TiO_2 + x(Li^+ + e^-) \rightarrow Li_xTiO_2 \qquad (1)$$

The most active form of TiO_2 for reaction 1 is anatase, in which the insertion coefficient *x* is usually close to 0.5.[1−4] Various theoretical[5−7] and experimental[1,3−5,8−14] aspects of reaction 1 have been addressed in the past. Investigations of X-ray diffraction,[13,15] electrical and optical properties,[14] photoelectron spectroscopy,[16] X-ray absorption,[17] and ^{7}Li NMR[15,17−19] unanimously show that anatase converts during reaction 1 into a two-phase product, viz. lithium-poor tetragonal phase $Li_{0.01}TiO_2$ with the anatase structure (space group $I4_1/amd$) and orthorhombic lithium titanate, $Li_{0.5}TiO_2$ (space group *Imma*).

Investigations of single-crystal[8,9] and polycrystalline[3] electrodes have shown that the insertion capacity,

---

* Corresponding author. E-mail: kavan@jh-inst.cas.cz.
[†] Academy of Sciences of the Czech Republic.
[‡] High Power Lithium, Park Scientifique, PSE-B, EPFL.
[§] SusTech GmbH & Co. KG.
[||] ETHZ.
[⊥] Laboratory of Photonics and Interfaces, EPFL.

(1) Lindström, H.; Södergen, S.; Solbrand, A.; Rensmo, H.; Hjelm, J.; Hagfeldt, A.; Lindquist, S. E. *J. Phys. Chem. B* **1997**, *101*, 7717−7722.

(2) Kavan, L.; Kratochvilová, K.; Grätzel, M. *J. Electroanal. Chem.* **1995**, *394*, 93−102.

(3) Kavan, L.; Grätzel, M.; Rathousky, J.; Zukal, A. *J. Electrochem. Soc.* **1996**, *143*, 394−400.

(4) Kavan, L.; Attia, A.; Lenzmann, F.; Elder, S. H.; Grätzel, M. *J. Electrochem. Soc.* **2000**, *147*, 2897−2902.

(5) Lunell, S.; Stashans, A.; Lindström, H.; Hagfeldt, A. *J. Am. Chem. Soc.* **1997**, *119*, 7374−7380.

(6) Mackrodt, W. C. *J. Solid State Chem.* **1999**, *142*, 428−439.

(7) Nuspl, G.; Yoshizawa, K.; Yamabe, T. *J. Mater. Chem.* **1997**, *7*, 2529−2536.

(8) Hengerer, R.; Kavan, L.; Krtil, P.; Grätzel, M. *J. Electrochem. Soc.* **2000**, *147*, 1467−1472.

(9) Kavan, L.; Grätzel, M.; Gilbert, S. E.; Klemenz, C.; Scheel, H. J. *J. Am. Chem. Soc.* **1996**, *118*, 6716−6723.

(10) Huang, S. Y.; Kavan, L.; Grätzel, M.; Exnar, I. *J. Electrochem. Soc.* **1995**, *142*, 142−144.

(11) Lindström, H.; Södergen, S.; Solbrand, A.; Rensmo, H.; Hjelm, J.; Hagfeldt, A.; Lindquist, S. E. *J. Phys. Chem. B* **1997**, *101*, 7710−7716.

(12) Van de Krol, R.; Goossens, A.; Schoonman, J. *J. Phys. Chem. B* **1999**, *103*, 7151−7159.

(13) Van de Krol, R.; Goossens, A.; Meulenkamp, E. A. *J. Electrochem. Soc.* **1999**, *146*, 3150−3154.

(14) Van de Krol, R.; Goossens, A.; Meulenkamp, E. A. *J. Appl. Phys.* **2001**, *90*, 2235−2242.

(15) Wagemaker, M.; Van de Krol, R.; Kentgens, A. P. M.; Van Well, A. A.; Mulder, F. M. *J. Am. Chem. Soc.* **2001**, *123*, 11454−11461.

(16) Henningsson, A.; Andersson, M. P.; Uvdal, P.; Siegbahn, H.; Sandell, A. *Chem. Phys. Lett.* **2002**, *360*, 85−90.

(17) Luca, V.; Hanley, T. L.; Roberts, N. K.; Howe, R. F. *Chem. Mater.* **1999**, *11*, 2089−2102.

(18) Wagemaker, M.; Kentgens, A. P. M.; Mulder, F. M. *Nature* **2002**, *418*, 397−399.

(19) Wagemaker, M.; Kearley, G. J.; Van Well, A. A.; Mutka, H.; Mulder, F. M. *J. Am. Chem. Soc.* **2003**, *125*, 840−848.

10.1021/cm035046g CCC: $27.50

coulombic efficiency, reversibility, and stability of anatase depend on the electrode morphology. However, previous reports have mostly dealt with statistically packed nanocrystals without deliberately controlled particle structure and mesoscopic ordering.[1,3,5,10−13] Li insertion into organized, Pluronic-templated anatase exhibited some abnormal features, which were tentatively assigned to the presence of amorphous titania in the highly organized skeleton.[20]

The preparation of nanostructured anatase in the form of fibers, nanotubes, nanoribbons, and nanowires was attempted by templating with anodic alumina,[21−26] polymers,[27] and low-molecular-weight surfactants.[28−31] Of particular interest is a simple method based on hydrothermal recrystallization in aqueous NaOH pioneered by Kasuga et al.[32] There are also several reports on single-crystalline nanowires[21,26,33] and nanotubes.[31,34] Nevertheless, a perfect single-crystal-like structure, which would be analogous to a carbon nanotube, does not seem to be accessible with anatase. (Note that one claim for the anatase analogue of carbon nanotube[34] was later canceled).

The mechanism of alkaline hydrothermal conversion of titania into nanofibers (tubes, ribbons) was discussed by several authors,[32,35−41] but the results have often been contradictory. Most works have dealt with NaOH medium, but there were also occasional studies in KOH.[35,37] Important intermediates are layered alkali titanates, of the general formula $M_2Ti_nO_{2n+1}$ ($M = Na$, K, $3 \leq n \leq 6$). They have a monoclinic lattice, with parallel kinked layers of edge-sharing TiO_6 octahedra. Such layers intercalate alkali metal cations M^+, which can be further ion-exchanged with H^+ or H_3O^+ toward protonic hydrous titanates $H_2Ti_nO_{2n+1}\cdot mH_2O$. The reaction is topotactic; hence, the protonic titanates preserve the original layered structure.[42,43] An alternative of this material is orthorhombic $H_xTi_{2-x/4}\square_{x/4}O_4\cdot H_2O$ ($x \approx 0.7$, $\square$ = vacancy) with the lepidocrocite-type structure. It is characterized by stacked flat sheets of edge-sharing TiO_6 octahedra with intercalated H_2O and H_3O^+ (hydroxonium ions are balanced with titanium ion vacancies).[44−46] These layered crystals easily exfoliate into individual nanosheets, exhibiting high two-dimensional anisotropy: thickness of ca. 1 nm and lateral dimension of 0.1−1 μm.[44−46]

The layered protonic titanates seem to be the key structures in the synthesis of nanotextured materials via the alkaline hydrothermal treatment of TiO_2. They are, presumably, produced by the Na^+/H^+ ion exchange during subsequent acidic washing of the alkali autoclaved titania, but some authors have assumed that the protonic titanates grow also directly during the NaOH treatment.[35,36] The morphology has been characterized as nanotube,[32,35,36,38,39,41] fiber,[47] nanowire,[33,37] and nanoribbon.[40] The most typical structure is derived from exfoliated titanate nanosheets which may be rolled into a multiwalled nanotube with spiral cross section.[35,36,39] However, intermediate structures of flat or occasionally curved sheets[35,39−41] are also abundant in the product. (Since the titania nanotubes grow via rolling of the sheet precursors, they do not possess the closed cagelike structure like carbon nanotubes.)

The crystallographic description of these tubular/sheet materials is based on monoclinic protonic titanates[47] such as $H_2Ti_3O_7$,[35,36,41] but other authors considered also the anatase lattice[38,39,40,48] to be the basic structural motif of these sheets/tubes. This was supported by the TEM patterns showing fringes of 0.37 nm (a_0 lattice parameter of anatase) and 0.75−0.78 nm.[39,40] According to this model, the sheets grow along the (001) plane,[39,40] but sheets with denser stacking corresponding to the (101) planes can also be considered.[40] The anatase structure of sheets was also found in the lepidocrocite-like material after mild calcination.[44] Generally, the primary product of alkaline hydrothermal treatment of titania is the Na^+/H^+ titanate, which is free from any crystalline TiO_2 (anatase, rutile, etc.).[36,41] However, thermal dehydratation of protonic titanates leads to TiO_2 (presumably nonstoichiometric), while the anatase and rutile phases grow depending on the pretreatment conditions and the final calcination temperature.[35,36,38,41,42,44,47] Sometimes also TiO_2(B)[42,49] and "monoclinic" TiO_2[47] were identified as intermediate phases during heat treatment. (Note that the "mono-

---

(20) Kavan, L.; Rathousky, J.; Grätzel, M.; Shklover, V.; Zukal, A. *J. Phys. Chem. B* **2000**, *104*, 12012−12020.

(21) Zhang, X.; Yao, B.; Zhao, L.; Liang, C.; Zhang, L.; Mao, Y. *J. Electrochem. Soc.* **2001**, *148*, G398−G400.

(22) Lin, Y.; Wu, G. S.; Yuan, X. Y.; Xie, T.; Zhang, L. D. *J. Phys. Condens. Matter* **2003**, *15*, 2917−2922.

(23) Zhang, M.; Bando, Y.; Wada, K. *J. Mater. Sci. Lett.* **2001**, *20*, 167−170.

(24) Lei, Y.; Zhang, L. D.; Fan, J. C. *Chem. Phys. Lett.* **2001**, *338*, 231−236.

(25) Hoyer, P. *Langmuir* **1996**, *12*, 1411−1413.

(26) Miao, Z.; Xu, D.; Ouyang, J.; Guo, G.; Zhao, X.; Tang, Y. *Nano Lett.* **2002**, *2*, 717−720.

(27) Caruso, R. A.; Schattka, J. H.; Greiner, A. *Adv. Mater.* **2001**, *13*, 1577−1579.

(28) Kobayashi, S.; Hanabusa, K.; Hamaski, N.; Kimura, M.; Shirai, H. *Chem. Mater.* **2000**, *12*, 1523−1525.

(29) Jung, J. H.; Kobayashi, H.; van Bommel, K. J. C.; Shinkai, S.; Shimizu, T. *Chem. Mater.* **2002**, *14*, 1445−1447.

(30) Adachi, M.; Murata, Y.; Harada, M.; Yoshikawa, S. *Chem. Lett.* **2000**, 942−943.

(31) Adachi, M.; Murata, Y.; Okada, I.; Zaban, A.; Yoshikawa, S. *J. Electrochem. Soc.* **2003**, *150*, G488−G493.

(32) Kasuga, T.; Hiramatsu, M.; Hoson, A.; Sekino, T.; Niihara, K. *Langmuir* **1998**, *14*, 3160−3163.

(33) Xu, C.; Zhan, Y.; Hong, K.; Wang, G. *Solid State Commun.* **2003**, *126*, 545−549.

(34) Liu, S. M.; Gan, L. M.; Liu, L. H.; Zhang, W. D.; Zeng, H. C. *Chem. Mater.* **2002**, *14*, 1391−1397.

(35) Chen, Q.; Zhou, W.; Du, G.; Peng, L. M. *Adv. Mater.* **2002**, *14*, 1208−1211.

(36) Du, G. H.; Chen, Q.; Che, R. C.; Yuan, Z. Y.; Peng, L. M. *Appl. Phys. Lett.* **2001**, *79*, 3702−3704.

(37) Du, G. H.; Chen, Q.; Han, P. D.; Yu, Y.; Peng, L. M. *Phys. Rev. B* **2003**, *67*, 035323−0353237.

(38) Seo, D. S.; Lee, J. K.; Kim, H. *J. Cryst. Growth* **2001**, *229*, 428−432.

(39) Yao, B. D.; Chan, Y. F.; Zhang, X. Y.; Zhang, W. F.; Yang, Z. Y.; Wang, N. *Appl. Phys. Lett.* **2003**, *82*, 281−283.

(40) Yuan, Z. Y.; Colomer, J. F.; Su, B. L. *Chem. Phys. Lett.* **2002**, *363*, 362−366.

(41) Sun, X.; Li, Y. *Chem. Eur. J.* **2003**, *9*, 2229−2238.

(42) Sasaki, T.; Komatsu, Y.; Fujiki, Y. *Chem. Mater.* **1992**, *4*, 894−899.

(43) Sasaki, T.; Watanabe, M.; Komatsu, Y.; Fujiki, Y. *Inorg. Chem.* **1985**, *24*, 2265−2271.

(44) Sasaki, T.; Nakano, S.; Yamauchi, S.; Watanabe, M. *Chem. Mater.* **1997**, *9*, 602−608.

(45) Sasaki, T.; Watanabe, M. *J. Am. Chem. Soc.* **1998**, *120*, 4682−4689.

(46) Choy, J. H.; Lee, H. C.; Jung, H.; Kim, H.; Boo, H. *Chem. Mater.* **2002**, *14*, 2486−2491.

(47) Yin, S.; Fujishiro, Y.; Wu, J.; Aki, M.; Sato, T. *J. Mater. Proc. Technol.* **2003**, *137*, 45−48.

(48) Zhou, Y.; Cao, L.; Zhang, F.; He, B.; Li, H. *J. Electrochem. Soc.* **2003**, *150*, A1246−A1249.

(49) Izawa, H.; Kikkawa, S.; Kolzum, M. *J. Phys. Chem.* **1982**, *86*, 5023−5026.

clinic" TiO_2 reported in ref 47 seems to be identical to TiO_2(B)).

Li et al.[48] have recently reported on the lithium insertion into hydrothermally grown TiO_2 nanotubes. The material showed good capacity and cycle life. Its cyclic voltammogram exhibited some features of organized mesoporous anatase made by surfactant templating,[4,20] but this analogy was not commented on in ref 48. The present paper aims at addressing these issues by a systematic study of lithium insertion into titania nanostructures made by hydrothermal growth in NaOH medium. There is a challenge that the rich structural chemistry of hydrothermally grown titania nanostructures may be mirrored also in their electrochemical properties.

Experimental Section

Materials. Thirty-four research samples were obtained from SusTech GmbH & Co. KG, Darmstadt, Germany. Their general synthetic protocol was as follows: 8 mL (72.9 mmol) of $TiCl_4$ was dissolved in 20 mL of water. Then, 10 N NaOH was added to a total volume of 150 mL. The mixture was autoclaved at 250 °C for 6 h. Subsequently, the material was washed with hydrochloric acid and water and further autoclaved in water or weak acidic solvents for up to several hours. The individual samples are listed in the Supporting Information along with their basic properties (BET surface areas and phase composition). The concentration of anatase phase was determined from powder X-ray diffraction according to a method developed by Banfield et al.[50] Rutile (Bayer R-U-F, containing 3.7 wt % anatase) served as an inner reference in the phase analysis. Nanocrystalline anatase Bayer PKP09040 (154 m^2/g as-received; 89 m^2/g after sintering into a thin-film electrode)[3] was used as another reference material, and it further served for comparative experiments with *n*-butyllithium (vide infra). Still another reference material (C240, 89 m^2/g after sintering into a thin-film electrode) was made by the sol−gel method and autoclaved in water at 240 °C. (Both Bayer PKP09040 and C240 are pure anatase nanocrystals with ordinary grain morphology (see ref 3 for details)).

Preparation of Electrodes. A powder sample was dispersed in an aqueous medium into a viscous paste according to the previously developed methods.[3,51,52] The powder (0.3 g) was mixed under stirring or gentle mortaring with 0.8 mL of 10% aqueous solution of acetylacetone. Subsequently, 0.8 mL of 4% aqueous solution of hydroxypropylcellulose (Aldrich, MW 100 000) was added and finally 0.4 mL of 10% aqueous solution of Triton-X100 (Fluka). Before use, the prepared slurry was homogenized by stirring. If the slurry was too viscous, it was further diluted by water. Titanium grid (5 × 15 mm, Goodfellow) was used as the electrode support. Electrodes were prepared by dipcoating; the coated area was ca. 5 × 5 mm. The prepared electrodes were dried in air and finally calcined in air at 450 °C for 30 min. The amount of active electrode material was between 0.2 and 0.7 mg. Blank experiments confirmed that a bare Ti grid had negligible electrochemical charge capacity compared to that of the active material. Alternatively, the slurry was also deposited on a sheet of conducting glass (F-doped SnO_2, TEC 8 from Libbey-Owens-Ford, 8 Ω/square) using a doctor-blading technique.[3,53] The sheet of conducting glass had the dimensions $3 \times 5 \times 0.3$ cm^3. Scotch tape at both edges of the support (0.5 cm) defined the film thickness and left part of the support uncovered for electrical contact. The film was finally calcined for 30 min in air at 450 °C. After cooling to room temperature, the sheet was cut into 10 electrodes, 1.5×1 cm^2 in size; the geometric area of the TiO_2 film was 1×1 cm^2. Sometimes the TiO_2 layers on conducting glass were mechanically unstable and delaminated easily from the support after electrochemical treatment. The layers deposited on a Ti grid were satisfactorily stable.

Methods. Electrochemical measurements were carried out in a one-compartment cell using an Autolab Pgstat-30 (Ecochemie) controlled by the GPES-4 software. The reference and auxiliary electrodes were from Li metal; hence, potentials are referred to the Li/Li^+ (1 M) reference electrode. $LiN(CF_3SO_2)_2$ (Fluorad HQ 115 from 3M) was dried at 130 °C/1 mPa. Ethylene carbonate (EC) and 1,2-dimethoxyethane (DME) were dried over the 4A molecular sieve (Union Carbide). The electrolyte solution, 1 M $LiN(CF_3SO_2)_2$ + EC/DME (1/1 by volume) contained 15−40 ppm H_2O as determined by Karl−Fischer titration (Metrohm 684 coulometer). All operations were carried out under argon in a glovebox. Transmission electron microscopy (TEM) images were obtained on a Tecnai F30 microscope with a 300-keV field emission electron gun. The BET surface areas of the prepared materials were determined from nitrogen adsorption isotherms at 77 K (ASAP 2010, Micromeritics). Powder X-ray diffraction (XRD) was studied on a Siemens D-5000 diffractometer using Cu Kα radiation. Samples treated by *n*-butyllithium (10 min of stirring in 1.6 M solution in hexane (Aldrich) with a molar ratio Li/Ti ∼ 2) were washed with hexane and dried under Ar. The airtight sample container covered by Kapton foil was used for recording XRD patterns.[15] Raman spectra were excited by an Ar^+ laser at 2.54 eV (Innova 305, Coherent) and recorded on a T-64000 spectrometer (Instruments, SA) interfaced to an Olympus BH2 microscope (objective 50×). Microscopic measurements allowed focusing on different sampled areas (different grains of the solid material) to test the homogeneity of studied samples.

Results and Discussion

Figure 1 shows a typical morphology of the prepared samples. The materials contain nanoribbons or elongated nanosheets, which may be curved and partly or fully rolled into tubes.[32,35,36,38−40] The rolling is visualized on the high-resolution image, along with the fringes parallel to the ribbon axis. This morphology is reminiscent of that reported by Su et al.[40]

The phase analysis according to Banfield[50] (see Experimental Section) usually indicated a low content of crystalline TiO_2 in most materials tested. Phenomenologically, this indicates the presence of some "X-ray amorphous" (XRA) phase. The term XRA refers to material, which does not exhibit distinct diffraction peaks, but which may still possess low-range ordering. Hence, it might well be the titania nanosheet, nanotube, or simply a nanocrystal, which is too small to be detectable by powder XRD. (Note that the pristine exfoliated nanosheets of the lepidocrocite-like titania are also virtually "X-ray amorphous",[44−46] but electron diffraction indicates their two-dimensional face-centered orthogonal arrangement.[54]) The actual XRA concentrations of all tested materials are quoted in the Supporting Information.

According to XRD, all the tested materials contained anatase as the main phase. The materials Lor-035-092A (67 m^2/g, XRA = 80%) and Lor-035-013B (18 m^2/g, XRA >95%) exhibited some features at $2\Theta \sim 10°$ (Cu Kα),

---

(50) Zhang, H.; Finnegan, M.; Banfield, J. F. *Nano Lett.* **2001**, *1*, 81−85.

(51) Kavan, L.; O'Regan, B.; Kay, A.; Grätzel, M. *J. Electroanal. Chem.* **1993**, *346*, 291−307.

(52) Nazeeruddin, M. K.; Kay, A.; Rodicio, I.; Humphry-Baker, R.; Mueller, E.; Liska, P.; Vlachopolous, N.; Grätzel, M. *J. Am. Chem. Soc.* **1993**, *115*, 6382−6390.

(53) Burnside, S. D.; Moser, J.; Brooks, K.; Grätzel, M.; Cahen, D. *J. Phys. Chem. B* **1999**, *103*, 9328−9332.

(54) Sasaki, T.; Ebina, T.; Kitami, Y.; Watanabe, M. *J. Phys. Chem. B* **2001**, *105*, 6116−6121.

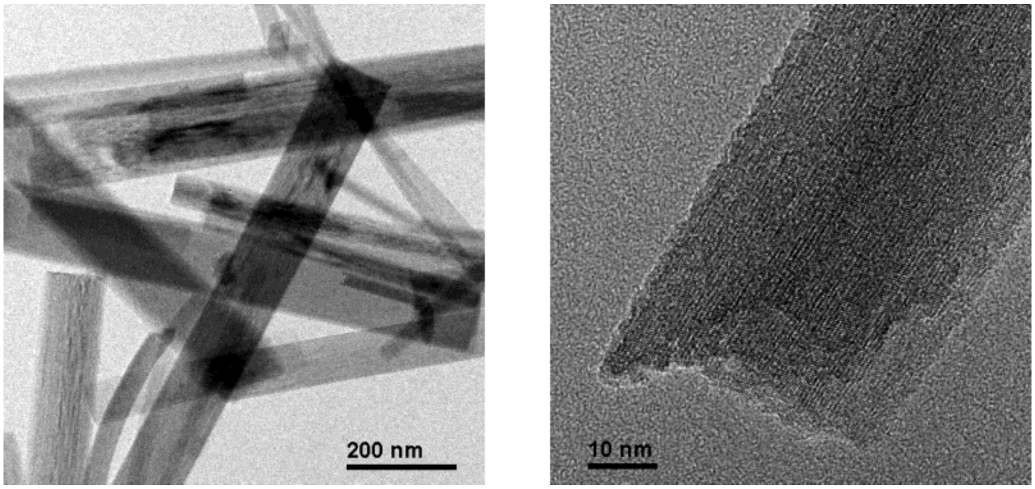

Figure 1. TEM picture demonstrating a typical morphology of the SusTech materials (sample Lor-035-013B, XRA>95%; see Supporting Information for further details).

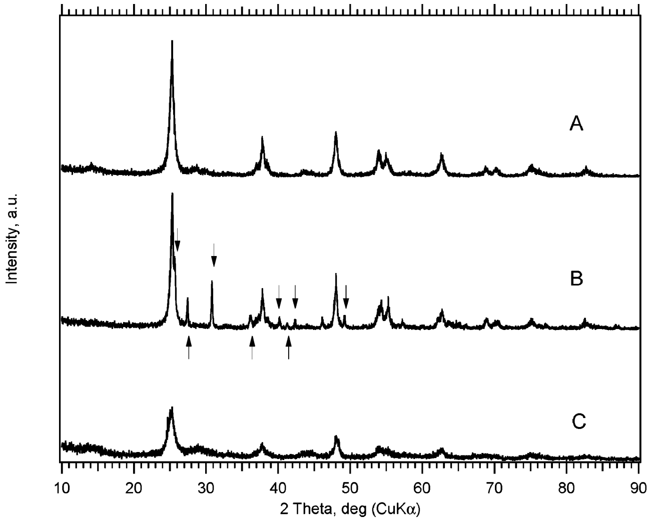

Figure 2. X-ray diffraction pattern of selected SusTech materials: [A] sample Lor-035-088C (XRA = 17%), [B] sample Lor-035-099A (XRA = 48%), and [C] sample Lor-035-092D (XRA = 56%). The plot [B] evidences the presence of anatase, rutile (upward-directing arrows), and brookite (downward-directing arrows).

which is a diagnostic diffraction for the layered protonic titanates. Most other materials exhibited only weak- or negligible peaks in this region. In several cases also rutile and brookite impurities were found. This is demonstrated in Figure 2 on the diffractogram of sample Lor-035-099A (53 m^2/g, XRA = 48%), which can be indexed as a mixture of anatase, rutile, and brookite.

Further insight into the phase composition of the SusTech materials can be obtained from micro-Raman spectroscopy. This technique allows selecting a sampled area of several micrometers in size, and by scanning of the sample surface, we can distinguish different Raman-active phases in a sample. Figure 3 displays illustrative examples of mixed-phase (plots A, B, D) and pure-phase (plot C) materials. The latter plot evidences a pure anatase phase in Lor-035-098c (XRA <1%), in accord with X-ray diffraction. Most other SusTech materials exhibited pure anatase also by the Raman tests (see Supporting Information). However, plots B and D demonstrate that, with the mentioned spatial resolution, we can, sometimes, find sampled micro-areas corresponding to brookite[55] and rutile, respectively. Spectrum A is an example of an anatase + brookite mixture seen in one position on the sample Lor-035-112B2 (XRA = 32%), but we can also focus to another area in the same material, exhibiting mostly the rutile phase. Several samples from the tested set of materials contained all three main phases of TiO_2, that is, anatase, rutile, and brookite, while we can find a “Raman-pure” phase in the sampled area of several micrometers in size.

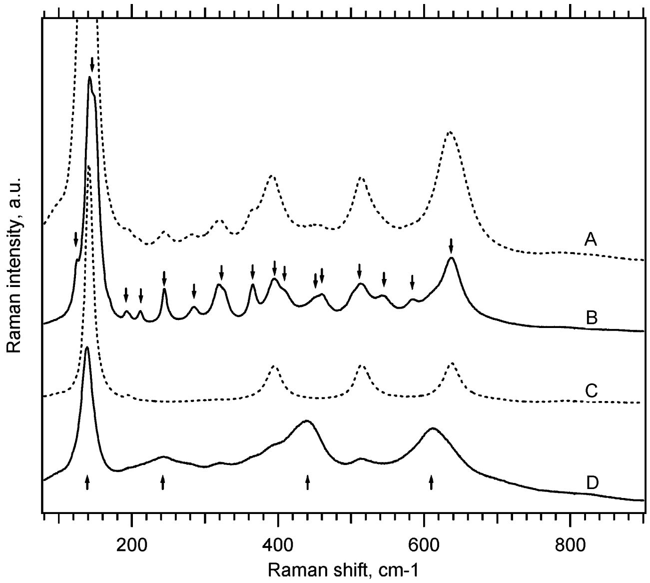

Figure 3. Micro-Raman spectra of selected SusTech materials: [A] Lor-035-112B2 (XRA = 32%), [B] Lor-035-099A (XRA = 48%), [C] Lor-035-098c (XRA <1%) spectrum assignable to pure anatase, and [D] Lor-035-112B2 different sample area (cf. plot [A]). Downward-directing arrows, brookite; upward-directing arrows, rutile.

Figure 4 shows an example of a cyclic voltammogram at the conditions of Li^+ insertion into the material Lor-035-071A (135 m^2/g, XRA = 71%; pure anatase seen by XRD and Raman). This voltammogram exhibits an unusual shape, if we compare it to the voltammograms

---

[55] Tompsett, G. A.; Bowmaker, G. A.; Cooney, R. P.; Metson, J. B.; Rodgers, K. A.; Seakins, J. M. *J. Raman Spectrosc.* **1995**, *26*, 57–62.

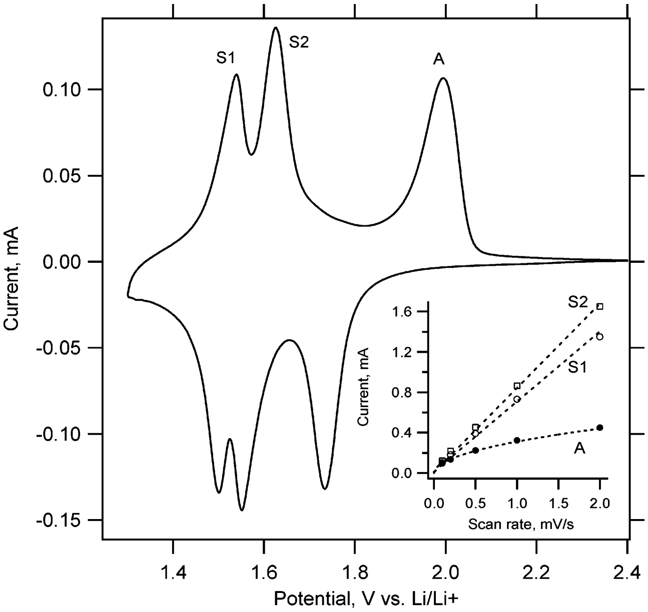

Figure 4. Cyclic voltammograms of the material Lor-035-071A (135 m^2/g, XRA = 71%; pure anatase seen by XRD and Raman). Electrolyte solution: 1 M $LiN(CF_3SO_2)_2$ + EC/DME (1:1, v:v); scan rate 0.1 mV/s. Inset: anodic peak current vs the scan rate.

of "ordinary" anatase, both in the form of single crystal[8,9] or nonorganized nanocrystalline[1−4,13] electrodes. The voltammogram is dominated by two pairs of peaks denoted S1 and S2. The formal potentials of S1 and S2 peaks are 1.52 and 1.59 V vs Li/Li^+, respectively. The remaining pair of peaks (formal potential 1.88 V; denoted A) is commonly observed in anatase electrodes.[1−4,8,9,13] The same effect was previously reported only in the mesoporous anatase films made by supramolecular templating with Pluronic.[20] In this case, the extra peaks (S-peaks) were tentatively assigned to the presence of "amorphous titania".[20]

Inserted in Figure 4 is a plot of the peak current vs scan rate. The peak current ($I_{p,A}$) of A-peaks scales with the square root of the scan rate, v, as is expected for diffusion-controlled irreversible kinetics,[1,12]

$$|I_{p,A}| = 0.4958nFAc(D\alpha nFv/RT)^{1/2} \qquad (2)$$

where n is the number of electrons, A is the electrode area, c is the maximum concentration of Li^+ (or Ti^{3+}) in the accumulation layer (c = 0.024 mol/cm^3 for x = 0.5; cf. eq 1), D is the chemical diffusion coefficient of Li^+, and the other symbols have their usual meaning.

On the other hand, the peak currents of S1/S2 peaks ($I_{p,S}$) scale with the first power of the scan rate, which is characteristic for capacitive charging:

$$|I_{p,S}| = A\,dQ/dt = AC\,dE/dt = ACv \qquad (3)$$

Q is the voltammetric charge and dE/dt the scan rate, v. However, the characteristic shape of the voltammogram with small peak-to-peak splitting (ca. 50−100 mV at v = 0.1 mV/s) points at some surface-confined faradaic process.

The capacitive and/or surface-confined faradaic process is developed explicitly on materials which are rich in XRA phase. Figure 5 shows an example material, which has almost no A-peaks, but a broad feature in the area of S1/S2 peaks. This is reminiscent of the behavior of "amorphous" titania made by anodic oxidative hydrolysis of $TiCl_3$.[20]

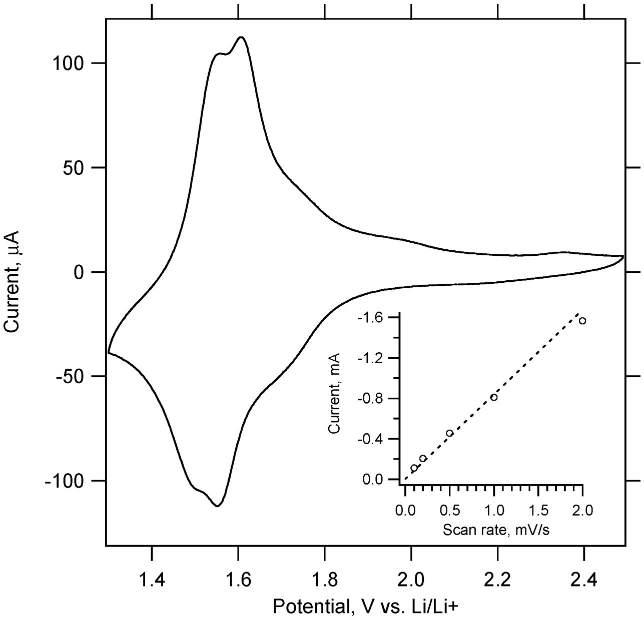

Figure 5. Cyclic voltammograms of the material Lor-035-013B (calcined for 7 h at 400 °C, XRA > 95%). Electrolyte solution: 1 M $LiN(CF_3SO_2)_2$ + EC/DME (1:1, v:v); scan rate 0.1 mV/s. Inset: cathodic peak current vs the scan rate.

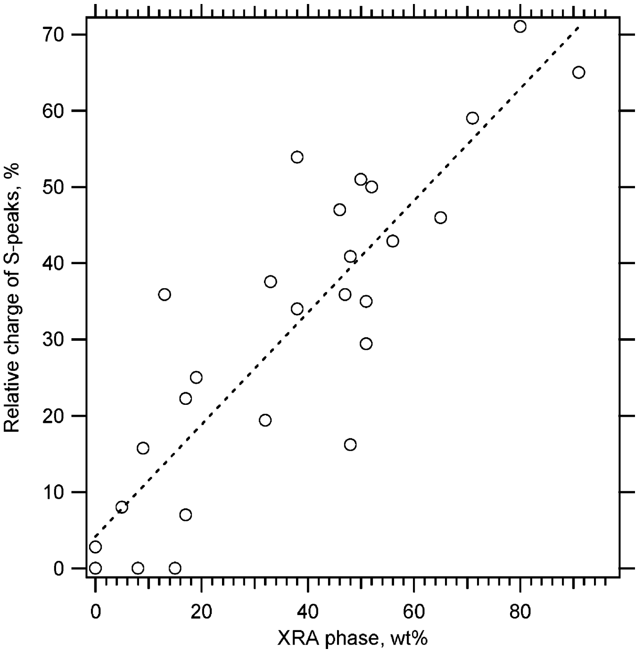

Figure 6. Integral voltammetric charge of the S-peaks (S1 + S2; referred to the total charge) from the anodic branch of cyclic voltammograms (scan rate 0.2 mV/s) is plotted as a function of the concentration of "X-ray amorphous" (XRA) phase in the material. The dashed line is a linear fit of experimental points.

Twenty-six different materials from the tested set of samples exhibited well-developed S-peaks. Their formal potentials (1.52 and 1.59 V) were reproducible with a deviation smaller than ±0.01 V for all the "S-active" samples. The area (charge) of S-peaks was variable, but it correlated with the content of XRA phase in the particular material. Figure 6 displays the proportion of integral voltammetric charge of the S1/S2 peaks (re-

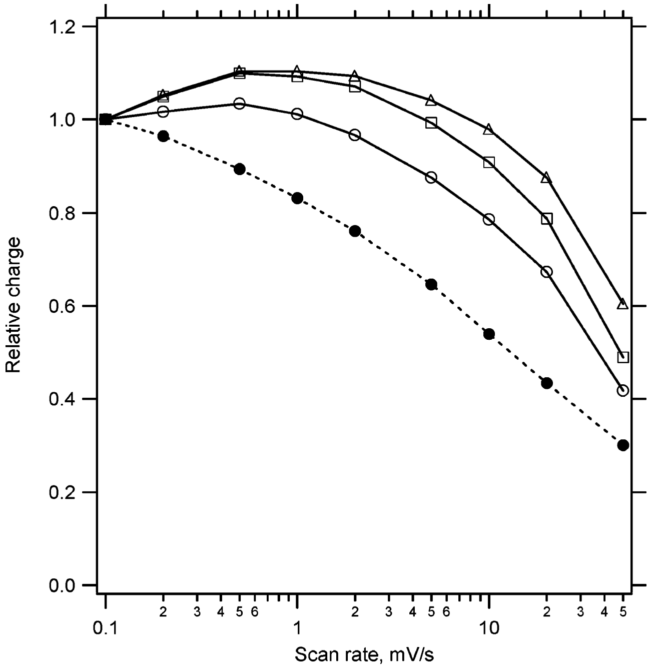

Figure 7. Integral voltammetric charge from the anodic branch of cyclic voltammograms (as in Figures 4, 5) is plotted as a function of scan rate. The charge was normalized against the charge capacity of the same electrode at the slowest scan (0.1 mV/s). Open points, material Lor-035-119A (85 m^2/g XRA = 19%); squares, material Lor-035-119B (43 m^2/g, XRA = 38%); triangles, material Lor-035-071a (135 m^2/g, XRA = 71%). Full points + dashed line, reference nonorganized nanocrystalline anatase C240 (89 m^2/g, XRA ≅ 0).

ferred to the total charge capacity) as a function of the concentration of XRA phase. This correlation matches the heuristic conclusion of ref 20 that the S-peaks are signatures of “amorphous titania” in the sample. The explicit advantages of hydrothermally grown TiO_2 nanostructures over the Pluronic-templated materials[20] consist of (i) broad selection of materials with varying proportion of XRA phase and (ii) their availability as powders in macroscopic quantity. This allows investigation of this peculiar effect in detail.

Figure 7 plots the total voltammetric charge of the material Lor-035-071a (anatase, XRA = 71%; 135 m^2/g) against the scan rate. For comparison, the same curve is plotted for two other similar SusTech samples and compared to that of nonorganized nanocrystalline anatase (C240, 89 m^2/g) made by sol−gel.[3] As the absolute charge capacities of each testing electrode fluctuated (between ca. 150 and 400 mC), the data in Figure 7 were normalized with respect to the actual charge of the same electrode at the slowest scan (0.1 mV/s) which was set as unity. Figure 7 demonstrates that the SusTech materials delivered the reference charge already at ca. 1−5 mV/s, while there seems to be even some unexpected increase above one at medium scan rates (0.2−1 mV/s). The same peculiarity in $Q-v$ plots was observed also for the Pluronic-templated materials,[20] and this study has confirmed that such a behavior is another characteristic feature of materials exhibiting S-peaks. Ordinary nonorganized nanocrystalline anatase shows the “normal” monotonic increase of voltammetric charge with decreasing scan rate (cf. also refs 3 and 20).

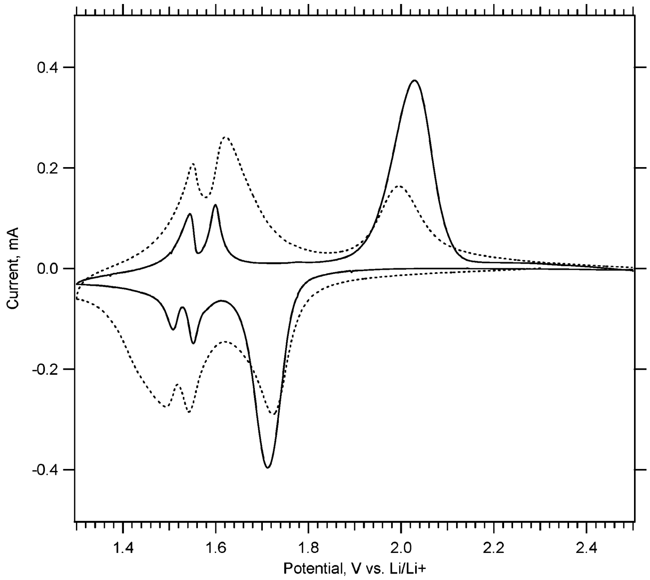

Figure 8. (Dashed line): Cyclic voltammogram of material Lor-035-094b (XRA = 91%). (Full line): The same material after heat treatment for 40 h at 500 °C. The absolute currents are not comparable since the plots represent two different electrodes. Electrolyte solution: 1 M $LiN(CF_3SO_2)_2$ + EC/DME (1:1, v:v); scan rate 0.2 mV/s.

The voltammetric charge in ordinary anatase corresponds to the A-peaks only, and the process is controlled by a diffusion of Li^+ in the solid (eq 2). On the other hand, the materials with S-peaks show a pronounced charge, which is assigned to a surface-confined charge transport. This process mimics the fast capacitive charging (eq 3). The analogy goes further, as the capacitive charging is also more sensitive to self-discharge, as for any supercapacitor. This may explain the appearance of a maximum in the $Q-v$ plot shown in Figure 7. The charging in S-peaks should not be confused with the ordinary double-layer charging, which is inherently free from any peaks (cf. also ref 20). We suggest that the charge of S-peaks can be considered as a faradaic pseudocapacitance, specific for certain materials containing the XRA phase (vide infra).

The absolute faradaic capacity of our materials cannot be measured very precisely, owing to the small mass of active electrode material (see Experimental Section). Nevertheless, there was a clear trend for increasing the Li-charge capacity with increasing S-peak area (XRA content). For slow voltammetric charging ($v \sim 0.1$ mV/s) the materials without S-peaks (XRA → 0) exhibited a reversible charge capacity of about 600 C/g, which is a typical value for anatase electrodes (with A-peaks only).[1−4] The “S-active” materials exhibited significantly larger capacities, up to ca. 800 C/g. A similar enhancement of the capacity of hydrothermally grown TiO_2 nanotubes was reported by Li et al.[48] Obviously, the S-peaks increase the Li-storage capacity, due to a more favorable stoichiometry, accessible in the pseudocapacitive process (vide infra).

The S-peaks in Pluronic-templated materials were found to be completely quenched by long-term (40 h) heat treatment at 450 °C.[20] Our nanostructures showed similar tendency, although their thermal stability was higher. This is illustrated by the behavior of one example material in Figure 8. The heat treatment of this material at 500 °C for 40 h does not cause a complete disappearance of S-peaks, but only decreases their intensity. The analogy of our materials with Pluronic-templated ones[20] manifests itself also by larger A-peaks splitting in annealed materials. We recall an empirical correlation showing that the splitting of A-peaks is linearly proportional to the particle size of anatase.[4] This confirms the hypothesis that the anatase crystals grow upon heat treatment from the XRA phase.

The nature of S-peaks is still not yet fully understood. They occur specifically in Li^+-containing electrolyte solutions; that is, they are not produced by larger cations, such as K^+.[20] Phenomenologically, their incidence correlates with the presence of “amorphous” titania, both in Pluronic-templated materials[20] and in the hydrothermally grown nanostructures, presented here (cf. Figure 6). On the other hand, the perfect reproducibility of the position of S-peaks (among a wide selection of materials, including the Pluronic-templated ones[20]) points at a process involving well-defined structural conditions. This is difficult to reconcile with the presence of a poorly defined “amorphous” titania. S-peaks rather indicate a distinguished nanophase whose structure is regular and defined, albeit not X-ray detectable. (Note that the “truly amorphous” titania does not show the S-peaks, but just a broad envelope of features at similar potentials.[20])

On the basis of the data collected in this work, we propose that the S-peaks are caused by the interaction of Li^+ ions with titania nanosheets. The nanosheets are formed via exfoliation of layered protonic titanates, and during calcination, they are converted to a nonstoichiometric TiO_2, preserving the sheet morphology. The nanosheets may even show the anatase-like ordering, oriented along the *c*-axis.[39,40] Analogously, the calcination of lepidocrocite-like titania leads to anatase-like sheets oriented along the *c*-axis.[56] The parent protonic titanates, such as $H_2Ti_3O_7$ and $H_2Ti_4O_9$, are semiconductors, whose band gap energy is larger by ca. 0.1 eV compared to that of anatase.[57] (Note, however, a reference for the opposite statement, too.[41]) Also the lepidocrocite-like titania shows slightly larger band gap energy (3.24 eV), which increases however significantly upon exfoliation into individual nanosheets.[46,58] Recent theoretical calculations further confirmed that such a two-dimensional titania shows larger band gap energy than anatase.[59]

The increase of band gap energy, ΔE_g in ultrasmall crystallites[60] or ultrathin layers[58,59] of TiO_2, has been attributed to the quantum-size effect:

$$\Delta E_{\mathrm{g}} = \frac{h^2}{8\mu_{xy}}\left(\frac{1}{{L_x}^2} + \frac{1}{{L_y}^2}\right) + \frac{h^2}{8\mu_z {L_z}^2} \tag{4}$$

where h is the Planck constant, μ designates the reduced effective masses of the excitons, and L corresponds to the crystal dimension. The subscripts x and y denote coordinates parallel to the layer, and z is perpendicular to the layer. Since $L_z \ll L_x$, L_y, the first term in eq 4 can be neglected for a nanosheet. The blue shift of ΔE_g in ca. 1−2-nm-sized anatase crystals is accompanied by a negative shift of the flatband potential by ca. 0.2 V.[60] We may note that the cathodic S-peaks are negatively shifted by nearly the same potential difference compared to the cathodic A-peak (Figure 4). Consequently, the nanosheets are idle at the potential of Li^+ insertion into anatase, and they start to accommodate Li^+ only below their flatband potential. We may even rationalize why the S-peaks occur in two pairs, if we accept the notion that the nanosheets have (101) or (001) orientations[40] and that the different faces of anatase can have different flatband potentials.[8] In fact, we have shown that the flatband potentials of (101) and (001) faces differ by 0.06 V and the ability of accommodating Li^+ is also different.[8] (Note that the separation of S-peak is 0.07 V, which is close to the mentioned separation for the two anatase faces.) The nature of Li^+/nanosheet interaction is unknown, but we may note that a nanosheet composed from edge-sharing TiO_6 octahedra[35,42−44,54,58,61] contains two types of oxygen atoms: those which are shared by the neighboring octahedra and those which belong to a single octahedron on the topmost position on the surface (Scheme 1). These topmost oxygens are ca. 0.15 nm above the surface layer composed of Ti atoms and shared oxygens.[45]

Scheme 1. Cross-sectional View on the Titania Nanosheet Composed from Edge-Sharing TiO_6 Octahedra[a]

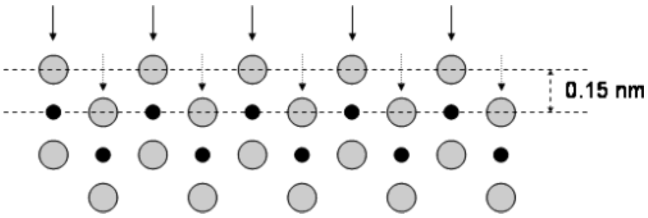

[a] The oxygen atoms at the topmost corner positions are marked by full arrows and oxygen atoms at the edge-sharing positions are marked by dashed arrows. The small full points stand for Ti atoms.

It is tempting to suggest that these two oxygen sites are responsible for the double-peak structure of S-peaks. Recently, Wagemaker et al.[19] have demonstrated two distinct positions in a network of TiO_6 octahedra, where Li may be accommodated. This provides another rational for the doublet structure of the S-peaks.

The pseudocapacitive behavior of S-peaks is readily explained in terms of the interaction taking place on the nanosheet surface. The nanosheet is composed of just two planes of edge-sharing TiO_6 octahedra (cf. Scheme 1), which are either kinked (monoclinic structures) or perfectly flat (lepidocrocite-like structures).[35,42−45,49,57,58,61] Hence, the compensation of electronic charge, injected into the conduction band, does not require any solid-state transport of Li^+ cations. This hypothesis may apply both for the flat nanosheets as well as for the curved ones, and, eventually, for the nanotubes with spiral-like rolling. These structures are

---

(56) Fukuda, K.; Sasaki, T.; Watanabe, T.; Nakai, I.; Inaba, K.; Omote, K. *Cryst. Growth Des.* **2003**, *3*, 281−283.

(57) Kim, Y. I.; Atherton, S. J.; Brigham, E. S.; Mallouk, T. E. *J. Phys. Chem.* **1993**, *97*, 11802−11810.

(58) Sasaki, T.; Watanabe, M. *J. Phys. Chem. B* **1997**, *101*, 10159−10161.

(59) Sato, H.; Ono, K.; Sasaki, T.; Yamagishi, A. *J. Phys. Chem. B* **2003**, *107*, 9824−9828.

(60) Kavan, L.; Stoto, T.; Grätzel, M.; Fitzmaurice, D.; Shklover, V. *J. Phys. Chem.* **1993**, *97*, 9493−9498.

(61) Sasaki, T.; Watanabe, M.; Michiue, Z.; Komatsu, Z.; Izumi, F.; Takenouchi, S. *Chem. Mater.* **1995**, *7*, 1001−1007.

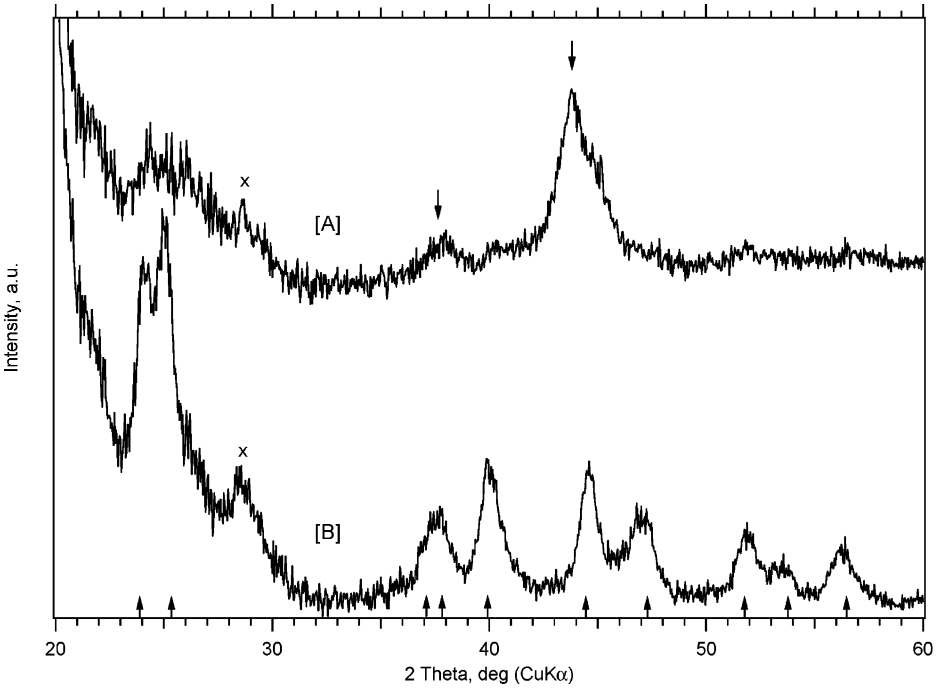

Figure 9. X-ray diffraction pattern of materials after reaction with *n*-butyllithium: [A] sample Lor-035-094b (150 m^2/g, XRA = 91%, anatase only seen by XRD and Raman); [B] nanocrystalline anatase Bayer PKP09040 (154 m^2/g, XRA ≅ 0, anatase only seen by XRD and Raman). The signal of Kapton foil is marked by ×. The diffraction lines of orthorhombic $Li_{0.5}TiO_2$ are marked by upward-directing arrows and the lines of cubic $LiTiO_2$ are marked by downward-directing arrows.

open; hence, their surface is accessible for electrochemical reactions. This raises the question whether similar nanosheets occur also in the Pluronic-templated materials (exhibiting S-peaks),[20] despite explicit differences in the synthetic protocol of these materials.[20,62−65] The Pluronic-templated TiO_2 contains, reportedly, anatase nanocrystals embedded in "amorphous" titania, whose structure was not specified.[20,62−65] The assembly is mesoporous with either a 2-D hexagonal (*p*6*m*) or a 3-D cubic (*Im*3*m*) arrangement.[63] However, Stucky et al.[65] have recently reported an additional structure designated as *lamellar titania*, which may grow in Pluronic-templated materials at larger concentrations of Pluronic polymer. It appears therefore that the S-peaks observed in ref 20 with the Pluronic-templated materials arise from a lamellar form of titania and not an amorphous one as originally suggested by us.[20] The present study clearly shows that the appearance of the characteristic feature of the S-double peaks in the cyclic voltammogram can be used as a diagnostic tool for the presence of such sheetlike titania nanostructures.

The specific nature of our materials is also demonstrated by their chemical reaction with *n*-butyllithium. This reagent is known to mimic the electrochemical Li insertion, corresponding to a potential of ca. 1 V vs Li/Li^+ electrode.[15] Figure 9 shows that the ordinary nanocrystalline anatase (Bayer PKP09040) is converted to an orthorhombic lithium titanate $Li_{0.5}TiO_2$, in agreement with previously published data.[13,15] (A quantitative conversion into this sole product was traced even for the ratio Li/Ti = 0.7.[15]) At the same conditions, our materials with high XRA content produce upon chemical lithiation another phase, which can be indexed as cubic lithium titanate $LiTiO_2$.

We have usually observed mixtures of both phases (orthorhombic and cubic) after the treatment with *n*-butyllithium. However, the materials exhibiting large S-peaks (large XRA content) showed also larger proportion of the cubic titanate. An explicit example is the material Lor-035-094b (150 m^2/g, XRA = 91%, anatase only seen by XRD and Raman), which gave almost pure cubic lithium titanate $LiTiO_2$ after the reaction with *n*-butyllithium (Figure 9). Apparently, the nanosheets are easily accessible to chemical reduction, yielding a Li-rich product under the conditions, when bulk anatase gives only the orthorhombic lithium titanate $Li_{0.5}TiO_2$. Note that this conclusion agrees with the electrochemically determined Li-storage capacities, exceeding 600 C/g ($x \cong 0.5$), vide ultra.

In summary, TiO_2 exhibiting S-peaks is a promising charge storage material. It accommodates Li^+ by three different mechanisms: (1) Li insertion into the anatase lattice (with subsequent reversible conversion to orthorhombic titanate), (2) double-layer charging, and (3) the surface-confined charge storage specific for certain "amorphous" titania, which was identified here as interaction with titania nanosheets. While the mechanisms (1, 2) are ubiquitous in all Li-insertion hosts, the mechanism (3) is a specific property of special TiO_2 materials only. The double-layer charging (effect 2) is omnipresent at all potentials below the flatband potential. On the other hand, the effects (1) and (3) occur at well-distinguished potentials. This offers another spe-

---

(62) Yang, P.; Zhao, D.; Margolese, D. I.; Chmelka, B. F.; Stucky, G. D. *Chem. Mater.* **1999**, *11*, 2813−2826.

(63) Crepaldi, E. L.; Soler-Illia, G. J. A. A.; Grosso, D.; Cagnol, F.; Ribot, F.; Sanchez, C. *J. Am. Chem. Soc.* **2003**, *125*, 9770−9786.

(64) Yang, P.; Zhao, D.; Margolese, D. I.; Chmelka, B. F.; Stucky, G. D. *Nature* **1998**, *396*, 152−155.

(65) Alberius, P. C. A.; Frindell, K. L.; Hayward, R. C.; Kramer, E. J.; Stucky, G. D.; Chmelka, B. F. *Chem. Mater.* **2002**, *14*, 3284−3294.

cific application of our materials: Depending on the applied potential window, the material behaves either as a Li-insertion host (between ca. 1.7 and 2.1 V) or as a pure supercapacitor (between ca. 1.3 and 1.7 V). Figures 4 and 6 evidence that the ratio of charge of supercapacitor/Li insertion can vary in a broad range from 0 to ca. 2.3. These two different charging regimes may find application in special energy storage devices. Larger Li-storage capacity, up to ca. 800 C/g, and faster kinetics of Li charging are other explicit advantages of these materials.

Acknowledgment. This work was supported by NTera Ltd., the Swiss CTI Top Nano-21 program (Contract No. 5775.1), the EC-COST Action D14/0002/99, and the Grant Agency of the Czech Republic (Contract No. 203/03/0824). We are grateful to Prof. Joop Schoonman (Delft University of Technology) for reading the manuscript and helpful comments.

Supporting Information Available: Survey of the tested SusTech materials (PDF). This material is available free of charge via the Internet at http://pubs.acs.org.

CM035046G

Lithium Storage in Nanostructured TiO_2 Made by Hydrothermal Growth by Kavan et al**.**

SUPPORTING INFORMATION Survey of the tested SusTech materials

Sample No.	Sample code (SusTech)	BET area (m^2/g)	XRA phase wt%	phase comp.[*]	Notes
1	Lor-035-024d	20	<1	A+B	
2	Lor-035-094b	150	91	A	
3	Lor-035-097a	38	11	A	
4	Lor-035-090d	34	8	A	
5	Lor-035-0981c	57	17	A	
6	Lor-035-071a	135	71	A	
7	Lor-035-118	79	53	A	
8	Lor-035-119A	85	19	A	
9	Lor-035-119B	105	38	A	
10	Lor-035-119C	144	46	A	
11	Lor-035-191	300	0?	A	250 nm nanotubes, i/o ∅ 8/15 nm
12	Lor-035-112B		>95	A?	amorph.; Zr^{4+} doped
13	Lor-035-098d	112	43	A	
14	Lor-035-098A	33	45	A	
15	Lor-035-090B	43	38	A	
16	Lor-035-098b	54	3	A	
17	Lor-035-103B		47	A+R	
18	Lor-035-103C	42.6	51	A+R+B?	B detectable by Raman only
19	Lor-035-092B	130	65	A	
20	Lor-035-099D		48	A+R	
21	Lor-035-099C		33	A	
22	Lor-035-088A		12	A	
23	Lor-035-092A	67	80	A+R+B	B detectable by Raman only
24	Lor-035-088B	59	9	A	
25	Lor-035-088C		17	A+B	B detectable by Raman only
26	Lor-035-099A	53	48	A+R+B	
27	Lor-035-112B2		32	A+R+B	
28	Lor-035-098c	64	<1	A	
29	Lor-035-112A2		<1	A	
30	Lor-035-097b	45	<1	A	
31	Lor-035-092D		56	A+B	B detectable by Raman only
32	Lor-035-097d	47	<1	A	
33	Lor-035-013B	18	>95	A?	XRD peak @ 11 deg (titanate?)
34	Lor-035-013B	18	>95	A+ monocl.	Calcined at 400 °C for 7 hours; traces of monoclinic TiO_2 ?

[*] A=anatase, R=rutile, B=brookite. Determined by XRD and Raman spectroscopy.

Journal of The Electrochemical Society, **151** (8) A1301-A1307 (2004)
0013-4651/2004/151(8)/A1301/7/$7.00 © The Electrochemical Society, Inc.

Lithium Insertion into Anatase Inverse Opal

Ladislav Kavan,[a,b,*,z] Markéta Zukalová,[a] Martin Kalbáč,[a] and Michael Graetzel[b]

[a]*J. Heyrovský Institute of Physical Chemistry, Academy of Sciences of the Czech Republic,*
CZ-18223 Prague 8, Czech Republic
[b]*Laboratory of Photonics and Interfaces, Swiss Federal Institute of Technology, EPFL, Ecublens,*
CH-1015 Lausanne, Switzerland

Anatase inverse opal was prepared either in the form of powder or thin layers via templating with polystyrene latex spheres. The four different methods employed for the TiO_2 deposition were anodic oxidative hydrolysis of $TiCl_3$, liquid-phase deposition from $(NH_4)_2TiF_6$ solution, and deposition from titanium(IV) isopropoxide either in the vapor phase or in propanolic solution. Electrochemical preparation from $TiCl_3$ gave the best results. The pores were narrower by *ca.* 30% compared to the nominal size of latex spheres, as documented by scanning electron microscopy and by the position of the stop band in the optical spectrum. The anatase inverse opals exhibit sluggish electrochemical performance for Li-insertion compared to nontemplated anatase with more dense packing of nanocrystals. This is due to poor electrical contacts between the particles in the nanocrystalline network. The limited number of necking points for charge transport is documented by transmission electron microscopy images. Cyclic voltammograms of Li-insertion showed two pair of extra peaks (S peaks) with formal potentials of 1.5 and 1.6 V, respectively, for both templated and nontemplated electrodeposits. The S peaks were absent in the opals prepared by the remaining three synthetic methods.
[DOI: 10.1149/1.1769273]

Manuscript received November 6, 2003. Available electronically July 20, 2004.

Silica and titania belong to the most attractive materials considered for fabrication of photonic crystals.[1,2] In the first case, the natural opal has an appealing pattern of monodisperse submicrometer SiO_2 spheres in an air matrix, whereas in the second case the inverse opal, *i.e.*, air spheres in TiO_2 matrix were demonstrated as a promising model for photonic bandgap materials.[3,4] Anatase TiO_2 is favored for this application by high refractive index and good transparency for the visible light. Recently, Mallouk *et al.*[5] have applied the anatase inverse opal for the dye-sensitized solar cell (Grätzel cell). The photoanode of this cell was prepared by sandwiching a layer of anatase inverse opal between the conducting glass electrode and the second layer of nonordered anatase nanocrystals. By tailoring of the stop band position, this assembly could improve the photocurrent efficiency by 26% due to localizing of the red part of the solar spectrum in the composite structure.[5]

Optimization of optical properties of the photoanode of the dye-sensitized solar cell should be linked to the optimization of electrical and electrochemical properties of the same electrode. To address these issues, electrochemical properties of anatase inverse opal in the dark may bring additional information. This can, in principle, be carried out only below the potential of the flatband, while the lithium insertion electrochemistry is a suitable tool of choice. Apparently, the heterogeneous charge-transfer proceeds at similar conditions in both processes; the electrons are either injected from the back contact and compensated with Li^+ ions transported from the electrolyte/anatase interface (Li-insertion) or the electrons are injected from the photoexcited dye at the anatase/electrolyte interface, and collected on the back contact (dye-sensitized solar cell). In both cases, the charge transport in the anatase skeleton plays a role, controlling the overall efficiency of both processes.

The Li insertion can monitor tiny structural aspects of anatase electrodes, ranging from the macroscopic single crystal[6,7] to nanocrystalline ones.[8-16] Most previous reports have dealt with statistically packed nanocrystals with uncontrolled particle structure and mesoscopic ordering.[9,11-16] Two exceptions to this rule are studies of Li-insertion into anatase nanotubes[17] and into highly organized mesoscopic skeleton of Pluronic-templated anatase.[10] In the latter case, the Li-insertion electrochemistry revealed exceptional features (S peaks), which do not seem to be addressable by the usual methods, such as X-ray diffraction and Raman spectroscopy.[10] The insertion/extraction of Li to/from the TiO_2 lattice is described by the equation

$$TiO_2 + x(Li^+ + e^-) \rightarrow Li_xTiO_2 \qquad [1]$$

The most active form of TiO_2 for Reaction 1 is anatase, in which the insertion coefficient, x is usually close to 0.5.[8,9,11,13,18] The same process in anatase inverse opal is worth exploring for possible applications both in Li-ion batteries and for optimization of photoanodes of solar cells. This was the motivation for the present study.

Experimental

Materials and electrodes.—Thin-film electrodes were fabricated with the aid of a latex template film on conducting glass electrode (F-doped SnO_2, TEC 8 from Libbey-Owens-Ford, 8 $\Omega/\square$). The conducting glass was cleaned by sonication in methanol, water, and finally by the ozone UV cleaner (Jelight Co., Inc.). The layer of latex template was grown by evaporation according to Ref. 5 as follows: aqueous suspension (0.1 wt %) of monodisperse, carboxylate-modified polystyrene latex spheres (Seradyn Co.) was sonicated for 30 min. The latex film was grown on vertically positioned conductive glass by complete evaporation of this suspension at 60°C for 2 days. The template layer was reasonably uniform, *ca.* 3 μm thick (alpha-step profilometer, Tencor Instruments). Figure 1 shows the UV-vis absorption spectra of two different films made from latex spheres of diameters 243 and 250 nm, respectively. The first template (243 nm spheres) was further used for the preparation of all inverse opal layers reported in this paper (except for the powder of inverse opal reported below).

The voids in the opal template layer on the conducting glass were filled by three different methods (electrodeposition, liquid-phase deposition, and vapor-phase deposition) as specified below. Finally the latex template was removed by calcination at 450°C for 30 min. The three methods of titania deposition in the voids of latex template were as follows: (*i*) electrochemical deposition from 50 mM aqueous solution of $TiCl_3$, pH 2.4 by galvanostatic oxidation at 10 $\mu A/cm^2$ for 10 h.[19] (*ii*) Liquid-phase deposition from a mixture of 0.2 M $(NH_4)_2TiF_6$ + 0.3 M H_3BO_3, pH 3, adjusted by HCl. The solutions of $(NH_4)_2TiF_6$ and H_3BO_3 were prepared separately and mixed only before application. The reaction was carried out at 60°C during 30 min.[5,20,21] (*iii*) Deposition from a vapor phase; the glass-supported template layer was exposed to a vapor of titanium(IV) tetraisopropoxide at 100°C for 10 min.[22] Also for methods 1 and 2, blank (nontemplated) layers were prepared. The synthetic protocol was identical, except that the layer was deposited on bare conducting glass without any latex template.

The inverse opal powder was prepared according to a modified protocol pioneered in Ref. 3, 4. The solution of latex particles in

---

[*] Electrochemical Society Active Member.
[z] E-mail: kavan@jh-inst.cas.cz

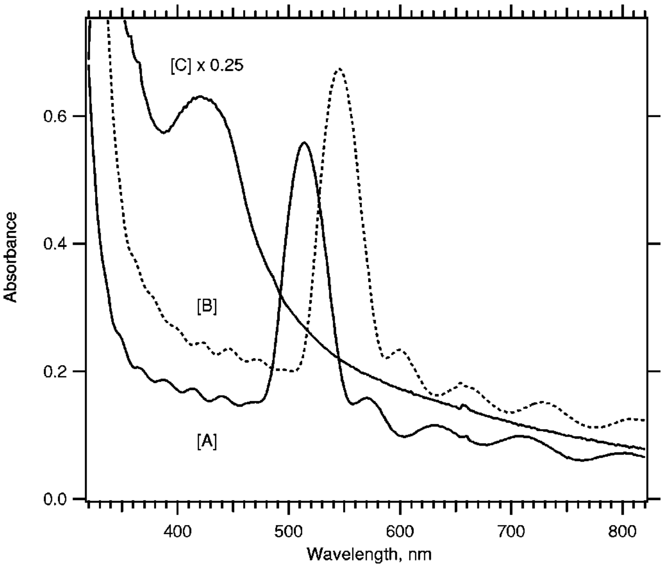

Figure 1. Absorption UV-vis spectra of layers deposited on conducting glass. [A] (solid line) latex polystyrene film (243 nm spheres). [B] (dashed line) latex polystyrene film (250 nm spheres). [C] (solid line) anatase inverse opal grown via electrodeposition in the 243 nm latex film. The absorbance scale is multiplied by a factor of 0.25 for spectrum [C].

water (4.5 vol %, 500 nm in diameter, provided by MPICI Golm, Germany) was centrifuged at 4000 rpm for 26 h. After drying at ambient temperature, 1 g of the template was disintegrated into lumps and soaked with 2-propanol. Subsequently 20 mL of titanium(IV) isopropoxide was added drop wise and the mixture filtered on a Buechner funnel. The composite was dried in air and then under vacuum at room temperature for 7 h and annealed at 575°C for 2.5 h under air flow (heating rate 5°C/min). The final product was a flakey powder with a typical opal-like iridescence. Electrodes were prepared as follows: 0.3 g of the powder were mixed under the slow addition of 4 × 0.15 mL of 10% aqueous solution of acetylacetone, 0.3 mL of 4% aqueous solution of hydroxypropylcellulose (Mw 100,000) and 0.3 mL of 10% aqueous solution of Triton-X100. The obtained slurry was deposited on a sheet of conducting glass using a doctor-blading technique.[18] The film was finally calcined for 30 min in air at 450°C. Pluronic P-123 was obtained from BASF and anatase powder (50.1 m^2/g) was from Alpha. Other chemicals were from Aldrich or Fluka, and were used as received.

Methods.—UV-vis spectra were measured on Hewlett-Packard 8450 diode array spectrometer. The Brunauer-Emmett-Teller (BET) surface areas were determined from nitrogen adsorption isotherms at 77 K (ASAP 2010, Micromeritics). Scanning electron microscopy (SEM) images were obtained by Hitachi S-4700 apparatus. The glass-supported layers were inspected both in surface and cross-sectional views, in the latter case the sample was cut mechanically. Transmission electron microscopy (TEM) images were obtained on Tecnai F30 microscope with 300 keV field emission electron gun. Powder X-ray diffractometry (XRD) was studied on a Siemens D-5000 diffractometer using Cu Kα radiation. Electrochemical measurements were carried out in the one-compartment cell using an Autolab Pgstat-30 (Ecochemie) controlled by GPES-4 software. The reference and auxiliary electrodes were from Li metal, hence potentials are referred to the Li/Li^+ (1 M) reference electrode. $LiN(CF_3SO_2)_2$ (Fluorad HQ 115 from 3M) was dried at 130°C/1 mPa. Ethylene carbonate (EC) and 1,2-dimethoxyethane (DME) were dried over the 4 Å molecular sieve (Union Carbide). The electrolyte solution, 1 M $LiN(CF_3SO_2)_2$ + EC/DME (1/1 by mass) contained 10-15 ppm H_2O as determined by Karl Fischer titration (Metrohm 684 coulometer). All operations were carried in a glove box under argon (containing typically 1-5 ppm of O_2 and H_2O).

Results and Discussion

The latex template deposited on conducting glass exhibited well-developed stop bands in addition to the ordinary interference fringes of the thin film (Fig. 1).[5,20,23] The thickness of the latex layer (δ) can be calculated from the number of interference fringes, k occurring between the wavelengths λ_1 and λ_k[24]

$$\delta = \frac{k\lambda_1\lambda_k}{2n_{\text{eff}}(\lambda_1 - \lambda_k)} \qquad [2]$$

where n_{eff} is the effective refractive index of the two-phase medium, *i.e.*, air and polystyrene (with refractive indices n_{air} and n_{p}, respectively)[24]

$$n_{\text{eff}} = [(1 - f)n_{\text{air}}^2 + fn_{\text{p}}^2]^{1/2} \qquad [3]$$

f is the fraction of volume filling, *i.e.*, 0.74 assuming close packing of spheres. The calculation gives (for $n_{\text{p}} = 1.6$) the thickness δ equal to 2.7 μm, which is close to the value determined by alpha-step profilometry (3 μm) and to the thicknesses reported by other authors for the same fabrication procedure.[5] The diameter of polystyrene spheres (D) controls the position of the stop band (λ_{p}). For a normal incidence of light and the (111) reflection of the fcc structure, this dependence is as follows[20]

$$\lambda_{\text{p}} = 1.633Dn_{\text{eff}} \qquad [4]$$

Figure 1 and Eq. (4) give the diameter of latex spheres in the template films 215 and 230 nm. Shrinkage occurs already after drying of the latex template; Mallouk *et al.*[5] reported that the 243 nm spheres shrink to 215 nm after drying, which matches our results perfectly. (Note, however, some mismatch between Ref. 5 and the cross-cited Ref. 20.)

Titania replicas of this template film were fabricated by three different deposition methods (see the Experimental section). The absorption spectra of titania inverse opals were free from interference fringes, the stop band was superimposed on a light-scattering background (cf. plot [C] in Fig. 1) and was between 420-480 nm for all samples. The spectra were comparable to those, reported by other authors for analogous synthetic procedure (with the stop bands at *ca.* 450-486 nm).[5] Our stop band at 420-480 nm (cf. Fig. 1) translates into the diameter of pores in the anatase framework of 170-200 nm (Eq. 4; $n_{\text{eff}} \cong 1.5$).[20]

Figures 2A and B depict the morphology of inverse opal powder made by filling of the voids in a latex template from a propanolic solution of Ti(IV) isopropoxide. SEM images of the actual electrode film proved no significant mechanical damage of the porous powder during deposition on conducting glass (see the Experimental section). The diameter of pores is *ca.* 350 nm, which is smaller by *ca.* 30% compared to diameters of pristine latex spheres (500 nm). The TEM pattern (Fig. 2B) demonstrates that the skeleton of inverse opal is built from nanocrystals, *ca.* 10-20 nm in size. An X-ray diffractogram of the powder inverse opal can be indexed as a pure anatase phase. The crystallite size (coherent length of the crystal lattice) was approximated from the X-ray line width to be about 20 nm, which is in remarkable accord with the TEM images (Fig. 2B). The other inverse opals were prepared only in the form of micrometer-thick films, which are difficult to analyze by conventional X-ray diffraction (XRD). However, anatase seems to be the single phase present in all materials discussed in this work. Also the electrochemical tests (*vide infra*) do not reveal rutile or any other phases beyond anatase.

Typical morphology of thin films of inverse opal is demonstrated on Fig. 2C. The layers made by liquid or vapor-phase depositions (preparative methods *ii* or *iii*, see the Experimental section) do not show any ordering in the SEM surface view (Fig. 2C, left panel). Apparently, the growth of titania outside the voids of the latex

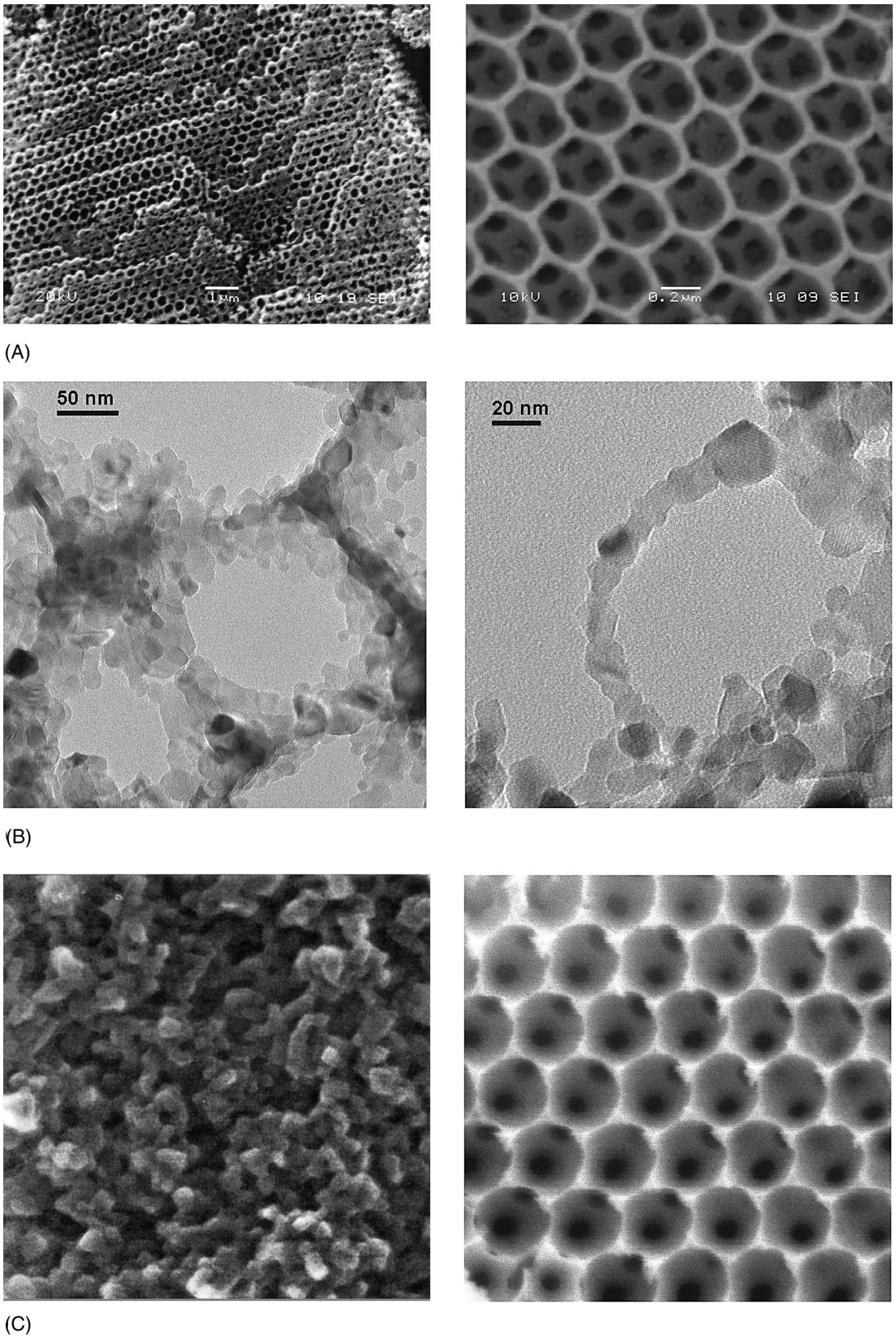

Figure 2. (A) SEM pictures of the inverse opal powder made from a propanolic solution of titanium(IV) tetraisopropoxide. (B) TEM pictures of the inverse opal powder made from a propanolic solution of titanium(IV) tetraisopropoxide. (C) Left panel: SEM picture of the inverse opal layer made by liquid-phase deposition from $(NH_4)_2TiF_6$, surface view, picture size 215×215 nm^2; right panel: SEM picture of the inverse opal layer made by electrodeposition from $TiCl_3$ solution, cross-sectional view, picture size 1073×1073 nm^2.

template is difficult to prevent during the liquid[20] or vapor phase deposition. Nevertheless, these layers are opal-ordered in the bulk, as demonstrated by their cross-sectional SEM views (cf. also Ref. 5, 20).

The best opal-ordering was observed in the layers made by electrodeposition (Fig. 2C, right panel). The diameter of pores is *ca.* 180 nm (Fig. 2C, right panel), which is again by *ca.* 30% smaller than the diameter of the parent latex spheres (243 nm). The diameters, visualized by SEM, agree well with the diameters calculated from the position of the stop band (170-190 nm, see above).

Figure 3 shows cyclic voltammograms of the studied materials. Chart A is for a blank layer made by template-free electrodeposition from the $TiCl_3$ solution. At the used deposition conditions (50 mM $TiCl_3$, pH 2.4, galvanostatic deposition 10 μA/cm^2, 10 h) the passed charge (0.36 C/cm^2) translates into the specific mass, $m = 0.148$ mg/cm^2 of TiO_2, which grew by anodic oxidative hydrolysis of $TiCl_3$[19]

$$Ti^{3+} + H_2O \rightarrow TiOH^{2+} + H^+ \qquad [5]$$

$$TiOH^{2+} + H_2O - e^- \rightarrow TiO_2 + 3H^+ \qquad [6]$$

The TiO_2 layer thickness, measured by alpha-step profilometer,

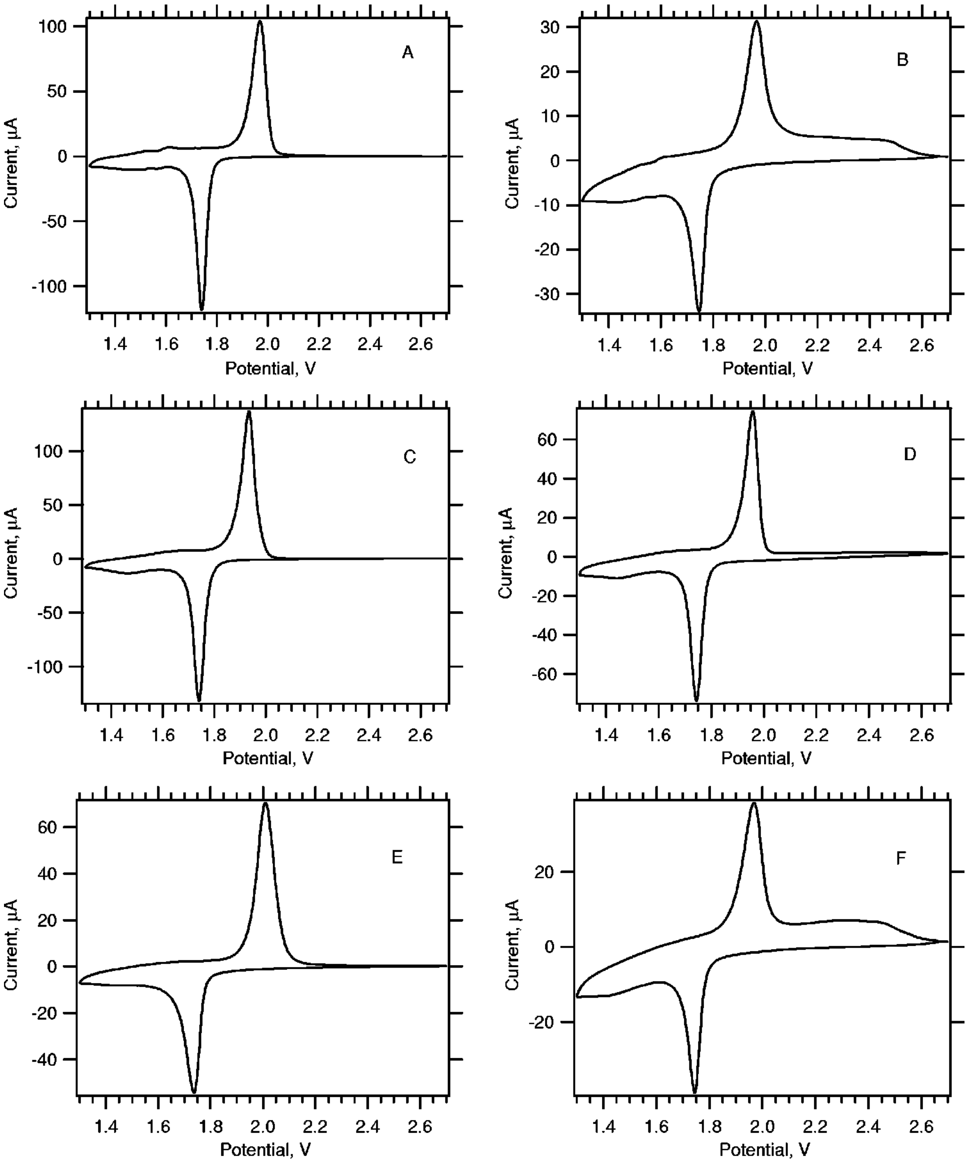

Figure 3. Cyclic voltammograms of Li insertion into the prepared materials. Electrolyte solution: 1 M $LiN(CF_3SO_2)_2$ + EC/DME (1:1 by mass); scan rate 0.1 mV/s. (A) Layer made by electrodeposition from $TiCl_3$ (10 μA/cm^2, 10 h, pH 2.4) nontemplated, (B) the same as (A) but templated as inverse opal. (C) Layer made by liquid-phase deposition from hexafluorotitanate (nontemplated), (D) the same as (C) but templated as inverse opal, (E) Inverse opal made from a solution of titanium(IV) tetraisopropoxide (powder precursor) (F). Inverse opal made by vapor deposition of titanium(IV) tetraisopropoxide.

was 0.6 μm. The porosity, *p* (defined as the volume of pores referred to a total electrode volume) scales with a layer thickness δ

$$p = 1 - V_{\mathrm{anatase}}/V_{\mathrm{total}} = 1 - m/\delta\rho_{\mathrm{A}} \qquad [7]$$

For the density of anatase $\rho_A = 3.89$ g/cm^3, the nontemplated electrodeposited layer (as in plot A) had a porosity of 36%. This value is larger, compared to the porosity of layers grown in the potentiostatic regime.[19] In the latter case, the electrodeposition was reported to be faster by *ca.* one order of magnitude (currents about 100 μA/cm^2).[19] The potentiostatic deposition produced layers of densely packed ultrasmall (*Q*-sized) crystallites.[25] However, such a fast deposition cannot be carried out on a template-covered glass, since the current above *ca.* 30 μA/cm^2 (for the projected electrode area) would require too high overvoltages.

The integral anodic voltammetric charge for Li extraction of the electrode in Fig. 3, plot A was 103 mC/cm^2 at 0.1 mV/s, which gave the lithium insertion coefficient $x = 0.57$ assuming the mass of TiO_2 equal to 0.148 mg/cm^2 (Eq. 1). A comparable Li-insertion voltammogram of the layer of electrodeposited inverse opal is shown on chart B, Fig. 3. The conditions for TiO_2 growth were identical (50 mM $TiCl_3$, pH 2.4, galvanostatic deposition 10 μA/cm^2, 10 h). In this case, the layer thickness was less uniform than in the reference nontemplated layer (plot A) and varied between *ca.* 1.5 to 2 μm as measured by alpha-step profilometer. Assuming the same electrodeposited mass (0.148 mg/cm^2) the corresponding porosity is 75 to 81% (Eq. 7) which agrees reasonably well with the theoretical value for a close packing of pores in TiO_2 matrix (74%). However, the reversible integral voltammetric charge of Li insertion was only 70 mC/cm^2 ($x = 0.39$) at 0.1 mV/s, which was considerably less than for the nontemplated layer (chart A). The voltammogram of inverse opal has an unusual shape pointing at a larger iR drop in the layer. There is also some residual anodic charge, which is extracted only at larger overvoltages, above *ca.* 2.1 V *vs.* Li/Li$^+$, when the ordinary (nontemplated) layer is already free from any lithium (cf. plot A).

The layers made by liquid-phase deposition do not allow for a similar quantitative analysis. The reason is that the TiO_2 layer grows from a homogeneous medium by consecutive hydrolysis[21]

$$TiF_6^{2-} + nH_2O \rightarrow [TiF_{6-n}(OH)_n]^{2-} + nHF \qquad [8]$$

where the produced HF is quenched by H_3BO_3

$$4HF + H_3BO_3 \rightarrow HBF_4 + 3H_2O \qquad [9]$$

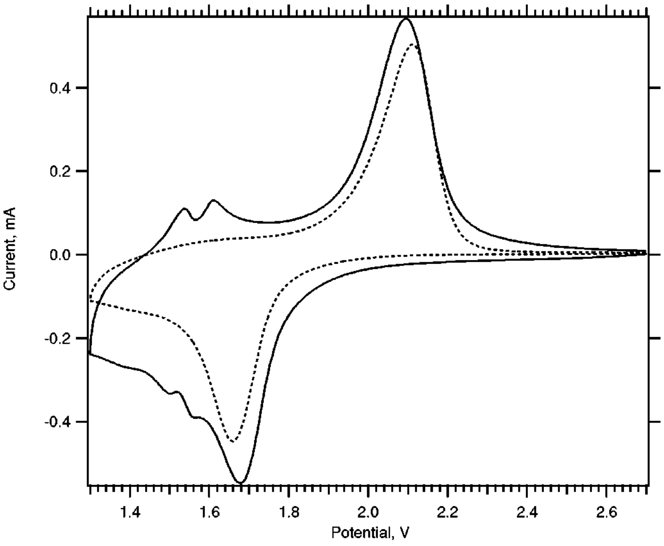

Figure 4. Cyclic voltammogram of inverse opal made by electrodeposition (solid line) and inverse opal made by liquid-phase deposition (dashed line). Electrolyte solution: 1 M $LiN(CF_3SO_2)_2$ + EC/DME (1:1 by mass); scan rate 2 mV/s.

Apparently, the titania formation occurs in a bulk of supersaturated medium, while the reaction rate is influenced by temperature, time, and concentration of reactants. Hence, the amount of deposited titania inside the voids of the latex template is less defined compared to the electrodeposition, where the TiO_2 films grow only at the electrode/electrolyte interface and the deposition rate is controlled by pH and by the passed charge (Eq. 5 and 6).[19,25] The voltammograms of Li-insertion on nontemplated and templated layers made by liquid-phase deposition are shown in Fig. 3, charts C and D, respectively. Qualitatively, we see a similar tendency, *i.e.*, hindered Li-insertion into the templated layer. The blocking of Li-insertion is here less expressed, which may be due to casual deposition of nonordered anatase crystallites on top of the latex film from the reaction mixture (Eq. 8 and 9, cf. Fig. 2C). These crystallites improve the packing and electrical contacts inside the layer, which is, however, made from less perfect inverse opal.

Sluggish Li-insertion is apparent also for inverse opals made by vapor deposition (chart F), although the corresponding nontemplated layers are not available for comparison. The same applies also for the inverse opal powder, made by the soaking of the template with the propanolic solution of Ti(IV) isopropoxide (Fig. 3, plot E). However, in the latter case, the electrode is made of statistically arranged porous microcrystalline particles. Even if the particles keep the inverse opal ordering (cf. Fig. 2A, B), the overall layer porosity (Eq. 6) was *ca.* 60%, *i.e.*, the layer was more dense than the ideally close-packed inverse opal ($p = 74\%$). This may explain that voltammogram E in Fig. 3 resembles those of nontemplated materials (Fig. 3A and C).

If we focus on the Li-insertion voltammograms at larger scan rates, we trace explicit differences between the materials made by electrodeposition and by liquid-phase deposition (both templated and nontemplated ones) (Fig. 4). The material made by liquid-phase deposition exhibits just one pair of insertion/extraction peaks, as it is commonly observed in many anatase electrodes.[8,9,13,18] A similar simple voltammogram was also found for materials made from Ti(IV) isopropoxide, both from propanolic solution and vapor phase (as in charts E and F, Fig. 3). The layers made by electrodeposition were exceptional by showing two additional pairs of peaks with the formal potentials of 1.5 and 1.6 V, respectively. Such peaks are reminiscent of the so-called S peaks, which were so far reported solely in the highly organized anatase layers made by supramolecular templating with Pluronic P-123.[10] In the cited paper[10] the occurrence of S peaks was tentatively ascribed to a surface-confined process specific for amorphous titania in the material.[10] The arguments for surface process were: (i) small peak-to-peak splitting of each pair of peaks and (ii) the peak current proportional to the scan rate, as it is expected for capacitive charging

$$i = \frac{dQ}{dt} = C\frac{dE}{dt} = Cv \qquad [10]$$

i is the voltammetric current density, C is interfacial capacitance, and dE/dt is the scan rate, v. The process is distinct from the diffusion-controlled Li^+ insertion into the anatase lattice, where i is assumed to scale with $v^{1/2}$ (vide infra). It is interesting to note that identical S peaks (albeit with smaller intensity) occur in our electrodeposited material in spite of a completely different synthetic route compared to the Pluronic templating. The slow galvanostatic electrodeposition is beneficial for the occurrence of S peaks, since the faster potentiostatic deposition (at 0 V *vs.* SCE, with *ca.* 10 times larger currents) produced only an unresolved envelope of features in the region of S peaks (cf. Fig. 10 in Ref. 10).

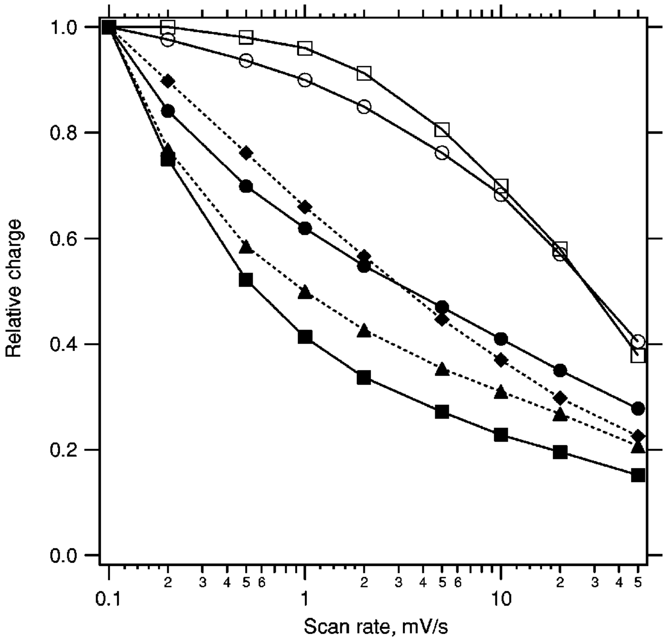

Figure 5. Integral voltammetric charge from the anodic branch of cyclic voltammograms is plotted as a function of scan rate. The charge was normalized against the charge capacity of the same electrode at the slowest scan (0.1 mV/s). Open squares: material made by electrodeposition from $TiCl_3$ (nontemplated). Solid squares: the same material, but templated as inverse opal. Open circles: material made by liquid-phase deposition from hexafluorotitanate (nontemplated). Solid circles: the same material, but templated as an inverse opal. Dashed line with diamonds: inverse opal made from a solution of titanium(IV) tetraisopropoxide (layer made from a powder precursor); dashed line with triangles: inverse opal made by vapor deposition of titanium(IV) tetraisopropoxide.

The S peaks (as in the solid line in Fig. 4) occur with comparable intensity both for templated and nontemplated electrodeposits. We have attempted to promote the S peaks by electrodeposition from an electrolyte solution containing Pluronic P-123. Typical electrolyte composition was 50 mM $TiCl_3$, 1 wt % Pluronic P-123, pH 2.4. Nevertheless, the voltammograms of the thus prepared materials were very similar to those in Fig. 4 (solid line) and the intensity of S peaks did not change markedly, even if the as-deposited layer was kept for several days of gel-aging at 50°C before calcination. (This procedure is known to be essential for producing high-quality mesoscopic materials in the course of Pluronic templating.[10,26])

Figure 5 displays the reversible voltammetric charge of Li insertion against the scan rate. As the absolute charge capacities of each testing electrode fluctuated (between *ca.* 82 to 126 mC at the scan rate of 0.1 mV/s), the data in Fig. 5 were normalized with respect to the actual charge of the same electrode at the slowest scan (0.1 mV/s) which was set as unity. Figure 5 demonstrates unequivocal differences between the templated and nontemplated materials, the former showing considerably worse performance. This is expressed both for the inverse opals made by electrodeposition and by hydrolysis of hexafluorotitanate. Dashed lines present two other inverse opals, where the corresponding nontemplated reference material was not available. They were prepared from titanium(IV) tetraisopropoxide, either by deposition from propanolic solution or from vapor phase. The markedly slower charging of inverse opals is expressed in all cases. On the other hand, the best charging rate is achieved for nontemplated electrodeposited layers. The shape of the charge/scan-rate plots (Fig. 5) is reminiscent of those of the Pluronic templated materials, where the good charging at higher scan rates was ascribed to fast capacitive charging attributed to S peaks (Eq. 8).[10]

A more quantitative insight into the Li-charging kinetics can be obtained, if we calculate the corresponding rate constants of Li insertion. Assuming that the cyclic voltammograms can be treated in terms of irreversible kinetics, the insertion peak current, I_p, scales with the heterogeneous rate constant, k_0, as follows[13]

$$I_p = 0.227nFck_0 \exp\left[\frac{-\alpha nF(E_p - E_0)}{RT}\right] \qquad [11]$$

n is the number of electrons in the rate-determining step, A is the active electrode area, c is the maximum concentration of Li^+ (or Ti^{3+}) states in the accumulation layer (0.024 mol/cm^3 for $x = 0.5$, cf. Eq. 1), E_p is the peak potential, E_0 is the formal potential which is estimated from the center between the peak potentials for the slowest scan and the other symbols have their usual meaning. For Li extraction, the exponent in Eq. 11 changes to $(1 - \alpha)nF(E_p\text{-}E_0)/RT$. The charge-transfer coefficient, α for Li insertion can be calculated from the equation

$$\alpha = 1.857\frac{RT}{nF(E_p - E_{p/2})} \qquad [12]$$

where $E_{p/2}$ is the half-peak potential. For Li extraction, the left side of Eq. 12 changes to $(1 - \alpha)$.

Figure 6 shows the corresponding plot of Li-extraction peak current *vs.* overpotential for the templated and nontemplated electrodeposited layers. If we assume that the active electrode area, A, is identical for all electrodes, the fitting of data in Fig. 6 shows that the rate constant, k_0 is smaller by a factor of about 3 for the templated inverse opal compared to the nontemplated material. The absolute values of k_0 cannot be calculated for our electrodeposits, as the value of A is unknown. Nevertheless, we can make a similar calculation for the powder-opal electrode (as in plot E, Fig. 3) assuming the area A can be here approximated by the BET surface area of the parent powder (40.1 m^2/g). A similar evaluation routine as in Fig. 6 and Eq. 11 (data not shown) gives $k_0 = 1 \cdot 10^{-10}$ cm/s for the inverse opal powder. A suitable reference material for this inverse opal is a powder anatase from Alpha, which has a comparable BET surface area of 50.1 m^2/g. This material exhibited $k_0 = 3 \cdot 10^{-10}$ cm/s, which is similar to the values reported for analogous nonorganized materials.[13,18] Hence, we have again a comparable difference between templated and nontemplated materials as in the case of electrodeposits.

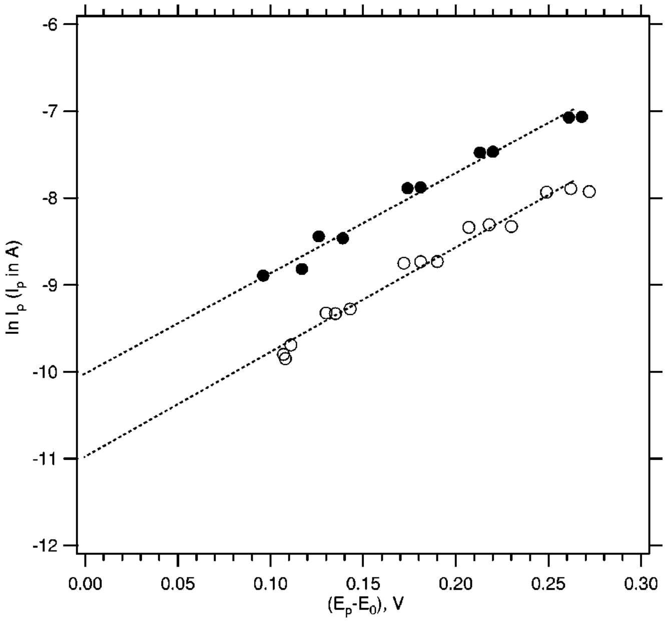

Figure 6. Voltammetric peak current, I_p for Li extraction as a function of E_p-E_0. Experimental data for two different nontemplated electrodeposits (full points) and three different templated electrodeposits. The layers were electrodeposited from $TiCl_3$ (10 μA/cm^2, 10 h, pH 2.4). Electrodes were tested in 1 M $LiN(CF_3SO_2)_2$ + EC/DME (1:1 by mass); scan rates between 5 to 0.1 mV/s.

Conclusions

The anatase inverse opals exhibit sluggish electrochemical performance for Li insertion compared to nontemplated anatase with more dense packing of nanocrystals. This is probably due to poor electrical contacts between the particles in the extremely open nanocrystalline network of the assumed porosity of 74%. The limited number of necking points for charge transport between crystals is documented in Fig. 2B. Such a problem may emerge also in other applications, if the anatase inverse opal is used as an electrode material, *e.g.*, in dye-sensitized solar cells.[5]

Acknowledgments

This work was supported by the Swiss CTI Top Nano-21 program (contract no. 5775.1), the EC-COST Action D14/0002/99 and the Grant Agency of the Czech Republic (contract no. 203/03/0824 and 203/01/0617).

J. Heyrovský Institute of Physical Chemistry assisted in meeting the publication costs of this article.

References

1. D. W. McComb, B. M. Treble, C. J. Smith, R. M. De La Rue, and N. P. Johnson, *J. Mater. Chem.*, **11**, 142 (2001).
2. Y. Xia, B. Gates, Y. Yin, and Y. Lu, *Adv. Mater. (Weinheim, Ger.)*, **12**, 693 (2002).
3. B. T. Holland, C. F. Blanford, and A. Stein, *Science*, **281**, 538 (1998).
4. J. E. G. J. Wijnhoven and W. L. Vos, *Science*, **281**, 302 (1998).
5. S. Nishimura, N. Abrams, B. A. Lewis, L. I. Halaoui, T. E. Mallouk, K. D. Benkstein, J. Van de Langemaat, and A. J. Frank, *J. Am. Chem. Soc.*, **125**, 6306 (2003).
6. L. Kavan, M. Grätzel, S. E. Gilbert, C. Klemenz, and H. J. Scheel, *J. Am. Chem. Soc.*, **118**, 6716 (1996).
7. R. Hengerer, L. Kavan, P. Krtil, and M. Grätzel, *J. Electrochem. Soc.*, **147**, 1467 (2000).
8. L. Kavan, K. Kratochvilová, and M. Grätzel, *J. Electroanal. Chem.*, **394**, 93 (1995).
9. L. Kavan, M. Grätzel, J. Rathousky, and A. Zukal, *J. Electrochem. Soc.*, **143**, 394 (1996).
10. L. Kavan, J. Rathousky, M. Grätzel, V. Shklover, and A. Zukal, *J. Phys. Chem. B*, **104**, 12012 (2000).
11. S. Y. Huang, L. Kavan, M. Grätzel, and I. Exnar, *J. Electrochem. Soc.*, **142**, 142 (1995).
12. R. Van de Krol, A. Goossens, and E. A. Meulenkamp, *J. Electrochem. Soc.*, **146**, 3150 (1999).
13. H. Lindström, S. Södergen, A. Solbrand, H. Rensmo, J. Hjelm, A. Hagfeldt, and S. E. Lindquist, *J. Phys. Chem. B*, **101**, 7717 (1997).
14. H. Lindström, S. Södergen, A. Solbrand, H. Rensmo, J. Hjelm, A. Hagfeldt, and S. E. Lindquist, *J. Phys. Chem. B*, **101**, 7710 (1997).
15. S. Lunell, A. Stashans, H. Lindström, and A. Hagfeldt, *J. Am. Chem. Soc.*, **119**, 7374 (1997).

16. R. Van de Krol, A. Goossens, and J. Schoonman, *J. Phys. Chem. B*, **103**, 7151 (1999).
17. Y. Zhou, L. Cao, F. Zhang, B. He, and H. Li, *J. Electrochem. Soc.*, **150**, A1246 (2003).
18. L. Kavan, A. Attia, F. Lenzmann, S. H. Elder, and M. Grätzel, *J. Electrochem. Soc.*, **147**, 2897 (2000).
19. L. Kavan, B. O'Regan, A. Kay, and M. Grätzel, *J. Electroanal. Chem.*, **346**, 291 (1993).
20. S. Nishimura, A. Shishido, N. Abrams, and T. E. Mallouk, *Appl. Phys. Lett.*, **81**, 4532 (2002).
21. H. Kishimoto, K. Takahama, N. Hashimoto, Y. Aoi, and S. Deki, *J. Mater. Chem.*, **8**, 2019 (1998).
22. T. Miyasaka, Y. Kijitori, T. N. Muramaki, M. Kimura, and S. Uegusa, *Chem. Lett.*, **2002**, 1250.
23. A. Richel, N. P. Johnson, and D. W. McComb, *Appl. Phys. Lett.*, **76**, 1816 (2000).
24. P. Jiang, J. F. Bertone, K. S. Hwang, and V. L. Colvin, *Chem. Mater.*, **11**, 2132 (1999).
25. L. Kavan, T. Stoto, M. Grätzel, D. Fitzmaurice, and V. Shklover, *J. Phys. Chem.*, **97**, 9493 (1993).
26. E. L. Crepaldi, G. J. A. A. Soler-Illia, D. Grosso, F. Cagnol, F. Ribot, and C. Sanchez, *J. Am. Chem. Soc.*, **125**, 9770 (2003).

Chem. Mater. **2005,** *17,* 1248−1255

Pseudocapacitive Lithium Storage in TiO_2(B)

Markéta Zukalová,[†] Martin Kalbáč,[†] Ladislav Kavan,*[,†,‡] Ivan Exnar,[§] and
Michael Graetzel[‡]

*J. Heyrovský Institute of Physical Chemistry, Academy of Sciences of the Czech Republic,
Dolejškova 3, CZ-18223 Prague 8, Czech Republic, Laboratory of Photonics and Interfaces,
EPFL, Ecublens, CH-1015 Lausanne, Switzerland, and High Power Lithium, Park Scientifique,
PSE-B, EPFL, Ecublens, CH-1015 Lausanne, Switzerland*

Received October 6, 2004. Revised Manuscript Received December 16, 2004

Phase-pure TiO_2(B) with microfibrous morphology was prepared via a newly developed method from amorphous TiO_2. Cyclic voltammetry evidences that Li-insertion into TiO_2(B) is governed by a pseudocapacitive faradaic process, whose rate is not limited by solid-state diffusion of Li^+ in a broad interval of scan rates. This unusual behavior was discussed in terms of the crystal structure of the TiO_2(B) host, having freely accessible parallel channels for Li^+-transport perpendicular to the (010) face. The characteristic Li-insertion electrochemistry of TiO_2(B) allows re-interpretation of several previous reports, which did not consider explicitly this relation or the presence of TiO_2(B) in various TiO_2 materials of different origin.

Introduction

TiO_2(B) is a metastable monoclinic modification of titanium dioxide. It was first synthesized in 1980 by Marchand et al.[1,2] from a layered titanate $K_2Ti_4O_9$ via K^+/H^+ ion exchange followed by calcination.[1−3] Some other layered titanates, namely, $Na_2Ti_3O_7$ and $Cs_2Ti_5O_{11}$, also give TiO_2(B) upon ion exchange and thermal dehydratation.[4,5] The $H_2Ti_4O_9 \cdot H_2O$ can be exfoliated into nanosheets by tetrabutylammonium cations and further converted into oriented TiO_2(B) films.[6] Alternatively, $H_2Ti_4O_9 \cdot H_2O$ can be transformed to TiO_2(B) by solvothermal treatment.[7−9] The TiO_2(B) materials prepared from $H_2Ti_xO_{2x+1}$ ($x = 3-5$) are presumably all microcrystalline, the BET surface areas being 14−30.4 m^2/g.[2,10] Nanocrystalline TiO_2(B) (crystal size 5−10 nm) was first prepared by annealing of sol−gel derived SiO_2-TiO_2 amorphous film at 900 °C.[11] TiO_2(B) was also observed during ball milling of anatase.[12,13] (Note some mismatch in the notation of TiO_2(B) and the badelleyite-type TiO_2 ($P2_1/c$ space group) in ref 12). The "β-TiO_2" (apparently TiO_2(B)) was observed in titania films made by laser deposition.[14]

TiO_2(B)[15−18] and "monoclinic TiO_2" (apparently TiO_2(B))[8] were traced during the synthesis of titania nanotubes by hydrothermal treatment of TiO_2 in NaOH medium. This subject was pioneered by Kasuga et al.[19] in 1998, albeit "bundles of fibrous units" and TiO_2(B) were found in hydrothermally treated TiO_2/NaOH much earlier, too.[20] By tuning of the temperature and concentration of NaOH, either titanate nanotubes or TiO_2(B) nanowires were synthesized selectively.[18] The structure of hydrothermally grown nanotubes has been a subject of some confusion in the past, but recent studies point at the layered titanate, $H_2Ti_3O_7$, as the main constituent of these nanotubes.[17,18,21] There was an alternative suggestion that the hydrothermally grown titanate nanotubes are composed of orthorhombic lepidocrocite-like species, $H_xTi_{2-x/4}\square_{x/4}O_4 \cdot H_2O$ ($x \approx 0.7$, $\square$ = vacancy),[22] which transforms directly to anatase by heating.[22,23] However, this work was criticized by others,[17] and the sole presence of monoclinic titanates (trititanates) seems to explain the

---

* Corresponding author. E-mail: kavan@jh-inst.cas.cz.
[†] Academy of Sciences of the Czech Republic.
[‡] Laboratory of Photonics and Interfaces.
[§] High Power Lithium.

(1) Marchand, R.; Brohan, L.; Tournoux, M. *Mater. Res. Bull.* **1980**, *15*, 1129.
(2) Tournoux, M.; Marchand, R.; Brohan, L. *Prog. Solid State Chem.* **1986**, *17*, 33.
(3) Brohan, L.; Verbaere, A.; Tournoux, M.; Demazeau, G. *Mater. Res. Bull.* **1982**, *17*, 355.
(4) Feist, T. P.; Davies, P. K. *J. Solid State Chem.* **1992**, *101*, 275.
(5) Feist, T. P.; Mocarski, S. J.; Davies, P. K.; Jacobson, A. J.; Lewandowski, J. T. *Solid State Ionics* **1988**, *28−33*, 1338.
(6) Sugimoto, W.; Terabayashi, O.; Murakami, Y.; Takasu, Y. *J. Mater. Chem.* **2002**, *12*, 3814.
(7) Yin, S.; Uchida, S.; Fujishiro, Y.; Aki, M.; Sato, H. *J. Mater. Chem.* **1999**, *9*, 1191.
(8) Yin, S.; Fujishiro, Y.; Wu, J.; Aki, M.; Sato, T. *J. Mater. Proc. Technol.* **2003**, *137*, 45.
(9) Yin, S.; Wu, J.; Aki, M.; Sato, T. *Int. J. Inorg. Mater.* **2000**, *2*, 325.
(10) Wallenberg, L. R.; Sanati, M.; Andersson, A. *Microsc. Microanal. Microstruct.* **1990**, *1*, 357.
(11) Kogure, T.; Umezawa, T.; Kotani, Y.; Matsuda, A.; Tatsumisago, M.; Minami, T. *J. Am. Ceram. Soc.* **1999**, *82*, 3248.
(12) Bose, P.; Pradhan, S. K.; Sen, S. *Mater. Chem. Phys.* **2003**, *80*, 73.
(13) Sen, S.; Ram, M. L.; Roy, S.; Sarkar, B. K. *J. Mater. Res.* **1999**, *14*, 841.
(14) Lackner, J. M.; Waldhauser, W.; Ebner, R.; Major, B.; Schoberl, T. *Surf. Coat. Technol.* **2004**, *180−181*, 585.
(15) Gao, X.; Zhu, H.; Pan, G.; Ye, S.; Lan, Y.; Wu, F.; Song, D. *J. Phys. Chem. B* **2004**, *108*, 2868.
(16) Sasaki, T.; Komatsu, Y.; Fujiki, Y. *Chem. Mater.* **1992**, *4*, 894.
(17) Suzuki, Y.; Yoshikawa, S. *J. Mater. Res.* **2004**, *19*, 982.
(18) Armstrong, A. R.; Armstrong, G.; Canales, J.; Bruce, P. G. *Angew. Chem., Int. Ed.* **2004**, *43*, 2286.
(19) Kasuga, T.; Hiramatsu, M.; Hoson, A.; Sekino, T.; Niihara, K. *Langmuir* **1998**, *14*, 3160.
(20) Nishizawa, H.; Aoki, Y. *J. Solid State Chem.* **1985**, *56*, 158.
(21) Chen, Q.; Du, G. H.; Zhang, S.; Peng, L. M. *Acta Crystallogr., Sect. B* **2002**, *58*, 587.
(22) Ma, R.; Bando, Y.; Sasaki, T. *Chem. Phys. Lett.* **2003**, *380*, 577.
(23) Fukuda, K.; Sasaki, T.; Watanabe, M.; Nakai, I.; Inaba, K.; Omote, K. *Cryst. Growth Des.* **2003**, *3*, 281.

10.1021/cm048249t CCC: $30.25

hydrothermal synthesis of nanotubes adequately.[17,24] Since the $H_2Ti_3O_7$ can be thermally dehydrated to TiO_2(B),[4,5,17] the existence of TiO_2(B) nanotubes is supported, too.[17]

Banfield et al.[25] first found TiO_2(B) in nature. Its crystal structure was determined by Marchand et al.[1] (Note an error in ref 1, where the TiO_2(B) was confused with $K_2Ti_8O_{17}$). The structure was further refined by theoretical methods[26] and by X-ray[5] and neutron diffraction.[4] TiO_2(B) has monoclinic unit cell (space group $C2/m$) with $a = 1.21787$ nm, $b = 0.37412$ nm, $c = 0.65249$ nm, and $\beta = 107.054°$.[4] The structure is isotypic to that of Na_xTiO_2 (bronze), $x \cong 0.2$, where the name "TiO_2(B)" comes from.[27] (This name was, however, historically generated in a different way, first for VO_2(B)[28] and other isomorphous oxides including TiO_2(B)).[29] The same crystal structure is also represented by the mineral $Na_2Fe_2Ti_6O_{16}$ (freudenbergite).[30] Hence, TiO_2(B) can equally be called "freudenbergite modification of TiO_2", but this notation is not common. The structure of TiO_2(B) is characterized by two edge-sharing TiO_6 octahedra which are linked to the neighboring doublet of octahedra by corners. The density of TiO_2(B) is 3.64−3.76 g/cm[3,2,11,25] hence, it is smaller than that of anatase, rutile, or brookite.

The electronic structure of TiO_2(B) was calculated by Nuspl et al.[31] TiO_2(B) is an n-type semiconductor with a band gap of 3−3.22 eV,[9,32] which is similar to rutile and anatase. Consequently, TiO_2(B) shows photoanodic[32] and photocatalytic[8,9] activity in UV light. The photocatalytic activity may be even superior to that of Degussa P25.[8,9] Because of its open structure, TiO_2(B) accommodates hydrogen via electrochemical reduction of inserted protons, and this hydrogen can be extracted photoelectrochemically in visible light.[32]

TiO_2(B) also accommodates Li^+ to form Li_xTiO_2(B). The insertion coefficient x was 0.75−0.85 by the reaction with n-butyl-lithium and 0.5−0.75 by electrochemistry.[2,29,33−35] The electrochemical reversibility of lithium insertion was, reportedly, not very good.[2] Recently, high electrochemical capacity ($x = 0.82$, i.e., 275 mAh/g) was reported for hydrothermally grown TiO_2(B) nanowires.[18] A comparative theoretical study of Li-insertion into anatase and TiO_2(B) points at beneficial properties of the latter.[31] The TiO_2(B) lattice has parallel infinite channels, in which Li^+ can be accommodated, without any significant distortion of the structure.[31] This paper aims at deeper understanding of the Li insertion into TiO_2(B). It will allow rationalization of some previous reports,[15,36−40] in which the interaction of Li with TiO_2(B) was probably overlooked.

Experimental Section

Materials. The precursor, X-ray amorphous TiO_2, was prepared by precipitation of the aqueous solution of K_2TiF_6 (Aldrich) with ammonium hydroxide solution (25 wt %, Fluka). The product was washed with H_2O and dried, $S_{BET} = 584$ m^2/g. Alternatively, the amorphous TiO_2 ($S_{BET} = 518$ m^2/g) was prepared by hydrolysis of titanium isopropoxide at 0 °C as described elsewhere.[41]

Sample A. 3.5 g of amorphous TiO_2 was autoclaved in 100 mL of 10 M NaOH at 250 °C for 48 h and then washed with H_2O and autoclaved in 0.1 M HNO_3 at 200 °C for 2.5 h. The dried sample was then calcined at 500 °C for 1 h. The surface area of the product was 34.7 m^2/g.

Sample B. 10 g of amorphous TiO_2 was mixed with 7.78 g of Cs_2CO_3 (Aldrich) and mortared carefully. The mixture was then decarbonated at 800 °C for 4 h, mortared again, and annealed at 800 °C in a crucible with a tight lid for 24 h, twice, with grinding at the interval. The product was then mortared and ion-exchanged with 1 M HCl (100 mL per 1 g of product) for 4 × 24 h at vigorous stirring with the fresh acid exchanged every 24 h. The dried sample was finally calcined at 500 °C for 1 h. The product contained <10 ppm K (according to ICP analysis) and its surface area was $S_{BET} = 29.5$ m^2/g.

Sample C. This material was prepared according to the original synthetic protocol of TiO_2(B).[1] An intimate mixture of 20 g KNO_3 (Aldrich) and 31.6 g of TiO_2 (Bayer, PKP04090) was annealed at 1000 °C for 2 days. The product was mortared and hydrolyzed with 0.4 N HNO_3 (100 mL of HNO_3 per 1 g of product) for 3 days at vigorous stirring with the fresh acid every 24 h. The sample was dried in air at ambient temperature and then under vacuum overnight and was calcined at 500 °C for 30 min. The final product contained 120 ppm K (according to ICP analysis), and its surface area was $S_{BET} = 9.9$ m^2/g.

Preparation of Electrodes. Powder sample was dispersed in aqueous medium into viscous paste according to the previously developed methods.[42−44] The powder (0.3 g) was mixed under stirring or gentle mortaring with 0.8 mL of 10% aqueous solution of acetylacetone. Subsequently, 0.8 mL of 4% aqueous solution of hydroxypropylcellulose (Aldrich, MW 100 000) was added, and finally 0.4 mL of 10% aqueous solution of Triton-X100 (Fluka) was also added. Before use, the prepared slurry was homogenized by stirring. If the slurry was too viscous, it was further diluted by water. Titanium grid (5 × 15 mm, Goodfellow) was used as the electrode support. Electrodes were prepared by dip-coating, and the coated area was ca. 5 × 5 mm^2. The prepared electrodes were

---

(24) Sun, X.; Li, Y. *Chem. Eur. J.* **2003**, *9*, 2229.
(25) Banfield, J.; Veblen, D.; Smith, D. *Am. Mineral.* **1991**, *76*, 343.
(26) Catlow, C. R. A.; Cormack, A. N.; Theobald, F. *Acta Crystallogr.* **1984**, *B40*, 195.
(27) Andersson, S.; Wadsley, A. D. *Acta Crystallogr.* **1962**, *15*, 194.
(28) Theobald, F.; Cabala, R.; Bernard, J. *J. Solid State Chem.* **1975**, *17*, 431.
(29) Zachau-Christiansen, B.; West, K.; Jacobsen, T.; Skaarup, S. *Solid State Ionics* **1992**, *53−56*, 364.
(30) Ishiguro, T.; Tanaka, K.; Marumo, F.; Ismail, M. G. M. U.; Hirano, S.; Somiya, S. *Acta Crystallogr.* **1978**, *B34*, 255.
(31) Nuspl, G.; Yoshizawa, K.; Yamabe, T. *J. Mater. Chem.* **1997**, *7*, 2529.
(32) Betz, G.; Tributsch, H.; Marchand, R. *J. Appl. Electrochem.* **1984**, *14*, 315.
(33) Kawamura, H.; Muranishi, Y.; Miura, T.; Kishi, T. *Denki Kagaku* **1991**, *59*, 766.
(34) Zachau-Christiansen, B.; West, K.; Jacobsen, T.; Atlung, S. *Solid State Ionics* **1988**, *28−30*, 1176.
(35) Brohan, L.; Marchand, R. *Solid State Ionics* **1993**, *9−10*, 419.
(36) Kavan, L.; Rathousky, J.; Grätzel, M.; Shklover, V.; Zukal, A. *J. Phys. Chem. B* **2000**, *104*, 12012.
(37) Kavan, L.; Rathousky, J.; Grätzel, M.; Shklover, V.; Zukal, A. *Microporous Mesoporous Mater.* **2001**, *44−45*, 653.
(38) Kavan, L.; Kalbac, M.; Zukalova, M.; Exnar, I.; Lorenzen, V.; Nesper, R.; Grätzel, M. *Chem. Mater.* **2004**, *16*, 477.
(39) Kavan, L.; Zukalova, M.; Kalbac, M.; Grätzel, M. *J. Electrochem. Soc.* **2004**, *151*, A1301.
(40) Zhou, Y.; Cao, L.; Zhang, F.; He, B.; Li, H. *J. Electrochem. Soc.* **2003**, *150*, A1246.
(41) Zhang, H.; Finnegan, M.; Banfield, J. F. *Nano Lett.* **2001**, *1*, 81.
(42) Kavan, L.; O'Regan, B.; Kay, A.; Grätzel, M. *J. Electroanal. Chem.* **1993**, *346*, 291.
(43) Nazeeruddin, M. K.; Kay, A.; Rodicio, I.; Humphry-Baker, R.; Mueller, E.; Liska, P.; Vlachopolous, N.; Grätzel, M. *J. Am. Chem. Soc.* **1993**, *115*, 6382.
(44) Kavan, L.; Grätzel, M.; Rathousky, J.; Zukal, A. *J. Electrochem. Soc.* **1996**, *143*, 394.

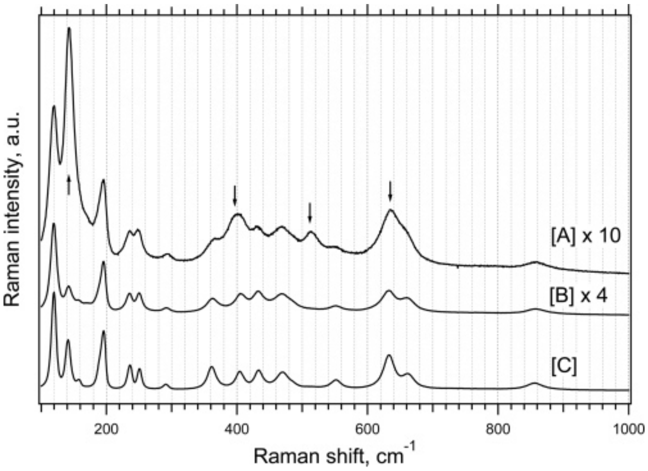

Figure 1. Raman spectra of the prepared materials A−C. Spectra B and C are assignable to monoclinic TiO_2(B), spectrum A also shows the anatase peaks (marked by arrows) in addition to TiO_2(B). The Raman intensities of samples A and B are multiplied by a factor of 10 and 4, respectively. Spectra are offset for clarity.

dried in air and finally calcined in air at 450 °C for 30 min. The amount of active electrode material was between 0.2 and 0.7 mg. Blank experiments confirmed that a bare Ti grid had negligible electrochemical charge capacity compared to that of the active material. Alternatively, the slurry was also deposited on a sheet of conducting glass (F-doped SnO_2, TEC 8 from Libbey−Owens−Ford, 8 Ω/square) using a doctor-blading technique.[44] The sheet of conducting glass had dimensions: 3 × 5 × 0.3 cm^3. A Scotch-tape at both edges of the support (0.5 cm) defined the film thickness and left part of the support uncovered for electrical contact. The film was finally calcined for 30 min in air at 450 °C. After cooling to room temperature, the sheet was cut into 10 electrodes 1.5 × 1 cm^2 in size; the geometric area of the TiO_2 film was 1 × 1 cm^2. To improve the mechanical properties, the electrode was sometimes pressed by stainless steel blocks (5000 N/cm^2).

Methods. Electrochemical measurements were carried out in a one-compartment cell using an Autolab Pgstat-30 (Ecochemie) controlled by the GPES-4 software. The reference and auxiliary electrodes were from Li metal, hence, potentials are referred to the Li/Li^+ (1M) reference electrode. $LiN(CF_3SO_2)_2$ (Fluorad HQ 115 from 3M) was dried at 130 °C/1 mPa. Ethylene carbonate (EC) and 1,2-dimethoxyethane (DME) were dried over the 4A molecular sieve (Union Carbide). The electrolyte solution, 1 M $LiN(CF_3SO_2)_2$ + EC/DME (1/1 by volume), contained 15−40 ppm H_2O as determined by Karl Fischer titration (Metrohm 684 coulometer). All operations were carried out under argon in a glovebox. The BET surface areas of the prepared materials were determined from nitrogen adsorption isotherms at 77 K (ASAP 2010, Micromeritics). Raman spectra were excited by an Ar^+ laser at 2.41 eV (Innova 305, Coherent) and recorded on a T-64000 spectrometer (Instruments, SA). Scanning electron microscopy images were obtained using JEOL JSM-03 microscope. Powder X-ray diffraction (XRD) was studied on a Siemens D-5000 diffractometer using CuKα radiation. Transmission electron microscopy (TEM) images were obtained on Tecnai F30 microscope with 300 keV field emission electron gun.

Results and Discussion

Figure 1 shows Raman spectra of the prepared materials. Sample A is, apparently, a mixture of anatase and TiO_2(B), but the spectra of samples B and C can be assigned to TiO_2(B)[4,5,18] only. The mixture of TiO_2(B) with anatase[5,15,18] or rutile[17] is a typical product of calcination of hydrothermally grown layered titanates (such as $H_2Ti_3O_7$).[15,18] The same holds for calcination products from $H_2Ti_xO_{2x+1}$ ($x = 3, 4, 5$) obtained by an ordinary solid-state reaction protocol.[2,4−6,16] The structure of $H_2Ti_xO_{2x+1}$ is characterized by corrugated ribbons containing 3, 4, or 5 TiO_6 octahedra in flat sections.[4] Since TiO_2(B) has only two edge-sharing TiO_6 octahedra in the corresponding sections, the transformation of $H_2Ti_xO_{2x+1}$ ($x = 3-5$) into TiO_2(B) is, apparently, not topotactic, but it is promoted by the kinks in the precursor's structure.[4,10]

Some authors did not explicitly mention the formation of TiO_2(B) during calcination of titanate nanotubes ($H_2Ti_xO_{2x+1}$). The obvious reasons are two: either the temperature was high enough to recrystallize TiO_2(B) into anatase and rutile or the TiO_2(B) phase was simply overlooked. The later problem was articulated by Kogure et al.:[11] TiO_2(B) may easily be unnoticed in a mixture with large concentration of anatase because of an overlap of the main diagnostic XRD peaks, especially in nanocrystalline materials with broad diffraction maxima (cf. Figure 2). Raman spectroscopy is a convenient analytic tool (cf. Figures 1 and 2), since TiO_2(B) can be unambiguously distinguished from anatase and other TiO_2 phases. (Note ref 15 for the opposite conclusion, which, however, may look questionable, if we inspect the actual Raman spectrum presented in ref 15.)

The diffractogram of sample B (Figure 2) matches well the pattern of monoclinic TiO_2(B) from JCPD PDF No.35-0088. Hence, its phase purity is confirmed both by XRD and Raman spectroscopy (cf. Figure 1). The XRD of sample C (Figure 2) is similar but exhibits an extra peak at 2 theta = 11.8°, which indicates some amount of unconverted hydrogen titanates, such as tetratitanate ($H_2Ti_4O_9 \cdot 0.25\ H_2O$) or octatitanate ($H_2Ti_8O_{17} \cdot 0.4H_2O$). The latter species is formed from tetratitanate at 200−300 °C,[45] and its presence is supported also by the Li-insertion voltammogram (see below). The classical solid-state synthesis of $K_2Ti_4O_9$ precursor may give side products $K_2Ti_6O_{13}$ and $K_2Ti_2O_5$.[46,47]

The formation of pure TiO_2(B) in sample B (Figures 1, 2) is surprising. The employed synthetic protocol should, actually, lead to the orthorhombic lepidocrocite-like protonic titanate, $H_xTi_{2-x/4}\square_{x/4}O_4$. This species is characterized by ideally flat sheets of edge-sharing TiO_6 octahedra,[48−50] which convert directly into anatase,[22,23] without the intermediate crystallization of TiO_2(B). We have explored this discrepancy, and it turned out that the occurrence of TiO_2(B) is crucially dependent on the TiO_2 precursor in the synthesis of the first intermediate, that is, the Cs-titanate. Nanocrystalline anatase TiO_2 (Bayer) provided mixtures of TiO_2(B) and anatase or pure anatase in the final product, but the syntheses starting from amorphous TiO_2 (see Experimental section) lead, unexpectedly, to pure TiO_2(B).

---

(45) Suzuki, S.; Miyayama, M. *Key Eng. Mater.* **2003**, *248*, 151.
(46) Zaremba, T.; Hadrys, A. *J. Mater. Sci.* **2004**, *39*, 4561.
(47) Krogh Andersen, E.; Krogh Andersen, I. G.; Skou, E. *Solid State Ionics* **1988**, *27*, 181.
(48) Sasaki, T.; Nakano, S.; Yamauchi, S.; Watanabe, M. *Chem. Mater.* **1997**, *9*, 602.
(49) Sasaki, T.; Watanabe, M. *J. Am. Chem. Soc.* **1998**, *120*, 4682.
(50) Choy, J. H.; Lee, H. C.; Jung, H.; Kim, H.; Boo, H. *Chem. Mater.* **2002**, *14*, 2486.

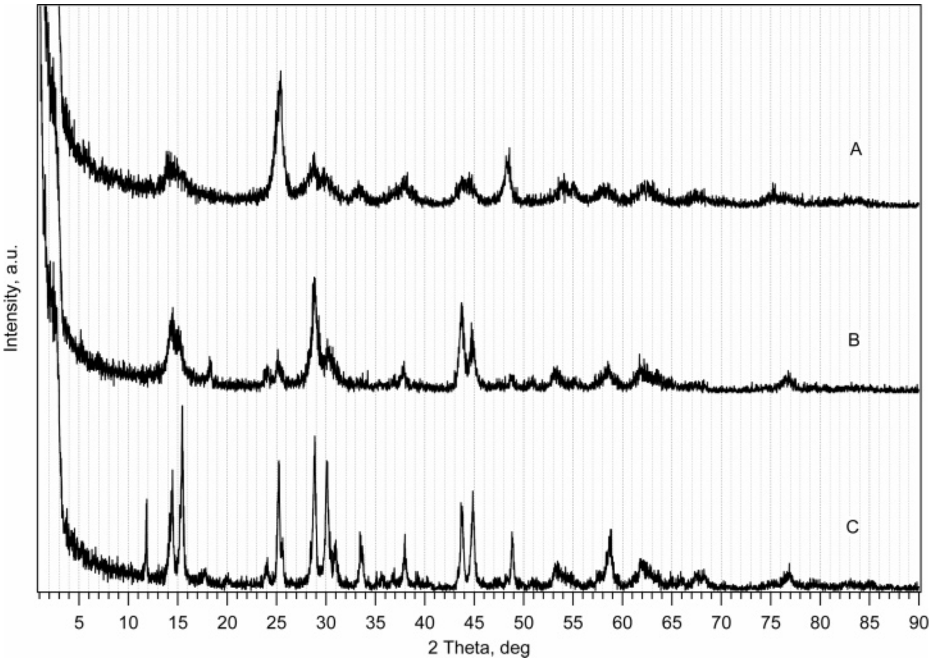

Figure 2. X-ray diffractograms of samples A−C. The plots are offset for clarity.

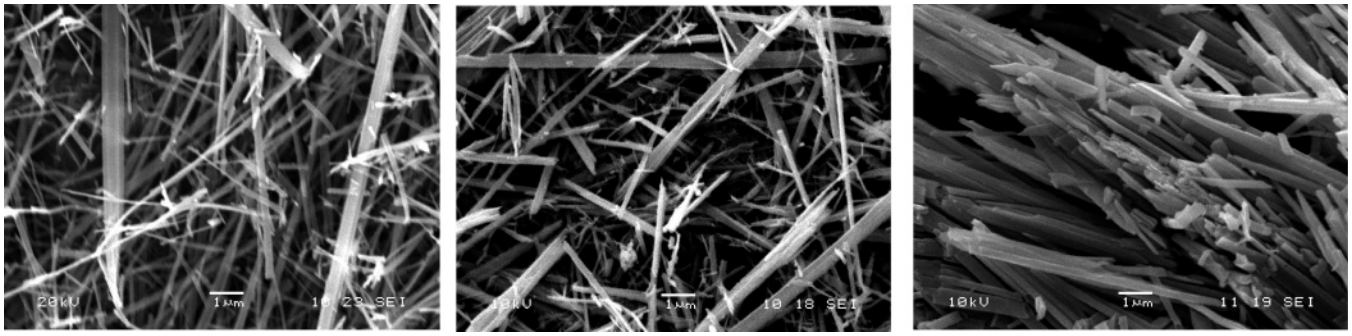

Figure 3. Scanning electron microscopy images of samples A−C (from left to right). Scale bars correspond to 1 μm.

Apparently, structures other than orthorhombic $Cs_xTi_{2-x/4}\square_{x/4}O_4$ ($x \approx 0.7$) may play a role in this case. For instance, if we assume the $Cs_2Ti_5O_{11}$ as an intermediate Cs-titanate, the formation of pure TiO_2(B) is smoothly explained.[4] Also, another flat structure, $Cs_2Ti_6O_{13}$, is partly transferable to TiO_2(B).[4] The particular reactions giving either orthorhombic lepidocrocite or monoclinic pentatitanate are only distinguished by a small difference in the stoichiometry of reactants: Cs/Ti = 0.4 for pentatitanate and Cs/Ti = 0.38 for lepidocrocite, respectively. Hence, the usual product is a mixture of both materials.[16]

All samples A−C show characteristic fibrous texture as indicated by scanning electron microscopy (SEM) (Figure 3). The fibers of sample C are of larger size, which is also mirrored by narrower XRD peaks, smaller BET area, and intense Raman peaks of this sample (see above). Generally, the fibers of TiO_2(B) are of polycrystalline,[18] mosaic[2] texture, but single crystalline[10] fibers can be observed, too. The mosaic and single crystalline fibers tend to be oriented parallel to the *b*-axis of the TiO_2(B) lattice.[2,10] This is also documented by a high-resolution TEM image of our sample B (Figure 4). The same orientation exists in $K_2Ti_4O_9$, which is a common precursor of TiO_2(B).[10]

Figure 5 shows schematically the TiO_2(B) structure in the (010) projection. This scheme is somewhat idealized, as the TiO_6 octahedra are slightly distorted in the real structure. However, it clearly depicts characteristic parallel channels running perpendicular to the (010) face. Since microfibrous particles of TiO_2(B) materials tend to be oriented along the *b*-axis[10,18] (cf. Figure 4), these channels also run parallel to the microfiber axis. The cross section of a channel is comparable to the size of "missing" TiO_6 octahedron in the

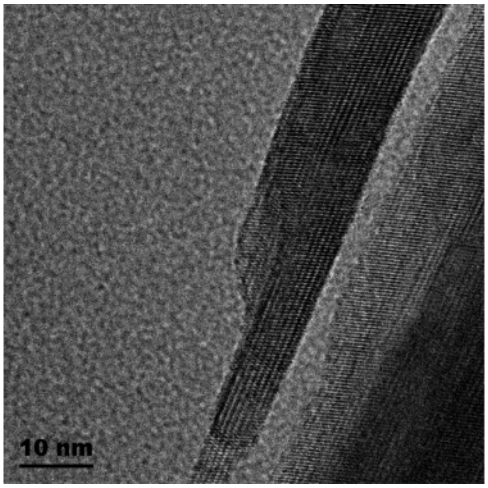

Figure 4. Transmission electron microscopy image of the sample B; scale bar corresponds to 10 nm.

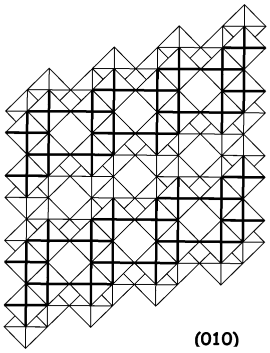

Figure 5. Projection of the idealized structure of TiO_2 (B) perpendicular to the (010) face.

structure (Figure 5), hence, the channel is large enough to accommodate Li^+ ions and to allow their easy transport along the fiber axis. This seems to be the key for understanding of the fast (pseudocapacitive) Li-storage in this material (see below).

Figure 6 displays cyclic voltammograms of Li-insertion into the samples A−C. The voltammogram of sample A exhibits a pair of cathodic/anodic peaks at 1.75 and 1.95 V (formal potential 1.85 V), which are characteristic for Li-insertion into anatase lattice.[38,39,44,51−56] We have previously denoted this pair of peaks as “A-peaks”.[38] In addition to that, the voltammogram shows two pairs of peaks with formal potentials of 1.52 and 1.59 V vs Li/Li^+, respectively, denoted S1 and S2, respectively.[38] The notation came from our earlier assumption that these S-peaks could be assigned to the surface-confined process in titania nanosheets[38] or in “amorphous phase”.[36,37] However, this assumption needs revision in view of the new facts accumulated in this paper (see below).

The sole features assignable to S-peaks occur in both samples B and C, which are almost pure TiO_2(B). This generates a logical conclusion that the S-peaks are, actually, signatures of TiO_2(B) phase. The Li-storage capacity (Li/Ti $= x$) at the slowest voltammetric scan (0.1 mV/s) was 0.53 (sample A), 0.68 (sample B), and 0.47 (sample C). These capacities are comparable to those reported for galvanostatic charging of bulk TiO_2(B) ($x = 0.5$)[29,34] but smaller than the values obtained for galvanostatic charging of TiO_2(B) nanowires ($x = 0.82$).[18] Also from theoretical arguments, the Li-insertion beyond $x = 0.5$ becomes rather difficult.[31] Sample C sometimes exhibited poorly reproducible electrochemistry. On the other hand, samples A and B gave well-defined voltammograms, which did not change significantly during tens of voltammetric cycles. The broad and overlapping S-peaks in sample C are reminiscent of the Li-insertion behavior of monoclinic octatitanate, $H_2Ti_8O_{17}$, which has just one pair of broad peaks in this potential region.[28] The octatitanate is formed by heating of the TiO_2(B) precursor, $H_2Ti_4O_9$, at moderate temperature, 200 °C, and we may recall that the XRD of sample C confirms the presence of unconverted titanates (see above). The titanates in sample C seem to influence mechanical properties of the electrode. The material is poorly workable during the electrode fabrication because of its hardness. Consequently, the films are less uniform and sensitive to mechanical cracking upon electrochemical treatment.

Figure 7 demonstrates the behavior of S-peaks in the phase-pure sample B at varying scan rates. The peak currents were normalized with respect to the peak current at the slowest scan (0.1 mV/s) and plotted against the scan rate (inset in Figure 7). Apparently, the currents scale with the first power of scan rate, which is characteristic for capacitive charging:

$$i = \mathrm{d}Q/\mathrm{d}t = C\,\mathrm{d}E/\mathrm{d}t = Cv \tag{1}$$

Q is the voltammetric charge, C is capacitance, and dE/dt is the scan rate, v. However, sole capacitive double-layer charging (eq 1) should give a featureless voltammogram (ideally rectangle assuming C invariant of potential). The peak structure with small peak-to-peak splitting (ca. 50−100 mV at $v = 0.1$ mV/s) points at a surface-confined charge-transfer process, which can be considered faradaic pseudocapacitance. The found Li-storage capacity ($x \approx 0.5$−0.7) considerably exceeds the “ordinary” capacity of the TiO_2 surface assuming solely the double layer plus the faradaic pseudocapacitance of surface states.[51] Consequently, this behavior is specific for the TiO_2(B), and we may suggest that its open structure with freely accessible channels[31] is responsible for the fast Li-charging of a TiO_2(B) crystal.

The different mechanism of Li-storage in TiO_2(B) and anatase is explicitly demonstrated at sample A which is a mixture of both phases (Figure 8A, B). The plot of peak currents against the scan rate is shown in Figure 8B. To analyze this dependence in a broader interval of v, we selected here the cathodic S-peaks and anodic A-peaks, which are better resolved at faster charging (cf. also Figure 7). (However, the general conclusions are equally valid for both cathodic and anodic peaks.) Apparently, the A-peaks scale with square root of the scan rate, v, as it is expected for diffusion-controlled irreversible process:[56,57]

$$|i| = 0.4958nFAc\,(D\alpha nFv/RT)^{1/2} \tag{2}$$

where n is the number of electrons, A is the electrode area, c is the maximum concentration of Li^+ (or Ti^{3+}) in the accumulation layer ($c = 0.024$ mol/cm^3 for $x = 0.5$), D is the diffusion coefficient, and the other symbols have their usual meaning. Figure 8B confirms that this dependence can be fitted to experimental points for $v <\approx 2$ mV/s. (For higher scan rates, the fit shows systematic deviation due to uncompensated iR drop of the cell.) The behavior described by eq 2 is typical for Li-insertion into ordinary anatase lattice.[36−39,44,51−56] The $i \approx v^{1/2}$ dependence was even found

---

(51) Kavan, L.; Kratochvilová, K.; Grätzel, M. *J. Electroanal. Chem.* **1995**, *394*, 93.

(52) Van de Krol, R.; Goossens, A.; Meulenkamp, E. A. *J. Electrochem. Soc.* **1999**, *146*, 3150.

(53) Hengerer, R.; Kavan, L.; Krtil, P.; Grätzel, M. *J. Electrochem. Soc.* **2000**, *147*, 1467.

(54) Kavan, L.; Attia, A.; Lenzmann, F.; Elder, S. H.; Grätzel, M. *J. Electrochem. Soc.* **2000**, *147*, 2897.

(55) Kavan, L.; Grätzel, M.; Gilbert, S. E.; Klemenz, C.; Scheel, H. J. *J. Am. Chem. Soc.* **1996**, *118*, 6716.

(56) Lindström, H.; Södergen, S.; Solbrand, A.; Rensmo, H.; Hjelm, J.; Hagfeldt, A.; Lindquist, S. E. *J. Phys. Chem. B* **1997**, *101*, 7717.

(57) Van de Krol, R.; Goossens, A.; Schoonman, J. *J. Phys. Chem. B* **1999**, *103*, 7151.

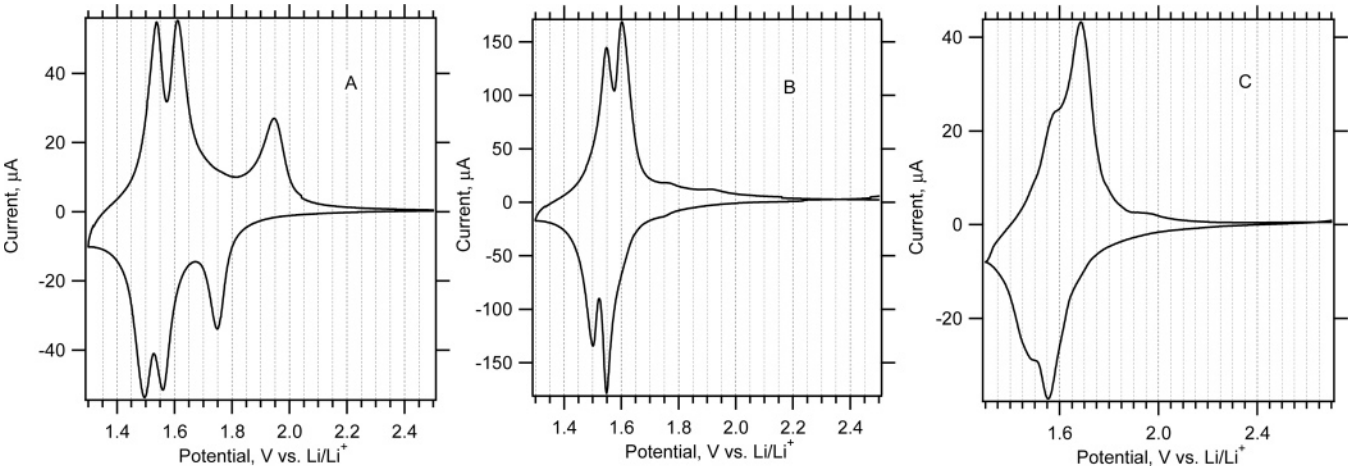

Figure 6. Cyclic voltammograms of samples A (chart A), B (chart B), and C (chart C) in 1M LiN(CF$_3$SO$_2$)$_2$ + EC/DME (1/1, v/v); scan rate 0.1 mV/s. The mass of active material was different for each particular electrode in charts A−C.

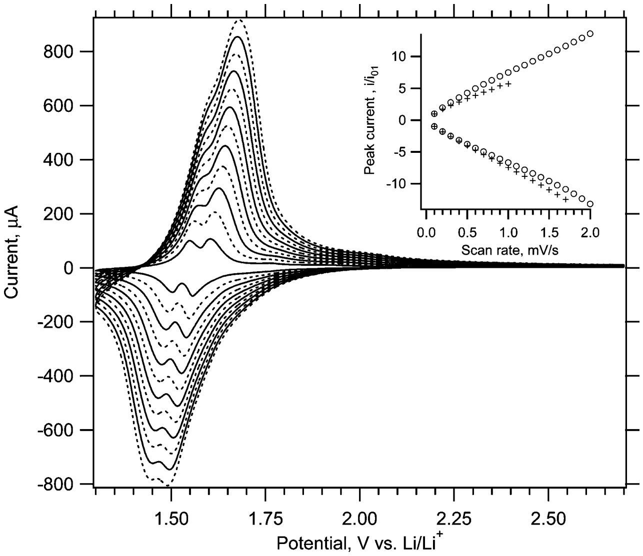

Figure 7. Cyclic voltammograms of sample B in 1M LiN(CF$_3$SO$_2$)$_2$ + EC/DME (1/1, v/v); scan rate 0.1−1.2 mV/s (in 0.1 mV/s steps for plots from bottom to top). Inset displays the normalized peak current, i/i_{01}, where i_{01} is the peak current at the slowest scan (0.1 mV/s) and i is the peak current at the actual scan rate. Circles and crosses denote two individual S-peaks.

for Li-insertion into titania nanosheets derived from lepidocrocite-like titanate.[58]

The conclusion that sample A accommodates Li either via the insertion into the anatase lattice or via the surface-confined pseudocapacitive process matches, phenomenologically, the conclusion of our previous works on similar materials.[36−39] Here we suggest, as new interpretation, that the S-peaks are assignable to TiO$_2$(B). The TiO$_2$(B) phase was, actually, traced in certain samples made by hydrothermal growth in ref 38 (see Supporting Information to ref 38). The apparent link between S-peak and TiO$_2$(B) was overlooked also by other authors, who had studied virtually identical systems.[15,40] Gao et al.[15] observed unstable features similar to S-peaks in a material declared as TiO$_2$(B) + anatase mixture, but these features were unclearly interpreted as "discrete phase or imperfections of the TiO$_2$ nanorod lattice". Analogously, the voltammogram of Zhou et al.[40] showed weak S-peaks, but they were not commented, nor was the presence of TiO$_2$(B) mentioned in this paper. Weak S-peaks were traceable also in TiO$_2$ made by galvanostatic oxidative hydrolysis of TiCl$_3$,[39] but TiO$_2$(B) was again unnoticed.

Strong S-peaks were detected in mesoscopic TiO$_2$ films made by templating with amphiphilic triblock copolymers (Pluronic).[36,37] The TiO$_2$(B) phase was not considered,[36,37] despite the fact that one Raman spectrum shown in ref 37 brought clear (but uncommented) evidence for TiO$_2$(B) in the Pluronic-templated material. Also, other papers dealing with Pluronic-templating[59−61] did not mention the TiO$_2$(B) phase, either. To rationalize this discrepancy, we have reproduced the relevant syntheses[36,37] and varied systematically the conditions (concentration of the precursor's solution, time of aging, temperature, heating program, etc.). The appearance of TiO$_2$(B)/S-peaks was poorly reproducible, and we failed to demonstrate pure TiO$_2$(B) in this way. In accord with other reports on Pluronic-templating,[36,37,59−61] the main crystalline phase was anatase, sometimes also brookite was observed,[60] while these crystals are embedded in a matrix of amorphous titania. The growth of metastable TiO$_2$(B) phase during the templating protocol requires, apparently, special conditions, which are not yet precisely known. The situation is reminiscent of the unexpected detection of TiO$_2$(B) during calcination of sol−gel derived SiO$_2$−TiO$_2$ amorphous film at 900 °C.[11] Also in this case, the matrix of amorphous silica promoted the growth and unusual stability of TiO$_2$(B).[11]

Li-insertion into pure TiO$_2$(B) was previously studied mostly by galvanostatic chronopotentiometry.[18,29,34] This technique is less suitable for the detection and analysis of the S-peaks. Nevertheless, derivation of the chronopotentiometric curve and plotting of dx/dE versus E shows clearly two pairs of cathodic/anodic peaks at ca. 1.6 and 1.5 V,[34] which is in remarkable accord with our voltammograms (Figures 6−8). Zachau-Christiansen et al.[34] have suggested

---

(58) Sakai, N.; Ebina, T.; Takada, K.; Sasaki, T. *J. Am. Chem. Soc.* **2004**, *126*, 5851.

(59) Yang, P.; Zhao, D.; Margolese, D. I.; Chmelka, B. F.; Stucky, G. D. *Chem. Mater.* **1999**, *11*, 2813.

(60) Crepaldi, E. L.; Soler-Illia, G. J. A. A.; Grosso, D.; Cagnol, F.; Ribot, F.; Sanchez, C. *J. Am. Chem. Soc.* **2003**, *125*, 9770.

(61) Choi, S. Y.; Mamak, M.; Coombs, N.; Chopra, N.; Ozin, A. *Adv. Funct. Mater.* **2004**, *14*, 335.

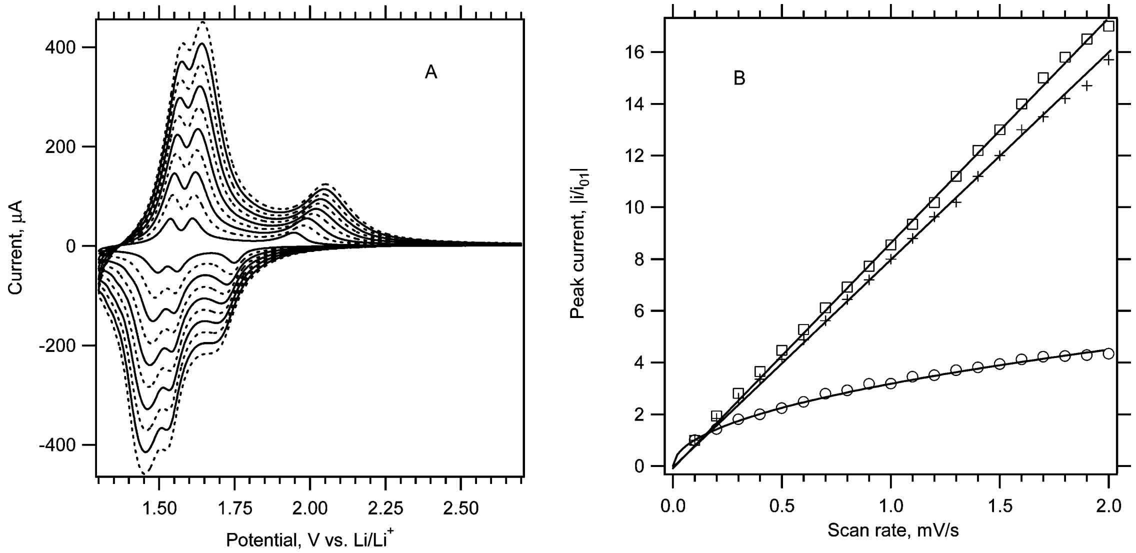

Figure 8. (A) Cyclic voltammograms of sample A in 1M $LiN(CF_3SO_2)_2$ + EC/DME (1/1, v/v); scan rate 0.1−1.0 mV/s (in 0.1 mV/s steps for plots from bottom to top). (B) Normalized peak current, i/i_{01}, where i_{01} is the peak current at the slowest scan (0.1 mV/s). Circles: anodic peak at ca. 2 V; crosses: cathodic peak at ca. 1.6 V, squares: cathodic peak at ca. 1.5 V.

that these peaks indicate two ordered superstructures with $x = 0.33$ and $x = 0.5$. Also, our S-peak at 1.6 V tends to be stronger than the S-peak at 1.5 V (Figures 6−8), that is, the first formed superstructure (at 1.6 V) is more populated by Li than the superstructure formed at 1.5 V. However, none of the previous electrochemical studies on TiO_2(B)[2,15,18,29,31,34,35] mentioned the pseudocapacitive nature of charging.

The fact that Li is accommodated in TiO_2(B) via pseudocapacitive process recalls the idea of fast transport of Li^+ in parallel channels of the TiO_2(B) lattice.[31] The channels run perpendicular to (010) face of TiO_2(B) (cf. Figure 5). This face is abundant at the cross section of typical microfibrous particles of TiO_2(B) (cf. Figures 3−5 and discussion thereof). During electrochemical insertion, Li^+ ions interact with the whole surface of a fibrous particle. Hence, Li^+ ions, perhaps, penetrate into the bulk fiber also in radial direction and not only through the cross section of a fiber (channel). Assuming the channels conduct rapidly Li^+ ions inside a particle, the rate-determining process is the primary interfacial Li^+-transfer at the fiber surface. This would provide rational for the surface-confined, pseudocapacitive process, controlling the overall kinetics. Such a “macroscopic” model highlights the role of fiber surface. The latter is dominated by the (100) and (001) faces, but the (010) face is negligibly engaged in the Li^+-transfer, occurring just at the tip of a fiber. We may further speculate that the two S-peaks reflect different energy barriers for Li^+ transfer at the (100) and (001) faces, which is quite reminiscent of the Li-insertion anisotropy in anatase.[53]

Alternatively, we may discuss these issues at “microscopic” level, too. Assuming that neither the intrachannel Li^+-transport nor the interfacial Li^+-transfer are rate-determining, the overall kinetics might still be controlled by trapping of Li^+ at certain sites at the inner wall of a channel. Also, this would mimic the pseudocapacitive faradaic process. Since all channels in the TiO_2(B) lattice are structurally equivalent,[31] there should be two distinct superstructures in Li_xTiO_2(B), which would give rise to the two S-peaks. Although $Li_{0.5}TiO_2$(B) is assumed to have crystallographically equivalent sites occupied by Li^+, there are further vacant sites up to the stoichiometry of $LiTiO_2$(B).[31] All these sites are quasi-octahedral with a coordination number of 5 (LiO_5),[31,35] while two kinds of these sites are detectable by ^{7}Li NMR.[35] If these two sites are occupied at $x < 0.5$, the occurrence of S-peaks-doublet is rationalized, too.

At this stage, we are unable to distinguish between the macroscopic and microscopic models and elucidate the origin of S-peaks unambiguously. However, our interpretation generates a logical question, whether the pseudocapacitive Li-storage would be observable also in other structures with one-dimensional parallel channels, such as ramsdellite[62] and hollandite[63] forms of TiO_2. This question was not yet clearly addressed, either. The TiO_2 (ramsdellite) accommodates Li reversibly up to ca. 200 mAh/g,[62] but the TiO_2 (hollandite) shows poor Li-storage electrochemistry despite the very wide open channels in the lattice.[63] Apparently, the good pseudocapacitive performance is observed only in structures having both the open pathways for bulk Li-transport and proper sites for reversible Li-anchoring in close vicinity of these pathways. TiO_2(B) seems to offer both these features simultaneously.

Conclusions

New synthetic protocol was elaborated giving phase-pure TiO_2(B) with microfibrous morphology. Amorphous TiO_2 was converted via a solid-state reaction with Cs_2CO_3 followed by the Cs^+/H^+ ion exchange and final calcination. Compared to traditional syntheses from $K_2Ti_4O_9$, the new product had finer fibers and also exhibited better electrochemical performance and stability.

Li-insertion electrochemistry of TiO_2(B) is basically different from that of anatase. Accommodation of Li in the

---

(62) Gover, R. K. B.; Tolchard, J. R.; Tukamoto, H.; Murai, T.; Irvine, J. T. S. *J. Electrochem. Soc.* **1999**, *146*, 4348.

(63) Noailles, L. D.; Johnson, C. S.; Vaughey, J. T.; Thackeray, M. M. *J. Power Sources* **1999**, *81−82*, 259.

TiO_2(B) lattice manifests itself by two pairs of peaks in cyclic voltammogram with formal potentials of ca. 1.5 and 1.6 V (S-peaks). Whereas the kinetics of lithium storage in anatase is controlled by solid-state diffusion of Li^+, the TiO_2(B) host accommodates lithium by a pseudocapacitive faradaic process, which is not controlled by diffusion at comparable conditions.

Pseudocapacitive electrochemical storage of Li^+ in TiO_2(B) fibers was discussed in terms of crystal structure of the host. The key effect seems to be fast Li^+ transport in the open channels running parallel to the *b*-axis. This direction coincides, usually, with the fiber axis in TiO_2(B) materials of fibrous morphology. The rate-limiting process might be either the Li^+-transport through the surface of fibrous particles or reversible trapping of Li^+ ions at the inner wall of the channel. This subject, apparently, requires further studies.

The assignment of S-peak to TiO_2(B) asks for reinterpretation of several previous reports, which did not consider this relation or the presence of TiO_2(B). The detection of S-peaks represents a sensitive and easy analytical tool for identification of this phase in titania materials. It turns out that the TiO_2(B) is present in a broad palette of TiO_2 materials of various origin.

Acknowledgment. This work was supported by the Grant Agency of the Czech Republic (contract No. 203/03/0824) and by the EC-COST Action D14/0002/99. We are grateful to Dr. L. Brabec (JHIPC) for SEM measurements. ICP analyses were carried out by Ecochem, a.s. Prague. M.Z. also thanks the Grant Agency of the Czech Republic for financial support (through grant No. 203/03/H140).

CM048249T

ELSEVIER

Available online at www.sciencedirect.com

SCIENCE DIRECT•

Progress in Solid State Chemistry 33 (2005) 253–261

Progress in Solid State Chemistry

www.elsevier.com/locate/pssc

Electrochemical and gas-phase photocatalytic performance of nanostructured TiO_2(B) prepared by novel synthetic route

M. Zukalová [a,*], M. Kalbáč [a], L. Kavan [a,c], I. Exnar [b], A. Haeger [d], M. Graetzel [c]

[a] *J. Heyrovský Institute of Physical Chemistry, Academy of Sciences of the Czech Republic, Dolejškova 3, CZ-18223 Prague 8, Czech Republic*

[b] *High Power Lithium, Park Scientifique, PSE-B, EPFL, Ecublens, CH-1015 Lausanne, Switzerland*

[c] *Laboratory of Photonics and Interfaces, EPFL, Ecublens, CH-1015 Lausanne, Switzerland*

[d] *Institute of Technical Chemistry, University Hanover, Callinstrasse 3, 30167 Hanover, Germany*

Abstract

Nanostructured phase pure TiO_2(B) with microfibrous morphology was synthesized by newly developed protocol employing amorphous TiO_2 as a precursor. Compared to traditional syntheses from $K_2Ti_4O_9$, the new product exhibited better electrochemical performance and stability. Cyclic voltammetry of Li-insertion into the TiO_2(B) evidences a pseudocapacitive faradaic process of Li accommodation which is basically different from the diffusion-controlled lithium storage in anatase or rutile. The presence of two pairs of peaks in cyclic voltammogram with formal potentials of ca. 1.5 and 1.6 V is specific for TiO_2(B). This enables to use cyclic voltammetry for identification of this phase in a broad palette of TiO_2 materials of various origin.

The photocatalytic activity of TiO_2(B) in a gas phase was evaluated using the total oxidation of propane with oxygen and the photocatalytic reduction of NO to N_2 in an oxygen rich gas mixture. For the total oxidation of propane in the gas mixture containing 300 ppm propane and 20% oxygen, the reaction rates per 1 m^2/g of the BET surface area of the catalyst for TiO_2(B) prepared by our protocol and Hombifine N (anatase, $S_{BET} = 300$ m^2/g) are comparable. For the photocatalytic NO reduction to N_2 in an atmosphere containing 20% oxygen the ratio of quantum yields for TiO_2(B) and Hombifine N was found to be 0.08, which is roughly equivalent to the ratio of their BET surface areas (0.09), despite different phase

---

* Corresponding author.
E-mail address: marketa.zukalova@jh-inst.cas.cz (M. Zukalová).

doi:10.1016/j.progsolidstchem.2005.11.036

composition of both materials. In comparison with the standard catalyst our material exhibited higher selectivity in the reduction of NO to N_2.

---

1. Introduction

TiO_2(B) was first synthesized in 1980 by Marchand et al. [1] by hydrolysis of titanate $K_2Ti_4O_9$ followed by heating at 500 °C. It is a metastable modification of TiO_2 with monoclinic unit cell (space group $C2/m$); $a = 1.21787$ nm, $b = 0.37412$ nm, $c = 0.65249$ nm, $\beta = 107.054^\circ$ [2]. The structure of TiO_2(B) is characterized by two edge-sharing TiO_6 octahedra which are linked to the neighboring doublet of octahedra by corners and is isotypic to that of Na_xTiO_2 (bronze), $x \cong 0.2$, where the name "TiO_2(B)" comes from [3].

TiO_2(B) accommodates Li^+ to form Li_xTiO_2(B). The insertion coefficient x was found to be 0.75–0.85 by the reaction with n-butyl-lithium, and 0.5–0.75 by electrochemistry [4–7]. The electrochemical reversibility of lithium insertion was, reportedly, not very good [4]. Recently, high electrochemical capacity ($x = 0.82$, i.e. 275 mAh/g) was reported for hydrothermally grown TiO_2(B) nanowires [8]. The TiO_2(B) lattice has parallel infinite channels, in which Li^+ can be accommodated, without any significant distortion of the structure [9].

By the examination of phase composition of other TiO_2 materials prepared by different synthetic protocol the presence of TiO_2(B) was detected either in the product of hydrothermal treatment of TiO_2 in NaOH solution [10–12] or in mesoporous titania thin films [13,14] prepared by supramolecular templating. Because of the presence of considerable amount of anatase in addition to TiO_2(B), all these materials are not appropriate for the detailed study of the electrochemical and photochemical behavior of TiO_2(B). To fulfill this task, we faced the challenge to develop a reliable and reproducible synthesis of phase pure TiO_2(B).

Good photocatalytic activity, nontoxicity and long-term photostability predetermine TiO_2 to be an important photocatalyst for environmental purification [15]. Two different polymorphs of TiO_2, anatase and rutile are commonly used in photocatalysis, with anatase showing a higher photocatalytic activity [16]. Since the presence of the former has been considered to be the key point for the photocatalytic activity of TiO_2 materials, the evaluation of a photocatalytic activity of monoclinic anatase-free phase pure TiO_2(B) might provide deeper insight into the relationship between crystalline structure and photocatalytic activity of titania. Photocatalytic [17,18] and photoelectrochemical [19] activities of TiO_2(B) contacting aqueous medium were reported previously, but to the best of our knowledge, there is no similar study of the photocatalytic activity of TiO_2(B) for gaseous reactants.

2. Experimental

2.1. Syntheses

The precursor, X-ray amorphous TiO_2, was prepared by the precipitation of the aqueous solution of K_2TiF_6 (Aldrich) with ammonium hydroxide solution (25 wt%, Fluka). The product was washed with H_2O and dried; $S_{BET} = 584$ m^2/g. Alternatively, the amorphous TiO_2 ($S_{BET} = 518$ m^2/g) was prepared by the hydrolysis of titanium isopropoxide at 0 °C as described elsewhere [20].

2.2. Sample A

Ten grams of amorphous TiO_2 was mixed with 7.78 g of Cs_2CO_3 (Aldrich) and mortared carefully. The mixture was then decarbonated at 800 °C for 4 h, mortared again and annealed at 800 °C in a crucible with a tight lid for 24 h twice, with grinding at the interval. The product was then mortared, and ion-exchanged with 1 M HCl (100 mL per 1 g of product) for 4 × 24 h at vigorous stirring with the fresh acid being exchanged every 24 h. The dried sample was finally calcined at 500 °C for 1 h. The product contained <10 ppm K (according to ICP analysis) and its surface area was $S_{BET} = 29.5\ m^2/g$.

2.3. Sample B

This material was prepared according to the original synthetic protocol of $TiO_2(B)$ [1] employing $K_2Ti_4O_9$ as an intermediate. The final product contained 120 ppm K (according to ICP analysis) and its surface area was $S_{BET} = 9.9\ m^2/g$.

2.4. Electrode preparation

Powder sample was dispersed in aqueous medium into viscous paste according to the previously developed methods [21–23]. Titanium grid (5 × 15 mm, Goodfellow) was used as the electrode support. Electrodes were prepared by dip-coating and finally calcined in air at 450 °C for 30 min. The amount of active electrode material was from 0.2 to 0.7 mg. Blank experiments confirmed negligible electrochemical charge capacity of a bare Ti grid compared to that of the active material.

2.5. Electrochemical measurements

Electrochemical measurements were carried out in a one-compartment cell using an Autolab Pgstat-30 (Ecochemie) controlled by the GPES-4 software. The reference and the auxiliary electrodes were from Li metal, hence, potentials are referred to Li/Li^+ (1 M) reference electrode. The electrolyte solution, 1 M $LiN(CF_3SO_2)_2$ + EC/DME (ethylencarbonate/dimethoxyethane, 1/1 by volume) contained 15–40 ppm H_2O as determined by Karl Fischer titration (Metrohm 684 coulometer). All operations were carried out under argon in a glove box. The BET surface areas were determined from nitrogen adsorption isotherms at 77 K (ASAP 2010, Micromeritics). Scanning electron microscopy images were obtained using JEOL JSM-03 microscope. Powder X-ray diffraction (XRD) was studied on a Bruker D8-Advance diffractometer using CuKα radiation. Transmission electron microscopy (TEM) images were obtained on Tecnai F30 microscope with 300 keV field emission electron gun.

2.6. Photocatalytic measurements

To investigate the reaction rate of the gas reactions in question, the catalyst material was suspended in water and fixed in a thin layer on a stainless steel plate. A mechanically stable catalyst layer of 55 cm^2 in area was achieved after drying at 50 °C for several hours. In the reactor, this catalytically active plate together with a glass plate formed the reaction chamber.

The plate was irradiated by the medium pressure UV-lamp HPA 1000/20 (Philips) through a filter absorbing IR-radiation. To adjust the irradiation intensity, the distance between the plate and the lamp was varied and the spectrum I_0 (λ) of the radiation at the catalyst surface was measured with a photodiode array spectrometer (Dr. Gröbel UV-Elektronik, Ettlingen). To calculate the absorbed irradiation intensity I_p, the absorption coefficient $\alpha(\lambda)$ of the active plate as a function of the wavelength λ was measured spectroscopically by diffuse reflectance using an integrating sphere (DMC 25, Carl Zeiss GmbH, Oberkochen).

The photoreactor was mounted into the experimental set-up consisting of the gas supply, the reaction and the analytic systems. The gas supply was realized with commercially available gas bulbs (Linde AG, Leuna). The flow rates of the gases were adjusted by flow meters (Bronkhorst AB, Ruurlo, NL). The gases were mixed in a mixing chamber. The reactor operated as a continuous stirred tank reactor in order to avoid local concentration gradients along the flow direction in the reaction chamber. This operation mode was achieved by recycling the effluent gas very quickly compared to the incoming gas flow rate. To ensure that steady state conditions were achieved, the reaction rate was measured for several hours (cf. Fig. 4 below). The composition of the incoming as well as that of the effluent gas was determined by an FTIR-analyser (IFS 28, Bruker, Hamburg). The temperature of the catalyst plate was adjusted by a heating plate and was controlled by a thermocouple. To eliminate adsorbed hydrocarbons, the catalyst plate was inserted into the photoreactor and irradiated for 3 h in an atmosphere containing 100% oxygen. The absorbed irradiation intensity was around 180 W/m^2 and the catalyst temperature 160 °C.

For the total oxidation of propane with oxygen, a gas mixture containing 300 ppm propane in oxygen/nitrogen mixture (20/80% v/v) was used as an educt. The volume flow was 200 mL/min and the absorbed irradiation intensity was 111 W/m^2. The photocatalytic reduction of NO was carried out in an atmosphere containing 300 ppm propane and 300 ppm NO in oxygen/nitrogen mixture (20/80% v/v), the absorbed irradiation intensity was 76 W/m^2. As a reference catalyst Hombifine N (Sachtleben, Duisburg, $S_{BET} = 300$ m^2/g) was tested under the same experimental conditions for comparison. The temperature of the catalyst plate was for all experiments 433 K.

3. Results and discussion

The phase purity of our product A was confirmed by XRD (Fig. 1) and Raman spectroscopy (data not shown). The diffractogram of this sample in Fig. 1 matches well the pattern PDF No. 35-0088 from JCPD, assigned to monoclinic TiO_2(B). If nanocrystalline anatase (Bayer) is used as the TiO_2(B) precursor, the synthetic procedure leads to orthorhombic lepidocrocite-like protonic titanate [24–26], $H_xTi_{(2-x)/4}\square_{x/4}O_4$, ($x \sim 0.7$, $\square$=vacancy). On the other hand, if amorphous TiO_2 is used as the precursor, the reaction surprisingly leads to a phase pure monoclinic TiO_2(B). The diffractogram of the product B prepared by the original synthetic protocol of TiO_2(B) [1] (Fig. 1) exhibits an extra peak at $2\theta = 11.8°$, which indicates some amount of unconverted hydrogen titanates, such as tetratitanate ($H_2Ti_4O_9 \cdot 0.25H_2O$) or octatitanate ($H_2Ti_8O_{17} \cdot 0.4H_2O$) in addition to TiO_2(B). The presence of unconverted hydrogen titanate impurities in the sample B was also confirmed by cyclic voltammetry of Li-insertion (see below). SEM image of sample A (Fig. 2) evidences its fibrous morphology. Generally, the fibres of TiO_2(B) are of polycrystalline [8], mosaic [27] texture, but single-crystalline [28] fibres can be observed, too. TEM images (data not shown) confirmed the tendency of the mosaic and single-crystalline fibres to be oriented parallel to the b-axis of the TiO_2(B) lattice [27,28].

Fig. 3 displays cyclic voltammograms of Li-insertion into the samples A, B. The voltammogram of sample A shows two pairs of peaks with formal potentials of 1.52 and 1.59 V vs. Li/Li$^+$, respectively, denoted S1 and S2, respectively [14], which were found to be an evidence of the presence of TiO_2(B) in the sample. The Li-storage capacity (Li/Ti $= x$) at the slowest

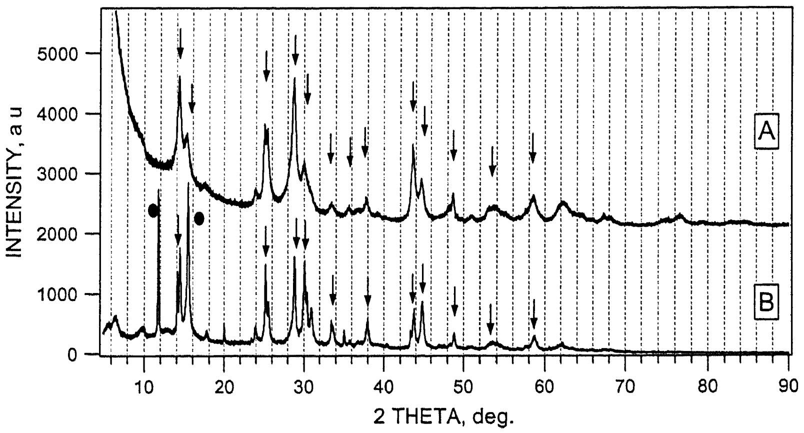

Fig. 1. X-ray diffractograms of samples A and B. The plots are offset for clarity. The peaks assigned to the $TiO_2(B)$ phase are marked by arrows, two peaks marked by full points evidence the presence of unconverted protonic titanates in the sample B.

voltammetric scan (0.1 mV/s) was 0.68 (sample A) and 0.47 (sample B). The absence of other features in Li-insertion voltammogram of the sample A proves its phase purity. On the other hand the sample B sometimes exhibited poorly reproducible electrochemistry. The broad and overlapping S-peaks in this sample are reminiscent of the Li-insertion behavior of monoclinic octatitanate, $H_2Ti_8O_{17}$, which is in good agreement with results following from the XRD analysis of this material (Fig. 1). Hence, cyclic voltammetry of Li-insertion can be used as a reliable analytical method to determine the phase composition of TiO_2 materials.

By the analysis of the dependence between the peak current of S-peaks and the scan rate the current was found to scale with the first power of scan rate, which is typical for capacitive charging:

$$i = \mathrm{d}Q/\mathrm{d}t = C\,\mathrm{d}E/\mathrm{d}t = Cv, \qquad (1)$$

Q is the voltammetric charge, C is capacitance and $\mathrm{d}E/\mathrm{d}t$ the scan rate, v. The peak structure with small peak-to-peak splitting (ca. 50–100 mV at $v = 0.1$ mV/s) points at a surface-confined charge transfer process, which can be considered faradaic pseudocapacitance. The found Li-storage capacity ($x \approx 0.5$–0.7) considerably exceeds the "ordinary" capacity of the TiO_2 surface assuming solely the double-layer plus the faradaic pseudocapacitance of surface states [29]. Consequently, this behavior is specific for the $TiO_2(B)$, and we may suggest that its open structure with freely accessible channels [9] is responsible for the fast Li-charging of a $TiO_2(B)$ crystal. In contrary to this, Li-insertion into anatase is a diffusion-controlled irreversible process [30,31] with the peak current scaling with the square root of the scan rate:

$$|i| = 0.4958nFAc\,(D\alpha nFv/\mathrm{R}T)^{1/2} \qquad (2)$$

where n is number of electrons, A is the electrode area, c is the maximum concentration of Li^+ (or Ti^{3+}) in the accumulation layer ($c = 0.024$ mol/cm^3 for $x = 0.5$), D is diffusion coefficient and the other symbols have their usual meaning. Provided that Li^+ ions penetrate into the bulk fiber of $TiO_2(B)$ in radial direction and the transport of Li^+ ions inside channels is fast, the

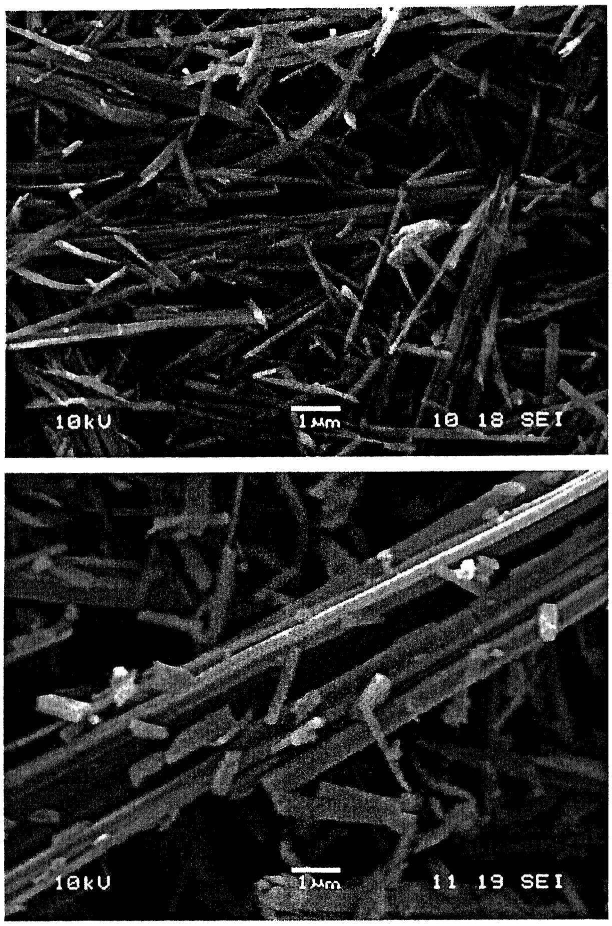

Fig. 2. Scanning electron microscopy images of samples A and B (from top to bottom). Scale bars correspond to 1 µm.

rate-determining process is the primary interfacial Li^+-transfer at the fiber surface. This would explain the surface-confined, pseudocapacitive process, controlling the overall kinetics.

The photocatalytic activity of TiO_2(B) in a gas phase was evaluated by the total oxidation of propane with oxygen and the photocatalytic reduction of NO to N_2 in an oxygen rich gas mixture (Fig. 4). Using the steady state material balance equation, the reaction rate per surface area r_A of a given reaction was calculated for a given flow rate $\dot{V}$ with the help of the concentration values of the reaction components in the incoming $\left(c_i^0\right)$ and the effluent (c_i) flow according to Eq. (3):

$$r_A = \frac{\dot{V}}{A}\left(c_i^0 - c_i\right) \tag{3}$$

The quantum yield, Q (%), was defined as a parameter to characterize the reaction system:

$$Q = \left(\frac{r_A}{I_p}\right)100 \tag{4}$$

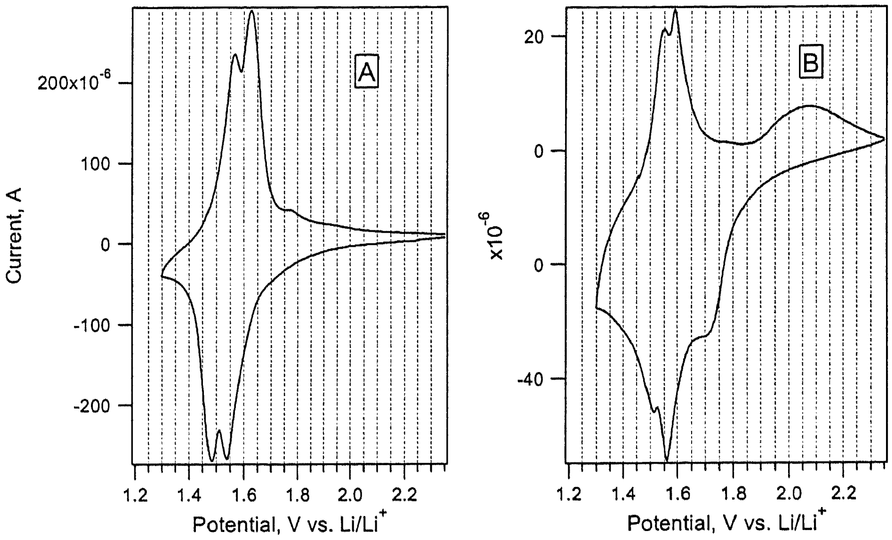

Fig. 3. Cyclic voltammograms of samples A (chart A) and B (chart B) in 1 M $LiN(CF_3SO_2)_2$ + EC/DME (1/1 v/v); scan rate 0.1 mV/s. The mass of active material was different for each particular electrode in charts A and B.

wherein I_p denotes the moles of photons absorbed per second and geometric surface area of the photocatalytically active plate.

For the total oxidation of propane, the reaction rates normalized per 1 m^2/g of the BET surface area of the catalyst were determined to be $1.37 \times 10^{-10}\ \mathrm{mol\ s^{-1}\ m^{-2}\ g}$ and $2.5 \times 10^{-10}\ \mathrm{mol\ s^{-1}\ m^{-2}\ g}$ for the sample A and Hombifine N, respectively. Considering the different phase composition of both the catalysts, it is interesting to note that the anatase-free monoclinic TiO_2(B) (sample A) and pure anatase (Hombifine N) exhibit comparable reaction rates per surface area. Even more interesting are the results obtained for the photocatalytic reduction of NO to N_2 in an oxygen rich gas mixture. The quantum yields of 0.46% and 5.84%

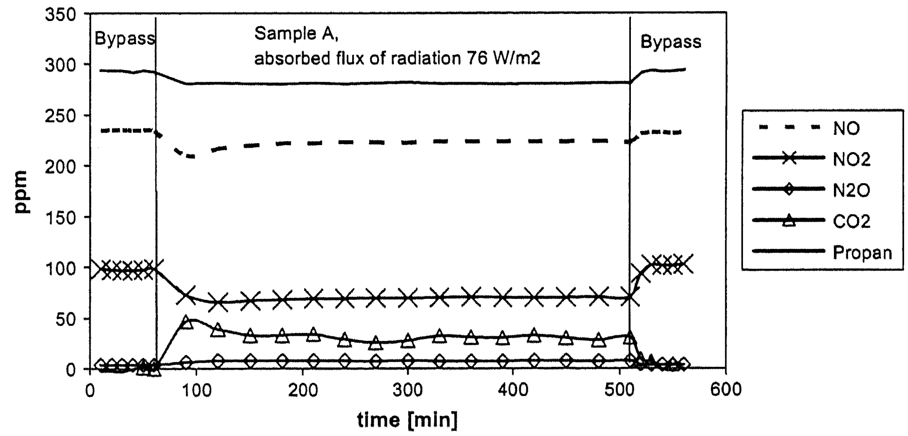

Fig. 4. Composition of the gas phase during the photocatalytic reduction of NO in an atmosphere containing 20% oxygen, using propane as the reducing agent (sample A).

were determined for our sample A and for Hombifine N, respectively. The ratio of these values (0.08) roughly equals to the ratio of their BET surface areas (0.09). However, the special feature of the sample A is its high selectivity with respect to the NO reduction. Using Hombifine N, 0.8 molecules of propane are needed to reduce one molecule of NO to 0.5 N_2, while if monoclinic TiO_2(B) is employed, only 0.4 molecules of propane are sufficient to reduce one molecule of NO. Since we are just in the beginning of the screening of the photocatalytic activity of TiO_2(B) prepared by our protocol, we are far from understanding the reasons of such a behavior. In any case, the results obtained until now encourage us to continue in photocatalytic experiments on TiO_2(B) and as the next step to verify its activity and selectivity during a long time photocatalytic process.

4. Conclusions

Nanostructured phase pure TiO_2(B) with microfibrous morphology was synthesized by the newly developed protocol employing amorphous TiO_2 as a raw material. Compared to TiO_2(B) obtained via traditional syntheses from $K_2Ti_4O_9$ [1], the new product exhibited better electrochemical performance and stability. Cyclic voltammetry of Li-insertion into the TiO_2(B) lattice confirmed pseudocapacitive faradaic process of Li accommodation, basically different from lithium storage in anatase whose kinetics is controlled by solid-state diffusion of Li^+. The detection of S-peaks proving the presence of TiO_2(B) represents a sensitive and easy analytical tool for the identification of this phase in titania materials.

The total oxidation of propane with oxygen and the photocatalytic reduction of NO to N_2 in an oxygen rich gas mixture were used for the evaluation of photocatalytic activity of synthesized material in a gas phase. In spite of the different phase composition of either the newly synthesized monoclinic TiO_2(B) or the standard Hombifine N, the reaction rates of the total oxidation of propane per unit of the BET surface area of the catalyst were comparable. In case of the photocatalytic reduction of NO to N_2 the quantum yields for both the sample A and Hombifine N are proportional to their BET surface areas. In addition to this, the sample A exhibits higher selectivity in the photocatalytic reduction of NO as compared to the standard material.

Acknowledgement

This work was supported by the Grant Agency of the Czech Republic (contract No. 203/03/0824) and by the EC-COST D35 Action, contract No. D35.002-1P05OC069. M.Z. also thanks the Grant Agency of the Czech Republic for financial support (through grant No. 203/03/H140).

References

[1] Marchand R, Brohan L, Tournoux M. Mater Res Bull 1980;15:1129.
[2] Feist TP, Davies PK. J Solid State Chem 1992;101:275.
[3] Andersson S, Wadsley AD. Acta Crystallogr 1962;15:194.
[4] Zachau-Christiansen B, West K, Jacobsen T, Skaarup S. Solid State Ionics 1992;53–56:364.
[5] Kawamura H, Muranishi Y, Miura T, Kishi T. Denki Kagaku 1991;59:766.
[6] Zachau-Christiansen B, West K, Jacobsen T, Atlung S. Solid State Ionics 1988;28–30:1176.
[7] Brohan L, Marchand R. Solid State Ionics 1993;9–10:419.
[8] Armstrong AR, Armstrong G, Canales J, Bruce PG. Angew Chem Int Ed 2004;43:2286.
[9] Nuspl G, Yoshizawa K, Yamabe T. J Mater Chem 1997;7:2529.

[10] Kasuga T, Hiramatsu M, Hoson A, Sekino T, Niihara K. Langmuir 1998;14:3160.
[11] Nishizawa H, Aoki Y. J Solid State Chem 1985;56:158.
[12] Kavan L, Kalbac M, Zukalova M, Exnar I, Lorenzen V, Nesper R, et al. Chem Mater 2004;16:477.
[13] Wang K, Morris M, Holmes JD. Chem Mater 2005;17:1269.
[14] Kavan L, Rathousky J, Grätzel M, Shklover V, Zukal A. J Phys Chem B 2000;104:12012.
[15] Yu J, Yu H, Cheng B, Zhao X, Yu JC, Ho W. J Phys Chem B 2003;107:13871.
[16] Linsebigler AL, Lu G, Yates JT. Chem Rev 1995;95:735.
[17] Yin S, Fujishiro Y, Wu J, Aki M, Sato T. J Mater Process Technol 2003;137:45.
[18] Yin S, Wu J, Aki M, Sato T. Int J Inorg Mater 2000;2:325.
[19] Betz G, Tributsch H, Marchand R. J Appl Electrochem 1984;14:315.
[20] Zhang H, Finnegan M, Banfield JF. Nano Lett 2001;1:81.
[21] Kavan L, O'Regan B, Kay A, Grätzel M. J Electroanal Chem 1993;346:291.
[22] Nazeeruddin MK, Kay A, Rodicio I, Humphry-Baker R, Mueller E, Liska P, et al. J Am Chem Soc 1993;115:6382.
[23] Kavan L, Grätzel M, Rathousky J, Zukal A. J Electrochem Soc 1996;143:394.
[24] Sasaki T, Nakano S, Yamauchi S, Watanabe M. Chem Mater 1997;9:602.
[25] Sasaki T, Watanabe M. J Am Chem Soc 1998;120:4682.
[26] Choy JH, Lee HC, Jung H, Kim H, Boo H. Chem Mater 2002;14:2486.
[27] Tournoux M, Marchand R, Brohan L. Prog Solid State Chem 1986;17:33.
[28] Wallenberg LR, Sanati M, Andersson A. Microsc Microanal Microstruct 1990;1:357.
[29] Kavan L, Kratochvilová K, Grätzel M. J Electroanal Chem 1995;394:93.
[30] Lindström H, Södergen S, Solbrand A, Rensmo H, Hjelm J, Hagfeldt A, et al. J Phys Chem B 1997;101:7717.
[31] Van de Krol R, Goossens A, Schoonman J. J Phys Chem B 1999;103:7151.